Characterisation of a turbulent separation over a ramp : entrainment and scaling laws

Francesco Stella

Centre Val de Loire UNIVERSITÉ Spirit of the Loire Valley

UNIVERSITÉ D'ORLÉANS

UNIVERSITE D'ORLEANS

ÉCOLE DOCTORALE ÉNERGIE, MATÉRIAUX, SCIENCES DE LA TERRE ET DE L'UNIVERS

Laboratoire PRISME

Thèse présentée par :

Francesco STELLA

soutenue le : **24 novembre 2017**

pour obtenir le grade de : **Docteur de l'Université d'Orléans**

Discipline : **Mécanique des fluides**

Caractérisation d'un décollement turbulent sur une rampe : entraînement et lois d'échelle

Characterisation of a turbulent separation over a ramp: entrainment and scaling laws

THÈSE DIRIGÉE PAR :

Azeddine KOURTA	Professeur, Université d'Orléans

RAPPORTEURS :

Olivier CADOT	Professeur, ENSTA-ParisTech
Luminita DANAILA	Professeur, Université de Rouen

JURY :

Jacques BORÉE	Professeur, ENSMA Poitiers
Olivier CADOT	Professeur, Université de Liverpool
Luminita DANAILA	Professeur, Université de Rouen
Eric GARNIER	Chercheur ONERA, HDR, ONERA Meudon
Azeddine KOURTA	Professeur, Université d'Orléans
Nicolas MAZELLIER	Maître de Conférences, Université d'Orléans
Jean-Pierre ROSENBLUM	Ingénieur, Dassault Aviation

La ciencia lo dijo y yo no miento.
A. Del Mono

Acknowledgments

I wish to thank my supervisors Prof. Azeddine Kourta and Dr. Nicolas Mazellier for giving me the opportunity of getting back to the academic world and prove myself as a PhD student. Their time, their ideas and insights, their loyalty and support throughout these three years were key ingredients of this work, as well as powerful stimulants for my scientific and professional growth. I also thankfully acknowledge the whole ESA team of the PRISME Laboratory for their warm welcome and the friendly work environment. In particular, Raffaele, Kevin, Audrey, Sophie, Pierric and even the terrible kids Marco and Stefano were fellow slaves of science with whom I shared a part of this journey. I would like to express my special gratitude towards Mr Stephane Loyer for his help in the design and set-up of experiments, and for its patience considering my destructive way of taming the secrets of hot-wire anemometry.

Until not so long ago, this might have been the full extent of my acknowledgments. Indeed, in the past, I often found that pages upon pages of head-bowing to friends, family and household gods were rather misplaced in scientific and technical works. "What did these people *actually do*?" - I used to think, while skipping to the hard, scientific matter.

Arrogant fool.

This PhD thesis is the work of a larger team than the one at the lab, that inspired me, supported me and cheered me up during the hard times. I warmly thank the ADSO crew: Clément, Maxime, Wilfried, Alba, Dounia, Alexey and Chloé, among many others, made my arrival and stay in Orléans much happier and easier. Each one of us was overwhelmed by his or her own scientific chaos, but at the same time we were all in it together. Sophie and Thomas-the-air-commander deserve a special place in this list: their generosity, their kindness and their wine cellar make me feel at home away from home. However, I want to take this opportunity to officially state that I will *not* take a cat.

I have a spiritual debt towards the precursors and inspirers of this whole PhD journey: Nacho and Pancho (with both of whom I might have *actual* debts for all the sushi), Victor (the answer is always 42), Txema and Raoul. Who is the oompa-loompa of science now? I also wish to thank Prof. Bordeneuve-Guibé, at ISAE/ENSICA, for his encouraging piece of advice on that old idea of looking for a PhD opportunity: it really worked!

I want to thank my whole family for their support and apologize in advance for all the wisdom that my PhD will now allow me to bestow on them, especially when unasked for. I thank my household gods (of course), the AC/DC for their energy, A. Del Mono for its deepness of mind.

But above all, I must thank the mighty oak that supports (and still stands) all my scheming and complaining. Thanks, Aud, for being here.

Contents

In this table of content, blue online indicates summaries in French.
Dans cette table des matières, la couleur bleue indique des résumés en Français.

List of Figures

List of Tables

Part I

Introductory matter

Introduction

Il existe de nombreuses raisons qui ont poussé la communauté scientifique à s'intéresser aux décollements turbulents massifs. En effet, ces écoulements surgissent dans un grand nombre d'applications industrielles, par exemple à l'arrière de corps épais (comme les véhicules terrestres) ou profilés (des ailes d'avions ou des ailette à haute incidence), à l'intérieur de chambres de combustion, de turbines et de oléoducs. Dans la plupart de ces situations, le décollement est l'une des sources principales de pertes aérodynamiques (par augmentation de la traînée, diminution de la portance ou les deux en même temps) et d'autres nuisances importantes comme des niveaux de bruit plus élevés ou des charges instationnaires plus intenses, conduisant sur le long terme à un vieillissement accéléré des structures. Dans certains cas, le décollement empêche d'utiliser ces systèmes à leur point de fonctionnement nominal, par exemple dans les prises d'air de certains moteurs à turbo-jet (Kumar & Alvi (2005)). Dans d'autres cas, les risques induits par le décollement sont si élevés, qu'on est prêt à accepter des solutions techniques onéreuses pour le retarder : un bon exemple est donné par les dispositifs d'hypersustentation des avions de ligne modernes, qui seraient superflus si la configuration *lisse* de l'aile ne décrochait pas aux incidences typiques du décollage et de l'atterrissage (voir par exemple Selby *et al.* (1992)). Ironiquement, le décollement est un problème même quand il est provoqué intentionnellement, comme dans les cas des freins aérodynamiques (*airbrakes*) ou des dispositifs de destruction de la portance (*spoilers*) : ces engins sont souvent lourds, ils demandent une maintenance coûteuse[1] et ils augmentent la traînée de façon efficace seulement à haute vitesse. Il apparaît donc que des solutions fiables pour la prédiction et le contrôle des décollements turbulents massifs apporteraient des gains économiques importants (à la fois sur les coûts de production et sur ceux d'exploitation) et un niveau de sécurité amélioré.

Ces considérations sont à la base de l'intérêt que suscitent, depuis longtemps, les écoulement décollés, dont l'étude commence probablement avec les travaux d'Eiffel sur la traînée aérodynamique et avec ceux de Prandtl et von Kármán sur le décollement à l'arrière d'un cylindre circulaire (voir Schlichting *et al.* (1968) et ses références). Ces premiers travaux avaient déjà identifié certaines des principales caractéristiques des écoulements décollés, en particulier la présence d'une large bulle de recirculation, dans laquelle la direction de la composante principale de la vitesse s'inverse, et le rôle important que la géométrie et le gradient de pression ont dans le déclenchement du décollement. Cette période a aussi porté les premiers essais de contrôle de décollement, par exemple avec une action sur la couche limite amont : la plupart des manuels racontent comment Prandtl a obtenu un recollement complet de l'écoulement autour d'un cylindre, en forçant la transition turbulente de la couche limite avec un fil. Entre les année 1940 et 1970, la compréhension des écoulements décollés à l'arrière de corps épais et profilés (souvent ressemblant sinistrement à des projectiles ou à des ogives de missile) a progressé, et elle a été étendue aux écoulements transsoniques et supersoniques[2]. Chapman *et al.* (1958) a mis en évidence l'importance de la couche cisaillée qui se développe, dans la plupart de ces écoulements, autour de la bulle de recirculation. L'optimisation de la traînée de pression et son contrôle par aspiration ou soufflage ont été longuement discutés au cours de ces années : des revues critiques des différentes théories proposées et de leurs résultats sont données par Nash (1963) et Nash (1967). Dans un effort similaire pour caractériser la traînée de pression, Roshko & Lau (1965) ont étudié la distribution de pression pariétale à l'aval de plusieurs corps épais. Leur travail a montré que, dans plusieurs cas, les distributions collapsent sur la même courbe universelle, si elles sont normalisées en utilisant la taille de la bulle de recirculation (indiquée avec le symbole L_R) et la pression dans la première moitié de la bulle

[1] Les réglementations sur la navigabilité EASA classifient l'ouverture asymétrique d'un *spoiler* de descente rapide parmi les pannes catastrophiques.

[2] L'impulsion des besoins belliqueux de la guerre froide est caractéristique des publications de cette période

(surnommée *pression de base*).

Progressivement, les recherches ont été concentrées sur un nombre limité de géométries, proposées comme prototypes des écoulements présentant un décollement et ensuite un recollement plus à l'aval. Des rampes de forme différente ont été adoptées, mais depuis les années 1970 la marche descendante (ou *backward-facing step*, BFS) est sûrement devenue l'objet principal des études sur les décollements massifs, grâce à sa géométrie simple, qui est un avantage important pour les simulations numériques, et son usage répandu dans les diffuseurs et les corps épais. En parallèle, de nouvelles techniques de vélocimétrie optique, comme la vélocimétrie laser Doppler (LDV) et ensuite la vélocimétrie par images de particules (PIV), ont commencé à fournir des mesures fiables de la vitesse et de la turbulence à l'intérieur de la bulle de recirculation, offrant ainsi une solution à l'un des principaux problèmes des expérimentateurs des périodes antérieures et ouvrant la voie à une nouvelle compréhension du fonctionnement interne des écoulements décollés. Leur simulation numérique a également concentré beaucoup d'efforts, initialement basés sur des équations de transport moyennées (*Reynolds Averaged Navier-Stokes equations*, ou RANS) et des modèles qui en ont été dérivés (Armaly *et al.* (1983), Obi *et al.* (1993) and Durbin (1995)). La disponibilité accrue de moyens de calcul de plus en plus puissants et accessibles a rendu possible le développement et l'amélioration continue des simulations complètements résolues, c'est-à-dire de la simulation numérique directe (*Direct Numerical Simulation*, DNS), et de simulations filtrées comme la simulation des grandes échelles (*Large Eddy Simulation*, LES). Sur ces bases, a été bâtie une image générale relativement complète de l'écoulement BFS, au moins dans un sens statistique. Ce travail se concentre sur les décollement *turbulents* massifs : de ce fait, seuls les écoulements de marche descendante turbulents sont considérés dans la synthèse proposée dans les paragraphes suivants. Ces écoulements consistent généralement en une expansion soudaine (souvent asymétrique, comme dans la figure 1.1), qui provoque un fort gradient de pression adverse favorisant le décollement. Ils ont généralement une seule large bulle de recirculation (mais Armaly *et al.* (1983) en a observé plusieurs dans des décollements transitionnels) statistiquement bidimensionnelle, avec une ligne de séparation relativement droite (Eaton & Johnston (1981)) : d'habitude L_R peut être définie de façon simple, comme la distance longitudinale entre le point de décollement et le point de recollement. Une couche cisaillée décollée se développe entre la bulle de recirculation et l'écoulement libre, en se comportant au départ comme une couche cisaillée libre (voir la revue par Simpson (1989)). La couche cisaillée décollée s'épaissit et ensuite percute la paroi au point de recollement, au-delà duquel elle donne naissance à une nouvelle couche limite. Cette dernière se réorganise assez lentement, parce que des traces de la couche cisaillée décollée perdurent dans l'écoulement sur une distance égale à plusieurs dizaines de hauteurs de marche (Simpson (1989), Song & Eaton (2003), Song & Eaton (2004) parmi d'autres).

Des efforts importants ont aussi été dediés à la compréhension des mécanismes instationaires complexes typiques de la couche cisaillée décollée, qui sont caracterisés par une large gamme d'échelles temporales et spatiales qui s'influençant reciproquement. Dans leurs études sur des écoulements BFS et des écoulements au-dessus de rampes, Eaton & Johnston (1981), Cherry *et al.* (1984), Friedrich & Arnal (1990), Le *et al.* (1997) and Kourta *et al.* (2015) ont observé qu'à des valeurs moderées du paramètre Re_h, qui est le nombre de Reynolds basé sur la hauteur de la marche, le point de recollement oscille longitudinalement, avec un mouvement dit de pulsation ou *flapping* (pourtant, cette pulsation n'a pas été observée dans la DNS et la LES de Dandois *et al.* (2007), au-dessus d'une rampe arrondie). Dans le même temps, l'existence d'une instabilité convective (Huerre & Monkewitz (1990)) a aussi été rapportée (Aubrun *et al.* (2000) et Kourta *et al.* (2015) parmi d'autres), qui serait similaire à la convection de structures à grande échelle typiques des couches cisaillées libres (Brown & Roshko (1974)). L'instabilité convective a été ciblée par des systemes de contrôle actifs, dans des expériences aussi bien que dans des simulations numériques, par exemple par Sigurdson (1995) et dans la LES de Dandois *et al.* (2007). Plus généralement, Le *et al.* (1997) a montré pour un écoulement BFS que la contribution à la production d'énergie cinetique turbulente, à son transport et à sa dissipation apportée par les échelles à haute fréquence et nombre d'onde est significative.

Malgré des efforts considérables, les décollements au-dessus de marches et de rampes se sont révélés difficiles à percer expérimentalement, au point que même les comportements de grandeurs du champ moyen comme L_R et la distribution de pression moyenne à la paroi manquent d'explications complètes. Durst & Tropea (1981) (parmi d'autres) ont montré que L_R est influencée par le rapport d'expansion ER, défini comme le rapport entre la section de l'écoulement à l'amont de la marche et celle à l'aval. Armaly *et al.* (1983) ont étudié l'effet de Re_h, et en particulier de la transition de l'écoulement à l'amont d'un état laminaire à un état turbulent. Ces chercheurs ont trouvé que L_R augmente avec Re_h quant l'écoulement est

laminaire. Pour des valeurs plus élevées de Re_h, le comportement de L_R n'est pas monotone : elle diminue au cours de la transition et elle atteint une valeur constante quand l'écoulement est complètement turbulent. Malheureusement, des tendances discordantes ont été observées (voir Eaton & Johnston (1981) pour une revue) et même Armaly *et al.* (1983) suggèrent que Re_h pourrait ne pas être un paramètre de similitude générique. Les désaccords semblent être liés, au moins en partie, à d'autres facteurs. Par exemple, Adams & Johnston (1988*b*) ont montré qu'une partie de la dispersion des mesures de L_R pourrait être imputée à l'influence de la turbulence résiduelle de l'écoulement extérieur, comme observé aussi par Isomoto & Honami (1989). Le rôle du gradient de pression a été mis en évidence par Kuehn (1980). Bradshaw & Wong (1972) ont révélé que le rapport entre l'épaisseur de la couche limite amont et la hauteur de la marche est aussi un paramètre qui affecte l'écoulement, en particulier au recollement. A ce propos, Adams & Johnston (1988*a*) ont trouvé que la couche limite amont peut influencer l'augmentation de pression qui a lieu au recollement, si elle est suffisamment épaisse par rapport à la hauteur de la marche. Des résultats concordants avec ces observations sont rapportés aussi par Westphal *et al.* (1984) et Jović (1998). Ce dernier travail analyse aussi l'évolution du coefficient de frottement à la paroi : de façon inattendue, les résultats confortent Re_h comme paramètre de similitude. Plus récemment, Nadge & Govardhan (2014) ont étudié systématiquement les effets de Re_h et ER, en gardant tous les autres paramètres pouvant affecter l'écoulement BFS constants ou dans des gammes de variation suffisamment petites pour être (considérées) négligeables. Ces chercheurs ont observé que la structure de l'écoulement devient indépendante de Re_h et ER, si Re_h est suffisamment élevé, en accord avec des travaux antérieurs. Les effets rajoutés par une marche inclinée (c'est-à-dire une rampe ou un diffuseur) ont été étudiés par Westphal *et al.* (1984) et Cherry *et al.* (2008) parmi d'autres. A ce propos, les données de Ruck & Makiola (1993) montrent que L_R diminue avec α, qui est l'inclination de la rampe (la marche descendante correspondant à $\alpha = 90^\circ$), et que le décollement peut ne pas se déclencher si α est suffisamment petit par rapport aux propriétés de la couche limite amont. De toute façon, Ruck & Makiola (1993) suggèrent aussi que l'écoulement de rampe devrait être qualitativement similaire à celui du BFS, par exemple pour ce qui concerne les dépendances en Re_h, si la valeur de α dépasse 20° - 30°. La prédiction numérique du décollement et les efforts pour le contrôler ont, eux aussi, rencontré des problèmes complexes. D'un côté, la plupart des application industrielles sont caractérisées par des nombres de Reynolds très grands, rarement à la portée des DNS ou même des LES à haute résolution (Šarić *et al.* (2007)). Cela implique que la prédiction des décollements turbulents ne peut s'appuyer que sur des simulations fortement filtrées, comme des LES à maillage grossier, ou sur des modèles basés sur les équations RANS, ou sur des méthodes hybrides RANS-LES (*Detached Eddy Simulation*, DES). Malheureusement, les prédictions de la LES dans un écoulement décollé sont vite détériorées par l'usage de maillages lâches (Temmerman *et al.* (2003), Kuban *et al.* (2012)), et les limites des modèles RANS du transport turbulent dans ces écoulements sont bien connues, en particulier pour ce qui concerne la prédiction de L_R, même dans les géométries les plus simples (voir par exemple Driver & Seegmiller (1985), Ahn *et al.* (1997), Garnier *et al.* (2012) et l'introduction de Mollicone *et al.* (2017)). D'un autre côté, l'identification des paramètres dimensionnant les écoulements décollés est essentielle à la conception de systèmes de contrôle efficaces et à leur extrapolation du laboratoire, vers l'échelle réelle des application industrielles. En fait, même dans le cas d'approches boîte noire, l'efficacité d'une boucle de contrôle dépend du dégré d'adéquation des paramètres de contrôle (par exemple, le choix et la position des capteurs et des actionneurs) et les caractéristiques de l'écoulement (par exemple ses fréquences naturelles et les régions sensibles). Pourtant, les interactions complexes entre des larges gammes d'échelles temporelles et spatiales, si typiques des écoulements turbulents, rendent la modélisation et la conception des systèmes de contrôle un vrai défi, auquel souvent on s'attaque en avançant par essais chronophages. Pour ces raisons, des études fondamentales, de nature expérimentale et numérique, sont encore nécessaires pour faire avancer la compréhension des mécanismes physiques qui pilotent les écoulements décollés.

Dans ce cadre, nous considérons qu'une piste prometteuse pourrait être ouverte par une analyse plus approfondie des propriétés de la couche cisaillée en général, et de l'entraînement en particulier. En fait, plusieurs travaux dans la littérature ont identifié l'influence de l'entraînement à travers la couche cisaillée sur tout le décollement. Chapman *et al.* (1958) ont été les premiers à faire l'hypothèse que le *backflow* (c'est-à-dire l'écoulement inversé qui rentre dans la bulle de recirculation) doit équilibrer la quantité de masse entraînée par la partie plus basse de la couche cisaillée décollée. Pour cela, l'entraînement à travers la couche cisaillée a un impact direct sur L_R, aussi bien que sur la distribution du coefficient de pression à la paroi C_p (voir Adams & Johnston (1988*a*), Adams & Johnston (1988*b*) et leurs références). Pour ce

qui concerne les simulations numériques, l'importance d'un calcul réaliste de la quantité de fluide entraîné par la couche cisaillée avait déjà été comprise par Friedrich & Arnal (1990). Dans le cadre du contrôle du décollement, le succès des stratégies de contrôle basées sur l'excitation des instabilités de la couche cisaillé (par exemple, pour faire varier L_R) est souvent expliqué en termes d'entraînement forcé dans la couche cisaillée (voir par exemple Sigurdson (1995) ou Barros *et al.* (2016) sur un décollement 3D à l'arrière d'un corps d'Ahmed). Récemment, Berk *et al.* (2017) ont expliqué l'interaction entre un jet synthétique et un écoulement BFS en termes d'entraînement, montrant aussi qu'en utilisant ce dernier on pourrait prédire les effets d'un actionneur sur L_R plus facilement qu'avec la fréquence d'actionnement normalisée. Chun & Sung (1996) ont mis en évidence qu'un entraînement plus intense est corrélé à un mélange turbulent plus fort dans la couche cisaillée décollée. D'autres chercheurs ont observé que des actionneurs passifs modifient l'entraînement dans la couche cisaillée aussi, en particulier en agissant sur le mélange turbulent dans la couche limite amont (Neumann & Wengle (2003), Neumann & Wengle (2004)).

Malgré son importance cruciale pour une prédiction fiable et pour le contrôle des écoulements décollés, la compréhension de la couche cisaillée décollée et de ses mécanismes d'entraînement semble largement inachevée. Premièrement, la discussion de la littérature disponible proposée ci-dessus, aussi bien que des revues plus étendues comme celles par Eaton & Johnston (1981), Adams & Johnston (1988*a*), Simpson (1989) et le travail de Nadge & Govardhan (2014), montrent que nous manquons de lois d'échelle quantitatives pour les décollements massifs, même s'il a été prouvé que L_R dépend de paramètres comme l'épaisseur et l'état (laminaire ou turbulent) de la couche limite amont, de Re ou de ER. De plus, le lien entre les caractéristiques à grande échelle comme L_R et la couche cisaillée décollée est généralement décrit qualitativement, et même alors rarement en considérant et en évaluant explicitement l'entraînement de fluide. Il semble donc nécessaire de combler ce vide et de proposer une image unique intégrant le développement de la couche cisaillée et ses dépendances, l'entraînement et les caractéristiques à grande échelle des décollements turbulents massifs.

Un problème annexe qui n'a pas été suffisamment considéré dans ces écoulements concerne l'échelle de la description de l'entraînement à travers la couche cisaillé. L'approche macroscopique adopté par la plupart des travaux sur les écoulement décollés semble incomplète quand elle est appliquée à l'étude de l'entraînement. En fait, la nature multi-échelle des interfaces turbulentes (et par conséquent des mécanismes de transfert) à travers lesquelles à lieu l'entraînement de fluide est bien connue au moins depuis le travail de Corrsin & Kistler (1955), et elle a été confirmée et exprimée dans le cadre de la théorie fractale par Sreenivasan & Meneveau (1986), Sreenivasan *et al.* (1989), Meneveau & Sreenivasan (1990) et plus récemment par Thiesset *et al.* (2016) parmi d'autres. Pour Corrsin & Kistler (1955), l'entraînement turbulent est un phénomène à petite échelle, fondamentalement visqueux, qui grignote (dont son surnom anglais de *nibbling*) des petites quantités de fluide irrotationnel en lui transférant de la vorticité. Dans la théorie de Corrsin & Kistler (1955), le *nibbling* est piloté par des sauts dans les champs de la vitesse et de la vorticité, qui ont lieu dans une couche visqueuse (le *viscous superlayer*) d'une épaisseur de l'ordre des plus petites échelles turbulentes de l'écoulement, qui se trouve à l'interface entre la région turbulente de l'écoulement de celle irrotationnelle. Cette interface est appelée TNTI, acronyme de l'anglais *Turbulent/Non Turbulent Interface*. Plus tard, un modèle alternatif pour l'entraînement a été proposé par Townsend (1966). Dans ce modèle, l'entraînement est un processus en deux étapes (Taveira *et al.* (2013)), dominé par les grandes échelles. La première étape ne fait pas intervenir la viscosité : les grandes échelles de la turbulence entraînent des poches de fluide extérieur dans la région turbulente de l'écoulement. Pendant la seconde étape, fondamentalement similaire au *nibbling*, la vorticité diffuse dans les poches irrotationnelles. En anglais, ce processus d'inclusion a été nommé *engulfment*. Initialement, les études expérimentales des années 1970 ont plutôt étayé ce modèle d'entraînement à grande échelle, surtout après que des grandes structures turbulentes ont été identifiées dans les couches cisaillées libres (Brown & Roshko (1974)). Au cours des dernières décennies, pourtant, le développement de techniques efficaces de vélocimétrie par images (comme la fluorescence induite par laser, PLIF, et la PIV) et la disponibilité accrue de jeux de données DNS ont permis d'observer d'amples portions de la TNTI et des champs de vitesse et de vorticité qui l'entourent, ouvrant la voie à une évaluation fine des flux qui traversent la TNTI. Ces nouvelles mesures ont confirmé l'existence d'une surcouche visqueuse et montré que dans plusieurs écoulements comme les jets turbulents (Westerweel *et al.* (2005), Westerweel *et al.* (2009), da Silva & Taveira (2010), Taveira *et al.* (2013)) et les couche limites turbulentes (Chauhan *et al.* (2014*c*), Borrell & Jiménez (2016)) les petites échelles sont, en fait, responsable de la plupart du transfert de masse à travers la TNTI. Toutefois, le rôle des grandes échelles a été

confirmé dans d'autres écoulements, par exemple dans les sillages (Bisset *et al.* (2002)). D'autres travaux, par exemple Hunt *et al.* (2006), Hunt *et al.* (2010) et da Silva & dos Reis (2011), ont montré l'importance des interactions locales entre la TNTI (ou d'autres interfaces turbulentes) et les grandes échelles. Philip & Marusic (2012) ont aussi suggéré que le poids relatif du *nibbling* et de l'*engulfment* pourrait changer d'un écoulement à un autre, en fonction du comportement des grandes échelles. Des conclusions similaires ont été tirées par Zhou & Vassilicos (2017), sur la base de la loi d'échelle de la dissipation de l'énergie cinétique turbulente. Même dans les écoulements dominés par le *nibbling*, ce dernier n'est pas bien corrélé à la turbulence à petite échelle (Holzner & Lüthi (2011)) : de ce fait, les grandes échelles doivent avoir une influence sur l'entraînement global (Krug *et al.* (2015)). En utilisant des données PLIF résolues dans le temps, Mistry *et al.* (2016) ont montré récemment que, pour un filtre de taille Δ, le flux de masse moyen à travers la TNTI d'un jet turbulent est indépendant de Δ, parce que le comportement fractal de la longueur de l'interface $L(\Delta)$ est compensée par la variation de $\boldsymbol{v_E}(\Delta)$, qui est la vitesse moyenne d'entraînement (c'est-à-dire la vitesse du fluide relative à l'interface) correspondante. Cela confirme les prédictions de Meneveau & Sreenivasan (1990) et conforte l'idée que l'entraînement turbulent est un phénomène multi-échelle, avec le transfert local (*nibbling*) s'adaptant aux taux d'entraînement globaux imposés par les grandes échelles. Ce concept peut être formulé comme dans l'éq. 1.1. Dans cette expression, les symboles $^{\nu}$ et ^{A} indiquent respectivement les quantités impliquées dans le *nibbling* et dans l'entraînement à grande échelle. L'éq. 1.1 pourrait avoir des implications importantes pour la modélisation numérique et la conception de systèmes pour le contrôle du décollement. D'un côté, elle semble indiquer qu'il serait possible de décrire correctement l'entraînement de fluide (et par consèquent le développement de la couche cisaillée, L_R et plusieurs autres quantités qui en résultent) à partir de simulations filtrées, au moins si les lois d'échelle de l'écoulement sont connues à toutes les échelles. De l'autre côté, l'éq. 1.1 suggère que des strategies visant l'excitation soit des petites échelles (celles caractéristiques de la dissipation d'énergie turbulente) soit des grandes (celles typiques de la production de l'énergie cinétique turbulente) peuvent également modifier l'entraînement. La première de ces deux approches comporte un actionnement à haute fréquence mais à basse énergie, tandis que le deuxième injecte beaucoup d'énergie à basse frequence. Cette séparation des fréquences d'excitation (et de leurs effets) en *hautes* et *basses*, par exemple par rapport à la fréquence naturelle de l'instabilité convective, n'est pas inhabituelle dans le cadre du contrôle du décollement. Par exemple, Wiltse & Glezer (1993) ont utilisé des actionneurs piézoélectriques pour contrôler une couche cisaillée décollée, en excitant directement les petites échelles. La fréquence d'excitation était un ordre de grandeur inférieure à la fréquence convective de l'échelle de Kolmorogov, mais beaucoup plus élevée que la fréquence naturelle des structures de la couche cisaillée. Cette stratégie a radicalement transformé la totalité de la cascade énergétique de la turbulence, sans pour autant changer l'écoulement moyen. Dandois *et al.* (2007) ont étudié l'effet de la fréquence de contrôle d'un jet synthétique sur le décollement au-dessus d'une rampe arrondie. Deux fréquences normalisée ont été testées, chacune produisant une forte variation de la longueur de recirculation, qui a été raccourcie par une basse fréquence de forçage mais allongée par une haute. Des comportements similaires ont été observés par Barros *et al.* (2016) sur un corps d'Ahmed. Plus généralement, Parezanović *et al.* (2015) a montré que les propriétés de la turbulence dans une couche cisaillée libre varient de façon différente, si la couche cisaillée est excitée à des fréquences beaucoup plus élevées ou beaucoup plus basses que la fréquence naturelle de l'instabilité convective. A ce propos, le travail de Berk *et al.* (2017) démontre clairement que l'entraînement peut fournir une clé d'interprétation alternative et puissante pour ces comportements, à la fois à haute et basse fréquence d'excitation.

Notre travail propose une nouvelle perspective sur les mécanismes physiques qui pilotent le développement des décollements turbulents massifs, en mettant l'accent sur l'entraînement turbulent de la masse à travers la couche cisaillée décollée. Nos objectifs principaux sont: 1) revisiter les dépendances et les lois d'échelle des décollements turbulents, avec une attention particulière pour celles qui règlent l'évolution de la couche cisaillée décollée; 2) étudier l'entraînement de la masse à travers la couche cisaillée décollée, avec une évaluation quantitative des échanges de masse entre les différentes régions de l'écoulement; 3) étudier l'influence des paramètres dimensionnant l'écoulement sur l'entraînement de masse, à grande aussi bien qu'à petite échelle. On ne peut qu'insister sur l'importance d'identifier les paramètres qui dimensionnent les décollements turbulents massifs (et l'entraînement en particulier) : ils sont la clé pour améliorer les modèles numériques pour la prédiction du décollement, aussi bien que la conception des systèmes de contrôle. Pour y parvenir, ce travail analyse expérimentalement l'évolution de la couche cisaillée décollée qui se développe sur une rampe descendante inclinée à 25°. L'écoulement, présenté dans la figure 1.2, est plutôt similaire

à l'écoulement BFS. Plus précisement, il a une seule bulle de recirculation avec un point de recollement instable. D'après Ruck & Makiola (1993), L_R devrait être comparable aux valeurs typiques des écoulements BFS, au moins si, sauf pour α, tous les autres paramètres de l'écoulement sont gardés constants. De façon similaire aux écoulements de marche descendante, une instabilité convective a été observée sur des rampes descendantes par Kourta *et al.* (2015). Nous avons utilisé deux rampes géométriquement similaires, mais avec des hauteurs de marche différentes. Cela nous a permis d'évaluer l'influence d'un ensemble de paramètres incluant 1.5 décade de Re_h, des rapports très différents entre l'épaisseur de la couche limite amont et la hauteur de la marche (δ_e/h) et presque une demi-décade d'un nombre de Reynolds turbulent relatif à la couche limite amont (Re_θ).

La particularité de notre étude est que les lois d'échelle de la couche cisaillée décollée sont étendues à l'entraînement de la masse. Dans ce cadre, un premier problème qui a été soulevé est lié au choix des frontières à travers lesquelles l'entraînement est estimé. Parmi plusieurs options, nous avons choisi d'analyser la TNTI et la ligne de séparation, qui sera indiquée avec l'acronyme RRI, de l'anglais *Recirculation Region Interface*. La TNTI se trouve entre la région cisaillée et l'écoulement extérieur. Ce dernier étant potentiel, la TNTI peut être considérée comme la frontière supérieure de la couche cisaillée. Quant à la RRI, elle enveloppe la bulle de recirculation, c'est-à-dire qu'elle sépare le fluide à vitesse longitudinale positive de celui à vitesse négative. D'après les différentes définitions des épaisseurs de la couche cisaillée données par Dandois *et al.* (2007), la RRI (c'est-à-dire le lieu des points où la vitesse longitudinale est nulle, voir par exemple Simpson (1989)) n'est pas, en toute rigueur, une des frontières de la couche cisaillée. Pourtant, l'analyse de la RRI apparaît être d'importance fondamentale, parce que la RRI est représentative du recollement de la couche cisaillée : par exemple, nous rappelons que la RRI moyenne est communément utilisée pour déterminer L_R. Même si son comportement n'a pas été étudié de façon complète, la RRI n'est rien de plus qu'une ligne de niveau du champ de vitesse et dans ce sens elle rentre dans les définitions des surfaces turbulentes données par Pope (1988). De ce fait, on s'attend à ce que la RRI partage les principales caractéristiques d'autres interfaces turbulentes, comme par exemple la TNTI, et en particulier une nature multi-échelle et un rôle dans le processus d'entraînement.

Enfin, nous proposons une évaluation qualitative de toute la gamme d'échelles (tout du moins résolues) qui existe dans nôtre écoulement décollé. Une analyse échelle par échelle des interfaces turbulentes peut nous aider à atteindre cet objectif, parce qu'il a été observé que les plus grandes et les plus petites échelles qui plissent une interface turbulente (en particulier la TNTI) sont représentatives de la gamme d'échelles contenue dans tout l'écoulement (Sreenivasan & Meneveau (1986), da Silva & Pereira (2008), de Silva *et al.* (2013), Chauhan *et al.* (2014*c*)).

Ce document est organisé en cinq parties. En plus de cette introduction, la partie I présente les équations de transport utilisées dans tout le travail. La partie II décrit les montages expérimentaux, à savoir les installations où les essais ont été conduits, les maquettes expérimentales et les techniques de mesure employées. Une description à grande échelle de la couche limite amont, du décollement turbulent massif et de leurs connections est discutée dans la partie III. Les paramètres de dimensionnement de la couche limite décollée sont aussi analysés, en particulier le long de la TNTI moyenne et de la RRI moyenne. La partie IV est dédiée au comportement statistique des deux interfaces et à l'entraînement de masse, à grande et à petite échelle. Les conclusions et les perspectives pour des travaux futurs sont données dans la partie V.

1

Introduction

There is much to gain at investigating massively separated turbulent flows. Indeed, these flows are common in a number of industrial applications, encompassing bluff bodies such as ground vehicles, streamlined bodies such as wings and blades at high incidence/pitch angle, combustion chambers, turbines and pipelines. In most of these applications, flow separation is one primary cause of losses of aerodynamic performances (drag increase, lift decrease or both) and of other noticeable detrimental effects such as increased noise and intense unsteady loads, eventually leading to accelerated structural fatigue. In some cases, flow separation prevents the use of these systems at their nominal operative conditions, for example in the air inlets of some turbo-jet engines (Kumar & Alvi (2005)). In other cases, induced risks are so great that we are ready to accept costly designs in order to delay separation: for example, consider the complexity and the weight of high-lift devices of modern airliners, that could be avoided if the *clean* configuration of the wing did not stall at incidences typical of take-off and landing (see e.g. Selby *et al.* (1992)). Ironically, separation is problematic even when it is an intended effect, as for airbrakes and emergency lift dumpers on aircraft: these devices are often heavy, they impose costly maintenance[1] and they efficiently increase drag only at high velocity. It appears, then, that sizeable economic gains (both on design and operative costs) and enhanced safety could be attained by reliably predicting and controlling massively separated turbulent flows.

This motivates a long lasting interest in separated flows, that probably begins with the studies on drag conducted by Eiffel and the well-known works by Prandtl and von Kármán on the separated flow behind a circular cylinder (see Schlichting *et al.* (1968) and references therein). These early works already identified some of the characteristic features of separated flows, in particular the presence of large recirculation regions, in which the main velocity component of the flow is inversed, and the important role of geometry and of pressure gradients in the onset of separation. This pioneering period also saw the first efforts for separation control, for example by acting on the incoming boundary layer: most textbooks report how Prandtl obtained a complete reattachment of the cylinder flow, by forcing the turbulent transition of the boundary layer with a thin wire. Between the 1940s and the 1970s, our insight in separated flows behind bluff and streamlined bodies (often suspiciously ressembling to bullets or missile heads) progressed and was extended to transonic and supersonic flows[2]. Chapman *et al.* (1958) highlighted the importance of the separated shear layers that, in most of these flows, developes around recirculation regions. The optimisation of pressure drag and its control by suction or blowing actuators was discussed at length in those years: critical summaries of different theories and of their results are proposed by Nash (1963) and Nash (1967). In a similar effort to characterise pressure drag, Roshko & Lau (1965) studied the wall-pressure distributions behind several bluff bodies. They showed that in many cases pressure distributions collapse on a universal curve, when normalised based on the size of the recirculation region (indicated with the symbol L_R) and pressure within its first half (the so-called *base pressure*).

Researchers progressively focused on a limited number of geometries, proposed as prototypes of separating/reattaching turbulent flows. Ramps of various shapes were adopted, but since the 1970s the backward-facing step (BFS) has certainly become the main object of studies on massive separations, due to the simiplicity of its geometry, which is an advantage for numerical simulations, and its widespread use in diffusers

[1] EASA airworthiness regulation classifies the asymmetric deployment of emergency descent spoilers as a catastrophic failure.

[2] The impulse of the belligerant needs of cold war is characteristically evident in many publications of this period.

and bluff bodies. At the same time, new optical velocimetry techniques, as Laser Doppler Velocimetry (LDV) and later on Particle Image Velocimetry (PIV), provided reliable velocity and turbulence measurements within the recirculation region, thus solving one of the main problems of experimentalists of previous periods and allowing new understanding of the internal functionning of separated flows. Much attention was also dedicated to the numerical simulation of separated turbulent flows, initially relying on models based on Reynolds Averaged Navier-Stokes (RANS) equations (see for example Armaly *et al.* (1983), Obi *et al.* (1993) and Durbin (1995)). The availability of increasingly powerful and accessible computational means made also possible the development and the continuous improvement of fully resolved simulations, i.e. Direct Numerical Simulations (DNS), and of filtered simulations as Large-Eddy Simulations (LES). On these bases, we have attained a relatively complete general picture of BFS flows, at least in a statistical sense. This work focuses on *turbulent* massive separations: for this reason, only turbulent BFS flows are reviewed hereafter. They generally consist in a sudden expansion (often asymmetric, as in figure 1.1) resulting in a strong adverse pressure gradient, which promotes separation. They usually present one large, statistically bidimensional recirculation region (but multiple ones have been observed by Armaly *et al.* (1983) for flows within the turbulent transition regime), with a rather straight separation line (Eaton & Johnston (1981)): L_R can be usually defined simply, as the streamwise distance between the separation and reattachment point. A separated shear layer develops between the recirculation region and the free-stream, initially behaving similarly to a free shear layer (see the review by Simpson (1989)). The separated shear layer grows and eventually hits the wall at the reattachment point, beyond which the flow relaxes to a new boundary layer (Le *et al.* (1997)). The latter recovers very slowly, as the turbulent signature of the separated shear layer persists for many step heights downstream of reattachment (Simpson (1989), Song & Eaton (2003), Song & Eaton (2004) among others).

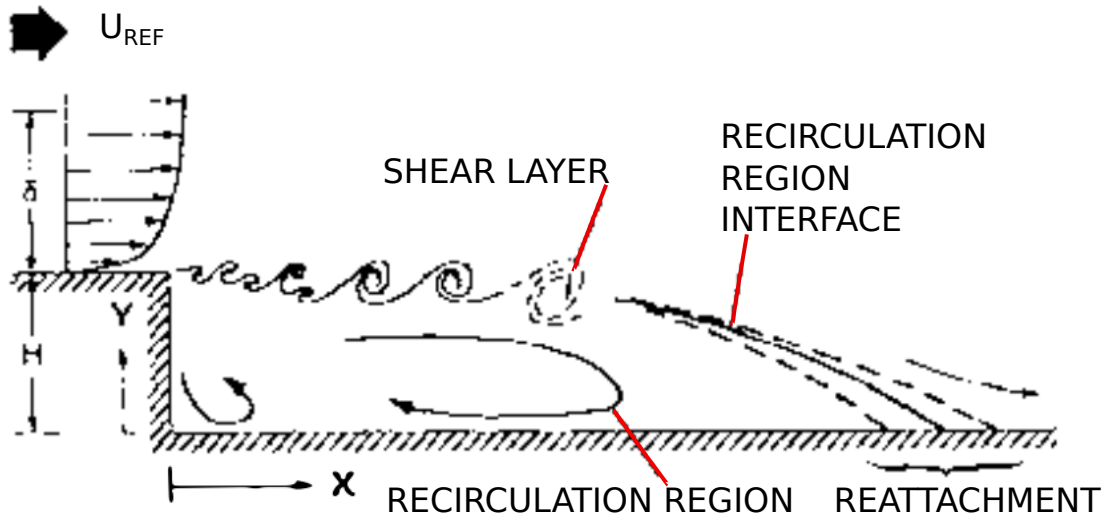

Figure 1.1: Schematic view of a backward-facing step flow. Adapted from Simpson (1989).

Important efforts have also been dedicated to understanding the complex, unsteady physics underlying separated shear layer development and reattachment, characterised by a wide range of time and length scales in mutual interplay. Eaton & Johnston (1981), Cherry *et al.* (1984), Friedrich & Arnal (1990), Le *et al.* (1997) and Kourta *et al.* (2015) observed that in BFS and ramps at moderate values of Re_h, the Reynolds number based on step height, the reattachment point exhibits a low frequency flapping motion (however the latter was not observed in the DNS and LES performed by Dandois *et al.* (2007) over a rounded ramp). At the same time, the existence of a convective instability (Huerre & Monkewitz (1990)) was also reported (Aubrun *et al.* (2000) and Kourta *et al.* (2015) among others), similar to the convection of large-scale structures typical of free shear layers (Brown & Roshko (1974)). The convective instability was targeted for purpose

of active control design, both in experiments and numerical simulations, for example by Sigurdson (1995) and in the LES by Dandois *et al.* (2007). More in general, Le *et al.* (1997) pointed out that in a BFS flow the turbulent production, transport and dissipation occurring at higher frequency/wavenumber ranges give significant contribution to the turbulent kinetic energy budget.

With little regard for our expectations, however, BFS and ramp flows proved hard to pierce experimentally, and even mean field features as the behaviours of L_R and of the mean wall pressure distribution still lack full understanding. Durst & Tropea (1981) (among others) highlighted that L_R is a strong function of the expansion ratio ER, defined as the ratio between the flow section downstream and upstream the step. Armaly *et al.* (1983) studied the effect of Re_h, and in particular of transition from a laminar to a turbulent incoming flow. They found that in the laminar regime L_R becomes longer for higher values of Re_h. For increasing Re_h, anyway, the behaviour of L_R is not monotonic: it decreases during transition and it reaches a constant value when the incoming flow is fully turbulent. However, contrasting trends have been observed by other researchers (see Eaton & Johnston (1981) for a review) and the very same work of Armaly *et al.* (1983) suggests that Re_h might not be a general similitude parameter. At least to some extent, discordances could be explained by other factors. For example, Adams & Johnston (1988*b*) showed that part of the L_R scatter might be due to the influence of free-stream turbulence, as also observed by Isomoto & Honami (1989). The role of the pressure gradient was stressed by Kuehn (1980). Bradshaw & Wong (1972) pointed out that the ratio between the thickness of the incoming boundary layer and height of the step is also a governing parameter of the flow, in particular at reattachment. In this respect, Adams & Johnston (1988*a*) found that the incoming boundary layer can affect pressure recovery at reattachment, if it is thick enough with respect to step height. Results consistent with their findings were also reported by Westphal *et al.* (1984) and Jović (1998). This latter work also investigated the evolution of skin friction: quite puzzling, this time results supported Re_h as a scaling parameter. More recently, Nadge & Govardhan (2014) made a systematic study of the effects of Re_h and ER, while all other parameters that can influence the BFS flow were kept constant or within (reportedly) negligibly narrow variations. These researchers found that the structure of the flow becomes independent of both Re_h and ER, if Re_h is high enough, in agreement with previous results. The effects of an inclined step (i.e. a ramp or a diverging duct) were studied by Westphal *et al.* (1984) and Cherry *et al.* (2008) among others. In this respect, data by Ruck & Makiola (1993) show that L_R decreases with the slope of the ramp α (the BFS flow corresponding to $\alpha = 90°$), and that the separation might not onset at all if α is sufficiently small with respect to the properties of the incoming boundary layer. Anyway, Ruck & Makiola (1993) also suggests that for values of α larger than 20°-30°, a ramp flow should be qualitatively similar to the BFS flow, for example for what concerns Re_h dependencies.

Research on numerical prediction of turbulent flow separation and on its control also encountered a number of complex issues. On one hand, most industrial applications feature very large Reynolds numbers, seldom reachable to DNS or even to highly resolved LES (Šarić *et al.* (2007)). This implies that the main vector to predict turbulent separations are strongly filtered simulations, as coarse-grid LES, or as models based on RANS equations, or as hybrid RANS-LES methods such as Detached Eddy Simulations (DES). Unfortunately, coarser grids have been shown to quickly deteriorate LES predictions of the properties of separated flow (Temmerman *et al.* (2003), Kuban *et al.* (2012)), and it is also well known that turbulence transport models used in RANS struggle at accurately predicting separating/reattaching flows, and in particular L_R, even in simple geometries (see e.g. Driver & Seegmiller (1985), Ahn *et al.* (1997), Garnier *et al.* (2012) and the introduction in Mollicone *et al.* (2017)). On the other hand, knowledge of the scaling parameters of separating/reattaching flows is essential to design efficient control systems and to ensure scalability from laboratory to full-scale applications. Indeed even for black box approaches, the effectiveness of a control loop will depend on how well design parameters (e.g. sensor/actuator choice and location) match flow parameters (e.g. natural frequency, sensitive regions). However, the complex physical interactions between a broad range of time and length scales, so typical of separated flows, make modeling and design of control systems a challenging issue, which is often addressed through time-consuming trial and error procedures. For these reasons, fundamental investigations, both of experimental and numerical nature, are still necessary to bring new insights in the physical mechanisms underlying separating/reattaching flows.

In this respect, we believe that a deeper analysis of shear layer properties in general, and of entrainment in particular, might be a promising path to follow. Indeed, many past works highlighted the influence of shear layer entrainment on separated flows. Chapman *et al.* (1958) were the first to postulate that the backflow (i.e. the reverse flow entering the recirculation region) must balance the amount of fluid that is entrained

by the bottom of the separated shear layer. As such, shear layer entrainment has a direct impact on the recirculation length L_R, as well as on the distribution of the pressure coefficient C_p (see Adams & Johnston (1988*a*), Adams & Johnston (1988*b*) and references therein). For what concerns numerical simulations, the importance of correctly computing the amount of fluid entrained by the separated shear layer was already identified in the LES by Friedrich & Arnal (1990). In the framework of flow control, instead, the relative success of control strategies based on forcing of shear layer instabilities (e.g. tuning of L_R) is often explained in terms of forced entrainment into the shear layer (see e.g. Sigurdson (1995) or Barros *et al.* (2016) on the 3D separated flow behind an Ahmed body). Interestingly, Berk *et al.* (2017) elegantly explained the interaction of a synthetic jet with a BFS flow in terms of entrainment, also showing that entrainment could be a more efficient predictor of the effect of the actuator on L_R than the normalised actuation frequency. Chun & Sung (1996) highlighted that increased entrainment is correlated to enhanced turbuled mixing in the separated shear layer. Other researchers showed that passive control actions also modify shear layer entrainment, in particular by acting on turbulent mixing in the incoming boundary layer (Neumann & Wengle (2003), Neumann & Wengle (2004)).

In spite of its crucial importance for reliable prediction and control of separated flows, the comprehension of the separated shear layer and of its entrainment mechanisms appears to be largely inachieved. For instance, the brief discussion of the available literature reported above, as well as more complete reviews as those by Eaton & Johnston (1981), Adams & Johnston (1988*a*), Simpson (1989) and the work of Nadge & Govardhan (2014), highlight that even if some dependencies of L_R and pressure distribution on parameters such as incoming boundary layer thickness and state (i.e. laminar or turbulent), Re or expansion ratio have been evidenced, quantitative scaling laws are often missing. Moreover, the link between large-scale features as L_R and the separated shear layer are generally described in a qualitative way, and even then seldom by explicitely considering and assessing entrainment through the separated shear layer. It seems then necessary to close this gap and propose a unique view integrating shear layer development and its dependencies, entrainment and large-scale features of massively separated turbulent flows.

An annexe problem that has not been extensively addressed in these flows concerns the scale of the description of shear layer entrainment. The macroscopic approach adopted by most past works on separated flows appears to be incomplete when applied to the investigation of entrainment. Indeed, the multiscale nature of the turbulent interfaces (and accordingly of the transfer mechanisms) through which entrainment takes place is known at least from the seminal work of Corrsin & Kistler (1955), and has been confirmed and expressed in the framework of fractal theory by Sreenivasan & Meneveau (1986), Sreenivasan *et al.* (1989), Meneveau & Sreenivasan (1990) and more recently by Thiesset *et al.* (2016) among others. Corrsin & Kistler (1955) interpreted turbulent entrainment fundamentally as a small-scale, viscous phenomenon, which nibbles bites of irrotational fluid into turbulence. Corrsin & Kistler (1955) theorised that such *nibbling* mechanism is driven by jumps in the vorticity and velocity fields, that take place at the so-called Turbulent/Non-Turbulent Interface (TNTI), on velocity and length scales that are of the order of the smallest scales of the flow (the so-called viscous superlayer). Later on, Townsend (1966) proposed an alternative, large-scale model for entrainment. In his view, entrainment is a two step process (Taveira *et al.* (2013)) dominated by large eddies. The first step is inviscid: large eddies drag pockets of external fluid into the turbulent bulk of the flow. In the second step, fundamentally similar to nibbling, vorticity is transferred to irrotational pockets by means of viscous diffusion. Based on its distinctive feature, this model is also known as the *engulfment* mechanism of entrainment. At first, experimental studies carried out during the 1970s seemed to support the leading role of engulfment in turbulent entrainment, in particular since large structures were identified in free shear layers (Brown & Roshko (1974)). During the last decades, however, the development of efficient image-based techniques (e.g. Planar Laser Induced Fluorescence (PLIF) and PIV) and the increased availability of DNS have given access to large portions of the TNTI and of the neighbouring velocity and vorticity fields, paving the way to finer assessment of fluxes through the TNTI. These new measurements confirmed the existence of a viscous superlayer and showed that in many flows as turbulent jets (Westerweel *et al.* (2005), Westerweel *et al.* (2009), da Silva & Taveira (2010), Taveira *et al.* (2013)) and turbulent boundary layers (Chauhan *et al.* (2014*c*), Borrell & Jiménez (2016)) small scales are actually responsible for most of mass transfer through the TNTI. However, the role of engulfment was confirmed in flows as wakes (Bisset *et al.* (2002)). Other works as Hunt *et al.* (2006), Hunt *et al.* (2010) and da Silva & dos Reis (2011) highlighted the importance of local interactions of the TNTI (or assimilable thin turbulent interfaces) with large eddies. Philip & Marusic (2012) also suggested that the relative weight of nibbling

and engulfment might change from flow to flow, depending on the behaviour of large-scale eddies. Similar conclusions were drawn by Zhou & Vassilicos (2017), based on scaling of the dissipation of turbulent kinetic energy. Even in flows dominated by nibbling, the latter was found to be poorly correlated to small-scale turbulence (Holzner & Lüthi (2011)): then, large scales do influence global entrainment (Krug *et al.* (2015)). Using time-resolved PLIF, Mistry *et al.* (2016) showed recently that, given a coarse-grain filter of size Δ, the mean mass flux through the TNTI of a turbulent jet is independent of Δ, since the fractal scaling of interface length $L(\Delta)$ is compensated by the scaling of $\boldsymbol{v_E}(\Delta)$, the corresponding mean entrainment velocity (i.e. the velocity of the fluid relative to the interface). This confirmed the predictions of Meneveau & Sreenivasan (1990) and gave support to the idea that turbulent entrainment is a multiscale phenomenon, with the local viscous transfer (nibbling) adapting to the global entrainment rate imposed by large scales, i.e.:

$$\boldsymbol{v_E}^{\nu} L^{\nu} = \boldsymbol{v_E}(\Delta) L(\Delta) = \boldsymbol{v_E}^{A} L^{A}, \tag{1.1}$$

where the symbols $^{\nu}$ and ^{A} indicate quantities respectively involved in nibbling and large-scale entrainment. Eq. 1.1 might have great implications in numerical modeling and in the design of control systems for separating/reattaching flows. On the one hand, it seems to imply that entrainment (and hence shear layer development, L_R and many related quantities) might be correctly reconstructed from filtered simulations, at least if the scaling laws of the flows are known at all scales. On the other hand, eq. 1.1 suggests that strategies targeting either small-scale forcing (dissipation range) or large-scale forcing (production range) can both achieve entrainment modification. The former approach implies high frequency/low energy forcing, whereas low frequency/high energy forcing is required for the latter. As already discussed, this distinction of forcing frequencies (and of their effects) in *high* and *low*, for example with respect to the natural frequency of the convective instability, is not unfamiliar in the context of separation control. For example, Wiltse & Glezer (1993) deployed direct small-scale excitation by means of piezoelectric actuators to control the shear layer of a jet. The excitation frequency was tuned to one order of magnitude lower than the convection frequency of the Kolmogorov scale, but was much larger than the natural roll-off frequency of the shear layer. This control strategy was able to alter significantly the entire cascade transfer of energy, while keeping the mean flow unchanged. Dandois *et al.* (2007) investigated the effect of control frequency of a synthetic jet on the separation over a rounded ramp. Two reduced frequencies were tested, each of these operating conditions leading to a strong modification of the recirculation length, which was reduced at low frequency forcing but increased at high frequency forcing. Similar findings are reported by Barros *et al.* (2016) on a Ahmed body. More in general, Parezanović *et al.* (2015) showed how turbulent properties of a free shear layer change if an external forcing is applied at frequencies that are much higher or lower of the natural frequency of the convective instability. In this respect, the work of Berk *et al.* (2017) cleary demonstrates that entrainment can provide an alternative, powerful interpretative key for these behaviours, both at high and low forcing frequency.

This work proposes a new perspective on the physical mechanisms governing the development of massively separated flows, centered on turbulent mass entrainment through the separated shear layer. Our main objectives are: 1) reviewing the dependencies and the scaling laws of massively separated flow, with a focus on the evolution of the separated shear layer; 2) performing an investigation of mass entrainment through the separated shear layer, with a quantitative assessment of mass exchanges between different regions of the flow; 3) investigating the influence of scaling parameters of the flow on mass entrainment, at both large and small scales. The importance of identifying the parameters that size massively separated flows (and entrainment in particular) cannot be stressed enough: they are the key to improve model-based, numerical prediction of flow separation and the design of control systems as well. To this end, this work experimentally investigates the evolution of the separated shear layer that develops behind a 25° descending ramp. The flow, represented in figure 1.2, is quite similar to a BFS flow. In particular, it has one single recirculation region with an unstable reattachment point. According to Ruck & Makiola (1993), L_R should be comparable to values typical of BFS flows, at least if parameters other than α are kept constant. Similarly to BFS flows, a convective instability was observed over descending ramps by Kourta *et al.* (2015). Two geometrically similar models were used, spanning different step heights. This allowed us to test the influence of a set of scaling parameters including 1.5 decades of Re_h, very different ratios of boundary layer thickness to step height (δ_e/h) and almost half a decade of a turbulent Reynolds number of the incoming boundary layer (Re_θ).

The specificity of our study, however, is that scaling laws of the separated shear layer are extended to

mass entrainment. In this respect, a first issue to be addressed relates to the choice of the boundaries through which entrainment will be estimated. Among other options, the choice was made of analysing the TNTI and the separation line, which will hereafter be called Recirculation Region Interface (RRI) for consistency. The TNTI lies between the free flow and the sheared region. Since the flow outside of the TNTI is unperturbed, in a way the TNTI can be considered as the upper boundary of the shear layer. The RRI, instead, wraps the backflow region, i.e. it separates positive mean streamwise velocities from negative ones. According to definitions of shear layer thickness reported in Dandois *et al.* (2007), the RRI (i.e. the set of points where the streamwise velocity is zero, see e.g. Simpson (1989)) is not, rigorously speaking, a boundary of the shear layer. However, the analysis of the RRI seems of fundamental importance, as the RRI is representative of shear layer reattachment: let us remind that the mean RRI is commonly used to determine L_R. Even if the behavior of the interface has not been thoroughly studied, the RRI is nothing more than a constant-velocity line and as such it falls in the definitions of turbulent surfaces given by Pope (1988). It is then expected that the RRI will share the salient characteristics of other turbulent surfaces, such as the TNTI, in particular a multiscale nature and a role in entrainment.

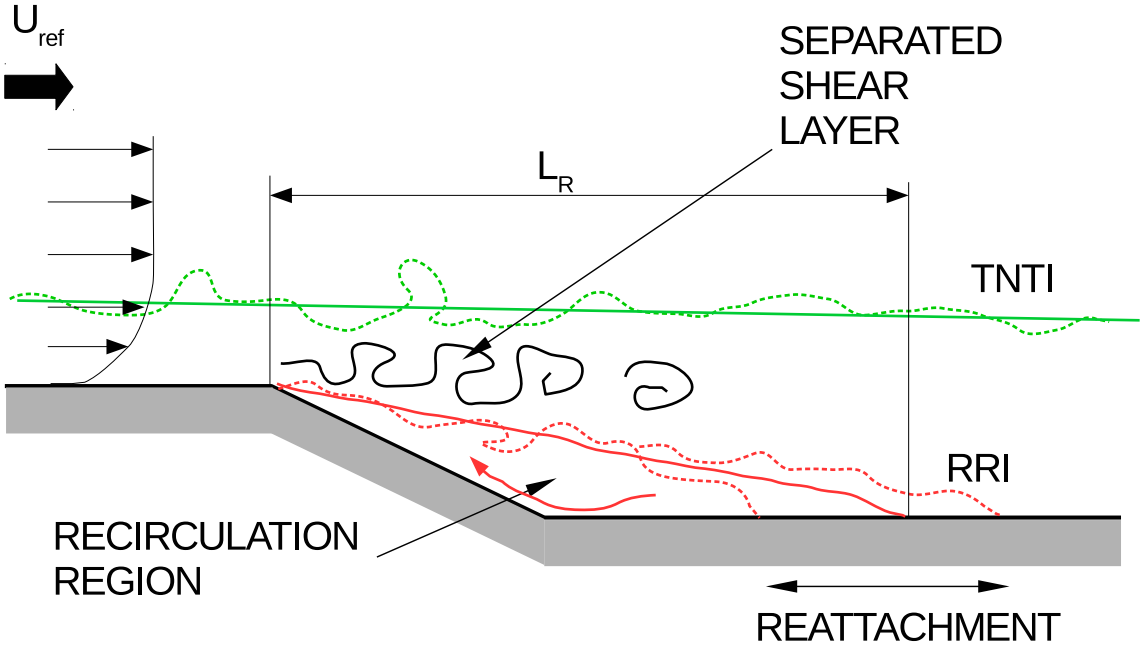

Figure 1.2: Schematic view of the turbulent separated flow behind a descending ramp. The TNTI is marked in green and the RRI in red. Dashed lines indicate instantaneous interfaces and solid lines mean interfaces.

Finally, we attempt a qualitative assessment of the full range of length scales that exists in our separating/reattaching flow. A scale-by-scale analysis of the turbulent interfaces might provide this kind of insight, because it has been observed that the largest and the smallest scales that wrinkle a turbulent interface (viz. the TNTI) are representative of the range of scales contained in the entire flow (Sreenivasan & Meneveau (1986), da Silva & Pereira (2008), de Silva *et al.* (2013), Chauhan *et al.* (2014*c*)).

The document is organised in five parts. Other than this introduction, Part I presents the transport equations used throughout this work. Part II describes the experimental set-up, including the facilities, the ramp models and the measurement techniques that were employed. A large scale characterisation of the incoming boundary layer, of the massively separated flow and of their connections is discussed in Part III. The scaling parameters of the separated shear layer are also analysed, in particular along the mean TNTI and the mean RRI. Part IV is dedicated to the statistical behaviour of the two interfaces and to mass entrainment, at both large and small scale. Conclusions and perspectives for future works are given in Part V.

2

Fundamental transport equations in local form

Equations de transport en forme locale

Ce chapitre présente les équations du transport de la masse, de la quantité de mouvement et de l'énergie cinétique. Leurs formes locales pour un fluide newtonien incompressible sont données respectivement par l'éq. 2.2 (équation de continuité), l'éq. 2.5 (équations de Navier-Stokes) et l'éq. 2.6 (équation de l'énergie cinétique). Lorsque l'écoulement est turbulent, le nombre de degrés de liberé est tellement grand qu'il est presque impossible d'extraire des mesures expérimentales toutes les informations requises pour resoudre ces équations. On utilise alors la fameuse décomposition de Reynolds (éq. 2.7) pour aboutir à des formulations moyennes, c'est-à-dire où les échelles de la turbulence sont filtrées et leur effets sont représentés uniquement par des paramètres globaux. On a donc l'éq. 2.9 pour le transport moyen de masse, l'éq. 2.10 pour la quantité de mouvement (indiquée avec l'acronyme anglais *RANS*, pour *Reynolds Averaged Navier-Stokes equations*) et l'éq. 2.11 pour l'énergie cinétique moyenne. L'équation de transport de l'énergie cinétique turbulente est aussi donnée dans l'éq. 2.12. Bien que nos données ne nous permettent pas d'estimer avec fiabilité les quantités impliquées, l'éq. 2.12 est un outil puissant, parce qu'elle met en évidence le rôle de la turbulence dans l'équilibre énergétique de l'écoulement.

2.1 Introduction

For future reference, this chapter presents the fundamental transport equations that express the balance of mass, momentum and kinetic energy that cross the boundaries of an eulerian fluid element. The so-called Reynolds decomposition, used throught this work, is also reported. Thorough demonstrations of these equations and of their properties can be found in Schlichting *et al.* (1968), Tennekes & Lumley (1972) and Pope (2000) among many others.

2.2 One point formulations

2.2.1 Equation of continuity

The continuity equation expresses the balance between the rate of change in density of the fluid within an eulerian fluid element and the quantity of fluid mass entering and leaving the element itself (Schlichting *et al.* (1968)). In its most general form, the continuity equation is written in tensor notation as follows:

$$\frac{\partial \rho}{\partial t} + \frac{\partial \rho u_i}{\partial x_i} = 0, \tag{2.1}$$

where the symbol ρ indicates density, u_i is one component of the velocity vector $\boldsymbol{u}$ and repeated indexes indicate summation. In this work, we only consider incompressible flows in which $\rho = const$. Then, eq.

2.1 reduces to:

$$\frac{\partial u_i}{\partial x_i} = 0, \tag{2.2}$$

which states that an incompressible velocity field is solenoidal, i.e. that deformations of the fluid element are always isochoric.

2.2.2 Navier-Stokes equations

The Navier-Stokes (NS) equations express the balance of momentum entering and leaving an eulerian fluid element and, in this respect, they are the adaptation to fluids of Newton's Second Law. A thorough demonstration of the NS equations is available in Schlichting *et al.* (1968), among others. Here we only report their general formulation in tensor notation for one fluid element, that is:

$$\frac{\partial \rho u_i}{\partial t} + u_j \frac{\partial \rho u_i}{\partial x_j} = \frac{\partial \sigma_{ij}}{\partial x_j} + \rho F_{Vi}. \tag{2.3}$$

In eq. 2.3, F_{Vi} are external volume forces (e.g. gravity) and σ_{ij} is the stress tensor. For newtonian fluids as air, the expression of σ_{ij} is given by:

$$\sigma_{ij} = -p\delta_{ij} + 2\mu s_{ij} - \frac{2}{3}\mu \frac{\partial u_i}{\partial x_i}\delta_{ij}, \tag{2.4}$$

where μ is the dynamic viscosity, $s_{ij} = \frac{1}{2}\left(\frac{\partial u_i}{\partial x_j} + \frac{\partial u_j}{\partial x_i}\right)$ is the rate of strain tensor and δ_{ij} is Kronecker's delta. For incompressible flows in which volume forces are negligible, as those investigated in this work, eq. 2.3 reduces to:

$$\frac{\partial u_i}{\partial t} + u_j \frac{\partial u_i}{\partial x_j} = \frac{1}{\rho}\frac{\partial \sigma_{ij}}{\partial x_j} = -\frac{1}{\rho}\frac{\partial p}{\partial x_i} + \nu \frac{\partial^2 u_i}{\partial x_j \partial x_j}, \tag{2.5}$$

in which $\nu = \mu/\rho$ is kinematic viscosity.

2.2.3 Kinetic energy equation

When investigating a turbulent flow, one of the most important aspects that must be taken into account is how energy is transported within the flow. In incompressible flows as those under study, the gas state equation loses significance and the velocity field becomes independent of the thermodynamic state of the fluid. A balance of kinetic energy is then sufficient to characterise transport of energy through the boundaries of a fluid element. The kinetic energy equation can be obtained by multiplying the NS equation by local velocity. With some manipulations, this leads to the following formulation:

$$\frac{\partial \rho u_i u_i/2}{\partial t} + u_j \frac{\partial \rho u_i u_i/2}{\partial x_j} = -u_j \frac{\partial p}{\partial x_j} + \nu \frac{\partial^2 \rho u_i u_i/2}{\partial x_j \partial x_j} - \mu \left(\frac{\partial u_i}{\partial x_j}\right)^2, \tag{2.6}$$

In addition to the usual terms due to instationarity, convection, pressure work and diffusion, the third term on the right-hand side of eq. 2.6 relates to the dissipation of kinetic energy into heat.

2.3 Reynolds-averaged formulations

Direct Numerical Simulation (DNS) is the ideal approach to study massively separated turbulent flows, as it gives access to all terms of eq. 2.2, eq. 2.5 and eq. 2.6 at all turbulent length and time scales (Fiscaletti *et al.* (2016)). Unfortunately, the computational cost of DNS increases very quickly with the Reynolds number of the flow (Pope (2000)), so that this kind of simulation is usually limited to Re that are sizeably lower than those targeted in this study (for example, compare table 7.2 to Le *et al.* (1997) and Mollicone *et al.* (2017)) and often not representative of operating conditions of industrial systems. A more affordable alternative is given by Large Eddy Simulations (LES), that have been used to investigate massively separated flows and their control with some success (e.g. Neumann & Wengle (2003) and Dandois *et al.* (2007)), but

for technical reasons LES was not available for this study either. Since simpler model-based computational approaches are uncapable of reliably predicting massively separated turbulent flows, this work is based on experimental measurements (mainly hot-wire and Particle Image Velocimetry), that will be detailed in chapter 4). In turbulent flows, however, a complete experimental description of velocity and pressure fields in all points in time and space is most often unreachable (Tennekes & Lumley (1972)). It is is then necessary to treat turbulent flows with methods yielding statistical descriptions of the flow, that can be fed with imperfect, usually under resolved experimental data. The first of such statistical methods is probably due to O. Reynolds, who proposed to decompose all flow quantities into a mean (i.e. stationary) component and into a fluctuating component, viz:

$$u_i = U_i + u_i' \qquad p = P + p', \tag{2.7}$$

where uppercase letters are used for mean components (e.g. U_i) and the *prime* symbol $'$ indicates fluctuations. By definition, it is:

$$\langle U_i \rangle = U_i \qquad \langle u_i' \rangle = 0, \tag{2.8}$$

where the symbol $\langle \bullet \rangle$ indicates ensemble averaging. By plugging eq. 2.7 (and other assimilable expressions) into the instantaneous flow equations, Reynolds obtained balances for the mean and the fluctuating fields, as detailed in the following subsection.

2.3.1 Continuity of mean and fluctuating fields

With Reynolds decomposition, the equation of continuity for the mean, incompressible flow (eq. 2.2) becomes simply:

$$\frac{\partial U_i}{\partial x_i} = 0, \tag{2.9}$$

A similar expression is obtained for fluctuating mass fluxes, by subtracting eq. 2.9 from eq. 2.2. This states that both the mean and the fluctuating velocity fields are solenoidal, i.e. fluctuating mass fluxes balance out exactly as the mean ones do.

2.3.2 Reynolds-Averaged Navier-Stokes equations (RANS)

Applying Reynolds decomposition to the transport equations for momentum leads to the Reynolds-Averaged Navier-Stokes (RANS) equations, one of the cornerstones of fluid mechanics, that for an incompressible flow are written as:

$$U_j \frac{\partial U_i}{\partial x_j} = -\frac{1}{\rho}\frac{\partial P}{\partial x_i} + \nu \frac{\partial^2 U_i}{\partial x_j \partial x_j} - \frac{\partial}{\partial x_j}\langle u_i' u_j' \rangle. \tag{2.10}$$

The RANS equations condensate all interactions between mean field and fluctuations into the last term of their right-hand side, which takes into account the mean transport of fluctuating momentum by turbulent velocity fluctuations Tennekes & Lumley (1972). The quantity $\langle u_i' u_j' \rangle$ is the so-called *Reynolds stress* tensor. Of course, the introduction of the 6 unknown independent components of Reynolds stress tensor into a system of only 5 equations opens the notorious *closure* problem, i.e. the relentless research on independent formulations of Reynolds stresses. Attempts to *close* the system often rely on an analogy with viscous stresses, by assuming proportionality of Reynolds stresses to strain rates. The most famous of such theories is probably Prandtl's mixing length theory, which, however, knows limited success in general applications (Tennekes & Lumley (1972)). In this work, the RANS equations are mainly used to interpret experimental data, so that the closure problem does not impact future discussions. Anyway, it is hoped that the outcome of this research might be used to improve turbulence models for massive turbulent separations and hence to contribute to close the RANS equations in these flows.

2.3.3 Mean and fluctuating kinetic energy

In a similar fashion as for the instantaneous kinetic energy (eq. 2.6), the equation for the mean kinetic energy is obtained by multiplying the RANS equation by the mean velocity U_i. This yields:

$$U_j \frac{\partial E_c}{\partial x_j} = -U_j \frac{\partial P}{\partial x_j} + \frac{\partial}{\partial x_j}\left(2\mu U_i S_{ij} - \rho U_i \langle u_i' u_j' \rangle\right) - 2\mu S_{ij} S_{ij} + \rho \langle u_i' u_j' \rangle S_{ij}, \tag{2.11}$$

where $E_c = 1/2\rho U_i U_i$. With respect to 2.11, Reynolds decomposition puts in evidence two new energetic terms. Firstly, $-2\mu S_{ij} S_{ij}$ accounts for the amount of energy that is dissipated by viscosity in the mean field. This term is negligibly small in most practical applications (Tennekes & Lumley (1972)): the mean field lacks an effective dissipative mechanism. More importantly, the *sink* term $+\rho\langle u_i' u_j'\rangle S_{ij}$ represents the amount of energy that the mean field loses in the interaction with fluctuations: it is the *production* $\mathcal{P}$ of turbulent kinetic energy. The role of $\mathcal{P}$ is better highlighted in the expression of turbulent kinetic energy. By applying Reynolds decomposition to eq. 2.6, averaging and subtracting eq. 2.11, some manipulations yield the following equation:

$$\rho U_j \frac{\partial k}{\partial x_j} = \frac{\partial}{\partial x_j}\left(-\langle u_j' p'\rangle - \rho\langle u_j' u_i' u_i'\rangle + 2\mu\langle u_j' s_{ij}'\rangle\right) - 2\mu\langle s_{ij}' s_{ij}'\rangle - \mathcal{P}, \tag{2.12}$$

in which $k = 1/2\langle u_i' u_i'\rangle$ is the turbulent kinetic energy and s_{ij}' is the fluctuating component of the strain rate tensor. Along with $\mathcal{P}$ and the usual transport terms, eq. 2.12 contains the dissipative term $\epsilon = -2\mu\langle s_{ij}' s_{ij}'\rangle$. Unlike its mean counterpart, ϵ is usually very intense and not negligible: turbulence dissipates energy effectively. In this respect, it is noteworthy that $\mathcal{P}$ appears in eq. 2.12 with an inversed sign, i.e. it is now a *source* term that feeds kinetic energy to fluctuations. In other words, the mean field attains its energetic equilibrium by transferring its excess energy into turbulence, that is able to dissipate it into heat much more effectively than viscosity alone.

Part II

Description of the experiments

3

Experimental setup

Montages expérimentaux

Les expériences présentées dans ce travail ont été conduites dans les installations du laboratoire PRISME, le plus souvent dans la soufflerie S2 (figure 3.1). Il s'agit d'une installation subsonique de type Eiffel, qui peut atteindre une vitesse de $50\,\mathrm{m\,s^{-1}}$ dans la veine d'essai. Cette dernière est longue de $2\,\mathrm{m}$ et a une section carrée de largeur $w = 0.5\,\mathrm{m}$. La vitesse en entrée de veine U_{inlet} est mesurée par un manomètre différentiel avec une incertitude de $0.5\ mmH_2O$. L'écoulement naturel dans la veine est homogène à moins de $1\,\%$ de U_{inlet} (figure 3.3(a) et figure 3.4(a)), tandis que le taux de turbulence résiduelle est de l'ordre de $0.3\,\%$ de U_{inlet} (figure 3.3(b) et figure 3.4(b)). La soufflerie S2 n'est pas équipée pour compenser la croissance de la couche limite. De ce fait, la vitesse locale U_∞ augmente de $2.5\,\%$ à $4\,\%$ de U_{inlet} le long de la veine d'essai (figure 3.5), mais cela ne semble pas perturber les expériences.

Dans une phase avancée de ce travail, une courte campagne expérimentale s'est déroulée dans la soufflerie à retour S1. Cette installation peut atteindre une vitesse de $60\,\mathrm{m\,s^{-1}}$, dans une veine d'essai longue de $5\,\mathrm{m}$ et ayant une section carrée de largeur $w = 2\,\mathrm{m}$. Une vitesse et une pression de référence sont prises par un tube de Pitot placé sur la ligne centrale de la veine, à $40\,\%$ de sa longueur. Le taux de turbulence résiduelle est de l'ordre de $0.4\,\%$ de U_∞.

Ce travail analyse le décollement turbulent massif qui se développe à l'aval d'une rampe descendante inclinée à $25°$. Deux maquettes expérimentales ont été utilisées : elles ont des rampes géométriquement similaires mais de hauteur différente. La rampe GDR, présentée en figure 3.7, a été conçue (indépendamment de ce travail) pour être intégrée à mi-hauteur, dans la veine de la soufflerie S1. La hauteur de la rampe est $h = 100\,\mathrm{mm}$, ce qui donne un rapport d'expansion $ER = 1.11$. La maquette est aussi large que la veine d'essai et le rapport d'aspect $AR = w/h$ est égal à 20 : d'après Eaton & Johnston (1981), cette valeur est suffisante pour assurer que le décollement moyen est bidimensionnel. La deuxième maquette est la rampe R2, dont la hauteur est $h = 30\,\mathrm{mm}$. Elle peut être intégrée à la soufflerie S2, en remplaçant le plancher de la veine d'essai (figure 3.1). Dans ce cas, on a $ER = 1.06$ et $AR \approx 17$, ce qui est encore suffisamment élevé pour garantir un décollement moyen bidimensionnel.

L'utilisation de ces deux maquettes complémentaires est un atout important de ce travail. Grâce au changement de h, les deux rampes permettent de balayer jusqu'à 1.5 decade du paramètre de similitude $Re_h = U_{ref}h/\nu$, qui est souvent utilisé pour comparer des décollements turbulents massifs sur des rampes ou des marches descendantes. Un autre paramètre d'intérêt est le ratio entre l'épaisseur de la couche limite à l'amont δ et la hauteur de la rampe. Etant donné que les couches limites qui se développent à l'amont des deux rampes ont des propriétés fondamentalement similaires, la variation de h nous permet d'analyser le comportement de l'écoulement en présence de deux valeurs de δ/h très différentes.

3.1 Introduction

This chapter presents the descending ramp geometry that was chosen as reference bluff body to onset a massive turbulent separation. As it will be explained, the separated flow was investigated over two geometrically similar descending ramps, spanning two different step heights. Together, the two experimental models allow us to cover almost 1.5 decades of the similarity parameter $Re_h = U_{ref}h/\nu$, where U_{ref} is a reference velocity and h is step height, which is often used to compare geometry-generated massively separated flows among each other (see Adams & Johnston (1988*b*) and references therein). This range is relatively wide and it corresponds well to some of the highest Re_h tested in previous works. In addition, since on the two ramps the incoming boundary layers have essentially similar thicknesses δ_e[1], the two models make it possible to study the effect on the flow of sizeably different values of the ratio δ_e/h. The experimental models were designed to be integrated within the main wind tunnels of PRISME laboratory. For this reason, sizes and characteristics of these facilities are reviewed before entering into the descriptions of the descending ramps.

3.2 The experimental facilities

3.2.1 The S2 wind tunnel

The S2 wind tunnel of PRISME laboratory (figure 3.1) is a subsonic, Eiffel type facility that can reach a maximum free-stream velocity of $50\,\mathrm{m\,s^{-1}}$. It has a $2\,\mathrm{m}$ long test section with a square cross section of width $w = 0.5\,\mathrm{m}$, preceded by a 16:1 contraction that guarantees a laminar flow at the inlet. A honeycomb and a settling chamber, equipped with fine screens, make sure that possible large turbulent structure are dissipated before reaching the test section. The pressure drop Δp_{IN} generated by the contraction is measured at the inlet of the test section, with a ***Furness Control*** micromanometer. Readings of Δp_{IN} have a declared accuracy of $0.01\ mmH_2O$ for $\Delta p_{IN} \in (1, 10)\ mmH_2O$ and $0.5\ mmH_2O$ for $\Delta p_{IN} > 10\ mmH_2O$. The range of inlet velocities $U_{inlet} \in 10\,\mathrm{m\,s^{-1}}$ to $40\,\mathrm{m\,s^{-1}}$ spanned in this work falls within this second domain. Values of U_{inlet} can be obtained simply from Δp_{IN}, under the assumption of negligible losses in the convergent. It is:

$$\Delta p_{IN} = g\rho_{H_2O}h_{H_2O} \approx \frac{1}{2}\rho U_{inlet}^2, \tag{3.1}$$

from which one obtains:

$$U_{inlet} \approx \sqrt{\frac{2g\rho_{H_2O}h_{H_2O}}{\rho}}, \tag{3.2}$$

where ρ_{H_2O} and ρ are the densities of water and air, respectively, g is gravity acceleration and h_{H_2O} is the reading provided by the *Furness* manometer. In common atmospheric conditions ($p_{atm} \sim 1 \times 10^5\,\mathrm{Pa}$ and T_{atm} ranging from $0\,^\circ\mathrm{C}$ to $40\,^\circ\mathrm{C}$), ρ_{H_2O} can be considered constant and approximatively equal to $998\,\mathrm{kg\,m^{-3}}$. On the contrary, ρ needs to be estimated, for example based on the gas state equation. This yields:

$$U_{inlet} \approx \sqrt{\frac{2g\rho_{H_2O}h_{H_2O}R_{air}T_{atm}}{p_{atm}}}, \tag{3.3}$$

in which $R_{air} = 286.9\,\mathrm{J\,kg^{-1}\,K^{-1}}$ is the gas constant for air. T_{atm} and p_{atm} are measured in the room of the wind tunnel, with accuracies of respectively $0.5\,^\circ\mathrm{C}$ and $1\,\mathrm{mbar}$. At the outlet of the test section, a short diffuser collects the flow and slows it down. Air is accelerated by a centrifugal fan placed after the diffuser. The fan is driven by a triphase electric engine, piloted by a manual RPM controller. Figure 3.2 reports the transfer function of the engine-fan assembly, showing that the streamwise velocity at the inlet of the empty test section depends linearly on RPM. Figure 3.3(a) presents vertical profiles of streamwise velocity in the empty test section: velocity is homogeneous along the Y axis within $\pm 0.5\,\%$ of the local free-stream velocity U_∞, measured along the centerline. Spanwise homogeneity is less satisfactory, since mean streamwise velocities are now within $\pm 1\,\%$ of U_∞ (figure 3.4(a)). Residual turbulence, evaluated with the square root of the streamwise Reynolds stress $\sqrt{\langle (u')^2 \rangle}$ (see § 2.3.2), is generally lower than $0.3\,\%$

[1] We consider here the thickness of the boundary layer at the edge of the ramp. See chapter 7 for further details.

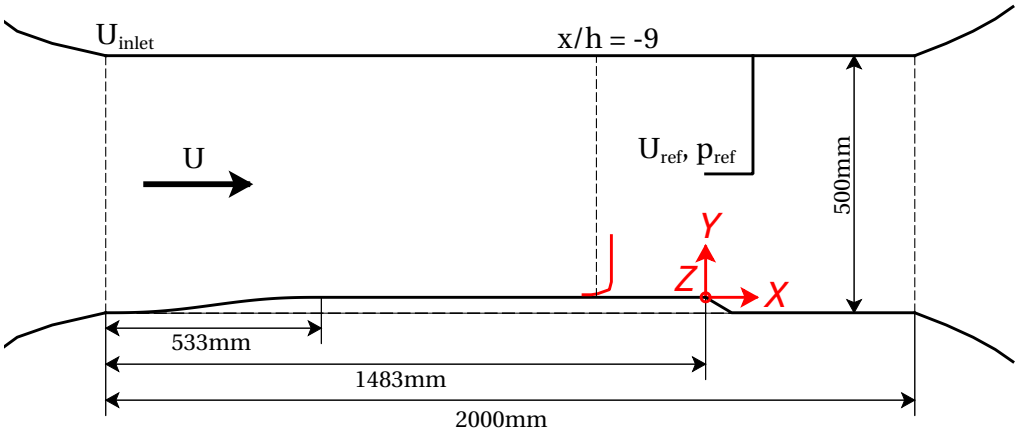

Figure 3.1: Dimensions of the R2 ramp. The boundary layer measured at $x/h = -9$ (red line) is used as a reference for scaling parameters.

of U_∞ (figure 3.3(b) and figure 3.4(b)). At sections further downstream, the region close to the wall has higher turbulent intensities, but these are probably due to developing boundary layers. Indeed, the S2 wind tunnel is not equipped with tunable walls and hence it cannot compensate for boundary layer growth. This being so, figure 3.5(a) shows that U_∞ increases with respect to U_{inlet} along the streamwise direction, as the growing displacement thickness (not measured in the empty test section) reduces the apparent width of the test section. The increase of U_∞ is of the order of $2.5\,\%$ to $4\,\%$ of U_{inlet}, slightly decreasing with U_{inlet}, which remains acceptable. On the contrary, residual turbulence is relatively uniform at $0.2\,\%$ of U_∞ along the entire test section (figure 3.5(b)).

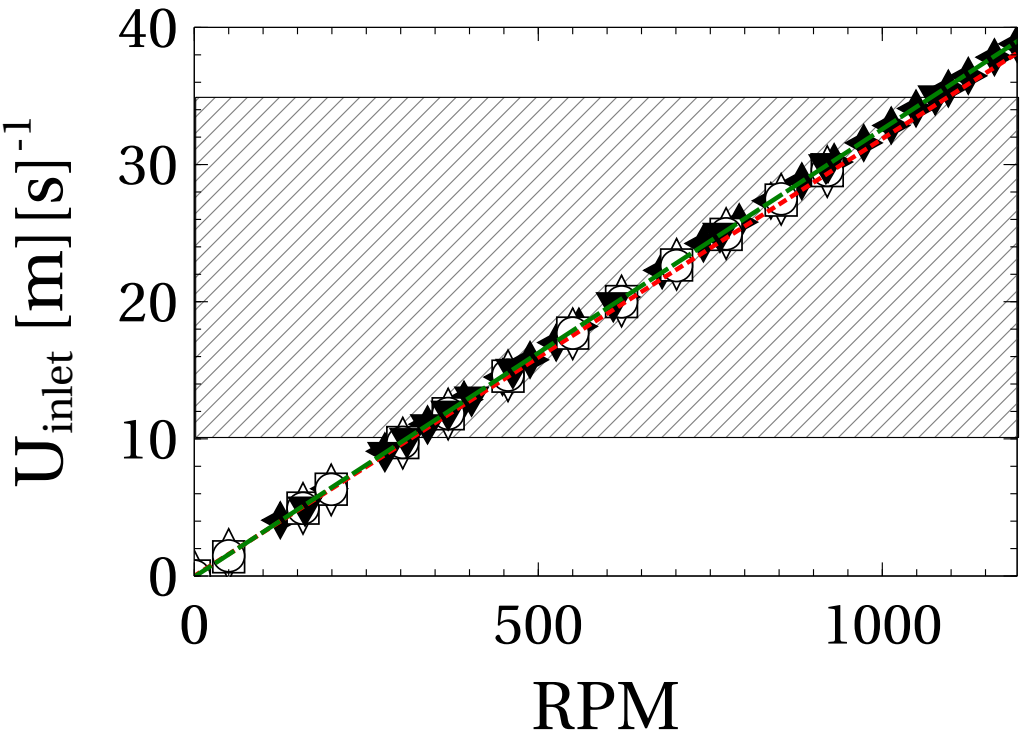

Figure 3.2: Transfer function *RPM-to-U_{inlet}* of the engine-fan assembly in the S2 wind tunnel. Empty symbols (◯, □, ◊) report three data series recorded with an empty test section, over a time span of three days. T_{atm} ranges between 21.5 °C and 25 °C, p_{atm} is about 1020 mbar. Filled symbols (▲, ✦) indicate two data series obtained with the R2 ramp replacing the floor of the wind tunnel, recorded one month apart. For ▲, T_{atm} ranges between 18.1 °C and 19.7 °C, and $p_{atm} \approx 990$ mbar. As for ✦, T_{atm} ranges between 21.1 °C and 22 °C, and $p_{atm} \approx 1020$ mbar. ····· linear fit of empty symbols; – – – linear fit of filled symbols. The shaded area qualitatively marks the range of U_{inlet} spanned in this work.

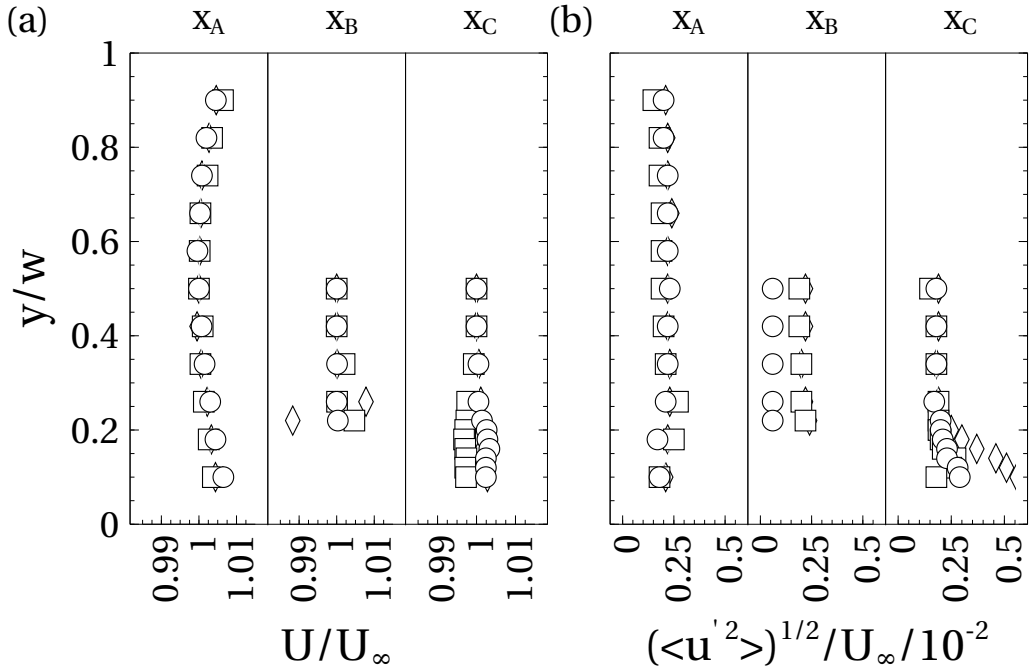

Figure 3.3: Vertical profiles of streamwise velocity in the empty test section of the S2 wind tunnel, at $z/w = 0$ (mid-width): (a) U_∞/U_{ref}; (b) $\sqrt{\langle u'^2 \rangle}/U_\infty$. Symbols ◯ $5\,\mathrm{m\,s^{-1}}$, □ $14.5\,\mathrm{m\,s^{-1}}$, ◇ $28\,\mathrm{m\,s^{-1}}$. Locations are $x_A = -1483\,\mathrm{mm}$ (inlet), $x_B \approx -470\,\mathrm{mm}$, $x_C \approx -98\,\mathrm{mm}$.

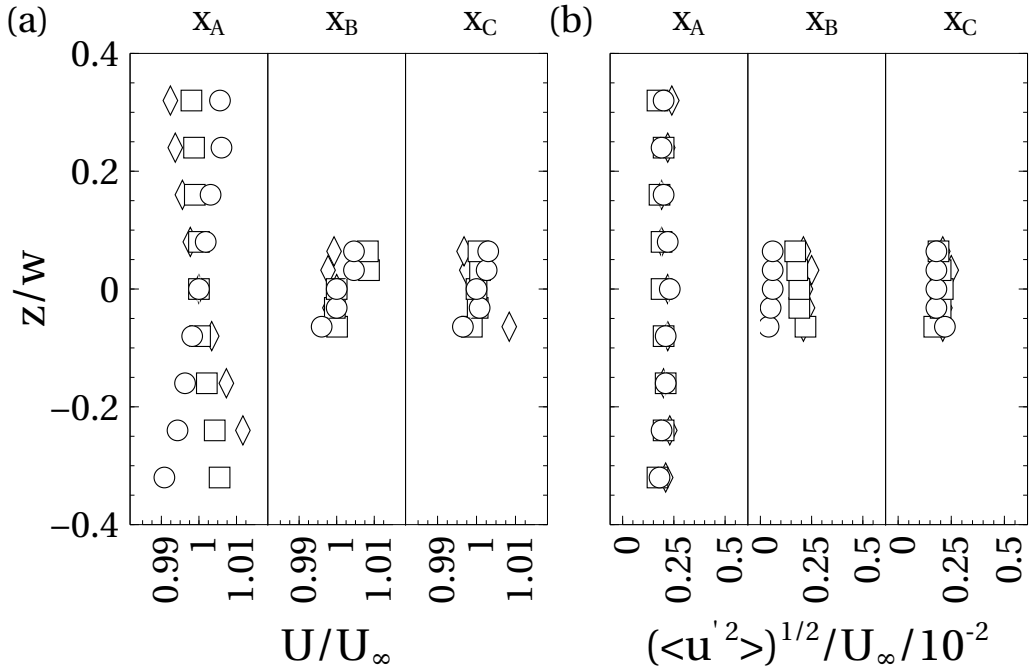

Figure 3.4: Horizontal profiles of streamwise velocity in the empty test section of the S2 wind tunnel, at $y/w = 0$ (mid-height): (a) U_∞/U_{ref}; (b) $\sqrt{\langle u'^2 \rangle}/U_\infty$. Symbols and locations as in figure 3.3.

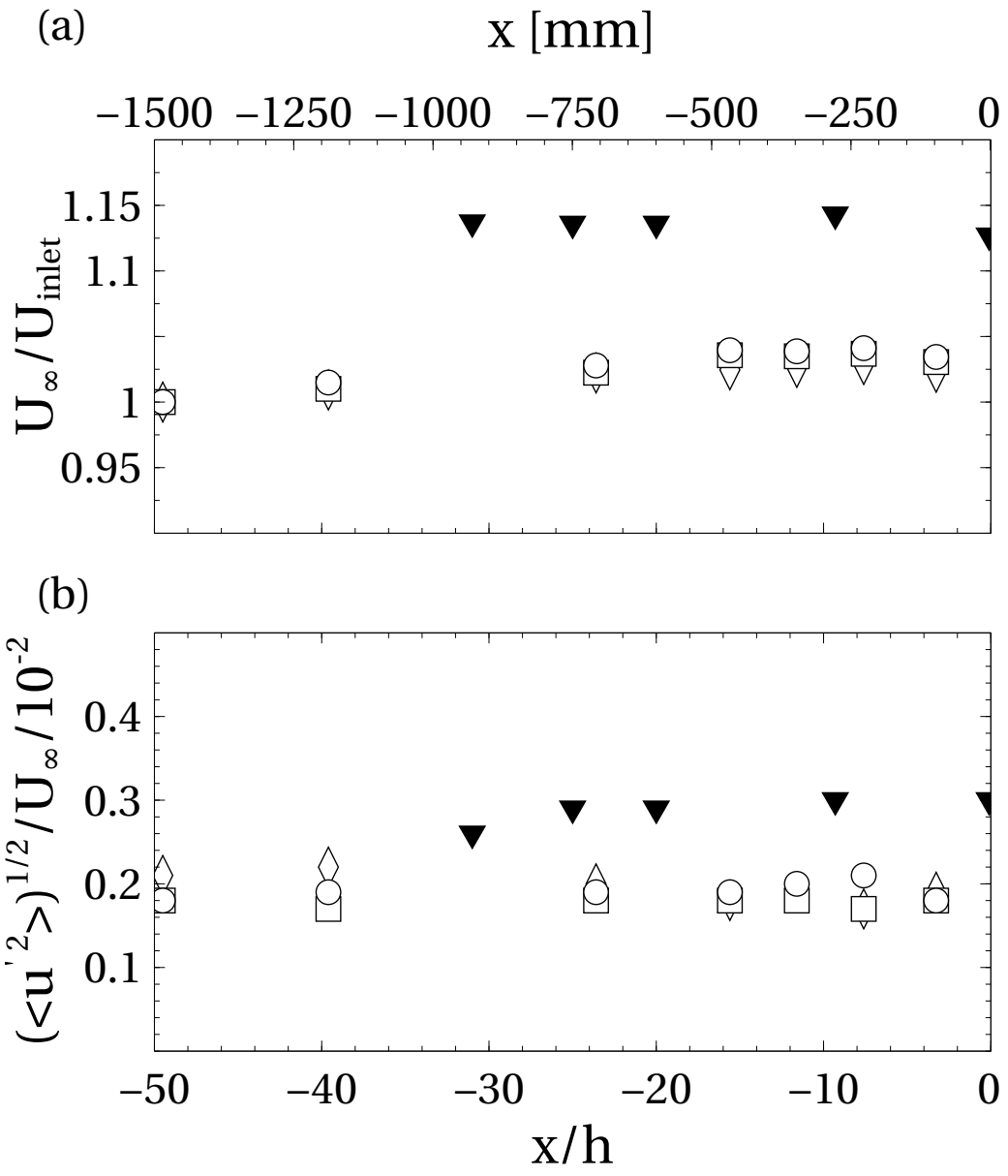

Figure 3.5: Streamwise evolution of free-stream properties in the S2 wind tunnel: (a) U_∞/U_{ref}; (b) $\sqrt{\langle u'^2 \rangle}/U_\infty$. Empty symbols indicate datasets obtained with an empty test section: ◯ $5\,\mathrm{m\,s^{-1}}$, □ $14.5\,\mathrm{m\,s^{-1}}$, ◇ $28\,\mathrm{m\,s^{-1}}$. Filled symbols indicate datasets having the R2 ramp replacing the floor of the test section: ▼ $20\,\mathrm{m\,s^{-1}}$. The origin of the reference system is defined in figure 3.1.

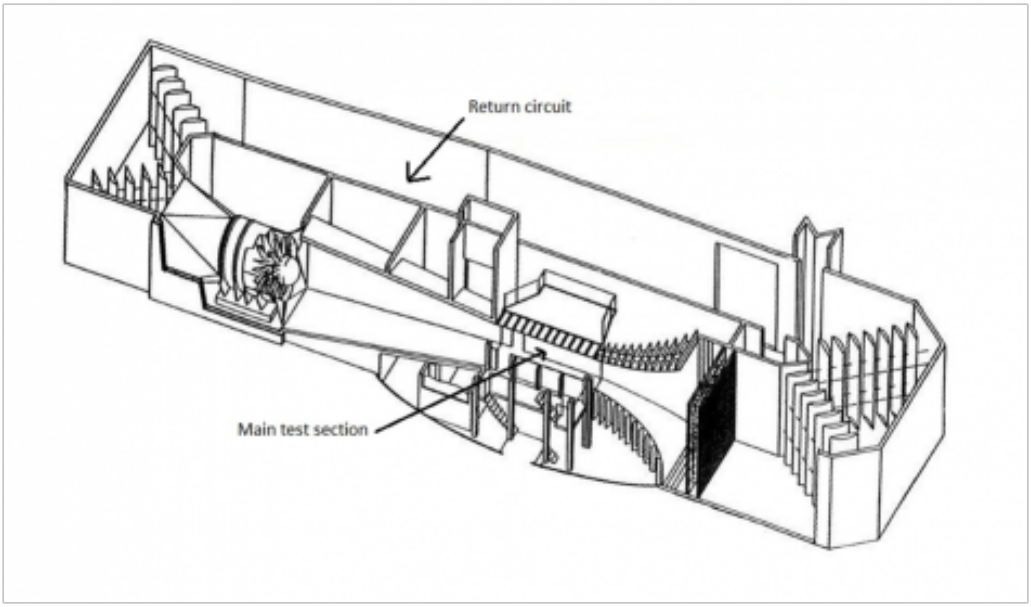

Figure 3.6: View of the S1 closed loop wind tunnel, from Joseph *et al.* (2015).

3.2.2 The S1 wind tunnel

The S1 wind tunnel is the subsonic, closed loop wind tunnel of PRISME Laboratory (figure 3.6). It can attain a maximum free stream velocity of $60\,\mathrm{m\,s^{-1}}$. Its test section is $5\,\mathrm{m}$ long and it has a square cross section of width $w = 2\,\mathrm{m}$. Reference velocity and pressure are measured with a Pitot tube, placed at mid-width, roughly at $40\,\%$ of test section length. Atmospheric pressure and temperature are automatically measured and used to provide a reading of free stream velocity. This facility was available at a late time for this research, and allocated time was sufficient to complete the characterisation of the boundary layer of one of the two experimental models (the GDR ramp, see § 3.3.1). Due to time constraints, it was not possible to verify the main velocity properties of the test section (as done for the S2 wind tunnel at § 3.2.1), which however are well documented. In particular, maximum residual turbulence intensity in the empty test section ranges between $0.3\,\%$ and $0.4\,\%$ of free stream velocity, while free stream velocity is homogeneous within $0.5\,\%$, over at least $60\,\%$ of test section width (Thacker *et al.* (2013), Kourta & Leclerc (2013), Kourta *et al.* (2015)).

3.3 Experimental models

The reference geometry for this research is a descending, $25°$ ramp that causes the massive separation of an incoming turbulent boundary layer. This prototype geometry was chosen by the French federative program *Groupement de Recherche* (GDR) *2502*, to which this work contributes, to develop separation control theory and techniques. It corresponds to a wide range of aeronautical and automotive geometries in which separating/reattaching flows may commonly occur: diffusers, high lift devices and the rear ends of many automobiles are all adequately represented. With respect to literature, a descending ramp is a less conventional choice for studying separating/reattaching flows than the backward-facing step (BFS), which is generally considered as the simplest member of this family of flows and hence the most convenient for gathering general (or generalisable) knowledge (Eaton & Johnston (1981)). In any case, it will be shown that a part of our results compare excellently with known BFS behaviours (e.g. pressure distributions at § 6.3): then, it seems reasonable to hope that the *new* observations reported in this work will also apply with some generality.

Experiments were carried out on two geometrically similar $25°$, descending ramps. The first one is the so-called *GDR ramp*, that was designed independently from this work as a test-bench for separation control. Studies based on the GDR ramp (or one preparatory mock-up) include Debien *et al.* (2014), Kourta *et al.* (2015) and Joseph *et al.* (2016). A description of the GDR ramp is given at § 3.3.1. At a very early stage of this work, it was felt that the ratio between the thickness of the incoming boundary layer (δ) and the height of the step spanned by the ramp (h) was possibly one of the parameters governing the flow (in this respect, see § 8.4). Since the GDR ramp does not allow to actively control δ, the only solution to sizeably vary δ/h was to change h. A new ramp was then designed and manufactured, with a much lower h. This second model is called[1] the *R2 ramp*. Section 3.3.2 describes the R2 ramp and a synthetic comparison to the GDR ramp is reported in table 3.1. It appears that the two experimental models are quite complementary: together, they give access to a wide, continuous range of Re_h and to sizeably different values of the parameter δ/h. Anyway, it is pointed out that most of the data presented in this work were collected on the R2 ramp, in part because of availability of experimental facilities, but also because the necessary characterisation of a new model fostered extensive study. The analysis of the GDR ramp is based on existing PIV datasets provided by Dr. P. Joseph, and on complementary measurements (essentially hot-wire and PIV) carried out to characterise the incoming boundary layer.

	h/mm	AR	ER	$Re_h/10^4$	δ_e/h
GDR	100	20	1.11	7 to 35	≈ 0.3
R2	30	17	1.06	1 to 8	≈ 1

Table 3.1: Comparison of the main properties of the two experimental models. $AR = w/h$ is the aspect ratio, $ER = H_2/(H_2 - h)$ is the expansion ratio, δ_e/h is the ratio between the thickness of the incoming boundary layer, evaluated at the upper edge of the descending ramp, and step height.

3.3.1 The GDR ramp

The GDR ramp, depicted in figure 3.7, is designed to be placed in the S1 wind tunnel of the PRISME laboratory, approximatively at half-height of the test section. Since it is exposed to the flow on all sides, its leading edge consists of the first $30\,\%$ of a NACA0015 profile, merging smoothly onto a flat plate on which the boundary layer develops. The massive separation occurs on a α = $25°$, salient edge, descendig ramp of step height $h = 100\,\mathrm{mm}$. The resulting expansion ratio $ER = H_2/H_1 = H_2/(H_2 - h)$ (see figure 3.7) is equal to 1.11. Since the width of the model is $w \approx 2\,\mathrm{m}$, the aspect ratio $AR = w/h$ is about 20, which guarantees that the mean flow is quasi bidimensional (see Eaton & Johnston (1981) and § 6.3). Finally, the flow relaxes on a second flat plate. Following the suggestions of Kourta *et al.* (2015), transition of the boundary layer is triggered with a zigzag tripper of height $0.5\,\mathrm{mm}$, placed at $x/h \approx -15.7$ (see § 7.2.4). In their work on a preliminary mock-up of the GDR ramp, Kourta *et al.* (2015) also showed that pressures distributions on the upper and lower sides of the NACA profile are not equilibrated, unless a flap downstream of the ramp is extracted at $\approx 7.5°$. However, the use of the flap was avoided (as suggested by these same authors), since it appears to induce an asymmetric separation. One particularity of the GDR model is the presence of three $1\,\mathrm{mm}$ wide slots placed on the descending ramp, just $2\,\mathrm{mm}$ downstream of its upper edge. These slots allow to operate three synthetic jets (not used during this study) produced by loudspeakers embedded in the model. Joseph *et al.* (2015) compared the pressure distribution on the GDR ramp with those measured by Kourta *et al.* (2015) on its preliminary mock-up, showing that slots do not appear to have a major influence on the massive separation. In future discussions of the GDR ramp, we use the cartesian coordinate system (X;Y;Z), centered at midspan on the upper ramp edge (see figure 3.7).

3.3.2 The R2 ramp

The R2 ramp is represented in figure 3.1 with its main dimensions. In principle, the R2 ramp needs the same elements as the GDR ramp: a leading edge that should not perturb the flow too much, a flat plate

[1] Admittedly, with a great immaginative effort.

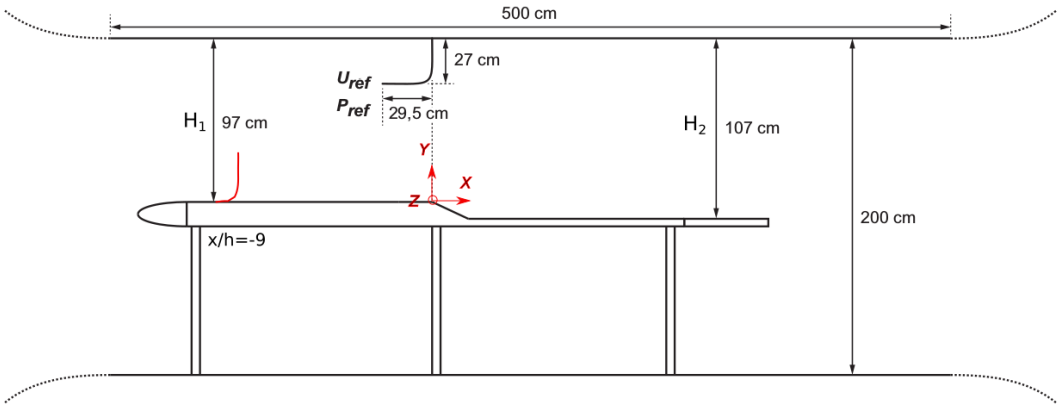

Figure 3.7: Dimensions of the GDR ramp. The boundary layer measured at $x/h = -9$ (red line) is used as a reference for scaling parameters. Image adapted from Kourta *et al.* (2015).

for boundary layer development, the $25°$, salient edge, descendig ramp and a flat plate for relaxation. In practice, the design had to comply with several additional requirements, the main ones being: 1) having a high enough h as to systematically produce a massive turbulent separation. 2) at the same time, having a low enough h as to guarantee a value of δ/h much higher than on the GDR ramp. 3) having a sufficiently high aspect ratio for the separation to be bidimensional. 4) to optimise the use of experimental facilities, being integrated into the test section of the S2 wind tunnel, which is much smaller than the S1 test section and hence more exposed to blockage effects. To avoid blockage problems, the R2 ramp replaces the floor of the test section. The junctions with the convergent and the diffuser of the wind tunnel must be smooth: then, classical aerofoil leading edges (as the NACA 0015 used for the GDR ramp) were avoided. Instead, an additional contraction, placed downstream of the convergent of the wind tunnel, lifts the flow of one step heigh h. The profile of the contraction follows a fifth-order polynomial, as prescribed by Bell & Mehta (1988) and Brassard & Ferchichi (2005). These works suggest that contractions of this type minimise the risk of local separations at the junction with the flat plate. A soft clay is utilised to further smooth junctions with the convergent and the diffuser of the wind tunnel. Once this general geometry is fixed, the main problem remains the choice of h. It is generally admitted that a minimum aspect ratio of 10 is necessary for a bidimensional separation (Eaton & Johnston (1981)), which gives a maximum value for step heigh of $50\,\mathrm{mm}$. However, requirement 2 is better fulfilled by lower h. At the time of the design, ratios $\delta/h > 1$ were considered unsafe for systematically producing a massive separation[1]. An iterative design process based on ANSYS Fluent RANS simulations highlighted that the condition $\delta/h \approx 1$ was met at $h = 30\,\mathrm{mm}$, which was retained as final h value. This yields an aspect ratio w/h of about 17 and once again the mean flow can be considered bidimensional (see § 6.3). Similarly to the GDR ramp, a zigzag tripper of height $0.5\,\mathrm{mm}$ is also installed on the R2 ramp, at $x/h \approx -49$, to fix the turbulent properties of the incoming boundary layer (see § 7.2.3). Further, a similar coordinate system, centered at midspan on the upper edge of the descending ramp, is also defined.

3.3.3 Behaviour of the S2 wind tunnel in presence of the R2 ramp

Some of the properties of the S2 wind tunnel change once the R2 model replaces the floor. Figure 3.5(a) shows that the streamwise evolution of U_∞ is much stronger than in the empty test section, with U_∞ growing to about $110\,\%$ of U_{inlet} before the upper edge of the ramp. Of course this increase is essentially due to the convergent of the ramp, that reduces the height of the test section of $6\,\%$. Interestingly, U_∞ does not grow sizeably over the flat plate. As for turbulent fluctuations, they remain constant to about $0.3\,\%$ of U_∞, which

[1] Later findings suggest that this assumption might be too strict, see § 8.4.

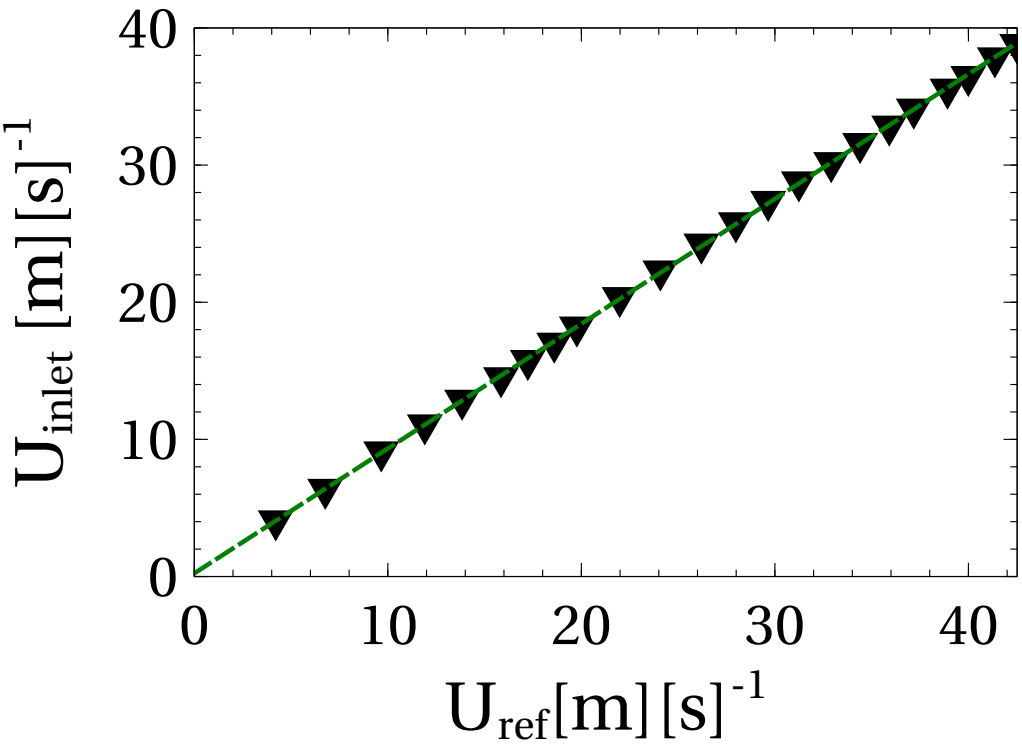

Figure 3.8: Transfer function relating reference velocity U_{ref} at the upper edge of the ramp to inlet velocity. - - - linear fit: the proportionality coefficient is about 0.91.

is slightly higher than in the empty test section (figure 3.5(b)). Although the presence of the convergent does not change the engine-fan transfer function much (see figure 3.2), the value of velocity at the inlet is not representative of velocity at the ramp. Then, a Pitot tube was installed above the upper edge of the ramp (see figure 3.1) to measure the reference velocity (indicated U_{ref}) and pressure (indicated p_{ref}) at separation. The Pitot tube was also pneumatically connected to the *Furness* manometer: in this way, Pitot readings could be used to set the RPM of the engine and attain target velocity conditions at the ramp. It is pointed out that for optical measurements the Pitot had to be extracted from the test section, in order to correctly illuminate the separated flow and avoid dangerous laser reflections. Then, a new transfer function was established (reported in figure 3.8), relating velocity at the ramp to inlet velocity. Using this curve and the transfer function given in figure 3.2, RPMs could be set based on velocity readings at the inlet of the test section, while approximating the target U_{ref} generally within $5\,\%$.

4

Measurement techniques

Techniques de mesure

Ce travail s'appuie principalement sur trois techniques de mesure complémentaires : vélocimétrie à fil chaud, vélocimétrie par images de particules (*Particle Image Velocimetry*, PIV) et mesures de pression statique pariétale. Le fil chaud fournit uniquement la norme d'une composante de vitesse en un point, mais ses résolutions temporelle et spatiale sont généralement très élevées. La PIV à deux dimensions et deux composantes (2D2C) apporte la norme et la direction de deux composantes de vitesse sur un plan, avec une résolution spatiale relativement bonne mais au prix, du moins dans le cas présent, d'une résolution temporelle virtuellement nulle, à savoir que deux champs de vecteurs successifs sont décorrélés. Son avantage principal est qu'elle donne accès à des mesures de vitesse fiables dans la bulle de recirculation. Les mesures de pression, qui ne sont pas bien résolues ni dans le temps ni dans l'espace, donnent une description de larges régions de l'écoulement à un coût très faible, tant sur le plan économique que du point de vue du temps de préparation et de mise en opération. De plus, elles donnent accès à des informations à la paroi qui sont plus difficiles à obtenir avec les autres techniques. Globalement, ce panel de mesures peut fournir une description relativement complète de l'écoulement à grande échelle et d'une partie importante de la gamme des échelles turbulentes de l'écoulement.

Le principe physique de la vélocimétrie à fil chaud est la convection de la chaleur d'un fil conducteur, tendu entre deux broches (voir figure 4.1), qui est chauffé par effet Joule et immergé dans un écoulement. Une longue série de travaux (par exemple King (1914), Collis & Williams (1959) et George *et al.* (1989) parmi d'autres) a démontré qu'il est possible d'établir des lois semi-empiriques qui relient la tension appliquée au fil chaud à la vitesse de l'écoulement, comme des lois en puissance (éq. 4.7) ou polynomiales (éq. 4.8). Plus de détails sont disponibles dans des textes de référence comme Bruun (1996). Cette étude a fait usage de fils chauds à une composante, pilotés en mode *température constante* : cela signifie que la tension est réglée en continu par un pont de Wheatstone, de sorte à garder la température du fil à une valeur établie (voir 4.2). Un modèle à broches droites Dantec 55P11 a été utilisé dans l'écoulement libre et un modèle à broches coudées Dantec 55P15 a été choisi pour les mesures en proche paroi. Les deux sondes ont le même capteur, dont les caractéristiques sont présentées dans le tableau 4.1. La résolution spatiale de ces fils est adaptée à l'étude de la TNTI dans la région externe de la couche limite. Au contraire, elle n'est pas suffisamment élevée pour capturer tout le spectre de la turbulence dans des régions plus proches de la paroi (Philip *et al.* (2013)). La résolution temporelle du montage utilisé nous permet d'atteindre des fréquences d'acquisition élevées allant de $20\,\mathrm{kHz}$ à $60\,\mathrm{kHz}$, selon les expériences. Les chaînes d'acquisition utilisées sont décrites plus en détail dans le tableau 4.2. Le fil chaud a deux inconvénients qui ne permettent pas son utilisation dans la bulle de recirculation : il ne peut pas mesurer la direction de l'écoulement et il est intrusif, ce qui produit des interactions complexes avec le décollement. La PIV permet de pallier ces inconvénients.

La PIV reconstruit le champ de vitesse à partir du déplacement d'un traceur. L'écoulement est éclairé deux fois par un laser à haute puissance, à un intervalle de temps connu. A chaque émission laser, une image des particules est prise. Ensuite, une grille est définie sur le couple d'images et un vecteur vitesse moyen est associé à chacune de ses cases (appelées *fenêtres d'interrogation*) par un processus de maximisation de la

corrélation croisée des intensités lumineuses (voir figure 4.4 et figure 4.5). Dans ce travail, l'ensemencement a été assuré par des gouttelettes d'huile d'olive. Les couples d'images ont été acquis à une fréquence de $2.5\,\mathrm{Hz}$ (deux couples successifs ne sont donc pas corrélés) avec des caméras VC-Imager (4032 x 2688 pixels) du fabricant LaVision. Sur la rampe GDR, un *champ large* de taille $6h \times 2h$ qui couvre toute la bulle de recirculation moyenne est obetnu au moyen de deux caméras. Un *champ auxiliaire*, large de $1.4h \times 0.6h$ et centré sur $x/h = -9$, fournit les vitesses de la couche limite à l'amont. Les deux champs sont représentés en figure 4.6. Trois champs ont été définis sur la rampe R2 (figure 4.7). Un champ large ($9h \times 2.5h$) et un champ auxiliaire, avec des positions et des caractéristiques comparables à celles de la rampe GDR, sont complétés par un *champ détaillé*, de taille $1.5h \times 1.2h$, qui apporte une vue détaillée de la région autour de l'arête de la rampe. Les objectifs photographiques utilisés et les résolutions qui en résultent (en $\mathrm{mm\,px^{-1}}$) sont donnés dans le tableau 4.3. Tous les couples d'images ont été traités avec les algorithmes *multipass* du logiciel *Davis 8.3* de LaVision. La fenêtre d'interrogation finale était de $16 \times 16\,\mathrm{px}^2$ pour les données de la rampe R2, de $32 \times 32\,\mathrm{px}^2$ pour celles de la rampe GDR. Le champ détaillé de la rampe R2 offre la meilleure résolution finale, avec des fenêtres d'interrogation de moins de $0.2\,\mathrm{mm}$ de côté, ce qui est de l'ordre de l'échelle de Kolmogorov à la position de la TNTI moyenne, estimée au chapitre 7. Cela indique que le champ détaillé devrait être suffisamment résolu pour étudier au moins une partie de la gamme d'échelles de la turbulence. Tous les autres champs ont des fenêtres d'interrogation comprises entre $1.2\,\mathrm{mm}$ et $3.8\,\mathrm{mm}$ de côté : à cause de leur basse résolution, ils peuvent être utilisés avec confiance uniquement pour des analyses à grande échelle. Nous remercions le Dr. P. Joseph d'avoir mis à disposition les champs larges de la rampe GDR.

La distribution de pression à la paroi a été étudiée à l'aide de trois scanners de pression différentielle μDAQ-32C de Chell Instruments (tableau 4.4). La liaison pneumatique entre les prises de pression, dont la distribution sur les modèles expérimentaux est présentée en figure 4.8 et en figure 4.9, et les scanners est assurée par des tubes en vinyle de $2\,\mathrm{m}$ de longueur et de diamètre intérieur égal à $1.25\,\mathrm{mm}$. Ces caractéristiques déterminent une fréquence de coupure du signal acquis de seulement $20\,\mathrm{Hz}$ (van Ommen *et al.* (1999)) : par conséquent, seules les distributions de pression moyennes ont été étudiées. Pour garantir la convergence statistique, des signaux contenant entre 0.75×10^4 et 6×10^4 échelles de temps caractéristiques h/U_{ref} ont été employés.

4.1 Introduction

The discussion of chapter 2 highlighted that the Reynolds-averaged formulations of the transport equations need to be adopted for an experimental analysis of turbulent flows, because it is not possible to measure fluid variables as pressure and velocity in all points of the flow field. Even in this case, however, it is seldom possible to collect all required information with one single measurement technique, since the strong points of each technique inevitably imply some drawbacks. One classical example is the compromise that is to be found between the size of the field of view and the resolution yielded by an optical lens. For these reasons, in this work we exploited a set of complementary measurement techniques, including hot-wire anemometry, Particle Image Velocimetry (PIV) and pressure measurements at the wall of the experimental models. Planar fields provided by PIV are at the core of our investigations, but hot-wire signals add time-resolved (and to some extent spatially resolved) data that would be otherwise inaccessible to PIV. Wall-pressure measurements allow to explore the flow over very large surfaces at little cost. This chapter summarises the general working principles of each technique. Emphasis is given to the practical implementation in the two wind tunnels, to settings chosen for each experiment and to limitations affecting retrieved data.

4.2 Hot-wire anemometry

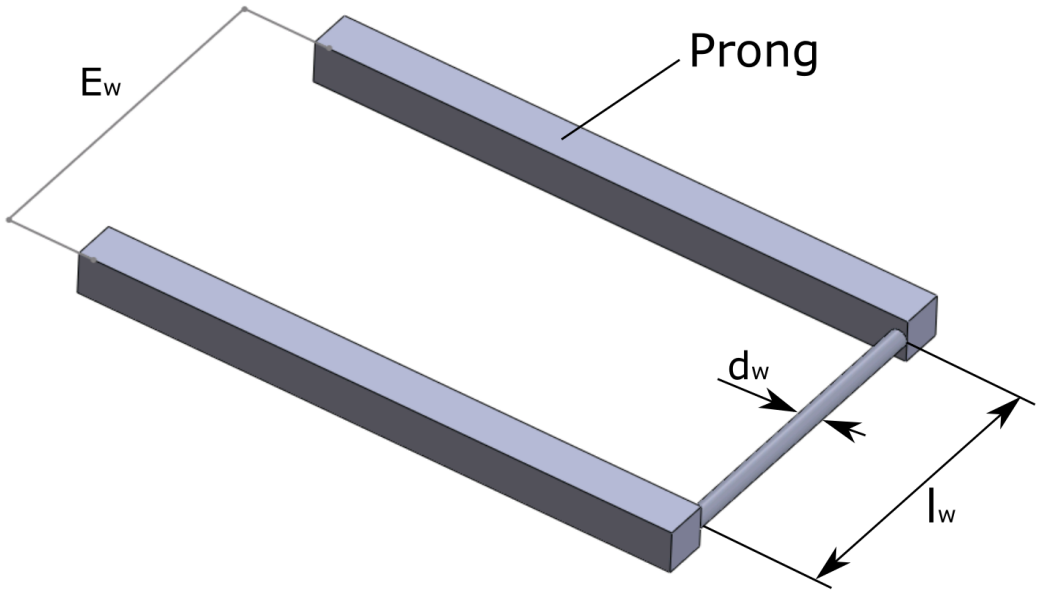

Figure 4.1: Representation of a single hot-wire.

Hot-wire probes are composed by one or more short sections of conductive wire, usually of very high aspect ratio, each held in place by two prongs (figure 4.1). Even if their origin can be traced back to the very first modern studies on Fluid Mechanics, hot-wire anemometers are still one of the main tools of the experimentalist, in particular in turbulence, because they can achieve very fast frequency responses at a fraction of the cost of most alternative techniques (e.g. Time Resolved PIV). This research makes extensive use of single component hot-wire probes, in particular to characterise the boundary layer upstream of separation. The present section reviews the fundamentals of hot-wire anemometry and provide information on the hot-wire experimental set-ups.

4.2.1 Basic features

The working principle of hot-wire anemometry is the convection of heat from a heated sensor, immersed in a flow (Bruun (1996)). If the heating of the sensor is controlled, measuring the amount of heat being transferred to the fluid gives information on properties of the flow and in particular on its velocity.

As the name suggests, the simplest implementation of this principle is a very thin cylindric wire, heated at a temperature T_w by resistive dissipation of an electric current I (the so called Joule effect). In this conditions, the termal equilibrium of a wire of length ℓ_w and diameter d_w can be written as:

$$I^2 R_w = \pi d_w \ell_w h_c \left(T_w - T_a\right) = \pi \ell_w \kappa_c \left(T_w - T_a\right) Nu. \tag{4.1}$$

In eq. 4.1, R_w is the electrical resistance of the wire. The symbols h_c and κ_c stand for the convective heat-transfer coefficient ($\mathrm{W\,K^{-1}}$) and the thermal conductivity ($\mathrm{W\,K^{-1}\,m^{-1}}$) of the fluid, respectively, at its ambient temperature T_a. The Nusselt number Nu expresses the ratio between convective and conductive heat-transfer at the surface of the wire as:

$$Nu = \frac{h_c d_w}{\kappa_c}. \tag{4.2}$$

It is well known that electrical resistance is a function of temperature, so that one can safely write:

$$R_w = R_{ref} \left[1 + \alpha_{ref} \left(T_w - T_{ref}\right)\right], \tag{4.3}$$

where T_{ref} is a reference temperature and α_{ref} is a termal coefficient measured at T_{ref}. Usually α_{ref} is provided by the manufacturer of the wire at $T_{ref} = 20\,^{\circ}\mathrm{C}$, but it is acceptable to put $R_a \alpha_a = R_{ref} \alpha_{ref}$, where the subscript $_a$ indicates quantities at ambient temperature. By plugging eq. 4.3 into eq. 4.1, one obtains:

$$\frac{I^2 R_w}{R_w - R_a} = \pi \ell_w \kappa_c R_a \alpha_a Nu \tag{4.4}$$

Eq. 4.4 is useful to express the amount of heat dissipated away from the wire in function of electrical parameters, but the relationship with flow velocity is not explicit. In order to make this link evident, it is convenient to express Nu as a function of $Re_w = U d_w / \nu$, for example by following the pioneering work of King (1914) with:

$$Nu = A_1 + B_0 Re_w^{0.5} = A_1 + B_1 U^{0.5}, \tag{4.5}$$

where A_1, B_0 and B_1 are empirical constants depending on fluid properties and ambient conditions. With this latter relationship and using Ohm's first law to make wire voltage E_w appear, eq. 4.4 becomes:

$$E_w^2 = \pi \ell_w \kappa_c R_a \alpha_a R_w \left(R_w - R_a\right) \left(A_1 + B_1 U^{0.5}\right) = A + B U^{0.5}. \tag{4.6}$$

A and B are once again empirical constants that have to be determined with a calibration procedure. It must be stressed that eq. 4.6 is correct only for $\ell_w / d_w \to \infty$. For wires of finite aspect ratio, heat may also be transferred to the prongs of the probe. This loss of heat produces a temperature distribution along the wire, which affects the performances of the probe. For a detailed explanation of the subject, the reader is referred to Bruun (1996), chapter 2 and references therein. For most common practical purposes, thermal effects can be taken into account by considering mean quantities along the wire and by modifying eq. 4.6 into:

$$E_w^2 = A + B U^n. \tag{4.7}$$

The exponent n is a function of Re_w, of fluid properties and of wire properties, in particular d_w. In air, Collis & Williams (1959) find that $n \approx 0.45$ for $0.02 < Re_w < 44$. Other authors have proposed methods to estimate n which better take into account Re_w effects (see Bruun (1996), section 4.4.1) but considering that in this study $d_w = 5\,\mu\mathrm{m}$ and $5 < Re_w < 15$, $n = 0.45$ seems to be an acceptable estimation.

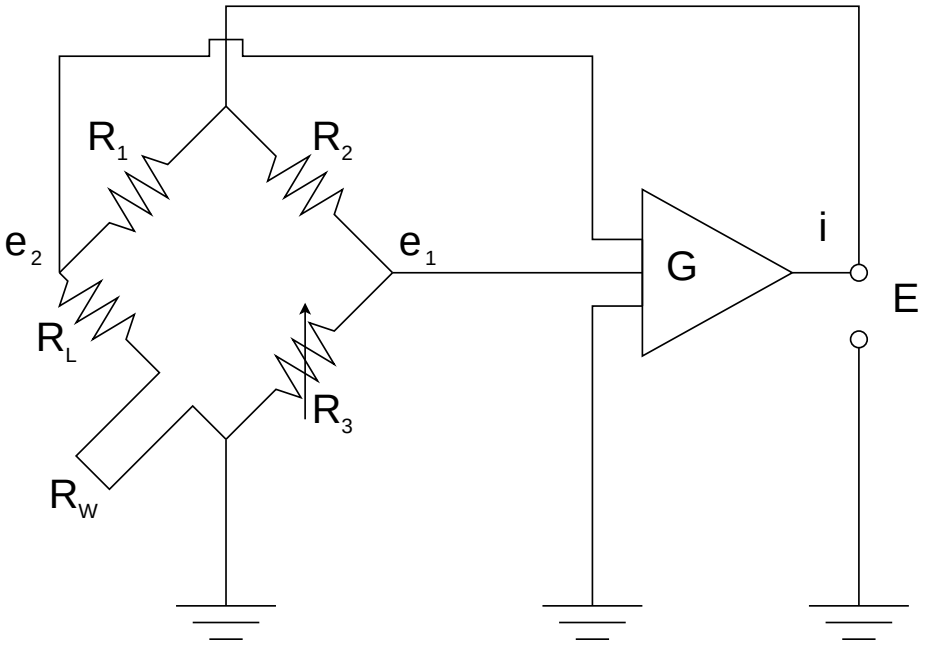

Figure 4.2: CT anemometer circuit. The resistances R_1, R_2, R_3 and $R_L + R_w$ compose a Wheatstone bridge. R_L is the lead resistance of the probe, including contributions due to cables and prongs. G is an amplifier.

4.2.2 Constant Temperature (CT) mode

In this work, single hot-wire probes were operated in Constant Temperature (CT) mode, i.e. by keeping T_w (and hence R_w) almost constant throughout the experiment. The hotwire probe is placed in an electrical circuit called Wheatstone bridge, shown in figure 4.2. The bridge is at equilibrium if the differential voltage $e = e_2 - e_1$ that reaches the operational amplifier is zero. Equilibrium at ambient temperature is imposed prior to calibration and operation, by tuning the resistor R_3. When the wire is exposed to a flow, T_w (and hence R_w) decreases, which alters the equilibrium of the bridge. In response to $e \neq 0$, the amplifier produces a current i which is inversely proportional to the variation of R_w. A feedback branch injects i at the top of the bridge: due to the additional dissipated current, T_w increases thus restoring the original value of R_w. By measuring the voltage E at the amplifier, it is possible to deduce the value of E_w and then compute U from eq. 4.7. The major interest of the CT mode is that the fast response of the amplifier and the small thermal inertia of the thin wire allow the hot-wire probe to react to very quick temperature variations, making it possible to sense a very large range of frequencies in a turbulent flow. This advantage explains the widespread use of the CT mode in the study of turbulence. The working point of the CT mode is often characterised by the so called *overheat ratio* R_w/R_a. Generally speaking, high overheat ratios contribute to make the probe more sensitive to velocity variations, but excessive values accelerate probe aging.

4.2.3 Calibration and temperature effects

As already mentioned, the constants A and B of eq. 4.7 need to be determined empirically, with a calibration procedure. Once the Wheatstone bridge is equilibrated at T_a, the voltage E_w is recorded for a number of known flow velocities U. This can be done either in the test section of the wind tunnel, if an alternative velocity measurement is available, or by using dedicated calibration units (e.g. Dantec 90H02 Flow Unit). Both options have been used in this study. A wide enough velocity range has to be spanned as to cover the entire range that is expected during the actual experiment. Once enough points have been collected, eq. 4.7 can be fitted on them with simple mathematical manipulations.

The calibration procedure based on eq. 4.7 has some disadvantages, the most evident one being that

voltage is expressed in function of velocity rather than the other way around. Starting from the 1980s, reliable polynomial calibration laws were proposed in the form:

$$U = \sum_{n=0}^{N} A_n E^n \tag{4.8}$$

See the work of George *et al.* (1989), among others, for a discussion of the main features of eq. 4.8. This approach being more practical, fourth degree polynomial calibration laws were used for most of the hot-wire measumerement exploited in this study. The coefficients of eq. 4.8 are yielded immediately by standard polynomial fit functions (e.g. *polyfit* in Matlab) or directly provided by the calibration utility of the Dantec Streamware software pack used for hot-wire data acquisition. Figure 4.3 shows that the two calibration laws are equivalent to most practical purposes: in both cases, errors are within $1\,\%$ of the real velocity value on the entire velocity range investigated in this study. Eq. 4.6 highlights that the physical relationship between U and E_w depends on ambient temperature, through electrical resistance and fluid properties. One unconfortable consequence is that the relationship between U and E_w will deviate from the model provided by the calibration law if T_a varies sizeably during measurements, causing increased errors in the estimation of U. Temperature is not actively regulated within the test sections of the facilities used in this study, so that for long experiments many factors can contribute to vary T_a, including skin friction dissipation, heating of electrical elements (e.g. in fan engines) and even the diurnal temperature variation. To minimise the impact of this problem, calibration has to be repeated often enough as to always have a reliable calibration law. As a rule of thumb, the hot-wire probe was recalibrated at least every 2 hours, or in between experiments at different free stream velocities (lasting approximatively 45 minutes) if temperature drifts of more than $1\,^{\circ}\mathrm{C}$ were observed. According to the manufacturer of the probes, this should keep errors induced on velocity within $\pm 2\,\%$.

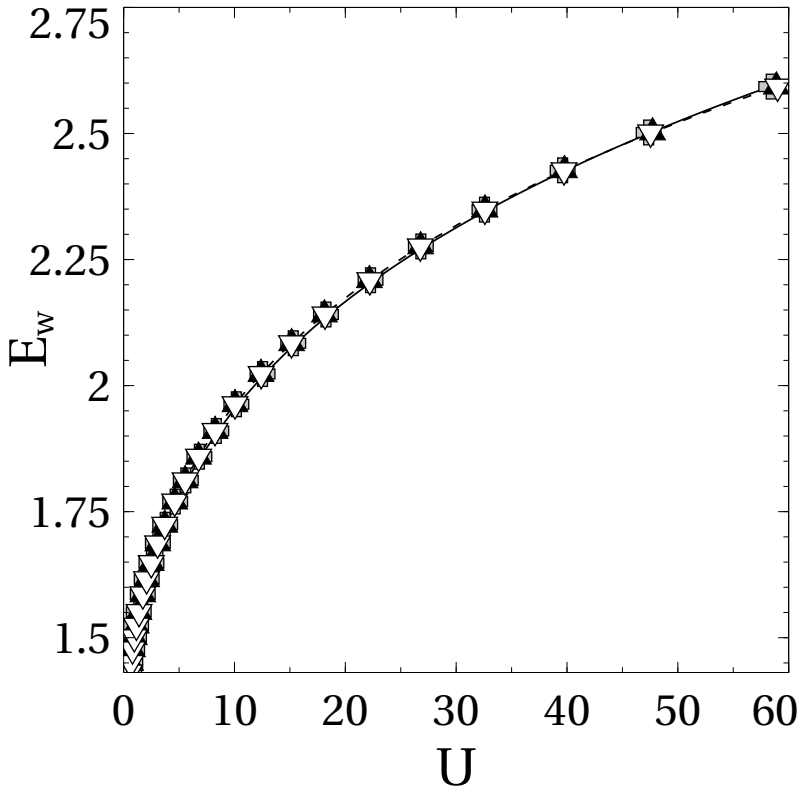

Figure 4.3: Hot-wire calibration curves. Symbols: ▽ recorded calibration points (E_w, U); velocity values obtained from recorded E_w with ✙ King's law (———) and ▲ a fourth degree polynomial (− − −).

4.2.4 Probe models and spatial resolution

Two on-the-shelf Dantec probes were used during this study: the straight-prong 55P11 model and the offset-prong, boundary layer 55P15 model. The two probes have the same sensor, the characteristics of which are summarised in table 4.1. Since ℓ_w is relatively high, spatial integration along ℓ_w is expected to have a sizeable attenuating effect on measurements of turbulent quantities (e.g. u'_{rms}), in particular close to the wall (see for example Wyngaard (1968), Ligrani & Bradshaw (1987), Örlü & Alfredsson (2010) and Philip *et al.* (2013)). Following Philip *et al.* (2013), one can have an assessment of such effect by comparing ℓ_w to λ_m, which is the characteristic length scale of the two-point velocity correlation along the length of the wire. According to those authors, it is $\lambda_m = 0.2\delta$ for $y/\delta > 0.5$, where δ is the boundary layer thickness (see 7.3.2). With reference to the results of table 7.2, this yields $\ell_w/\lambda_m \approx 0.20$ to 0.25, suggesting that hot-wire resolution should be sufficient to study the outer part of the boundary layer. This is pertinent to the study of the turbulent/non-turbulent interface (see § 9.2.2.4). However, in proximity of the wall it is rather $\ell_w/\lambda_m \sim \ell_w^+$, where the symbol $^+$ indicates normalisation in internal units (u_τ and ν/u_τ). Anticipating on table 7.2 once again, this gives $\ell_w/\lambda_m \approx 55$ to 105, depending on Re, which according to Philip *et al.* (2013) should induce attenuations of turbulent fluctuations up to $40\,\%$ to $60\,\%$ for scales smaller than ℓ_w. This contributes to explain the deviation between measured and predicted values of u'_{rms} in proximity of the wall, that are shown in section 7.3.

ℓ_w	d_w	material	max T_a	max U
$1.25\,\mathrm{mm}$	$5\,\mu\mathrm{m}$	Pt-plated tungsten	$150\,^\circ\mathrm{C}$	$500\,\mathrm{m\,s^{-1}}$

Table 4.1: Main characteristics of the sensor of the hot-wire probes 55P11 and 55P15 manufactured by Dantec Dynamics.

4.2.5 Acquisition chains

In most of the hot-wire experiments conducted in this research, E_w signals were acquired with a Dantec Streamline 90N10 frame, operating a 90C10 CTA anemometry module. This hardware includes signal conditioning: to improve signal to noise ratio, the acquired signal was centered on its mean value, amplified and then low-pass filtered. When the Streamline frame was not available, acquisition was executed with a DISA 55M01 anemometer. The signal was then conditioned with a Stanford Research System SIM900 mainframe, mounting a SIM983 amplifier module and a SIM965 filter module (configured as a Butterworth filter, $-48\,\mathrm{dB\,dec^{-1}}$ up to $500\,\mathrm{kHz}$). In both cases, the conditioned signal was digitised with a National Instrument PCI 6251 data acquisition board, working on a range of $\pm\,5\,\mathrm{V}$ and with a maximum acquisition frequency of $1\,\mathrm{MHz}$. The Dantec Streamware software pack was used to control the acquisition chain, as well as the robotic displacement system of the hot-wire probe. Details of the acquisition chain used for the main hot-wire experiments are reported in table 4.2.

Experiment	Probe	Calib. law	Frame	Num. samples	f_s/kHz	f_c/kHz
S1 characterisation	55P15	Polyfit	90N10	2^{19}	60	30
S1 boundary layer	55P15	Polyfit	90N10	2^{19}	60	30
S2 characterisation	55P11	King	SIM900	2^{17}	20	10
S2 boundary layer	55P15	Polyfit	90N10	2^{18}	20	10

Table 4.2: Summary of set-up parameters for the main hot-wire experiments. f_s is the sampling frequency and f_c is the cut-off frequency of the low-pass filter. In all experiments the overheat factor was set to 1.25.

4.2.6 Main hot-wire limitations

In spite of many strong points, hot-wire probes have some limitations that affect their exploitation in this study. In the first place, it must be stressed that eq. 4.1 to eq. 4.7 depend (implicitly or explicitly) on the

norm of U only. Consequently, one single hot-wire probe cannot retrieve the *sign* of velocity. This is far to be a small drawback in the present framework, since streamwise velocity changes sign at a sharp, instationary interface and remains negative in a large region of the flow. The hot-wire probe, then, cannot be used to reliably describe the recirculation region. In the second place, the hot-wire probe is inevitably intrusive, meaning that its insertion in the flow modifies the flow itself, for example by producing a wake. Of course, this wake prevents other reliable measurements downstream of the probe, but interactions with the flow can be less obvious and can have far-reaching consequences on observations. Finally, hot-wire probes available for this work only measure the streamwise component of velocity. Unfortunately, the vertical component is not negligeable over the massive separation (for example for mass transport, see chapter 11) and also needs to be measured. For all these reasons, it appears that available hot-wire probes are of limited use in the investigation of a massively separated flow. Among many measurement techniques that can perform this task, this study relies on Particle Image Velocimetry, as discussed in the next section.

4.3 Particle Image Velocimetry

Particle Image Velocimetry (PIV) is a non intrusive measurement technique that reconstructs the velocity field of entire plane flow regions at once. These characteristics, shared with a number of derivative techniques as Stereo-PIV or PTV, outweight the disadvantages of relatively expensive and complex experimental set-ups and explain the ever growing use of PIV in the investigation of fluid dynamics. The present study is no exception, since the analysis of the separating/reattaching shear layer is essentially developed from PIV measurements. This being so, the present section summarizes the basic principles of PIV and describes the set-ups adopted for measurements on both experimental models. It is pointed out that two-dimensional PIV, only retrieving two components of the velocity field (the so-called 2D2C-PIV) was used throughout this work. As such, limitations due to the unresolved third dimension and velocity component will also be briefly discussed. We kindly aknowledge the friendly support given by Dr. P. Joseph, who provided the velocity fields of the massive separation over the GDR ramp.

4.3.1 PIV principles

It is common knowledge that the topology of a flow (e.g. a wake) can be better visualised by seeding it with a tracer (e.g. smoke or a coloured dye). The core of PIV is that quantitative information on the velocity field can be drawn from tracer particles, if their displacement over a fixed time lapse is known. This is expressed trivially by:

$$\mathbf{U} = \frac{\mathbf{x_B} - \mathbf{x_A}}{\Delta t}. \tag{4.9}$$

The central problem of PIV (and all assimilable techniques) is the reliable estimation of particle displacement $\mathbf{d} = \mathbf{x_B} - \mathbf{x_A}$. The most common method to efficiently do so relies on a local, statistical best match between particle images (Raffel *et al.* (2007)). With reference to figure 4.4, let *ImgA* and *ImgB* be two sequential digital images of the seeded flow, taken at a known Δt one from the other. *ImgA* and *ImgB* are divided in (regular) subregions, called interrogation window. We consider one interrogation window W, of size $2K \times 2L$, on both images. Then, let $f(m,n)$ and $g(m,n)$ describe light intensity within W on *ImgA* and *ImgB*, respectively. The indexes m and n iterate on pixels within W. Provided that an appropriately seeded flow exists in W, particle will have moved during Δt and hence $f(m,n) \neq g(m,n)$. Anyway, if Δt is chosen wisely, $g(m,n)$ is correlated to $f(m,n)$ by particle displacement.

Following Raffel *et al.* (2007), the discrete cross-correlation of $f(m,n)$ and $g(m,n)$ is:

$$R_{fg}(\mathbf{d}) = R_{fg}(d_1\mathbf{e_1} + d_2\mathbf{e_2}) = \sum_{m=-K}^{K} \sum_{n=-L}^{L} f(m,n)g(m+d_1, n+d_2). \tag{4.10}$$

For a given value of $\mathbf{d}$, the sum of the product of intensities of overlapping pixels yields one value of R_{fg}. Applying eq. 4.10 to a wide enough range of $\mathbf{d}$ allows to reconstruct a *cross-correlation map*, an example of which is given in figure 4.5. On the map, peaks of R_{fg} corresponds to values of $\mathbf{d}$ for which $f(m,n)$ and $g(m,n)$ match each other particularly well. This being so, the value of $\mathbf{d}$ for which R_{fg} reaches its

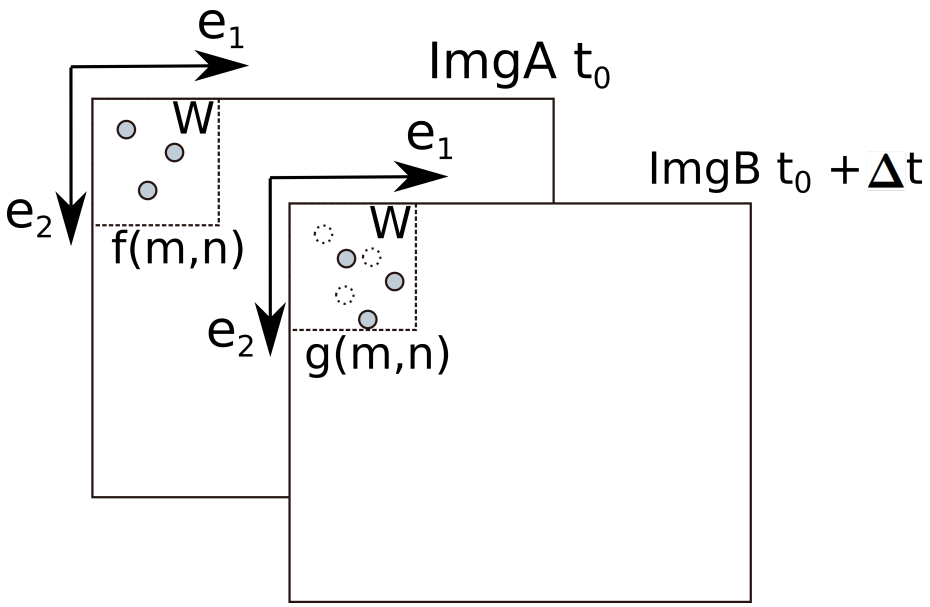

Figure 4.4: Representation of the working principle of PIV.

maximum can be used as best estimate of the mean particle displacement within W. Of course the process can be repeated to obtain one displacement for each interrogation window defined on *ImgA* and *ImgB*. It is important to introduce some limitations of the cross-correlation approach. Firstly, it is by essence a first-order method: only linear displacements within W can be correctly computed, while rotations and deformations remain inaccessible. Secondly, since $\mathbf{d}$ is obtained as an average on W, displacements of *packs* of particles smaller than W will be smoothed out. This comes to say that the size of W determines the spatial resolution of the PIV displacement (and hence velocity) field. It is then interesting to reduce the size of W as much as possible, provided that W is large enough for R_{fg} to be statistically reliable. In most usual PIV application, good compromises can be obtained for W as small as $16\,\mathrm{px}^2$.

4.3.2 Tracer particles

The choice of the tracer is of fundamental importance for PIV, because the characteristics of the particles can affect velocity measurements. Tracer particles should not react with the experimental fluid (air in the present case), and be small and light enough as not to change the properties of the flow noticeably. In addition, their time response should be short enough as to follow even the smallest velocity fluctuation in the flow faithfully. This last requirement can be assessed with the Stokes number, defined as:

$$St = \frac{\tau_p}{\tau_f}, \tag{4.11}$$

where τ_p is a characteristic time of the tracer particle and τ_f is the smallest time scale of the flow. According to Raffel *et al.* (2007) and Tropea *et al.* (2007), τ_p can be estimated from properties of the tracer and of air with:

$$\tau_p = \frac{\rho_p d_p^2}{18\mu}, \tag{4.12}$$

where $\mu = 18.2 \times 10^{-6}\,\mathrm{Pa \cdot s}$ is the dynamic viscosity of air and ρ_p and d_p are tracer particle density and mean diametre, respectively. One reasonable estimate of τ_f is provided by the Kolmogorov time $(\nu/\epsilon)^{1/2}$, where ν is the kinematic viscosity of air and ϵ is the turbulent dissipation rate (also see § 7.4). This implies that the choice of an appropriate tracer depends on properties of the experimental fluid as well as on those of the flow: the higher is Re, the strongest will be the constraint put on the response of tracer particles. All PIV measurements presented in this work utilised an aerosol of olive oil droplets to seed the flow. According

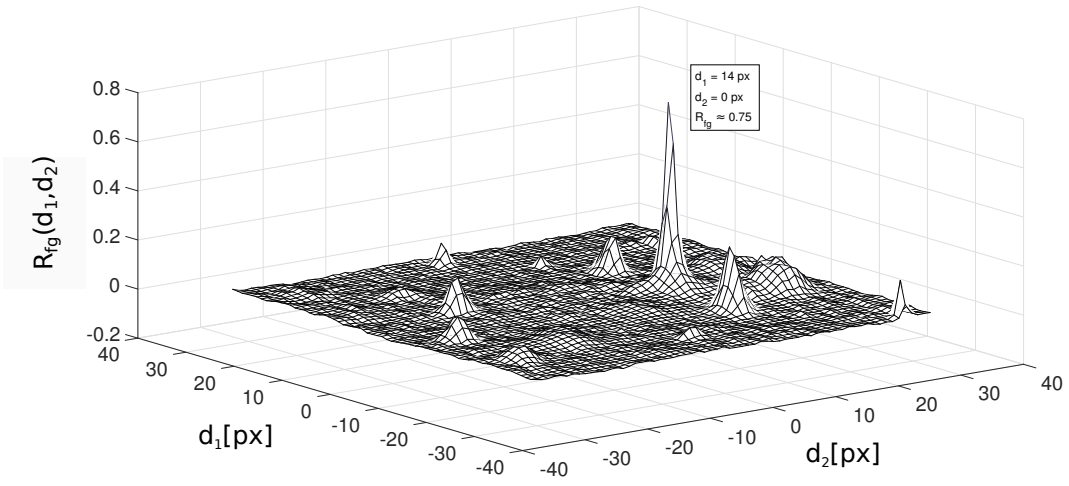

Figure 4.5: An example of cross-correlation map, obtained with an interrogation window of 64×64 px^2 from data of the detailed field.

to the specification of the aerosol generator, the mean particle diametre was $d_p \approx 1\,\mu\mathrm{m}$. For olive oil, it is $\rho_p \approx 970\,\mathrm{kg\,m^{-3}}$ and eq. 4.12 yields $\tau_p \approx 2.75\,\mu\mathrm{s}$. For the datasets used in this study, it is $\tau_f \approx 1.1\,\mathrm{ms}$. It follows from eq. 4.11 that $St \approx 2.5 \times 10^{-3}$: since $St \ll 1$, oil droplets should trace the flow accurately at all turbulent scales.

4.3.3 Image acquisition

In this work, the illumination of the flow is provided by a Quantel EverGreen, double pulse, monochromatic Nd:Yag laser (wavelength $532\,\mathrm{nm}$, rated $2 \times 200\,\mathrm{mJ}$). The laser beam is spread into a laser sheet by a semicylindrical lens. A spherical lens is then used to tune the thickness of the laser sheet, which is estimated to $0.75 \pm 0.25\,\mathrm{mm}$, depending on the experiment. For practical reasons, the flow was always illuminated from above. Section 6.3 shows that in a large neighbourhood of the streamwise symmetry plane of the test section the mean flow is almost bidimensional. Since this is a useful simplification for the analyses proposed in this work, the laser sheet was positioned close to the streamwise symmetry plane: depending on surface state and optical access, representative positions are $y/h = \pm 1$ for the R2 ramp; $y/h = 0 \pm 0.2$ for the GDR ramp. For each PIV experiment, 2000 particle image pairs were captured with LaVision VC-Imager cameras (4032 x 2688 pixels). A LaVision PTU 9 timing unit, driven by the LaVision Davis 8.3 software suit, insured synchronization with laser emissions. The time lapse between images was set in function of mean flow velocity and target interrogation window size: values adopted for each measurement are summarised in table 4.3. In any case, the maximum acquisition frequency of image pairs was of about $2.5\,\mathrm{Hz}$: consecutive image pairs are then uncorrelated. Different lenses were used, depending on the size of the facility and on the desired spatial resolution, as detailed in the following paragraphs.

4.3.3.1 GDR ramp

Images of the massive separation over the GDR ramp were acquired with two cameras simultaneously, respectively placed at $x/h \approx 1.3$ and $x/h \approx 4.3$. Each camera was equipped with a Nikon Nikkor 105 lens, yielding an image resolution of about $118\,\mu\mathrm{m\,px^{-1}}$ on a field of view of $4.6h \times 2h$. After correlation, simultaneous velocity fields were merged using post-processing tools of the Davis 8.3 software suit: the resulting, exploitable merged field is $6h$ wide and will be referred to as the *large GDR field*. An *auxiliary GDR field*, centered at $x/h = -9$, was also recorded to characterise the incoming boundary layer. One

camera was employed, equipped with a SIGMA 180 lens providing a resolution of about $54\,\mu\mathrm{m\,px}^{-1}$ on a field of view of $1.4h \times 0.6h$. Both GDR fields of view are represented in figure 4.6.

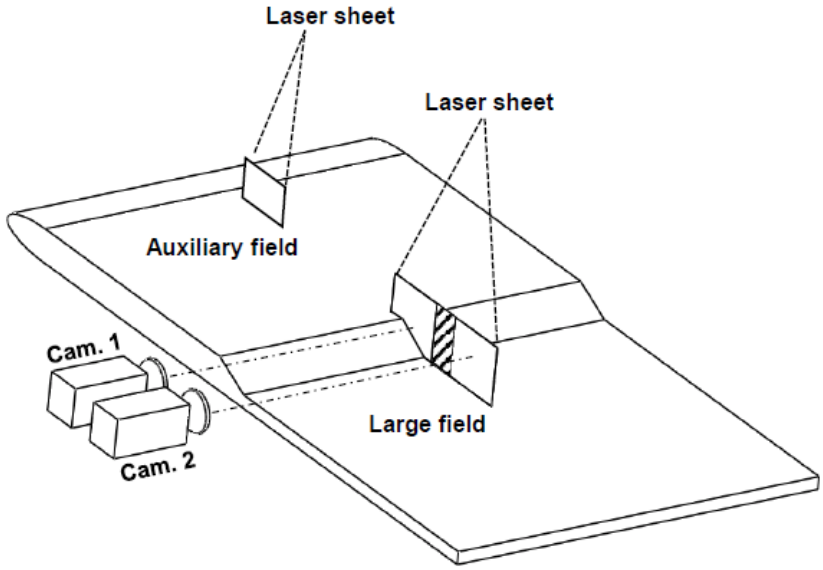

Figure 4.6: Fields of view of PIV experiments on the GDR ramp. Image courtesy of Dr. P. Joseph.

4.3.3.2 R2 ramp

In the case of the R2 ramp, large-scale velocity fields were obtained with one camera, equipped with a Zeiss $50\,\mathrm{mm}$ ZF Makro Planar T* lens, which provided a resolution of $78\,\mu\mathrm{m\,px}^{-1}$ and an exploitable field of view of $6h \times 2.5h$. Three sections of the flow were successively investigated with these settings, respectively centered at $x/h \approx -6$, $x/h \approx 2.5$ and $x/h \approx 5.5$ (figure 4.7). Statistics from the last two sections were merged into a single *large R2 field* (figure 4.7), field (a)) of about $9h \times 2.5h$, which covers the entire recirculation region. The first field, instead, provided a set of PIV images of the incoming boundary layer: it will be referred to as the *auxiliary R2 field* (figure 4.7) field (c)). In addition to these measurements, a $200\,\mathrm{mm}$ Nikon ED AF Micro Nikkor lens was used to investigate small-scale features of the flow on a *detailed field*, placed in the neighbourhood of the upper edge of the R2 ramp (figure 4.7, field (b)). In this latter case, spatial resolution was about $12\,\mu\mathrm{m\,px}^{-1}$ on an exploitable field of view of $1.5h \times 1.2h$.

4.3.3.3 On the estimation of image resolution

Image resolution was estimated by means of several in house or commercial calibration grids. Such grids carry regular patterns (e.g. a checkboard) the geometric parameters of which are known (e.g. the length in mm of the side of each square). Resolution is estimated by comparing the parameters of the pattern in one image (e.g. the length of the side in px) to the real ones.

4.3.3.4 Surface treatments on the experimental models

The experimental set-up is greatly simplified by the fact that laser sheet comes from above the flow. Anyway, this configuration has the drawback of generating strong laser reflections in proximity of the walls of the experimental models. This problem is common to many near-wall PIV experiments, but it is of particular importance for the separating/reattaching flow under study, for at least two reasons. Firstly, direction and intensity of laser sheet reflections change greatly due to the geometry of the model, in particular around the edges of the ramp. Secondly, reflections impact those areas that are of greatest interest in this study, i.e. the regions including the mean separation and reattachment points. This being so, the surface of the

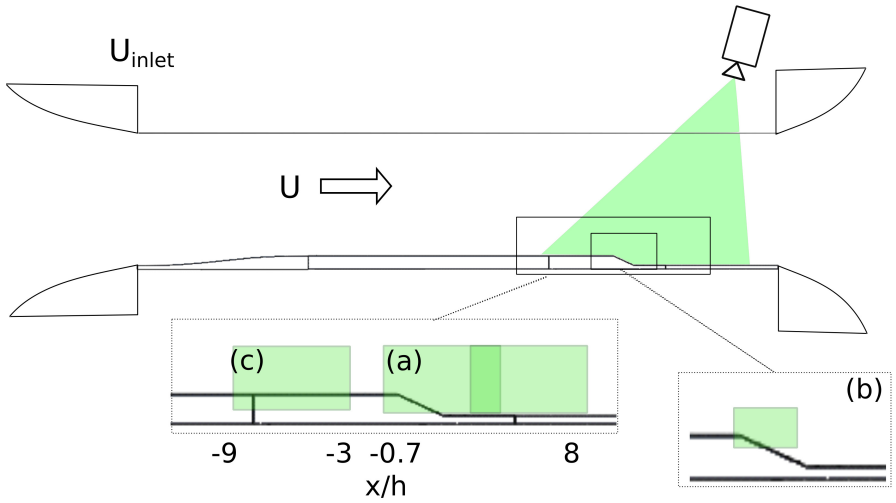

Figure 4.7: Fields of view of PIV experiments on the R2 ramp. Letters indicate the three PIV fields. (a) Large field; (b) Detailed field; (c) Auxiliary field.

experimental models was coated with several thin layers of rhodamine. Since rhodamine does not reflect much on the wavelength of the impinging laser sheet, a selective $532\,\mathrm{nm}$ filter added to the cameras allowed to capture most of the useful light reflected by particles, while attenuating the intensity of light reflected by the walls.

4.3.4 Image processing

Image pairs were processed with the LaVision Davis 8.3 software suite, as detailed in the following paragraphs.

4.3.4.1 Pre-processing

Before correlation, particle images were filtered in order to reduce light intensity fluctuations due to reflections or inhomogeneous illumination. To do so, a sliding average of image intensity was computed on a kernel of $7 \times 7\,\mathrm{px}^2$ to $8 \times 8\,\mathrm{px}^2$ and locally subtracted from the image. This processing acts as a high-pass filter, preserving small intensity fluctuations due to particles while attenuating large ones due to inhomogeneities in the background.

4.3.4.2 Image correlation

The main PIV processing step is correlation of image pairs. For technical reasons, different correlation algorithms were utilised. For datasets recorded on the GDR ramp, correlation was computed with a multipass, Fast Fourier Transform (FFT) correlation algorithm. Interrogation window size was first set to $64 \times 64\,\mathrm{px}^2$ and then reduced to $32 \times 32\,\mathrm{px}^2$ with $50\,\%$ overlapping. The resulting PIV resolution was $\Delta \approx 3.78\,\mathrm{mm}$ on the velocity fields composing the large GDR field; $\Delta \approx 1.73\,\mathrm{mm}$ on the auxiliary GDR field. As for the R2 ramp, image pairs were correlated with a multipass, GPU direct correlation algorithm. The size of the interrogation window was progressively refined from $64 \times 64\,\mathrm{px}^2$ to $16 \times 16\,\mathrm{px}^2$, in each case with $50\,\%$ overlapping. This yielded a PIV spatial resolution $\Delta \approx 1.25\,\mathrm{mm}$ for both large and auxiliary fields, $\Delta \approx 0.19\,\mathrm{mm}$ for the detailed field.

4.3.4.3 Post-processing

The first purpose of post-processing was to detect and replace false velocity vectors. To begin with, questionable vectors were pinpointed based on correlation peaks (see § 4.3.1). It is reminded that peaks in the correlation map indicate the most probable mean displacements. Then, a velocity vector was considered dubious and removed if the ratio between the highest and the second highest peaks was lower than a threshold, conventionally set to 1.2. Since spurious vectors can also be associated to high correlation peak ratios, an additional detection technique was used, based on median filters. Median filters effectively identify false vectors by their deviation with respect to the median value of a local set of vectors. In the case of the large GDR field, an iterative median filter was used, capable of removing several neghbouring vectors at once. As for the auxiliary GDR field and the R2 ramp, the chosen median filter was the universal outlier detector proposed by Westerweel & Scarano (2005). In any case, removed vectors were replaced with linear interpolations of the neighbouring ones. During post-processing, the velocity fields composing the large GDR field were also merged together with calibration utilities included in the LaVision DaVis 8.3 software.

4.3.4.4 Evaluation of PIV signal noise

PIV signal noise was assessed by comparing the square root of the streamwise Reynolds stress $\sqrt{\langle (u')^2 \rangle}$ to the value of residual turbulence of the wind tunnel. In the Malavard tunnel equipped with the GDR ramp, PIV gives a residual turbulence of about $1.5 \pm 0.1\%$ in the auxiliary field and $1\,\%$ to $2\,\%$ at separation, to be compared to hot-wire measured values of $0.45 \pm 0.15\%$ and $0.6 \pm 0.1\%$, respectively. In the Eiffel tunnel equipped with the R2 ramp, it is found that $\sqrt{\langle u'^2 \rangle}/U_\infty \approx 1.5\,\%$ to $2\,\%$ (PIV), for a residual turbulence of about $0.5\,\%$ (hot-wire), where U_∞ is the local free stream velocity. In this case the fields of view either overlap or are not too far apart, so that differences between the large/detailed field and the auxiliary field are negligible. Among other consequences, PIV noise can impact the investigation of turbulent interfaces. It is then important to compare the noise levels of these experiments with those achieved in other works on turbulent interfaces. The studies by de Silva *et al.* (2013) and Chauhan *et al.* (2014*c*) are particularly relevant, because in this research the TNTI is detected with the technique proposed by those authors (see § 9.2.2). de Silva *et al.* (2013) reported $\sqrt{\langle (u')^2 \rangle}/U_\infty \approx 1\,\%$ in the free flow, for a value of residual turbulence of about $0.2\,\%$. Both quantities are close to those measured in this work, which justifies the use of the available PIV datasets for investigating turbulent interfaces.

4.3.5 Considerations on PIV resolution

As already mentioned at § 4.3.1, the size of the interrogation window determines PIV spatial resolution. It is convenient to quantitatively assess the impact of finite resolution on the information on the flow that can be retrieved from PIV measurements. A straightforward way to do so is to compare Δ to the smallest scales of the flow, for example the Kolmogorov scale η. Values for the ratio Δ/η are reported in table 4.3. Estimations of η in the incoming boundary layer are provided in table 7.2, based on hot-wire measurements. We consider here the value of η at the height from the wall where the mean TNTI is located and we associate to the symbol Δ the length of the side of one (square) interrogation window. Although the hot-wire is likely to overestimate the values of η, it appears evident that none of the available PIV datasets resolves the whole range of spatial scales on which the flow develops. Anyway, the effects of finite resolution are sensible even for scales that are larger than Δ. This is particularly evident in the spectral domain. Foucaut *et al.* (2004) showed that power spectra obtained from PIV measurement are attenuated of $50\,\%$ at a cut-off wavenumber $k_c = 2.8/\Delta$, independent of the overlapping of interrogation windows, from which a cut-off wavelength λ_c can be easily obtained as $2\pi/k_c$ (see table 4.3). λ_c seems to be an acceptable estimate of the lower scale reliably resolved by PIV measurements, at least if spectra are computed with respect to the streamwise direction. As such, it appears that the GDR datasets should be exploited for investigating large-scale quantities exclusively. R2 datasets allow finer analysis, but only the detailed field gives access to a relatively wide subrange of the small scales of the flow.

4.3.6 Considerations on the third velocity component

2D-2C PIV (as most other planar imaging techniques) only resolves two components of the velocity field and gives access to the azimuthal component of vorticity at most. This is an important drawback when studying turbulence, which is intrinsically three-dimensional. Anyway, this limitation should not impact the analysis of the mean field too much, since the spanwise pressure distribution demonstrates that the latter is almost bidimensional (§ 6.3). Bias could be stronger when considering the smallest turbulent length scales resolved by the PIV (e.g. when investigating entrainment through instantaneous interfaces in chapter 12), since the third velocity component might become quantitatively relevant as turbulence approaches (assumed) isotropy. Although this issue is not solved in this study, it is hoped that the bidimensional analysis allowed by PIV data will also be qualitatively representative of entrainment in the spanwise direction. In this respect, the results reported by Veynante *et al.* (2010) are encouraging. These authors verified that properties of turbulent flames (viz. flame wrinkling) in the unresolved direction can be modelled from planar measurements, with very good agreement with DNS.

	GDR ($h = 100\,\mathrm{mm}$)		R2 ($h = 30\,\mathrm{mm}$)		
	Aux	Large	Aux	Large	Detailed
Lens	$180\,\mathrm{mm}$	$105\,\mathrm{mm}$	$50\,\mathrm{mm}$		$200\,\mathrm{mm}$
Field of view $/h^2$	1.4×0.6	$6 \times 2^*$	6×2.5	$9 \times 2.5^*$	1.5×1.2
$\mu\mathrm{m\,px}^{-1}$	54	118	78		12
Δ/px	32×32		16×16		16×16
Δ/mm	1.73	3.78	1.25		0.192
Δ/η	12 to 23	25 to 50	8.5 to 10		1.3 to 1.55
λ_c/mm	3.87	8.47	2.8		0.363
λ_c/η	30 to 50	70 to 100	18 to 23		2.3 to 3
$U_\infty/\mathrm{m\,s}^{-1}$	15, 20, 30, 40		15, 20, 25, 30, 35		15, 20, 25, 30
$\Delta t/\mu\mathrm{s}$	33, 23, 16, 12	55, 38, 25, 19	90, 67, 54, 45, 38		20, 15, 12, 10

Table 4.3: Summary of PIV parameters for all experiments discussed in this study. Fields of view marked by the symbol * are obtained by merging two smaller fields. Values of η (reported in table 7.2) are computed from hot-wire data in the boundary layers at $x/h \approx -9$ and $z/\delta \approx 0.65$, i.e. at the height from the wall where the mean TNTI is located.

4.4 Wall pressure measurements

Streamwise and spanwise wall pressure distributions were investigated with a pool of 3 μDAQ-32C differential pressure scanners, manufactured by Chell Instruments. Identification numbers and characteristics of the scanners are reported in table 4.4. Scanners were interfaced and multiplexed with an acquisition unit. Pneumatic connections were provided by vinyle tubes of inner diameter equal to $1.25\,\mathrm{mm}$. The length of the tube dependent on the experimental model: it was of about $2\,\mathrm{m}$ for the GDR ramp, of $1\,\mathrm{m}$ for the R2 ramp. The work of van Ommen *et al.* (1999) showed that pneumatic connections of similar length and diameter have cut-off frequencies as low as $20\,\mathrm{Hz}$. Accordingly, only mean pressure distributions were computed, using 3×10^4 samples acquired over about $50\,\mathrm{s}$. Considering a characteristic time scale $t_h = h/U_{ref}$, this represents between 0.75×10^4 and 2×10^4 t_h for the GDR ramp and 2.5×10^4 and 6×10^4 t_h for the R2 ramp, respectively, which was sufficient for statistical convergence. The layout of pressure taps on the two experimental models is detailed in the following paragraphs.

4.4.1 GDR ramp

The model was fitted with a total of 93 static pressure taps (figure 4.8). Due to the sizes of the model, streamwise pressure distribution was investigated on $x/h \in (-3, 7)$ only, along three longitudinal lines of pressure taps respectively placed at $y/h = -5$ (scanner 801), 0 (scanner 803) and 5 (scanner 802). Each line was composed of 23 pressure taps. Distance between pressure taps corresponds to the spatial resolution

of wall pressure measurements. On each longitudinal line, spatial resolution was finer in the neighbourhood of the edges of the ramp. Spanwise pressure distribution was assessed along 2 rows of pressure taps, respectively located at $x/h = -0.5$ and $x/h = 0.6$, both composed of 15 pressure taps. Each pressure scanner was connected to 5 taps of each row, chosen in function of their position relative to longitudinal lines. For example, the scanner collecting data from the leftmost longitudinal line was connected to the 5 leftmost taps of each row, and so on. The reference static pressure was provided by a Pitot tube, placed at $(x/h = -2.5; y/h = 0; z/h = 5.9)$. The dynamic pressure was also collected on each scanner.

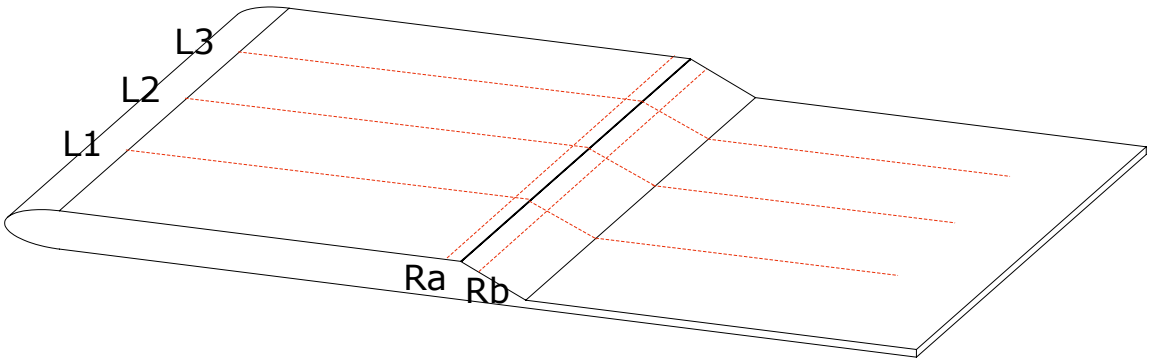

Figure 4.8: Placement of pressure taps on the GDR ramp. The streamwise lines of pressure taps are identified by markers **L1** ($y/h = -5$), **L2** ($y/h = 0$) and **L3** ($y/h = 5$). The two spanwise rows are identified by markers **Ra** ($x/h = -0.5$) and **Rb** ($x/h = 0.6$). CAD of the GDR ramp courtesy of Dr P. Joseph.

4.4.2 R2 ramp

The model was fitted with a total of 62 static pressure taps (figure 4.9), connected to pressure scanners 801 and 802. 38 pressure taps were distributed in the streamwise direction, once again with a finer spatial resolution in the neighbourhood of the edges of the ramp. Flow homogeneity in the spanwise direction was investigated along 3 rows of pressure taps, respectively located at $x/h = -7.67$ (6 pressure taps), -0.17 (8 pressure taps) and 0.36 (8 pressure taps). The Pitot tube providing the reference static pressure was placed at midspan, above the upper edge of the ramp $(x/h = 0; y/h = 0; z/h = 9)$. Dynamic pressure was once again collected on one free input of one of the scanners.

PID	Num. channels	$f_{s,max}$/Hz	Bit depth	FR/kPa	ϵ_p/FR %
801 802	32	625	16	2.5	0.25
803	32	625	16	6.9	0.25

Table 4.4: Summary of pressure scanner characteristics. $f_{s,max}$ is the maximum sampling frequency (intended in measurements per channel per second), FR is the full range of the scanner and ϵ_p represents measurement uncertainty.

4.5 On complementarity of measurement techniques

The measurement techniques that were described in previous sections compose a panel of complementary tools, the main characteristics of which are reported in table 4.5. Generally speaking, PIV is the best suited one to study the large-scale features of the recirculation region, since it is not intrusive and can retrieve both the norm and the sign of a two-component velocity vector. In addition, one of the PIV set-ups used in this

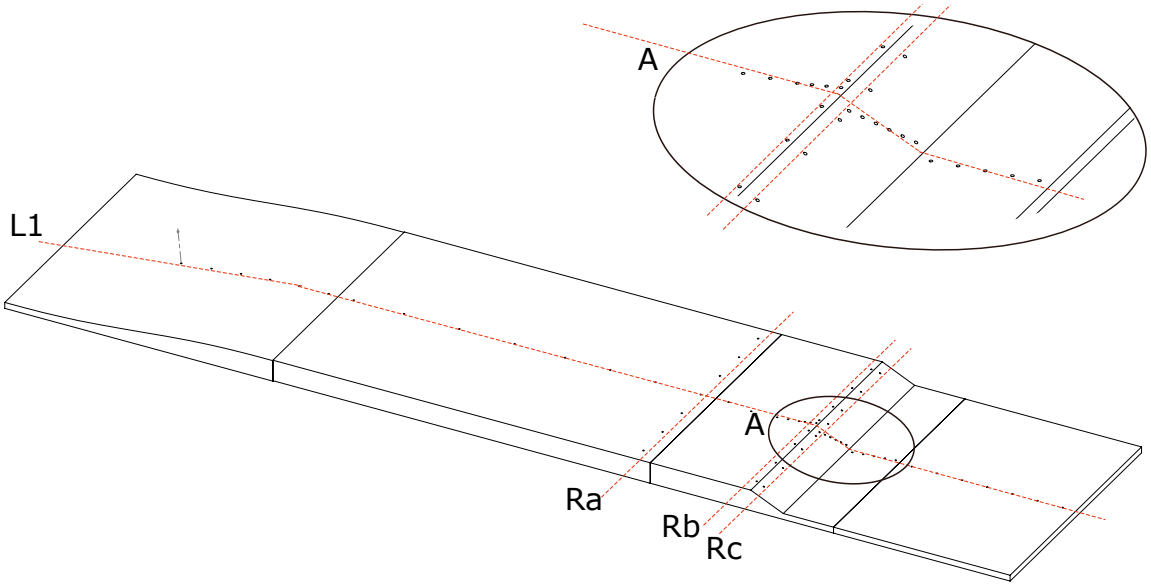

Figure 4.9: Placement of pressure taps on the R2 ramp. The streamwise line of pressure taps (y/h = 0) is indicated by marker **L1**, while the three spanwise rows are identified by markers **Ra** (x/h = -7.67), **Rb** (x/h = -0.17) and **Rc** (x/h = 0.36). Detail **A** reports a zoomed view of the descending ramp.

study is sufficiently resolved to also give access to the statistics of a relatively large part of the range of turbulent scales of the flow. However, in proximity of the wall PIV fields might be polluted by spurious vectors, due to laser reflections. Hence, hot-wire probes appear to be better suited for the characterisation of the incoming boundary layer, in which the properties of the flow in a thin region above the wall are of great importance. Hot-wire data are also time-resolved: although the spatial resolution of available probes is quite low, this feature allows an estimation of the smallest turbulent scales in the incoming flow that would not be possible with available PIV data alone. Finally, pressure data provide insight on large-scale features at the wall. In particular, they allow to verify if the massive separation is, in average, homogeneous in the spanwise direction (i.e. if the mean flow is bidimensional). Although this condition can be tested with PIV-based approaches (for example a mass balance, as in chapter 11), spanwise wall-pressure measurement can be exploited in a simpler and more immediate way, giving confidence to more complex analyses of the mean field. In addition, wall-pressure data are often the only ones available in real, industrial configurations: it seems then important to include them in the discussion and, when possible, correlate them to the features of the flow highlighted by less easily deployable techniques.

Technique	Quantities	Dimensions	Space resolution	Time resolution	Backflow	$(y - y_{wall})\,\vert_{min}$
HW	u	pointwise	medium	high	no	$\sim 0.1\,\mathrm{mm}$
PIV	u, v	planar	low to medium	none	yes	$\sim 3\,\mathrm{mm}$
Pressure scanners	Δp	pointwise-planar	low to medium	none	yes	0

Table 4.5: Summary of properties of the main measurement techniques used in this work. $(y - y_{wall})\,\vert_{min}$ represent the minimum distance from the wall at which the technique can provide reliable information, with reasonable experimental effort.

Part III

Characterisation of the flow

5

General overview of the flow

Caractérisation générale de l'écoulement

Ce chapitre montre les éléments principaux de l'écoulement décollé analysé dans ce travail. Cette discussion générique est basée sur le décollement à $Re_h = 13.3 \times 10^4$ uniquement. Les différences observées à d'autres valeurs de Re_h ainsi que de meilleurs paramètres de similitude seront présentés dans la suite.

Le champ de la composante de vitesse U (figure 5.1) montre bien que le décollement se produit à l'arête supérieure de la rampe. Ensuite, une couche cisaillée décollée se développe entre l'écoulement potentiel et la bulle de recirculation moyenne, impactant la paroi à $x \approx L_R$: son bord supérieur est la TNTI (voir chapitre 9) et son bord inférieur, la RRI. Les efforts de cisaillement moyens sont faibles (voire négligeables) à l'extérieur de ces lignes (figure 5.2). Le décollement induit une vitesse verticale $V > 0$ dans une région à l'aval de l'arête (figure 5.3). Cela produit un flux qui alimente l'épaississement de la couche cisaillée. Ce flux est équilibré par la quantité de masse qui entre dans la bulle de recirculation au recollement (indiqué par le terme anglais *backflow*). Ce mouvement circulaire du fluide entre couche cisaillée, *backflow* et bulle de recirculation est considéré comme l'un des moteurs des décollements turbulents massifs (Adams & Johnston (1988*a*) parmi d'autres).

La couché cisaillée est aussi la région de l'écoulement où la turbulence (analysée en termes d'efforts de Reynolds) est plus forte. La figure 5.4 montre que les efforts de cisaillement turbulents ne sont pas négligeables dans la bulle de recirculation, mais ils sont globalement plus intenses dans la couche cisaillée. Leur maximum est atteint au recollement : il s'agit là d'une différence importante par rapport au cisaillement moyen, qui tend à s'atténuer en s'éloignant du point de décollement. L'image est similaire pour les efforts turbulents normaux, représentés en figure 5.5 par l'énergie cinétique turbulente k : la RRI est perméable à k (contrairement à la TNTI) mais la couche cisaillée reste la région la plus active du point de vue de la turbulence (voir aussi la distribution de la production d'énergie cinétique turbulente, $\mathcal{P}$, en figure 5.7).

La longueur de la bulle de recirculation, indiquée par L_R, est définie comme la distance entre le point de décollement moyen et le point de recollement moyen. Dans cette étude, le premier est figé à l'arête supérieure de la rampe. Quant au deuxième, il est estimé en extrapolant la RRI moyenne (détectée sur le champ PIV avec le critère $U = 0$) jusqu'à la paroi de la rampe. Les valeurs de L_R ainsi obtenues, qui semblent être dans la dispersion observée dans la littérature, sont récoltées dans le tableau 5.1.

5.1 Introduction

This chapter introduces the main elements of the separated flow under study. For the moment, one suitable and straighforward choice for a parameter of similitude is the Reynolds number based on step height, Re_h, introduced in chapter 3. In this work, Re_h spans from 3×10^4 to 26.7×10^4, depending on h. Further sections will show that properties of the flow (e.g. its scaling parameters) are not exactly equivalent on the R2 ramp and the GDR ramp, and for increasing levels of incoming turbulence. Other parameters of similarity will then be introduced to take into account these phenomena and to propose original, general scaling laws for massively separated flows. Anyway, these differences are not of central importance in the framework of the qualitative, big picture view that is given here. For these reasons, the discussion will be based on the flow at $Re_h = 13.3 \times 10^4$ exclusively.

5.2 Mean velocity fields

Figure 5.1 shows the streamwise velocity field of the mean separated flow over the GDR ramp, at $Re_h = 13.3 \times 10^4$. The separation of the incoming boundary layer is induced by the sharp expansion of the test section. Downstream of the mean separation point, a separated shear layer develops between the free-stream and a large mean recirculation region, where $U < 0$. The latter extends up to the reattachment point, where the separated shear layer hits the wall. At reattachment, the separated shear layer splits in two, in part feeding the backflow into the recirculation region, in part moving further donwstream and relaxing into a new, slowly recovering, reattached boundary layer (Eaton & Johnston (1981), Adams & Johnston (1988*a*), Song & Eaton (2003) among others). The external boundary of the recirculation region is the RRI. In this study, it is defined by the isoline $U = 0$ on the mean streamwise velocity field. As for the TNTI, it is the upper edge of the shear layer. Details on the detection of the TNTI are given at § 9.2. For the moment, it can be conceived as an energy isoline, separating the region of the flow where $k = 1/2\left(\langle u'^2\rangle + \langle v'^2\rangle\right) \gg 0$ from the free-stream. Alternatively, it will be shown that the TNTI is well approximated by the velocity isoline where U reaches its free-stream value. Of course, strong mean shear is the dominant feature within the separated shear layer, at least in a large neighbourhood of the separation point (figure 5.2), while it is negligible in the free-stream and weak in most of the recirculation region. Other components of the strain rate tensor are also comparatively weak over most of the flow field.

Figure 5.3 reports the corresponding mean vertical velocity field. Significantly, one of the effects of separation is the induction of a large zone of positive vertical velocity, which is located donwstream of the mean separation point, within the recirculation region. Even if, as a whole, the free-stream acquires a negative vertical velocity, this mass flux feeding the separated shear layer prevents a sudden, negative acceleration of the flow right downstream of the edge of the ramp. Indeed, it appears that minimum negative velocities are reached only toward the reattachment point, i.e. in the region of shear layer impingment on the wall. All in all, the flow seems to form a sort of closed loop. Forward-moving fluid tends to descend the ramp and hit the wall. Then, due to the interaction with the wall, some of it deviates into the backflow. Finally, the backward-moving fluid rises up again at separation, being re-entrained by the separated shear layer (Adams & Johnston (1988*a*)). This qualitative picture effectively describes one of the main mechanisms at work in the separated flow under study. In spite of its *apparent* simplicity, it will provide the phenomenological bases for many of the discussions of further chapters.

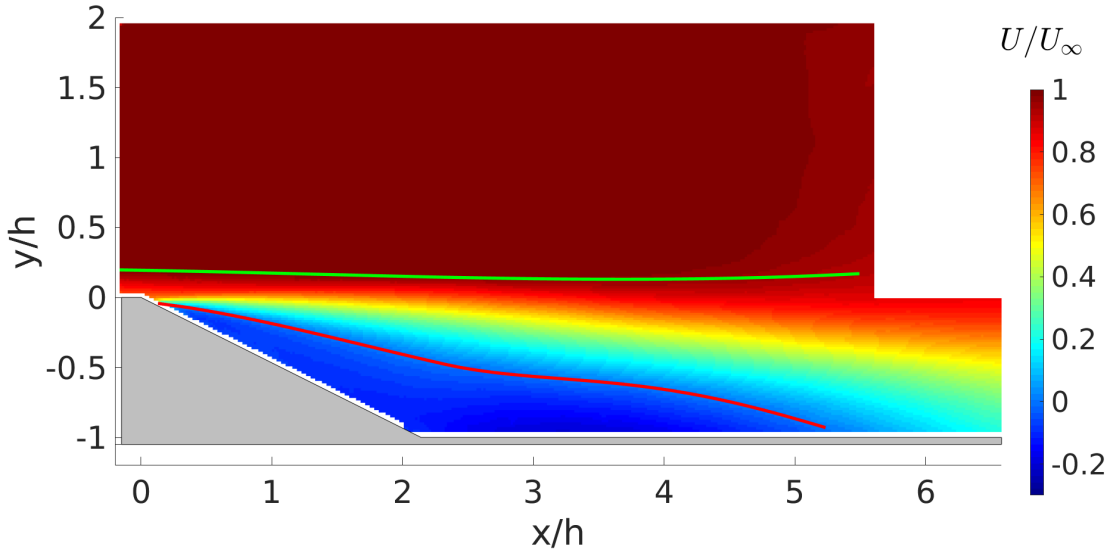

Figure 5.1: Mean streamwise velocity field at $Re_h = 13.3 \times 10^4$. —— Mean TNTI. —— Mean RRI.

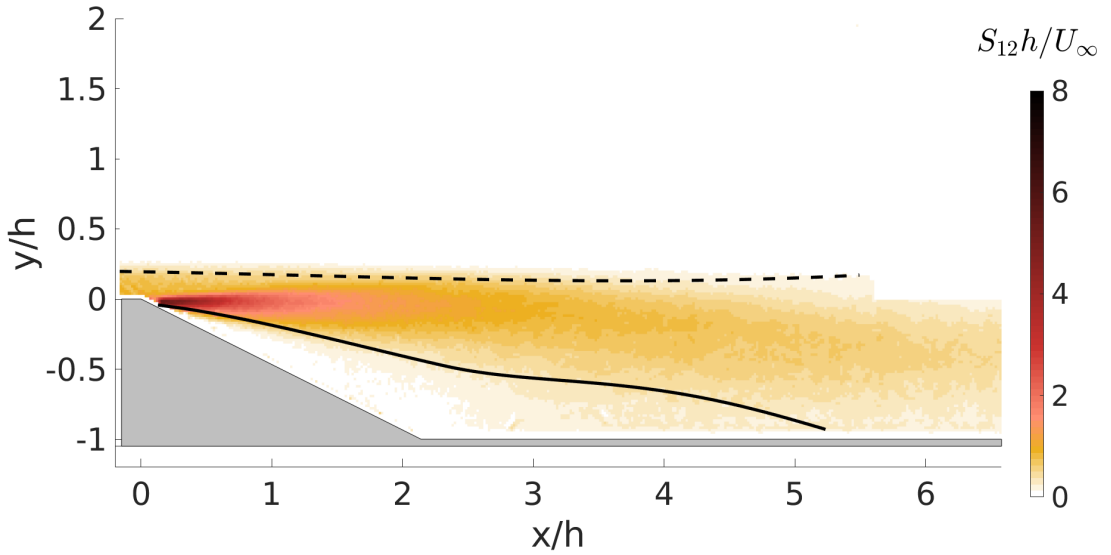

Figure 5.2: S_{12} strain rate field at $Re_h = 13.3 \times 10^4$. - - - Mean TNTI. —— Mean RRI

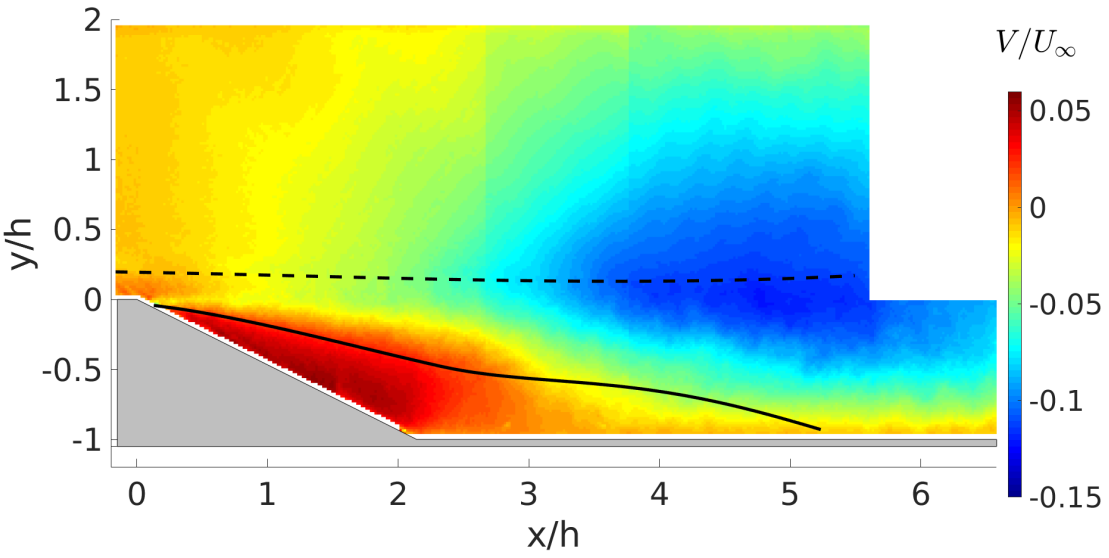

Figure 5.3: Mean vertical velocity field at $Re_h = 13.3 \times 10^4$. - - - Mean TNTI. ——— Mean RRI

5.3 Turbulence

The investigation of Reynolds stresses can provide a good starting point for the assessment of turbulence in the separated flow under study. Figure 5.4 presents the field of turbulent shear stresses $\langle u'v' \rangle$, which greatly influence shear layer growth (see § 8.6). The intensity of $\langle u'v' \rangle$ in the recirculation region is not negligible, in particular close to reattachment. However, it is evident that the term $\langle u'v' \rangle$ peaks within the separated shear layer, which, as a whole, has much higher levels of turbulent shear stresses than the recirculation region and, of course, the free-stream. Interestingly, turbulent activity is more intense in the second part of the shear layer, in contrast with mean shear that tends to fade away as one moves further downstream. The different evolution of terms of shear is of some importance and will be commented extensively in chapter 8.

As for the normal Reynolds stresses $\langle u'^2 \rangle$ and $\langle v'^2 \rangle$, their magnitude and behaviour is comparable to those just highlighted for $\langle u'v' \rangle$. For simplicity, the distribution of turbulent kinetic energy k (i.e. their sum) is reported in figure 5.5. Clearly, the separated shear layer is the most energetic zone of the flow, with increasing levels of k as the flow is considered further downstream. The RRI is permeable to k, while the TNTI wraps the highly energetic shear layer from the unperturbed, irrotational free-stream. In this respect, it is pointed out that, as shown in figure 5.5, moderate amounts of k leak out of the TNTI for $x/h > 2$. In principle, this is not consistent with the definition of TNTI. Anyway, it will be shown at § 9.2.2.7 that, to a large extent, this behaviour seems to be due to limitations of the GDR PIV datasets. To solve this problem, an alternative, velocity-based definition of the TNTI is introduced at § 9.4.

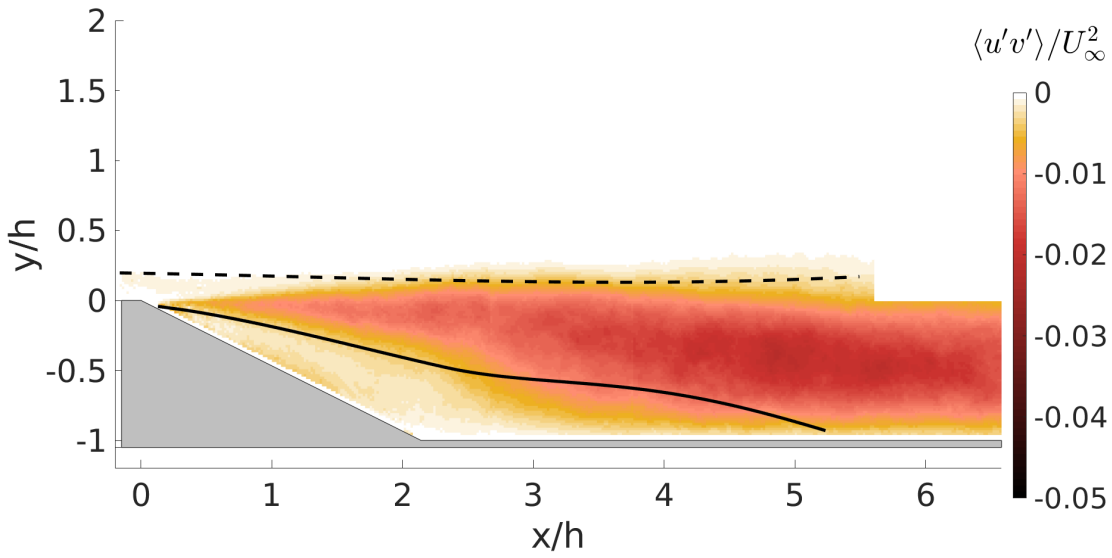

Figure 5.4: Turbulent shear stresses $\langle u'v' \rangle$ at $Re_h = 13.3 \times 10^4$. - - - Mean TNTI. ——— Mean RRI

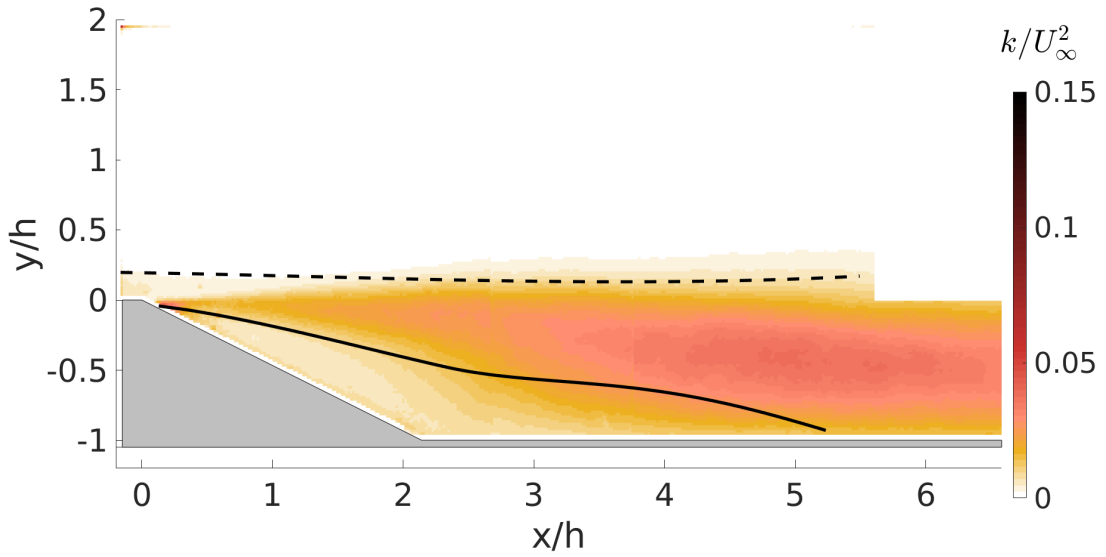

Figure 5.5: Field of turbulent kinetic energy k at $Re_h = 13.3 \times 10^4$.- - - Mean TNTI. ——— Mean RRI

5.4 RRI and mean recirculation length L_R

The mean RRI (commonly named mean separation line) has been often considered in previous studies on separated flows, independently of its role in transfer and in bounding the separated shear layer. For this reason, it seems important to further detail its definitions and its uses. As already mentioned, the simplest definition of RRI is given by $U = 0$ (Durst & Tropea (1981), Armaly *et al.* (1983), Simpson (1989), Nadge & Govardhan (2014)). An alternative definition of the mean RRI is based on the so called backflow coefficient χ, which represents the fraction of time that the flow moves downstream (Simpson (1989), Cuvier (2012)). Intuitively, regions of the flow that are exposed to the instantaneous backflow for more than half of the time are more likely to also belong to the average recirculation region. On the contrary, regions exposed to longer timespans of positive streamwise velocity will probably be in the separated shear layer or in the free-stream. This being so, the mean RRI is the set of points of the mean field where $\chi = 0.5$. This second definition better conveys the instable behavior of the recirculation bubble, the size of which changes continuously. Figure 5.6 proves that the two definitions of the RRI agree excellently. It this study, the definition $U = 0$ was preferred due to its simpler implementation.

The streamwise distance between the separation point and the reattachment point (indicated with L_R) is the characteristic length of the recirculation region. The significance of L_R as a scaling parameter for the separated flow has been proved in a number of previous works, including Roshko & Lau (1965), Eaton & Johnston (1981), Westphal *et al.* (1984), Adams & Johnston (1988*a*), Nadge & Govardhan (2014) (among many others) and it will be discussed extensively in the following chapters dedicated to the characterisation of the flow. In BFS flows (or other flows in which separation is geometrically fixed, as the present ramp flow), the assessment of L_R mainly requires to detect the mean reattachment point. Many alternative techniques to do so exist. For example, Chapman *et al.* (1958) uses the mean dividing streamline; Sigurdson (1995) visually identifies the mean reattachment point by means of tufts attached to its experimental model; Friedrich & Arnal (1990) place it at the streamwise location at which the mean wall shear stress is zero. In image-based or numerical analyses, the mean RRI is often used to compute L_R, by considering that separation takes place at the first point of the interface, and reattachment at the last one (e.g. Le *et al.* (1997) and Kourta *et al.* (2015)). Based on the mean RRIs yielded by PIV data, the ratio L_R/h ranges from 5.16 to 4.11 on the R2 ramp, from 5.36 to 5.09 on the GDR ramp (table 5.1). In each experiment, the location of the mean reattachment point moves upstream for increasing Re_h. Unfortunately, in most PIV datasets a thin region in close proximity of the wall was unexploitable, due to laser reflections. This means that the

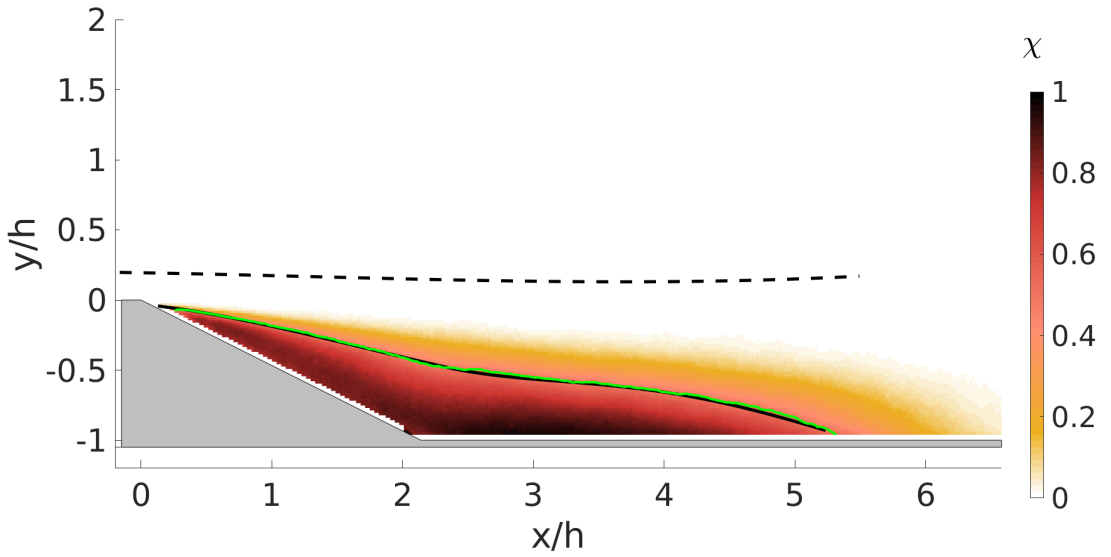

Figure 5.6: Comparison of different RRI definitions at $Re_h = 13.3 \times 10^4$, shown on the spatial distribution of backflow coefficient χ. ——— $U = 0$ definition; ——— χ definition. The mean TNTI (- - -) is also reported for reference.

last point of the *visible* RRI is not the true mean reattachment point, as it appears evident in figure 5.6. To improve the estimation of L_R, the RRI was then approximated with two polynomials, joint at the change in slope visible at $x/h \approx 2.5$. The polynomials were conditioned as to have a continuous first derivative. Then, the polynomial RRI was extrapolated up to $y/h = -1$. The corrected values of L_R/h so obtained are also listed in table 5.1 and will be used from now on. Considering ramp flows, the main term of comparison is probably Ruck & Makiola (1993), which observed values of L_R/h of the order of 7 for $\alpha = 25°$. However, their expansion ratios were at least 1.48, compared to $ER \approx 1.05$ to 1.1 in our case: as such, shorter L_R/h are not surprising. ER values closer to those used in this work are found in the literature on BFS flows. Here we consider data by Nadge & Govardhan (2014), that seem to be the most reliable since, in particular, these authors do not focus on L_R only, but study the evolution with Re_h and ER of the entire structure of the recirculation region. Values in table 5.1 are of the order of magnitude reported by Nadge & Govardhan (2014) for similar values of ER. Agreement with other works is also acceptable. For example, for $ER \approx 1.1$ and $\delta_e/h \approx 0.7$, Moss *et al.* (1979) find that $L_R/h \approx 5$ at $Re_h = 5 \times 10^4$, which compares very well with our measurements[1] (see Eaton & Johnston (1981), Adams & Johnston (1988*a*) and references within Le *et al.* (1997) for other examples). Unfortunately, the decreasing trend observed in our experiments does not agree with the saturated value of L_R (i.e. independent of Re_h and ER) observed by Nadge & Govardhan (2014), for $Re_h > 2 \times 10^4$. Among possible explanations, it seems noteworthy that values of Re_θ, the Reynolds number based on momentum thickness in the incoming boundary layer (see chapter 7) are globally much lower than in the present experiments: then, incoming turbulence is not comparable. The possible dependencies on Re_θ of L_R/h will be discussed at length in the following chapters of this work, starting from § 8.5.

As a final remark on the RRI, it is pointed out that even if the definitions of RRI do not directly relate to turbulence, this interface seems to be significant when investigating turbulent properties too. For instance, figure 5.4 and figure 5.5 suggest that the RRI roughly separates regions with different turbulent intensities. The sharp difference in mean shear highlighted by figure 5.2 encourages to consider the contribution to

[1] Aider & Danet (2006) also reports $L_R/h \approx 5.5$ with $ER \approx 1.2$ and $\delta_{99}/h \approx 1.2$, but for Re_h as low as 5.1×10^3. This nice example gives an idea of the scatter of L_R/h data found in the literature. However, this value of L_R/h seems to deserve some caution: as pointed out by the authors, the LES of Aider & Danet (2006) does not match the results retrieved from the DNS of Le *et al.* (1997) in similar conditions.

$Re_h/10^4$	3	4	5	6	7	10	13.3	20	26.7
Visible RRI	5.16	4.94	4.83	4.48	4.11	5.36	5.23	5.18	5.09
Polynomial RRI	5.42	5.22	5.1	4.79	4.4	5.62	5.49	5.37	5.22

Table 5.1: Evolution of the ratio L_R/h with Re_h.

turbulent production $\mathcal{P}$ accessible to 2D2C-PIV, that is:

$$\mathcal{P} = \langle u'^2 \rangle \frac{\partial U}{\partial x} + \langle v'^2 \rangle \frac{\partial V}{\partial y} + \langle u'v' \rangle \left(\frac{\partial U}{\partial y} + \frac{\partial V}{\partial x} \right). \tag{5.1}$$

The distribution of $\mathcal{P}$ is given in figure 5.7. It appears evident that turbulent kinetic energy is essentially produced *outside* of the recirculation region. This is in agreement with the DNS of a BFS flow reported by Le *et al.* (1997) and with the DNS of a separated boundary layer by Na & Moin (1998). Both studies show that turbulent production is negligible in the backflow of a separated boundary layer, but intense outside. Similar results, albeit more qualitative, are reported for ramp flows by Debien *et al.* (2014). Dandois *et al.* (2007) also reports that spanwise vorticity ($\Omega_3 = \partial V/\partial x - \partial U/\partial y$) is, as a whole, higher ouside the recirculation region. This is well verified in the present experiments too (figure 5.8). These findings suggest that the RRI might be more than a conventional demarcation of the recirculation region, with some role in the overall energy balance of the flow.

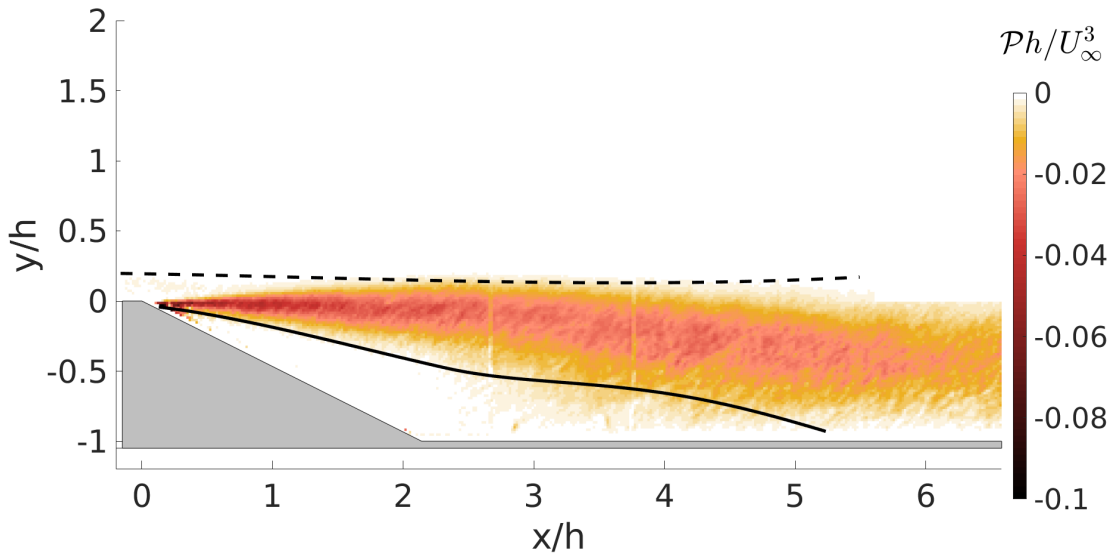

Figure 5.7: Distribution of turbulent production $\mathcal{P}$ at $Re_h = 13.3 \times 10^4$. - - - Mean TNTI. ——— Mean RRI

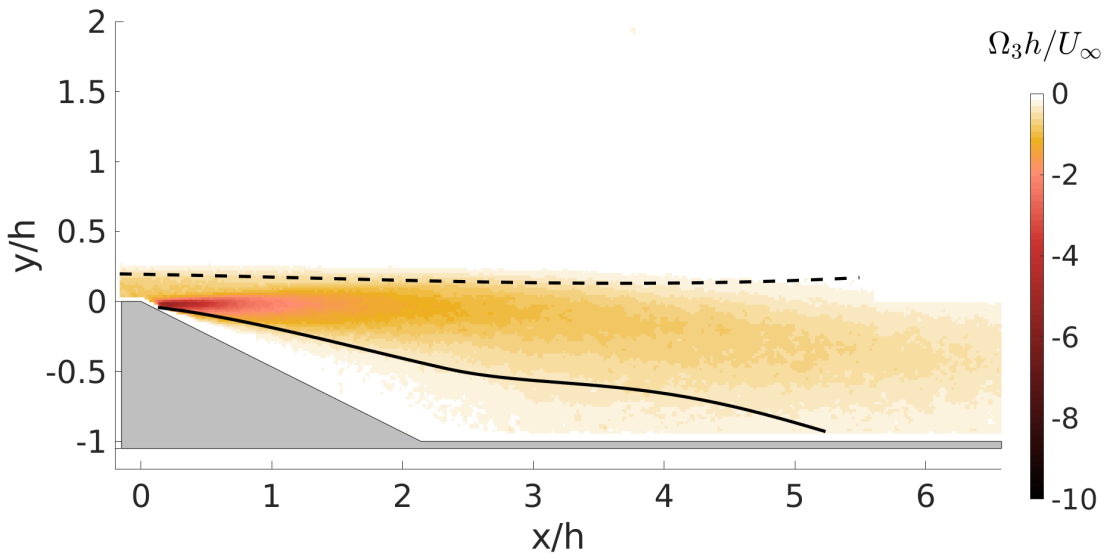

Figure 5.8: Distribution of spanwise vorticity Ω_3 at $Re_h = 13.3 \times 10^4$. - - - Mean TNTI. ——— Mean RRI

6

Wall pressure distributions

Caractérisation de la distribution de la pression à la paroi

La pression à la paroi est analysée sous forme de coefficients de pression C_p, définis comme en éq. 6.1 à partir de valeurs p_{ref} et U_{ref} fournies par le tube de Pitot. Sur la rampe R2, la distribution longitudinale de C_p et du gradient de pression C_{px}, normalisé sur h, est une fonction faible de Re_h (figure 6.1). Le gradient de pression n'est jamais nul, mais au-dessus de la plaque plane à l'amont de l'arête, il semble être suffisamment faible pour ne pas affecter de manière significative le développement de la couche limite. Une situation similaire est observée sur la rampe GDR (figure 6.2). De plus, la normalisation en h met en échelle les données des deux rampes sur toute la région du décollement et sur une large partie de la plaque plane à l'amont : cela suggère que la distribution de pression est la même dans les régions où les deux maquettes expérimentales sont géométriquement similaires.

Le décollement massif est marqué par un plateau de basse pression (indiqué par le symbole $C_{p,b}$) suivi d'une rapide augmentation du C_p, qui atteint un pic (indiqué par le symbole $C_{p,r}$) à $x/h \approx 7$ sur les deux rampes. En accord avec les observations de Adams & Johnston (1988*a*), les valeurs de $C_{p,r}$ sont influencées par le ratio δ_e/h, qui donne le rapport entre l'épaisseur de la couche limite à l'amont au décollement et la hauteur de la rampe (figure 6.3). En utilisant la formulation du C_p réduit proposée par Chapman *et al.* (1958) (indiquée par C_p^*), on trouve que la distribution longitudinale de C_p^* concorde bien avec la courbe pseudo-universelle de Roshko & Lau (1965) (figure 6.4). Il est aussi remarqué que la distribution de C_p^* semble être corrélée au développement de la couche cisaillée (voir § 8.2) : le plateau de pression correspond bien à un développement rapide de la couche cisaillée, tandis que l'augmentation de pression correspond à des taux d'épaississement faibles.

En ce qui concerne la distribution transversale de C_p, elle est homogène sur $60\,\%$ de l'envergure des deux maquettes expérimentales. Cela indique que l'écoulement décollé est en moyenne bidimensionnel (figure 6.5 et figure 6.6).

6.1 Introduction

Pressure distribution along the experimental model is related both to the evolution of the boundary layer and to the characteristics of separation (Adams & Johnston (1988*a*)). In this chapter, the distribution of pressure along the walls of both ramps will be examined, both in the streamwise and in the spanwise direction. Pressure data will be expressed in form of pressure coefficients C_p, defined as follows:

$$C_p = \frac{P_W - P_{ref}}{1/2\,\rho\,U_{ref}^2}, \tag{6.1}$$

where P_W is mean wall pressure and P_{ref} and U_{ref} are provided by the Pitot tube.

6.2 Streamwise wall pressure distribution

Figure 6.1 and figure 6.2 show the streamwise evolution of C_p over the R2 ramp and the GDR ramp, respectively. In both cases the streamwise coordinate is normalised on h. For technical reasons, the streamwise pressure distribution over the GDR ramp could be measured only over $x/h \in (-3, 7)$. To compensate for this drawback, the streamwise C_p distribution observed by Kourta *et al.* (2015) is also taken into account. Kourta *et al.* (2015) investigated the flow over a ramp that essentially differs from the GDR ramp only for the absence of the synthetic jet slots. Figure 6.2 proves that their pressure dataset agrees well with measurements on the GDR ramp. This being so, in what follows the Kourta *et al.* (2015) dataset is assumed to be representative of GDR ramp behavior and it is utilised to extend comparison with the R2 ramp over regions much upstream of separation.

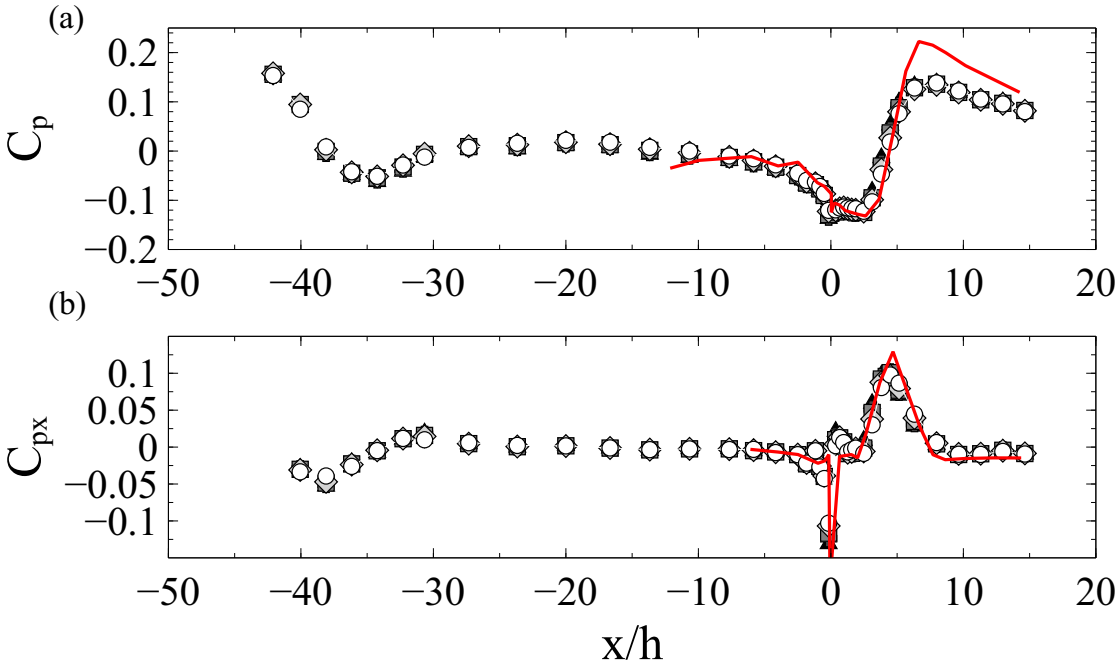

Figure 6.1: Streamwise evolution of (a) the wall pressure coefficient and (b) its dimensionless derivative along the R2 ramp. Symbols: ◯ $Re_h = 3 \times 10^4$; ◊ $Re_h = 4 \times 10^4$; ■ $Re_h = 5 \times 10^4$; ✚ $Re_h = 6 \times 10^4$; ▲ $Re_h = 7 \times 10^4$. —— Pressure data from Kourta *et al.* (2015).

The streamwise C_p distribution appears to be a relatively weak function of Re_h. On the R2 ramp, C_p stays roughly constant downstream of the contraction, until the flow approaches the ramp. Although not perfectly zero, the dimensionless pressure gradient $C_{px} = h\mathrm{d}C_p/\mathrm{d}x$ in this region is small (figure

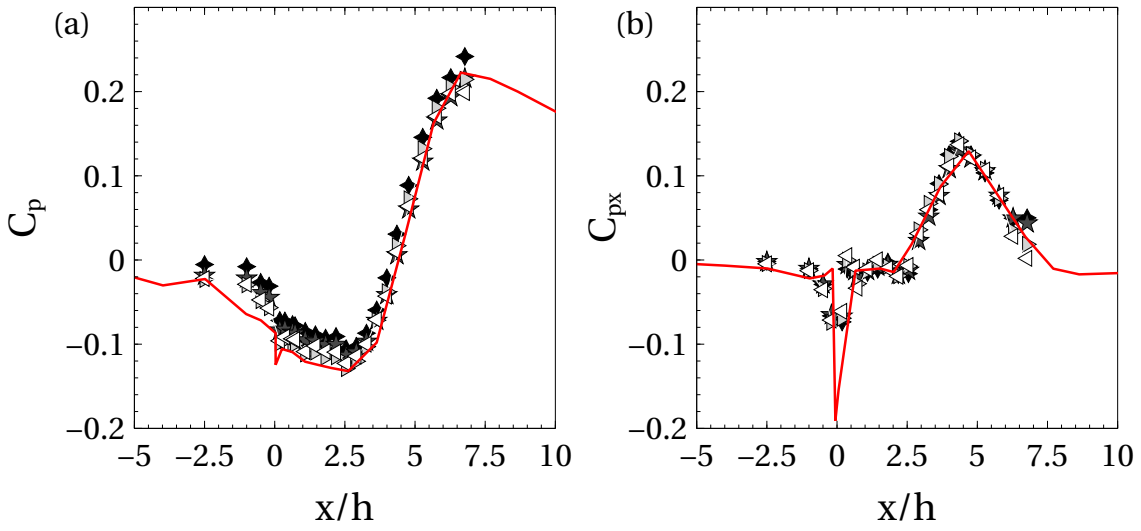

Figure 6.2: Streamwise evolution of (a) the wall pressure coefficient and (b) its dimensionless derivative along the GDR ramp. Symbols: ◁ $Re_h = 10 \times 10^4$; ▷ $Re_h = 13.3 \times 10^4$; ★ Re_h =20×10^4; ✦$Re_h = 26.7 \times 10^4$. ——— Pressure data from Kourta *et al.* (2015).

6.1(b)), so that its influence on boundary layer development is assumed to be mild. Using h to normalize the streamwise distance, C_p and C_{px} are in good agreement with Kourta *et al.* (2015) in all those regions where the geometries of the two experiments are comparable, that is downstream of the separation point and over a large fraction of the flat plate upstream of the edge of the ramp (figure 6.1). This simply indicates that, for ramps with the same geometry, the streamwise pressure distribution roughly scales with step height.

6.2.1 Focus on the separated flow

The onset of separation at the upper edge of the ramp ($x/h = 0$) induces a strong decrease of pressure, the value of which is substantially comparable between the two ramps (figure 6.1(a) and figure 6.2(a)). The recirculation region is characterized by a low pressure plateau followed by a rapid pressure rise that reaches a maximum at $x/h \approx 7$ on both ramps. In the following, the plateau and the peak C_p values will be referred to as *base* C_p (noted $C_{p,b}$) and *peak reattachment* C_p (noted $C_{p,r}$), respectively. Irrespective of h, $C_{p,b}$ lies in a small range of -0.10 to -0.12 for most tested Re_h. According to Adams & Johnston (1988*a*), scatter in values of $C_{p,r}$ can be explained by the different δ_e/h ratios, where δ_e is the boundary layer thickness at the edge of the ramp (see § 7.3.2). Similar observations were made by Tani *et al.* (1961). In our work, δ_e/h are of the order of 0.8 to 0.9 for the R2 ramp and 0.3 for the GDR ramp. In this respect, let us consider the reduced pressure coefficient C_p^*, defined by Chapman *et al.* (1958) as:

$$C_p^* = \frac{C_p - C_{p,b}}{1 - C_{p,b}}. \tag{6.2}$$

Figure 6.3 shows that the values of $C_{p,r}^*$ from the present study and from Kourta *et al.* (2015) agree acceptably well with the δ_e/h correlation observed by Adams & Johnston (1988*a*) in BFS flows ($ER = 1.25$, $Re_h = 3.6 \times 10^4$). Deviations might be due to several factors, including the geometry of the bluff body under study. For what concerns the R2 ramp, the value of ER is of some importance in explaining differences with respect to Adams & Johnston (1988*a*). Indeed, these authors show that for $\delta_e/h > 0.8$, $C_{p,r}^*$ saturates to a value imposed by the geometric expansion. In the present experiments the value of ER is about $15\,\%$ lower: for high enough values of δ_e/h, this difference could be sufficient to delay the saturation of $C_{p,r}^*$. In addition, the experiment of Adams & Johnston (1988*a*) was designed such that δ_e/h could be changed at constant U_∞, which is not the case in the present research. This might introduce Re_h effects into our data that, although mild, are not included in Adams & Johnston (1988*a*).

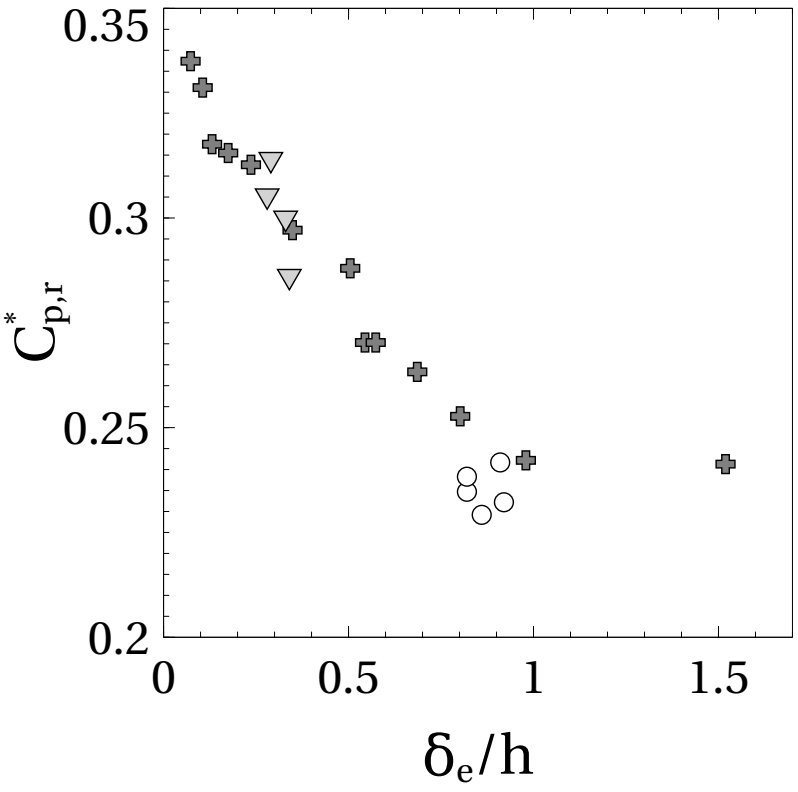

Figure 6.3: δ_e/h dependency of $C^*_{p,r}$. Symbols: ◯ R2 ramp; ▽ GDR ramp; ✚ BFS data by Adams & Johnston (1988*a*), $Re_h = 3.6 \times 10^4$ and $ER = 1.25$.

Roshko & Lau (1965) studied the streamwise C^*_p distribution in the separated flows generated by a number of different bluff bodies, including BFS. They found that C^*_p profiles collapse onto a (relatively) universal curve when streamwise distance is normalised on L_R. Figure 6.4 presents the streamwise C^*_p distribution, normalised as suggested by Roshko & Lau (1965), for both the R2 ramp and the GDR ramp. For x/L_R between 0 and 1, C^*_p data from the present work and from Kourta *et al.* (2015) collapse well on the curve observed by Roshko & Lau (1965): this supports the idea that L_R is the scale that organises the separated flow. Interestingly, the C^*_p distribution appears to be correlated to the development of the shear layer, that will be discussed at § 8.2: the region where entrainment drives shear layer growth ($x/L_R < 0.5$) corresponds to the $C^*_{p,b}$ plateau, while for $x/L_R > 0.5$ lower spreading rates seem to be linked with pressure recovery. The collapse of C^*_p distributions is less satisfactory for $x/L_R > 1$, as if after reattachment L_R was no longer the (unique) flow-organising scale. It is stressed that the streamwise C^*_p distribution does not seem to be influenced by the state (fully turbulent or not) of the incoming boundary layer (see § 7.3.1), which agrees with findings by Adams & Johnston (1988*a*).

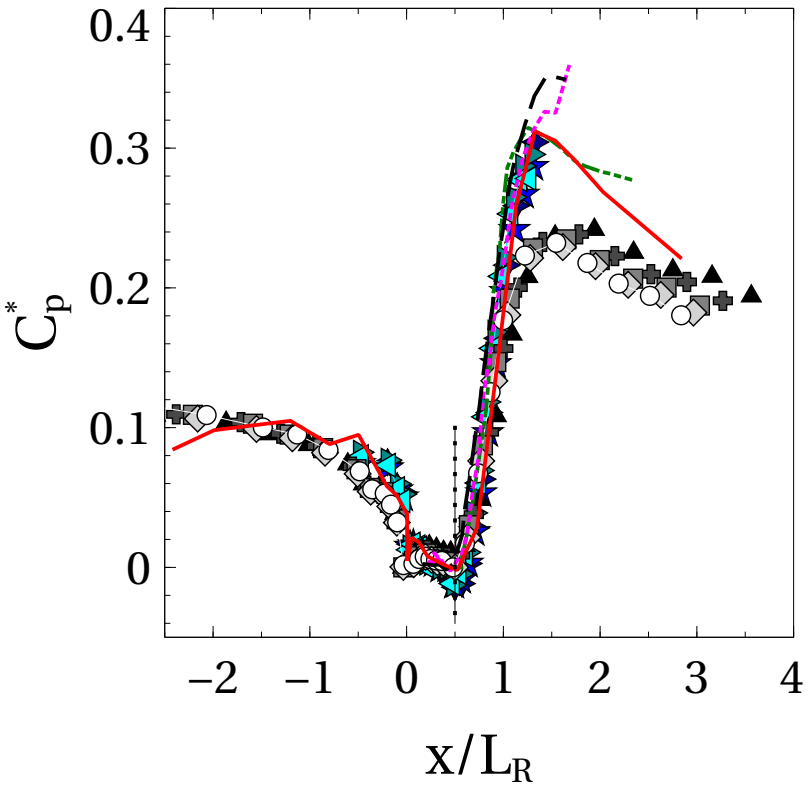

Figure 6.4: Streamwise wall distribution of reduced pressure coefficients. Symbols ——— Reduced pressure data from Kourta *et al.* (2015). – – – Roshko & Lau (1965) series A. ····· . Roshko & Lau (1965) series D. –·–· BFS data by Adams & Johnston (1988*a*). Other symbols as in figure 6.1 (gray shades) and figure 6.2 (blue shades).

6.3 Spanwise wall pressure distribution

Figure 6.5 reports the spanwise C_p distributions along the three R2 transverse rows of pressure taps (§ 4.4.2). The mean flow appears to be nearly bidimensional, so that the mean separation is homogeneous at least over $60\,\%$ of the width of the test section. Similar conclusions can be drawn for the GDR ramp (figure 6.6). In this case, the streamwise C_p distributions along the three longitudinal lines of pressure taps (§ 4.4.1) can also be compared: this confirms that the characteristics of the mean separation are homogeneous along most of the width of the model.

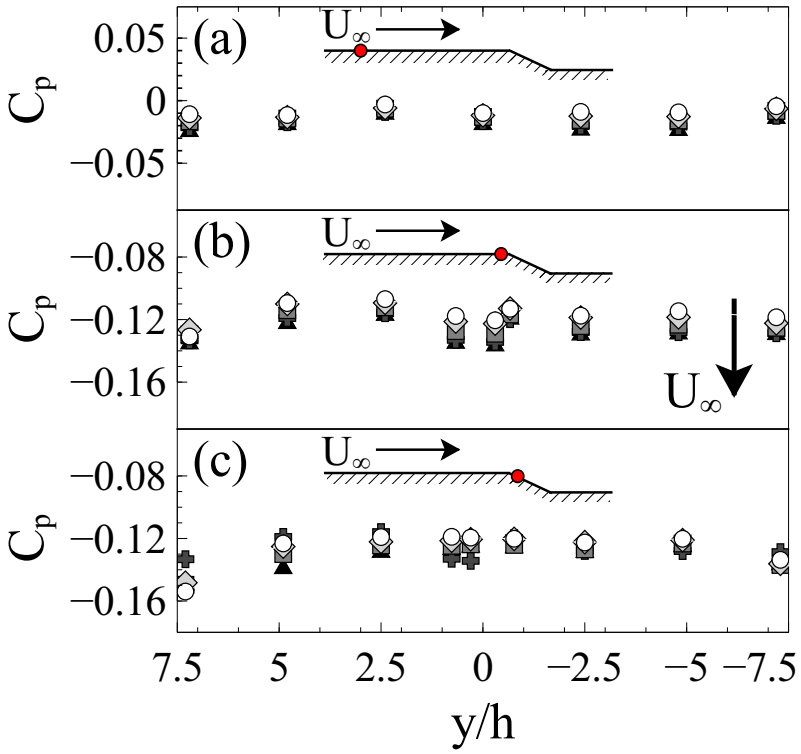

Figure 6.5: Spanwise pressure distributions on the R2 ramp. (a) **Ra** ($x/h = -7.67$); (b) **Rb** ($x/h = -0.17$); (c) **Rc** ($x/h = 0.36$). Symbols as in figure 6.1.

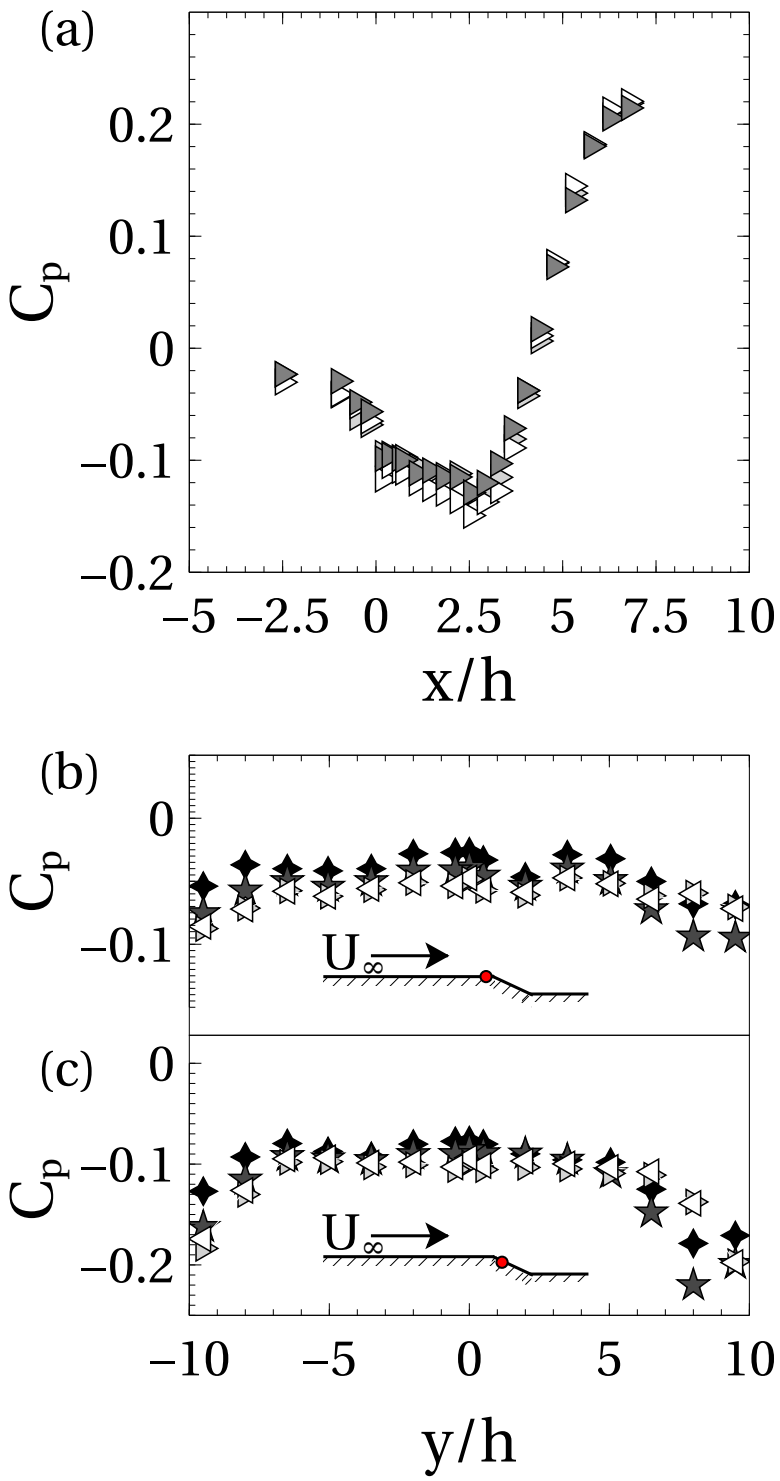

Figure 6.6: Spanwise homogeneity of wall C_p distributions on the GDR ramp: (a) comparison of the streamwise distribution along ▷ **L1** ($y/h = -5$), ▶ **L2** ($y/h = 0$) and ▷ **L3** ($y/h = 5$); (b) spanwise C_p distribution along **Ra** ($x/h = -0.5$); (c) spanwise C_p distribution along **Rb** ($x/h = 0.6$). Symbols in (b) and (c) as in figure 6.2.

7

The incoming boundary layer

Caractérisation de la couche limite amont

Il est important de caractériser la couche limite à l'amont de l'arête de la rampe, parce qu'elle établit les conditions initiales du décollement massif. Pour vérifier que la couche limite n'est pas trop affectée par le gradient de pression non nul (voir § 6.2), l'épaisseur de déplacement δ_1 (éq. 7.1a), l'épaisseur de quantité de mouvement θ (éq. 7.1b) et leur rapport H_{12} sont mesurés (au fil chaud) à plusieurs positions longitudinales. Leurs évolutions sont ensuite comparées avec des modèles semi-empiriques fournis, par exemple, dans Schlichting *et al.* (1968). La figure 7.3 et la figure 7.2 montrent que les mesures dans la couche limite sont en accord avec les modèles, sauf à proximité de l'arête de la rampe : dans cette région le gradient de pression est fort et tend à empêcher l'épaississement ultérieur de la couche limite. Sur la rampe R2, un turbulateur a été rajouté en entrée de veine pour assurer la répétabilité des mesures. Le rampe GDR avait déjà été équipée d'un turbulateur pendant un travail précédent (voir Kourta *et al.* (2015)).

Pour chaque valeur de Re_h, une couche limite de référence est mesurée à $x/h = -9$. À cette position, le gradient de pression longitudinale suit encore la loi d'échelle en h (figure 6.1 et figure 6.2), et il affecte peu le développement de la couche limite. De plus, Neumann & Wengle (2003) ont montré que l'état de la couche limite à $x/h < -4$ est corrélé à la longueur de la bulle de recirculation, ce qui est d'un grand intérêt dans le cadre de notre étude. Les figures 7.3 à 7.6 montrent que les profils de vitesse moyenne et fluctuante obtenues avec le fil chaud concordent avec les données DNS de Schlatter & Örlü (2010) et les mesures PIV dans les champs auxiliaires. Les caractéristiques intégrales de la couche limite de référence considérées ici incluent, outre δ_1, θ et H_{12}, des estimations de l'épaisseur de la couche limite δ et de la vitesse de frottement u_τ, obtenues avec le profil composite de vitesse proposé par Chauhan *et al.* (2009) (voir § 7.3.4). Il est spécifié que dans ce travail δ est la hauteur au-dessus de la paroi à laquelle $U/U_\infty \to 1$. Pour la suite, il est aussi intéressant d'avoir une estimation de δ_e, l'épaisseur de la couche limite à l'arête de la rampe. A cause du gradient de pression, la méthode de Chauhan *et al.* (2009) ne peut pas être utilisée à cet endroit. De ce fait, on estime δ_e sur les profils de vitesse moyenne, comme la hauteur au-dessus de la paroi à laquelle $U/U_\infty \to 0.998$. En complément de ces quantités intégrales, on calcule aussi des estimations de l'échelle de Kolmogorov à la position de la TNTI moyenne (voir le chapitre 9), dans l'hypothèse d'isotropie locale. Les propriétés de la couche limite à l'amont pour chaque valeur de Re_h sont résumées dans le tableau 7.2.

7.1 Introduction

It is important to investigate the incoming boundary layer because it provides the inital conditions from which the massive separation onsets. This chapter focus on a set of parameters, mostly of integral or large scale nature, that were chosen to characterise the boundary layer. The list includes boundary layer thicknesses (δ, δ_1, θ), the shape factor H_{12} and the friction velocity u_τ. An estimation of the smallest spatial scales within the boundary layer is also provided. A particularity of the present experiments is that the pressure gradient is not uniformly zero in the regions where the boundary layer develops. In part, this is due to the geometry of the test sections, that does not allow to compensate boundary layer development simply. Anyway, the descending ramp is assimilable to a sudden expansion: an upstream, induced pressure gradient may also be considered as one of the salient characteristics of the flow. For this reason, we take into account the effects of pressure gradient on the incoming boundary layer as a feature of the flow in its own right. Unless otherwise specified, the discussion of this chapter is based on hot-wire measurements taken at several sections along the experimental models.

7.2 Development of the incoming boundary layer

The turbulent properties of the incoming boundary layer can be influenced by the pressure gradients along the experimental models, that are discussed in details at § 6.2. Although quite weak on large regions upstream of separation, local pressure gradients can become intense, both in a favourable and adverse way, depending on the ramp and the considered position. In principle, this can have at least two opposite, macroscopic consequences on the boundary layer. Firstly, a favourable pressure gradient can reduce turbulent fluctuations, eventually leading to flow relaminarisation. On the contrary, an adverse pressure gradient can produce a localised separation, in particular at the leading edge of the GDR ramp (figure 3.7) or at the junction of the convergent to the flat plat on the R2 ramp (figure 3.1), that can leave persisting signatures in the turbulence of the boundary layer. These phenomena can add uncertainty to the behavior of the massive separation, so that it is important to identify and possibly neutralise them. Following Kourta *et al.* (2015), one simple approach to detect such behaviors is to study the development of the boundary layer at many downstream sections and check how it compares to models of turbulent growth under zero pressure gradient (ZPG) conditions. While small deviations are expected, larger ones are considered markers of undesireable behaviors.

7.2.1 Displacement and momentum thickness

Displacement thickness δ_1 and momentum thickness θ are integral parameters that can effectively relate the local state of a boundary layer. The former is a measure of the shift of the external streamlines caused by the development of the boundary layer (Schlichting *et al.* (1968)). δ_1 is defined as:

$$\delta_1(x) = \int_0^{y_{max}} \left(1 - \frac{U(x,y)}{U_{max}(x)}\right) \mathrm{d}y, \tag{7.1a}$$

where y_{max} is the distance from the wall where U_{max} is attained. As for θ, it expresses the loss of momentum due to friction (Schlichting *et al.* (1968)). In a pipe, θ can be interpreted as the reduction of radius that is necessary to transport the same amount of momentum with a frictionless flow. It is defined as:

$$\theta(x) = \int_0^{y_{max}} \frac{U(x,y)}{U_{max}(x)} \left(1 - \frac{U(x,y)}{U_{max}(x)}\right) \mathrm{d}y, \tag{7.1b}$$

The shape factor $H_{12}(x) = \delta_1(x)/\theta(x)$ is also of interest, because it is usually a synthetic index of the turbulent state of the flow.

7.2.2 Models of boundary layer development

Schlichting *et al.* (1968) (among others) provides models for the downstream growth of both $\delta_1(x)$ and $\theta(x)$ in a turbulent, Zero-Pressure Gradient (ZPG) boundary layer. In particular:

$$\delta_1(x) = x \frac{0.0477}{Re_x^{1/5}} \tag{7.2a}$$

$$\theta\left(x\right) = x\frac{0.0371}{Re_x^{1/5}} \tag{7.2b}$$

where $Re_x = U_\infty x/\nu$. Under ZPG conditions, H_{12} ranges within 1.3 and 1.4 for a fully turbulent boundary layer, while values of the order of 2.6 are typical of a laminar one.

7.2.3 B.L. development on the R2 ramp

The development of the boundary layer on the R2 ramp was investigated with a hot-wire probe, at 4 different streamwise sections spanning from $x/h = -33$ to $x/h = -9$. For each section, velocity was measured at approximatively 200 points, spaced by decreasing vertical steps ranging from $1\,\mathrm{mm}$ in the free stream to $5 \times 10^{-2}\,\mathrm{mm}$ near the wall. The lowest point was at about $0.15 \pm 0.05\ \mathrm{mm}$ from the wall: this is not sufficient to attain the viscous sublayer, but should be enough to faithfully reconstruct integral parameters as δ_1 and θ. Based on preliminary experiences, fully turbulent behaviour was expected for $Re_h = 4 \times 10^4$ ($U_\infty = 20\,\mathrm{m\,s^{-1}}$) and higher: then, measurements were performed at this reference Re_h. Measurements were repeated twice, one week apart. Figure 7.1 compares the measured evolution of δ_1 and θ with eq. 7.2. The agreement with the models is very good, if the transition point is placed approximatively at the inlet of the test section. In addition, H_{12} is within the range typical of ZPG boundary layers. This being so, the effect of pressure gradients is not too strong on the R2 ramp, at least up to $x/h = -9$. The origin of the theoretical models suggests that the boundary layer is tripped by the joint between the convergent of the wind tunnel and the R2 ramp. This behaviour caused some concerns regarding repeatability of measurements. Indeed, the R2 ramp is mounted into the wind tunnel for the time of experiments only, with a rather laborious integration process. Moreover, the joint between the convergent of the wind tunnel is handcrafted each time with a soft modelling clay, which leaves little hope to replicate the exact tripping condition for each experimental campaign. For these reasons, it was decided to fix the turbulent properties of the boundary layer with a $0.5\,\mathrm{mm}$ high, zig-zag tripper placed 1 step height downstream of the inlet ($x/h \approx -49$). Since the boundary layer is thinner than $0.5\,\mathrm{mm}$ at this location, the tripper increases its thicknesses of about $0.2\,\mathrm{mm}$, as reported in figure 7.1. However, this does not seem to be too serious an inconvenient (at least if the natural, untriggered flow is already fully turbulent) in comparison with the advantage of replicability of measurements. In this respect, table 7.1 reports values of δ_1 and θ obtained at the section $x/h = -9$ (the reference section, see § 7.3) during two different campaigns, carried out one year apart. For $Re_h \geq 4 \times 10^4$, measurements nicely agree within $4\,\%$ of the first values. This is not the case at $Re_h = 3 \times 10^4$, but it was later found that, due to uncertainties on U_{ref}, the boundary layer of the second campaign does not seem to be fully turbulent. In the same occasion, the boundary layer was also characterised in proximity of the edge of the ramp ($x/h \approx -0.1$). As expected, new data showed that in this region of stronger, favourable pressure gradients the boundary layer deviates from its predicted ZPG behaviour sizeably. Values of δ_1 and θ are also reported in figure 7.1 among *tripped* datapoints. A different symbol is used to mark later acquisition.

		3×10^4	4×10^4	5×10^4	6×10^4	7×10^4
δ_1	Campaign 2015	2.71	3.49	3.56	3.41	3.36
	Campaign 2016	3.64	3.53	3.52	3.28	3.42
θ	Campaign 2015	1.96	2.51	2.61	2.5	2.53
	Campaign 2016	2.66	2.59	2.62	2.44	2.61

Table 7.1: Comparison of boundary layer measurements at $x/h = -9$, taken during two different experimental campaigns.

7.2.4 B.L. development on the GDR ramp

Prior and independently from this research, the GDR ramp was equipped with a zig-zag tripper placed at $x/h \approx -15.7$. Size and position of the tripper were chosen following the prescriptions of Kourta *et al.* (2015), which characterised a preliminary mock-up ramp (indicated with MP ramp) that led to the production of the GDR ramp. According to these authors, the incoming boundary layer of the MP ramp was fully

turbulent starting from $x/h \approx -13$. A tripper was placed at $x/h \approx -15.7$ to fix transition, without changing the natural development of the turbulent boundary layer too much. The MP ramp and the GDR have substantially identical shapes, the main difference being the presence in the GDR ramp of the narrow slot for synthetic jets control, so that the same settings were adopted. This being so, our investigation of GDR boundary layer development was limited to verification of this description. Three sections were probed, placed at $x/h \approx -9$, $x/h \approx -2.7$ (i.e. the same linear distance from the edge of the ramp as the reference section of the R2 ramp) and $x/h \approx 0$. Similar measurement settings and limitations apply as in the case of the R2 ramp (also see table 4.2). However, measurements on the GDR ramp were taken for each target Re_h. Figure 7.2 shows that growths of δ_1 and θ agree fairly well with the semi-empirical models and with the origin observed by Kourta *et al.* (2015), in particular at higher Re_h. This seems consistent with a state of the boundary layer not being fully turbulent yet for $Re_h \leq 13.3 \times 10^4$ (see § 7.3.1).

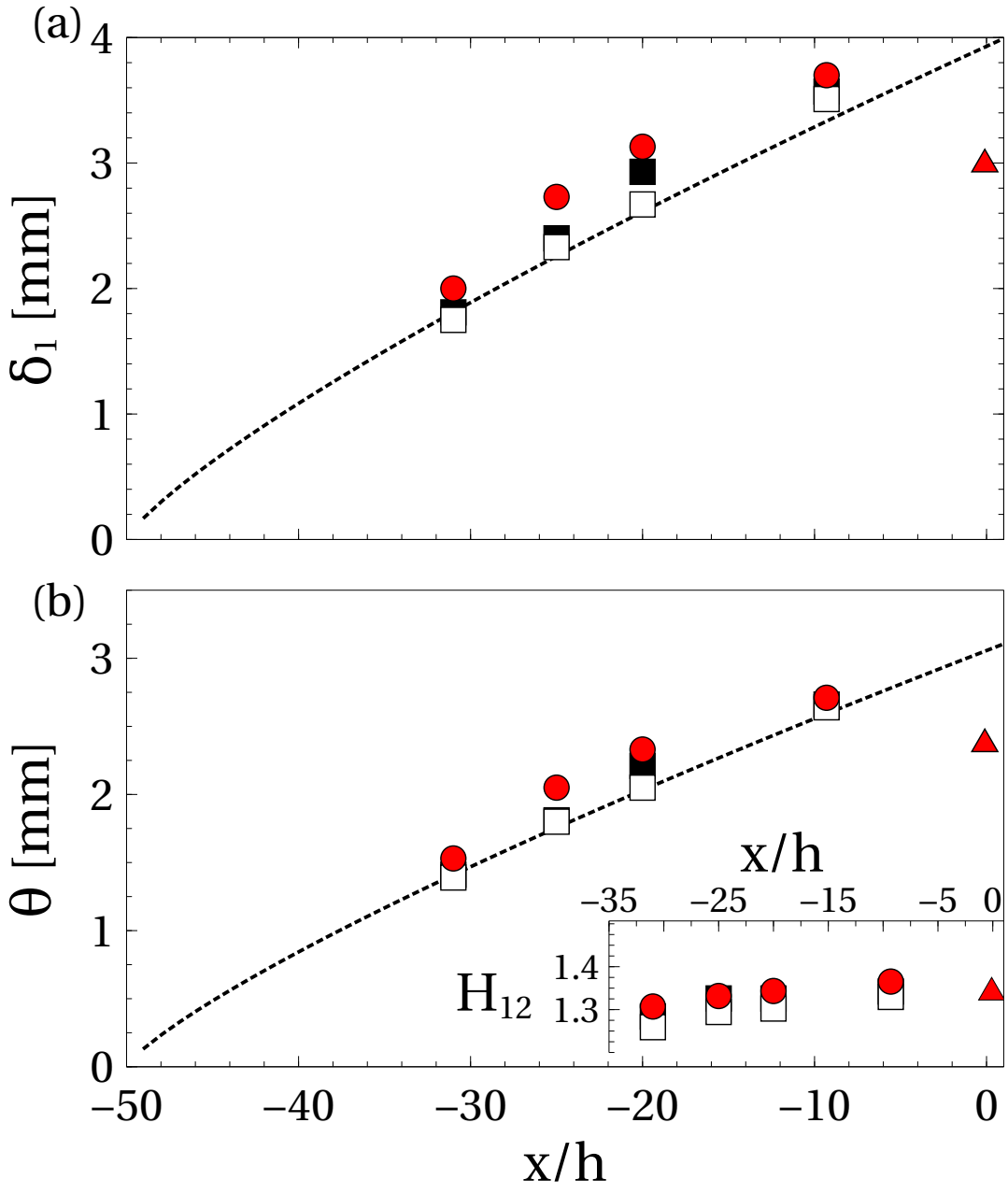

Figure 7.1: Boundary layer development over the R2 ramp. (a) Displacement thickness δ_1; (b) Momentum thickness θ. The insert reports the evolution of the shape factor H_{12}. Symbols: □ natural boundary layer, different colors indicating different sets of independent measurements; ● tripped boundary layer; ▲ tripped boundary layer at the edge of the ramp (additional measureament); – – – semi-empirical models of ZPG turbulent boundary layer growth, with origin at $x/h \approx -50$.

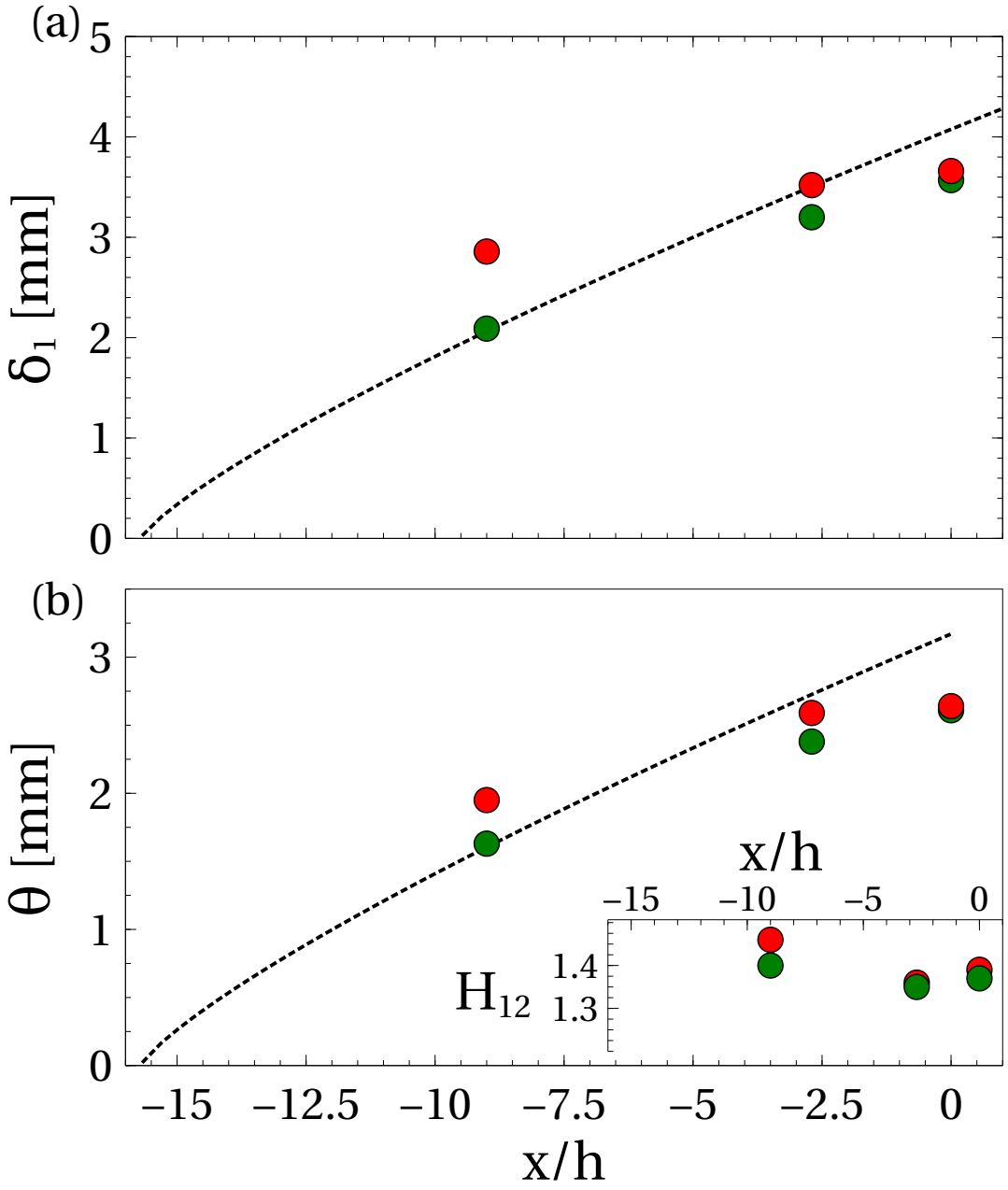

Figure 7.2: Boundary layer development over the GDR ramp. (a) Displacement thickness δ_1; (b) Momentum thickness θ. The insert reports the evolution of the shape factor H_{12}. Symbols: ● tripped boundary layer at $Re_h = 13.3 \times 10^4$; ● tripped boundary layer at $Re_h = 26.7 \times 10^4$; – – – semi-empirical models of ZPG turbulent boundary layer growth, with origin at $x/h \approx -15.7$.

7.3 A reference boundary layer

In the perspective of comparing the two ramps with each other and with other flows, one important concern is the choice of one suitable streamwise reference position where boundary layer properties are assessed. One straightforward option is a close neighbourhood of $x/h = 0$. This position has often been considered in the past (see Adams & Johnston (1988*a*) and references therein) and it will be shown in section 8.4 that boundary layer thickness at separation (reported in table 7.2) appears to have a fundamental role in determining scalings of the separated shear layer. However, in the flows under study this region has the drawback of being affected by the pressure gradient induced by separation and hence by geometry. This increases the probability of having boundary layer velocity profiles that diverge from the canonical forms and are hence difficult to compare from flow to flow. The obvious alternative is to place the reference section upstream, where the pressure gradient is weaker or, ideally, zero. This choice might be promising, because there is evidence that some degree of correlation exists between the properties of a separating/reattaching flow and those of the boundary layer much upstream of the separation point. For example, Neumann & Wengle (2003) reported that a passive actuator is most effective at reducing the recirculation region of a BFS flow when it is placed at least at $x/h = -4$. It is clear that this point is of extreme interest for separation control, because it might provide premise for synthesis of feed-forward control systems based on upstream boundary layer measurements. As so, the reference section was placed at $x/h \approx -9$. At this position the sizing criterion of Neumann & Wengle (2003) is satisfied and the wall pressure gradient approaches zero (see § 6.2). At the same time, the scaling laws of pressure distribution (see figure 6.4) seem to still hold, which is no longer true for more upstream positions. The boundary layers at the reference section were investigated in greater detail, in particular to retrieve information on important parameters as boundary layer thickness δ, friction velocity u_τ, and the smallest turbulent scales that exist in the incoming flow. These topics are treated in the following subsections. Based on δ and u_τ, examples of boundary layer profiles at the reference section, normalised both in external and internal units, are given in figures 7.3 and 7.5 for the R2 ramp, figure 7.4 and 7.6 for the GDR ramp. For comparison purposes, velocity profiles extracted from the DNS of a ZPG boundary layer (Schlatter & Örlü (2010)) are also reported, as well as those retrieved from the auxiliary PIV fields. On both ramps, one can notice a fairly good agreement for U profiles in the external regions of the boundary layer. The deviation observed at $y^+ < 50$ on the mean profile of the GDR ramp (figure 7.6) is ascribed to a blockage generated by the probe in proximity of the wall. As for $\sqrt{\langle (u')^2 \rangle}$, it generally collapses well on the DNS for $y^+ > 100$ ($y/\delta \approx 0.1$). The strong attenuation of the inner peak of $\sqrt{\langle (u')^2 \rangle}^+$ visible in figure 7.5 may be mainly attributed to spatial integration over the sensing length of the hotwire probe (see § 4.2.4)), but also to various effects such as pressure gradient and wall interferences. Among other uses, in section 9.2.1 boundary layer data is utilised to compute intermittency profiles of the TNTI. Since the TNTI is rather located in the outer region of the boundary layer, probe resolution is good enough for this purpose. It appears that PIV data are of lesser quality than hot-wire ones, in particular in the case of the R2 ramp. For instance, PIV noise in the external, irrotational flow is higher, as commented at § 4.3.4.4. In addition, due to wall reflections data are exploitable only down to a certain height above the wall, which is $y^+ > 500$ ($y/\delta > 0.38$) for the R2 ramp. The lowest reliable height might be slightly closer to the wall in the case of the GDR ramp. According to Chauhan *et al.* (2014*c*) and to the hot-wire based TNTI distributions observed at the reference section (§ 9.2.2.4), this extent is sufficient to cover almost the entire distribution of the TNTI.

The main reference boundary layer properties are summarised in table 7.2. These quantities will be used throughout this work to represent the characteristics of the incoming flow (e.g. its turbulent state) and try and identify connections with properties of the separated flow (e.g. figure 8.14). However, boundary layer thickness *at the edge of the ramp* will be utilised in further sections to study scaling within the separated shear layer (see for example § 8.4).

$Re_h/10^4$	3	4	5	6	7	10	13.3	20	26.7
δ/h	0.99†	0.96	0.98	0.97	0.97	0.18†	0.19†	0.20	0.18
δ_e/h†	0.92	0.86	0.82	0.82	0.91	0.34	0.28	0.33	0.29
$u_\tau/[ms^{-1}]$	0.68†	0.78	0.93	1.10	1.25	0.7†	0.86†	1.12	1.57
Re_{δ_1}	2878	4671	5787	6656	7555	3000	3994	5144	5573
Re_θ	2006	3262	4122	4738	5512	1788	2547	3617	4340
Re_τ	1270	1310	1750	2130	2646	840	1090	1456	1622
H_{12}	1.43	1.43	1.40	1.40	1.37	1.57	1.57	1.42	1.40
$\eta/h/10^{-4}$	50.0	48.7	44.3	43.3	41.3	12	10	8.5	9

Table 7.2: Boundary layer properties, measured at the reference section x/h = -9 using hot-wire data. The full boundary layer thickness δ and the friction velocity u_τ are obtained with the composite profile of Chauhan *et al.* (2009), with the exception of those marked with the symbol †, that were computed with the $\delta_{99.8}$ approximation and with the Clauser chart, respectively. It is $Re_h = U_\infty h/\nu$, $Re_{\delta_1} = U_\infty \delta_1/\nu$, $Re_\theta = U_\infty \theta/\nu$ and $Re_\tau = \delta u_\tau/\nu$. H_{12} is the shape factor ($\equiv \delta_1/\theta$). The Kolmogorov length scale, η is estimated at the height from the wall where the mean TNTI is located. All information for the R2 ramp was retrieved from data collected during the experimental campaign of year 2015, with the exception of δ_e (i.e. at the edge of the ramp) which was added during the experimental campaign of year 2016.

7.3.1 An assessment of the turbulent state at the reference section

Let us begin the investigation of the reference boundary layer by giving an immediate assessment of its turbulent state. Based on θ, the momentum thickness Reynolds number, indicated with Re_θ, is defined as:

$$Re_\theta = \frac{\theta U_\infty}{\nu}. \tag{7.3}$$

Values of Re_θ for the two ramps are listed in table 7.2. Re_θ is often considered a good macroscopic indicator of the turbulent state of the flow. In this respect, Song & Eaton (2004) suggests that the incoming boundary layer can be considered fully turbulent only if $Re_\theta > 3000$. According to this criterion, most of our datasets should correspond to fully turbulent boundary layers, with the exception of those at $Re_h = 3 \times 10^4$ (R2 ramp), $Re_h = 10 \times 10^4$ and $Re_h = 13.3 \times 10^4$ (GDR ramp). Interestingly, some of the macroscopic properties of the separated shear layer, in particular L_R, show a dependency on Re_θ, but the threshold $Re_\theta = 3000$ does not seem to be the most adequate to identify a fully turbulent state: a different criterion will be proposed in section 8.5. It is pointed out that Song & Eaton (2004) advice against the use of a turbulator to increase Re_θ, arguing that this does not make the behaviour of the tripped flow representative of a fully turbulent one. This should not be a problem on the GDR ramp, as the turbulator was placed in correspondence of the natural transition of the flow. As for the R2 ramp, it was shown that at the reference sections the variation of θ induced by tripping is of the order of $10\,\%$: for all the available R2 datasets, this does not seem sufficient to change the state of the flow with respect to the threshold $Re_\theta = 3000$.

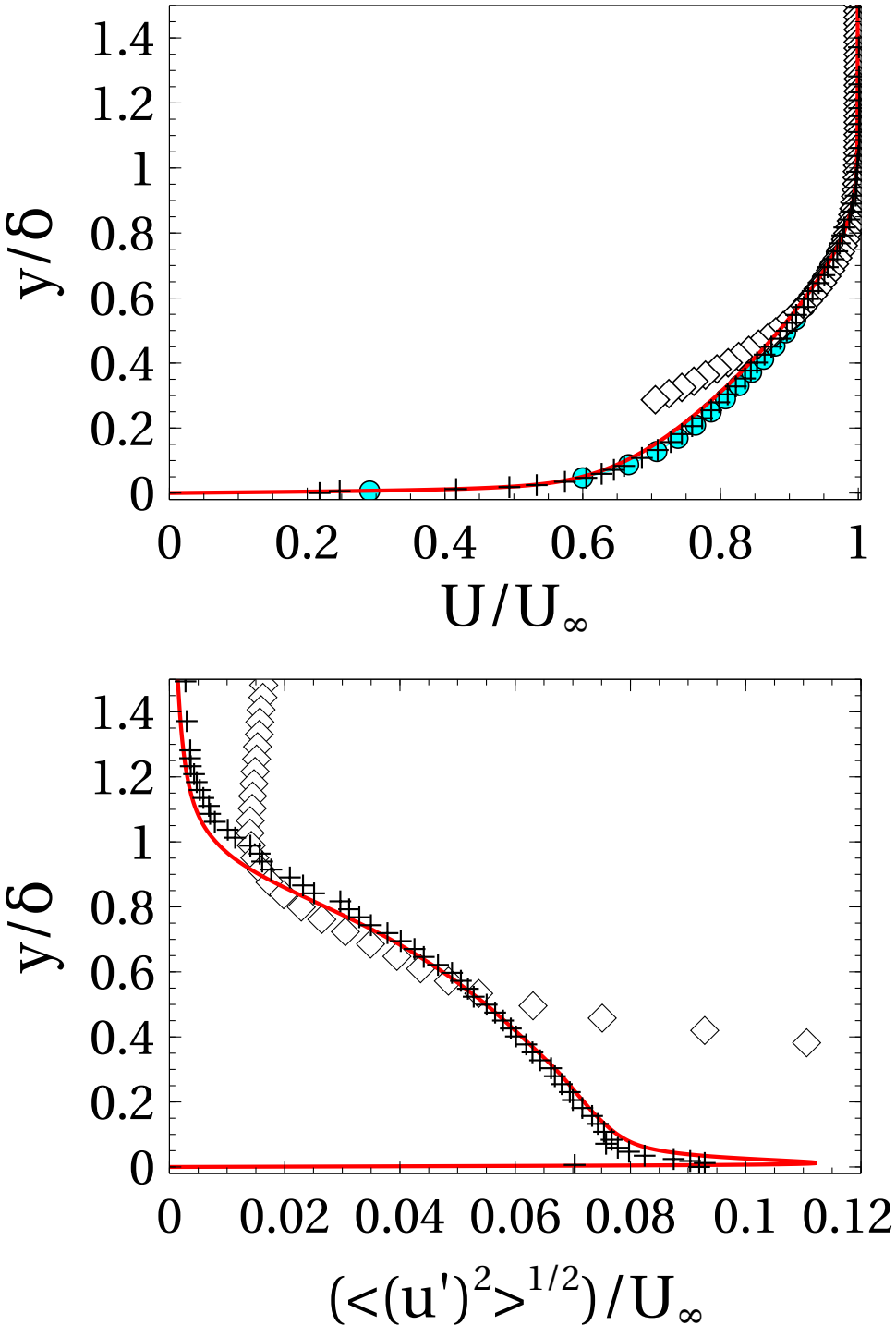

Figure 7.3: R2 reference boundary layer profile at $Re_\theta = 3262$ ($Re_\tau = 1310$), normalised in external units. (a) U/U_∞; (b) $\sqrt{\langle (u')^2 \rangle}/U_\infty$. + hotwire measurements at x/h = -9; ● composite boundary layer profile (Chauhan *et al.* (2009)); ◊ data from the PIV auxiliary field. —— DNS at $Re_\theta = 3270$ ($Re_\tau = 1043$) as given in Schlatter & Örlü (2010).

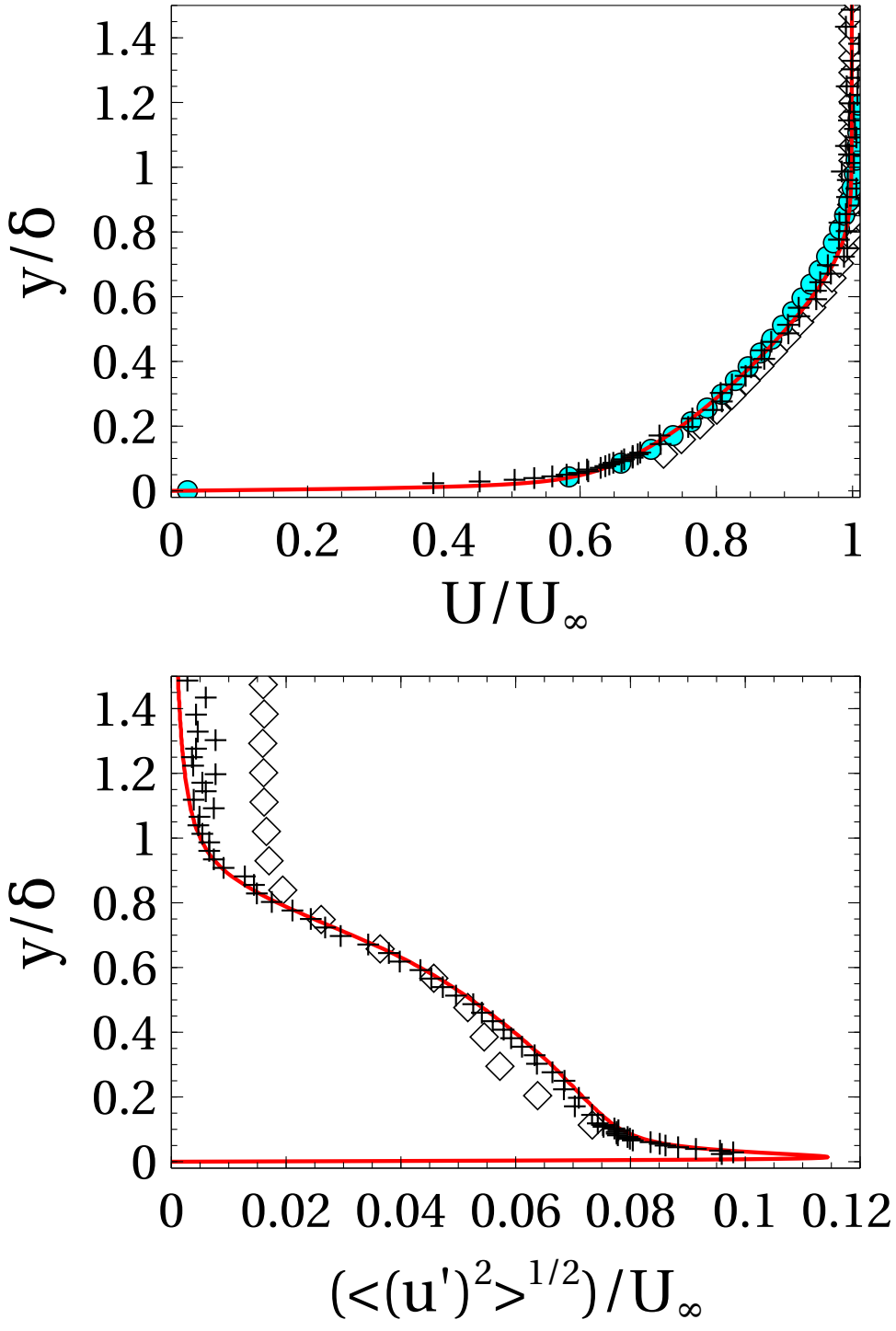

Figure 7.4: GDR reference boundary layer profile at $Re_\theta = 2547$ ($Re_\tau = 1090$), normalised in external units. (a) U/U_∞; (b) $\sqrt{\langle\langle u'\rangle^2\rangle}/U_\infty$. + hotwire measurements at x/h = -9; ● composite boundary layer profile (Chauhan *et al.* (2009)); ◊ data from the PIV auxiliary field. —— DNS at $Re_\theta = 2537$ ($Re_\tau = 830$) as given in Schlatter & Örlü (2010).

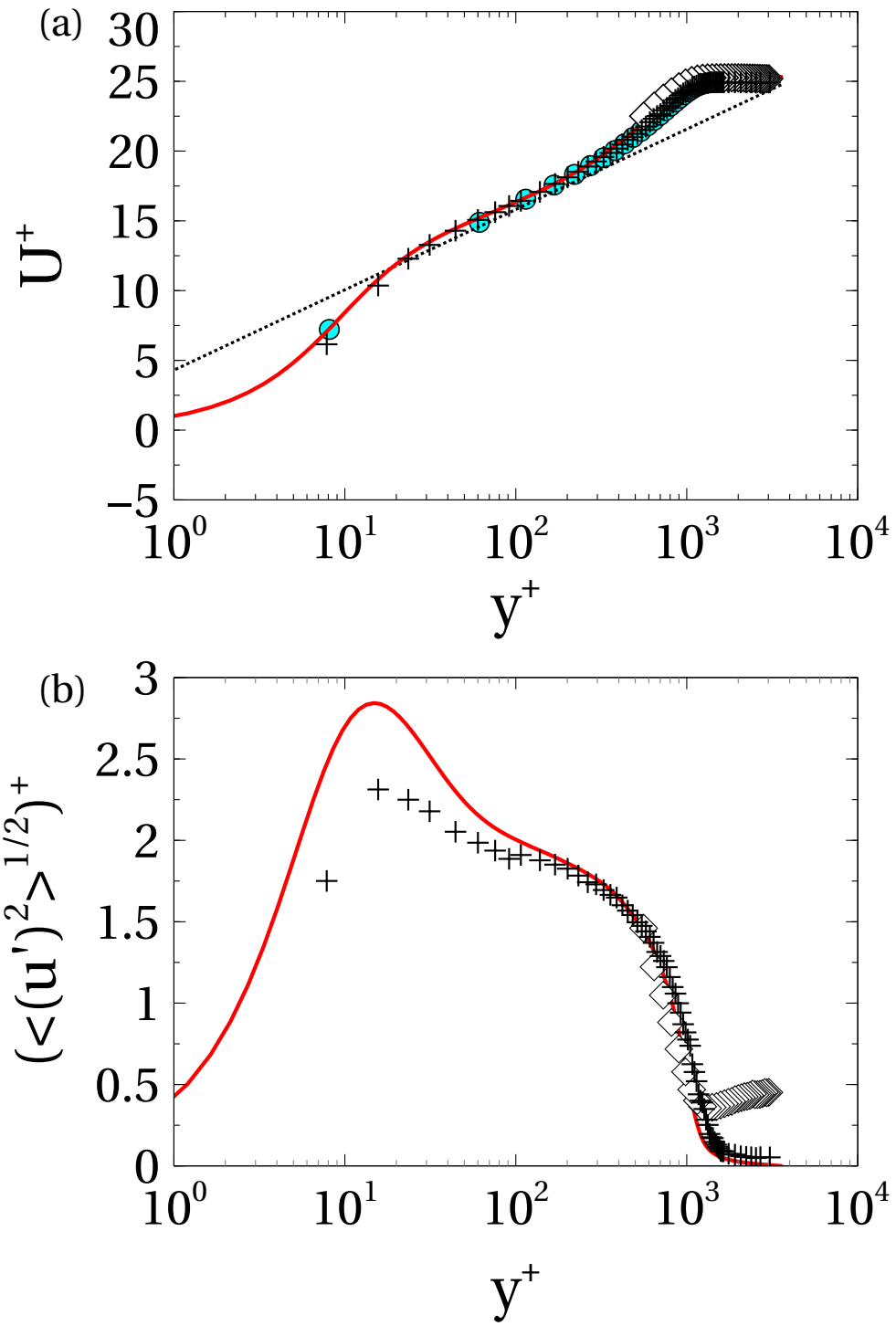

Figure 7.5: R2 reference boundary layer profile at $Re_\tau = 1310$ ($Re_\theta = 3262$), normalised in internal units. (a) U^+; (b) $\sqrt{\langle (u')^2 \rangle}^+$. Symbols as in figure 7.3.

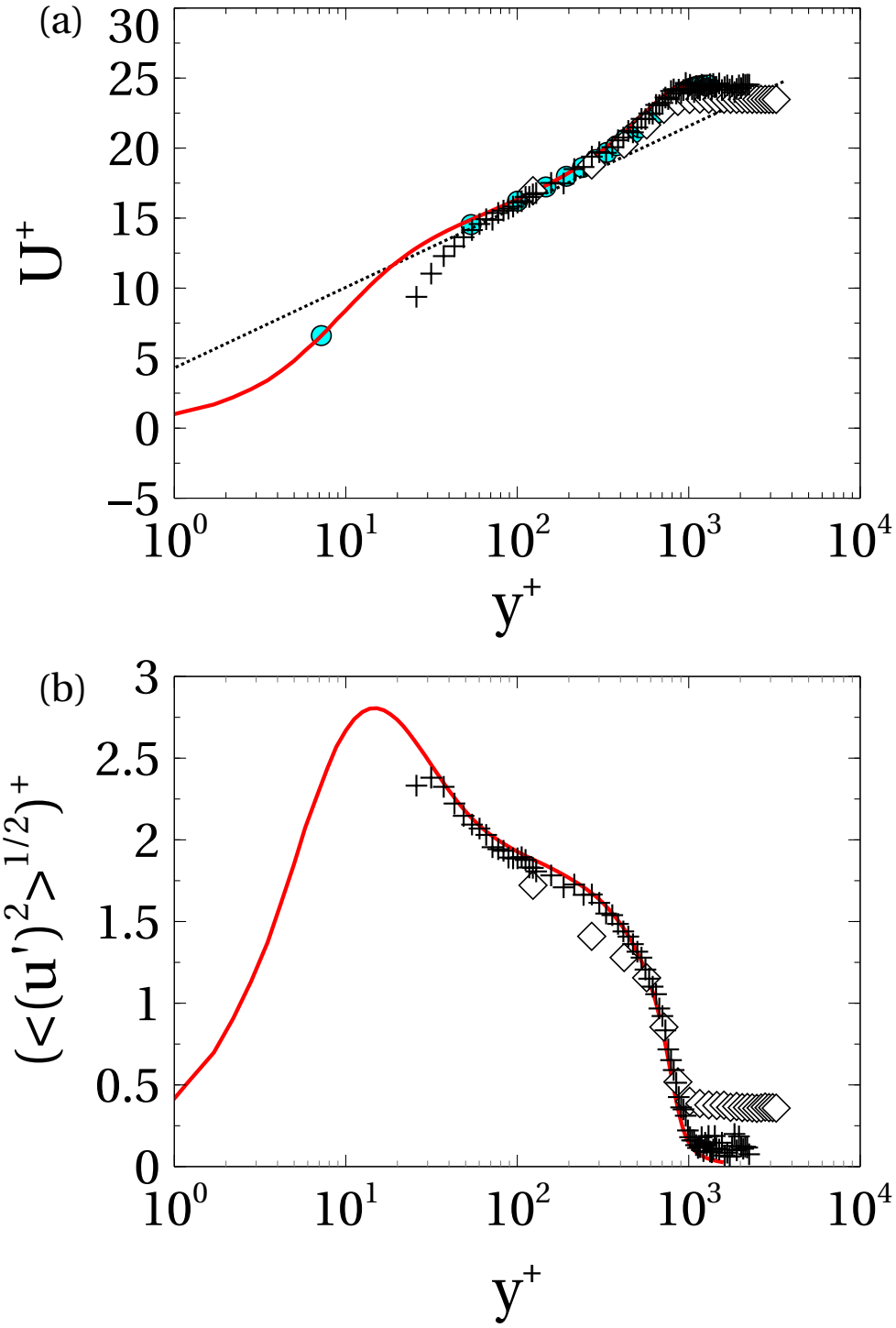

Figure 7.6: GDR reference boundary layer profile at $Re_\theta = 2547$ ($Re_\tau = 1090$), normalised in internal units. (a) U/U_∞; (b) $\sqrt{\langle (u')^2 \rangle}/U_\infty$. Symbols as in figure 7.4.

7.3.2 Full boundary layer thickness δ

The *full thickness* of the boundary layer, indicated with the symbol δ, is the asymptotic distance at which $U(x,y) = U_\infty(x)$ exactly, i.e. where the boundary layer blends into the external, irrotational flow (Chauhan *et al.* (2009)). In this work, δ is a parameter of great interest, at least for two reasons: firstly, the value of δ *at separation* (indicated with δ_e) greatly influences some of the properties of the separated flow (see § 8.4); secondly, in the boundary layer the spatial distribution of instantaneous TNTIs is contained, at least statistically, within δ (see § 9.2). Unfortunately, δ cannot be measured unambiguously (Fiedler & Head (1966)). It is then customary to approximate it with the conventional thickness δ_{99}, that is the distance from the wall at which $U(x,y) = 0.99U_\infty(x)$. However, the parameter δ_{99} is an approximation that is too crude when studying the TNTI, because it misses a sizeable fraction of the TNTI distribution in the boundary layer. For this reason, in this work δ_{99} is not used and δ is generally approximated with $\delta_{99.8}$, defined as the distance from the wall at which $U(x,y) = 0.998U_{max}(x)$. In the particular case of fully turbulent, ZPG boundary layers, the composite boundary layer profile developed by Chauhan *et al.* (2009) provides a more elegant and reliable method to estimate δ (see § 7.3.4). Then, at the reference section $x/h \approx -9$ this method was preferred to the $\delta_{99.8}$ approximation, at least for high enough values of Re_θ. Anyway, table 7.3 shows that, in most cases, $\delta_{99.8}$ at the reference section agrees sufficiently well with δ.

$Re_h/10^4$	3	4	5	6	7	10	13.3	20	26.7
$\delta_{99.8}/h$	0.99	0.83	0.94	0.97	1.00	0.18	0.19	0.19	0.18
δ/h	0.75	0.96	0.98	0.97	0.97	0.27	0.23	0.20	0.18

Table 7.3: Estimations of full boundary layer thicknesses at the reference section. $\delta_{99.8}$ is directly computed from hot-wire data, δ is found by fitting the composite profile of Chauhan *et al.* (2009) onto them.

7.3.3 Estimation of friction velocity u_τ: the Clauser chart method

One of the most common parameters used to describe wall friction is friction velocity u_τ, which is defined as:

$$u_\tau = \sqrt{\frac{\tau_w}{\rho}} = \sqrt{\nu \left.\frac{\partial U}{\partial y}\right|_{y=0}}, \tag{7.4}$$

where τ_w is the viscous shearing stress at the wall. u_τ has a fundamental role in scaling boundary layer properties, the most important example being the logarithmic velocity profile in the overlap region, the well known *log law*:

$$\frac{U(y)}{u_\tau} = \frac{1}{\kappa} ln\left(\frac{y u_\tau}{\nu}\right) + B, \tag{7.5}$$

in which κ and B are (supposed to be) universal constants. u_τ and ν/u_τ are often called the *inner scales* of the boundary layer. Normalisation on inner scales is indicated with the superscript $^+$. Unfortunately, direct assessment of u_τ (for example, by measuring the velocity gradient at the wall) is complex and sometimes, as in the case of this research, technically unreachable. In such situations it is then crucial to have an indirect estimation of u_τ. One of the most used approaches to do so is the Clauser chart method (Wei *et al.* (2005) among many others). Clauser's main starting assumptions are ZPG conditions and the existence of the universal log-law (eq. 7.5). Multiplying eq. 7.5 by u_τ/U_∞, one obtains:

$$\frac{U(y)}{U_\infty} = \frac{u_\tau}{\kappa U_\infty} ln\left(\frac{y U_\infty}{\nu}\right) + \frac{u_\tau}{\kappa U_\infty} ln\left(\frac{u_\tau}{U_\infty}\right) + B\frac{u_\tau}{U_\infty}. \tag{7.6}$$

Now, since U_∞, $U(y)$ and y are directly accessible, for a given set of "universal" constant the only unknown of eq. 7.6 is u_τ, that can be found readily by fitting eq. 7.6 to data in the log region. Table 7.4 reports values of u_τ obtained with the Clauser chart method and $\kappa = 0.39$ and $B = 4.3$ (Marusic *et al.* (2013)). The approach just described is elegant and efficient, to the point that acceptable values of u_τ can even be found manually, by varying the value u_τ as to form a beam of parallel lines and then choosing the one that best overlaps to available data (Wei *et al.* (2005)). Anyway, it must be stressed that the Clauser chart method

is not universally accepted, in particular for its initial hypotheses. Indeed, assuming a log-law to compute u_τ induces an artificial collapse on the universal, fully turbulent profiles of data normalised in inner units (George & Castillo (1997), Wei *et al.* (2005)), which can mask sizeable low Reynolds number effects. In principle, this problem might impact the estimations of u_τ provided in this research, because Reynolds number (in terms of Re_θ and Re_τ) are at most moderate. In particular, estimations at $Re_\theta < 3000$ should be considered with some care. This being said, it should not be forgotten that the main scope of the present work is the investigation of the separated shear layer, mostly on a large scale perspective. In this framework, these potential imperfections in scaling laws of the incoming boundary layer appear acceptable.

$Re_h/10^4$	3	4	5	6	7	10	13.3	20	26.7
Clauser chart	0.68	0.80	0.95	1.12	1.27	0.70	0.85	1.10	1.50
Composite fit	0.70	0.78	0.93	1.10	1.25	0.69	0.86	1.12	1.57

Table 7.4: Estimations of friction velocities u_τ at the reference section. All values are in $[\mathrm{m\,s^{-1}}]$.

7.3.4 Estimations of u_τ and δ with a composite boundary layer profile

The parameters δ and u_τ are, as a whole, relatively difficult to estimate, as already explained in previous subsections. Interestingly, Chauhan *et al.* (2009) proposed a parametric, composite boundary layer model that can be used to retrieve reliable and consistent estimations of both δ and u_τ. These authors match together an *inner* profile U^+_{inner}, modelling the flow from the wall to the log region, and a *wake* function $\mathcal{W}_{exp}$, describing the outer regions of the boundary layer. The outcome is an additive, composite mean velocity profile that is valid throughout the thickness of the boundary layer, formulated as follows:

$$U^+_{composite} = U^+_{inner} + \frac{2\Pi}{\kappa}\mathcal{W}_{exp}\left(\xi\right), \tag{7.7}$$

where $\xi = y^+/\delta^+$, Π is a wake parameter and κ is Von Karman's constant. The inner profile is given by:

$$\begin{aligned} U^+_{inner} = \frac{1}{\kappa} ln\left(\frac{y^+ - a}{-a}\right) + \frac{R^2}{a\left(4\alpha - a\right)}\Bigg[\left(4\alpha + a\right) ln\left(-\frac{a}{R}\frac{\sqrt{\left(y^+ - \alpha\right)^2 + \beta^2}}{y^+ - a}\right) \\ + \frac{\alpha}{\beta}\left(4\alpha + 5a\right)\left(atan\left(\frac{y^+ - \alpha}{\beta}\right) + atan\left(\frac{\alpha}{\beta}\right)\right)\Bigg] \end{aligned} \tag{7.8}$$

in which $\alpha = (-1/\kappa - a)/2)$, $\beta = \sqrt{-2a\alpha - \alpha^2}$ and $R = \sqrt{\alpha^2 + \beta^2}$. The constant a can be found by equating eq. 7.5 to eq. 7.8 at a value of y^+ within the log region. For κ =0.384 and $B = 4.17$, Chauhan *et al.* (2009) find $a = -10.3061$. With the values κ =0.39 and $B = 4.3$ used insofar in this research (see Marusic *et al.* (2013)), it is $a = -10.2900$. The difference between the two values of a appears to be negligible, in the framework of this study. As for the wake function, it is written as:

$$\begin{aligned} \mathcal{W}_{exp}(\xi) = \frac{1 - exp\left[-(1/4)\left(5a_2 + 6a_3 + 7a_4\right)\xi^4 + a_2\xi^5 + a_3\xi^6 + a_4\xi^7\right]}{1 - exp\left[-\left(a_2 + 2a_3 + 3a_4\right)/4\right]} \\ \times\left(1 - \frac{1}{2\Pi} ln\left(\xi\right)\right). \end{aligned} \tag{7.9}$$

$$a_2 = 132.8410, \quad a_3 = -166.2041, \quad a_4 = 71.9114$$

Once κ and B are chosen, eq. 7.7 is completely determined by u_τ, δ and Π. These parameters can be found simply, by fitting eq. 7.7 on available data, provided that ZPG conditions are met and Re_θ is high enough. Examples of fitted profiles are given in figures 7.3, 7.5, 7.4 and 7.6 . Values of δ and u_τ so retrieved are reported in table 7.3 and table 7.4, respectively. Comparison with estimations yielded by the Clauser chart method and by $\delta_{99.8}$, respectively, is generally quite good. As usual, the only exceptions are values of δ at $Re_\theta < 3000$, which is not surprising as the composite profile assumes a fully turbulent state. In these cases, $\delta_{99.8}$ was retained.

7.4 An assessment of the smallest scales of incoming turbulence

In anticipation of discussion of small-scale transfer through the TNTI (chapter 12), it is practical to have at least a qualitative assessment of the smallest spatial turbulent scales that exist in the incoming turbulent boundary layer. The Kolmogorov length η can be classically obtained as:

$$\eta = \left(\frac{\nu^3}{\epsilon} \right)^{1/4}, \tag{7.10}$$

where ϵ is the dissipation rate of turbulent kinetic energy. Under the hypothesis of local isotropy, a surrogate of ϵ can be estimated as:

$$\epsilon = 15\nu \left\langle \left(\frac{\partial u'}{\partial x} \right)^2 \right\rangle. \tag{7.11}$$

Taylor's hypothesis is invoked to reconstruct the space derivative of u' from its time derivative provided by hot-wire measurements. It must be stressed that the value of η so retrieved should be considered with some caution. On the one hand, the size of the hot-wire probe is probably too large to correctly resolve the smallest scales of the flow, so that attenuation due to spatial integration along the length of the wire should be expected (see § 4.2.4). On the other hand, the pertinence of local isotropy is questionable, either due to strong mean shear (as in proximity of the wall) or to intermittency of turbulence (e.g. in the wake region, see section § 9.2.2.4). For these reasons, values of η are provided in table 7.2 only at the location of the mean TNTI (where probe resolution should be sufficient) and as indicative order of magnitudes. Accordingly, in this work η estimations are only used to give broad comparisons with the smallest scales of the flow.

8

The separated shear layer

Caractérisation de la couche cisaillée décollée

Ce chapitre se concentre sur la couche cisaillée décollée, qui est l'un des éléments marquants d'un décollement massif. Son développement spatial dans le sens de l'écoulement est représenté par l'épaisseur de vorticité δ_ω (éq. 8.1a) ou par une épaisseur de quantité de mouvement généralisée θ_{SL} (éq. 8.1b). Les évolutions de ces deux paramètres sont présentées en figure 8.1 pour la rampe R2 et en figure 8.2 pour la rampe GDR. Dans les deux cas, on trouve que les courbes de chaque rampe sont mises en échelle par la hauteur de la marche h et la longueur de la bulle de recirculation L_R. Cette normalisation réduit les courbes des deux rampes à un seul faisceau, une fois qu'une valeur initiale dépendante de la couche limite à l'amont (et donc pas mise en échelle par h) est prise en compte (figure 8.3). Sur le domaine $x/L_R \in (0, 0.5)$, le taux d'épaississement de la couche cisaillée (alternativement $\mathrm{d}\delta_\omega/\mathrm{d}x$ ou $\mathrm{d}\theta_{SL}/\mathrm{d}x$) est constant et similaire à celui typique d'une couche cisaillée libre (éq. 8.3b et éq. 8.3a). Ces résultats sont en accord avec la littérature, par exemple Dandois *et al.* (2007). Avec de simples considérations géométriques (figure 8.5), on observe aussi que $\mathrm{d}\theta_{SL}/\mathrm{d}x \sim (L_R/h)^{-1}$ (et de même pour $\mathrm{d}\delta_\omega/\mathrm{d}x$).

L'évolution du gradient de pression moyen est étudiée en détail le long des interfaces de la couche cisaillée, en s'appuyant sur les équations RANS (éq. 8.5) et les jeux de données PIV. Le long de la RRI, le gradient longitudinal $\partial P/\partial x$ est déterminé principalement par les efforts de cisaillement (figure 8.6) : sur $x/L_R \in (0, 0.5)$, la composante moyenne $V\partial U/\partial y$ domine, mais la composante turbulente $\partial\langle u'v'\rangle/\partial y$ devient prépondérante sur $x/L_R \in (0.7, 1)$. Le long de la TNTI, $\partial P/\partial x$ est fortement influencé par la composante convective $U\partial U/\partial x$, parce que les composantes moyenne et turbulente du cisaillement tendent à se compenser (figure 8.7). En ce qui concerne le gradient vertical $\partial P/\partial y$ à la RRI, il est fondamentalement déterminé par les efforts turbulents normaux, en particulier $\partial\langle v'^2\rangle/\partial y$ (figure 8.8). Dans ces conditions, l'éq. 8.11 (Pope (2000)) prédit que $\partial P/\partial x$ à la TNTI est relié à $\partial P/\partial y$ à la RRI, ce qui est plutôt bien vérifié par les données au moins sur $x/L_R \in (0, 0.6)$.

La comparaison des gradients de pression sur les deux rampes suggère l'existence de lois d'échelle complexes, dépendantes à la fois de paramètres géométriques (notamment h et ER) et des caractéristiques de l'écoulement à l'amont (en particulier δ_e, l'épaisseur de la couche limite à l'arête de la rampe). Le long de la TNTI, on trouve empiriquement que les paramètres de similitude de plusieurs composantes de $\partial P/\partial x$ et $\partial P/\partial y$ dépendent de h et de δ_e à la fois (tableau 8.2 et figures 8.10 à 8.11). Le poids relatif de ces deux échelles semble être déterminé par la valeur du ratio δ_e/h : h prédomine si $\delta_e/h \ll 1$, mais l'influence de δ_e est la plus forte si $\delta_e/h \gg 1$. Nous avons modélisé ce comportement avec le coefficient $C_{h,\delta} = (1 + \delta_e/h)$. Même si l'origine de ce coefficient est liée à la TNTI, son usage semble aussi bien représenter l'influence que la couche limite à l'amont a sur la RRI (Adams & Johnston (1988*a*)), en particulier au recollement (tableau 8.3 et figure 8.12). De plus, les normalisations basées sur $C_{h,\delta}$ (tableaux 8.2 et 8.3) permettent d'extrapoler l'équation RANS longitudinale vers des valeurs asymptotiques de δ_e/h. On découvre que la rampe GDR ($\delta_e/h \approx 0.3$) est déjà représentative de la condition $\delta_e/h \ll 1$: dans ce cas, $\partial P/\partial x$ est déterminé par h uniquement (au moins pour une valeur de ER figée) dans tout l'écoulement. Pour $\delta_e/h \gg 1$, on prédit que les effets géométriques vont à nouveau dominer l'écoulement, mais cette fois sous l'influence de ER plutôt

que de h. La rampe R2 n'est pas représentative de cette condition ($\delta_e/h \approx 0.8$ to 1), mais montre un état intermédiaire où δ_e, h et ER ont tous un effet sur l'écoulement décollé.

L'évolution du ratio L_R/h observée au chapitre 5 n'est pas expliquée par l'influence de la géométrie : le paramètre de similitude Re_h ne met pas en échelle les valeurs de L_R/h des deux rampes. Nous analysons alors l'influence que la couche limite amont a sur la couche cisaillée décollée. Le paramètre Re_θ est choisi pour représenter l'état turbulent de la couche limite, tandis que L_R/h est utilisé comme mesure du développement de la couche cisaillée. On trouve que les données des deux rampes suivent une loi $L_R/h \sim Re_\theta^m$, où m est un exposant négatif (figure 8.14). De façon inattendue, m passe de -0.10 à -0.5 si Re_θ excède une valeur critique $Re_{\theta,c} \approx 4100$. L'évolution de L_R/h est très bien corrélée à l'évolution des efforts de cisaillement turbulents dans la couche cisaillée (figure 8.15 et figure 8.16). En particulier, en se basant sur les travaux de Chapman *et al.* (1958), on trouve que $L_R/h \sim \left(\overline{R^*_{uv}}\right)^{-1}$ (éq. 8.22), où $R^*_{uv,r} = -\langle u'v'\rangle|_{min}/U^2_\infty$ et la barre indique la moyenne sur une région proche du recollement (par exemple $x/L_R \in (0.7, 1)$).

La proportionnalité inverse entre $\mathrm{d}\theta_{SL}/\mathrm{d}x$ et L_R/h suggère que le taux d'épaississement de la couche cisaillée est un bon indicateur de la taille du décollement. Dans la mesure où $\mathrm{d}\theta_{SL}/\mathrm{d}x$ est déterminé par l'entraînement de fluide extérieur (Pope (2000) et § 11.5.2), ce dernier apparaît comme une variable importante pour la compréhension des écoulements décollés. Nos résultats indiquent que la quantité de fluide entraînée pourrait être reconstruite et modifiée soit à partir de la valeur de Re_θ dans la couche limite à l'amont, soit de celle de $\langle u'v'\rangle$ au recollement. Dans le premier cas, il faudrait viser des systèmes de *feed-forward*, dans le deuxième des systèmes de *feed-back*.

8.1 Introduction

The separated shear layer is probably one of the dominant feature of the massively separated turbulent flows under study. This chapter presents a data-driven characterisation of the shear layer, including a study of growth rates and of induced pressure gradients, showing that faster shear layer growth corresponds to shorter L_R. An asymptotic analysis of scaling parameters is then proposed, that suggests that the characteristics of the shear layer strongly depend on a complex, multi-scale mutual interaction between geometry and properties of the incoming boundary layer. For the particular set of experiments available for this research, it is shown that the influence of geometry on the overall topology of the flow is often predominant, but that the effect of incoming turbulence is sizeable, in particular in determining the rate of growth of the shear layer.

8.2 Shear layer development

The recirculation length L_R can be interpreted as the streamwise scale of shear layer development. The latter is often characterised with the streamwise evolution of either the vorticity thickness δ_ω or of a generalised momentum thickness θ_{SL}. According to Dandois *et al.* (2007), δ_ω and θ_{SL} are defined as follows:

$$\delta_\omega(x) = \frac{U_{max}(x) - U_{min}(x)}{(\partial U(x,y)/\partial y)_{max}}, \tag{8.1a}$$

$$\theta_{SL}(x) = \int_{y_{min}}^{y_{max}} \frac{U(x,y) - U_{min}(x)}{U_{max}(x) - U_{min}(x)} \left(1 - \frac{U(x,y) - U_{min}(x)}{U_{max}(x) - U_{min}(x)}\right) \mathrm{d}y, \tag{8.1b}$$

where $U_{min}(x)$ is a local minimum streamwise velocity and y_{min} is the vertical position at which it is attained. Figure 8.1 and figure 8.2 show clearly that L_R and h are appropriate scaling parameters for both δ_ω and θ_{SL}. On both ramps, normalised shear layer thicknesses collapse on a single curve, showing a characteristic slope change at $x/L_R \approx 0.5$. A similar slope change at a similar relative position was also observed by Dandois *et al.* (2007) on a round descending ramp. Apparently, the turbulent state of the incoming boundary layer does not impact shear layer growth greatly.

Table 8.1 lists estimations of $\delta_\omega(0)$ and $\theta_{SL}(0)$ obtained by interpolating the evolutions of δ_ω and θ_{SL} at $x/h = 0$. Values of $\delta_\omega(0)$ suggest that figure 8.1(a) and figure 8.2(a) might differ mainly for their intercept, that does not scale on h. Indeed, figure 8.3(a) proves that the evolutions of $\delta_{\omega,0} = \delta_\omega(x) - \delta_\omega(0)$, normalised on h, collapse very nicely onto each other. At least on $x/L_R \in (0, 0.5)$, this is also the case for $\theta_{SL,0} = \theta_{SL} - \theta_{SL}(0)$ (figure 8.3(b)) although values of $\theta_{SL}(0)$ change from one ramp to the other (see table 8.1). Interestingly, the two sets of $\theta_{SL,0}$ curves do not collapse any longer for $x/L_R \in (0.5, 1)$. This seems to be due to the quantity $U_{min}(x)$ appearing in eq. 8.1b: although it is generally verified that $U_{min}(x) \sim U_\infty$, lower $U_{min}(x)$ are attained on the GDR ramp for $x/L_R \in (0.5, 1)$ (figure 8.4). It is pointed out that if it is assumed (reasonably) that $\partial U(x)/\partial y \sim (U_\infty(x) - U_{min}(x))/h$, it follows immediately that the definition of δ_ω compensates for the difference in $U_{min}(x)$.

	$\delta_\omega(0)$	$\theta_{SL}(0)$	θ edge (H.W.)
R2	6	2.1 to 2.4	2.4 to 2.7
GDR	6	2 to 3	2.7 to 3

Table 8.1: Representative values of shear layer thicknesses at separation, $\theta_{SL}(0)$ and $\delta_\omega(0)$. Momentum thicknesses θ in proximity of the edge of the ramp, computed from hot-wire measurements, are also reported for reference. All quantities are expressed in $[\mathrm{mm}]$.

All in all, these observations confirm that L_R is the streamwise scale of the separated shear layer. As for the vertical scale, δ_ω and θ_{SL} are correctly normalised by ramp height h, at least in a large neighbourhood of the mean separation point, but only once the effect of the h-independent boundary layer thickness at separation is compensated for. This suggest that more than one vertical scale might govern the flow. This subject will be treated in some details at § 8.4.

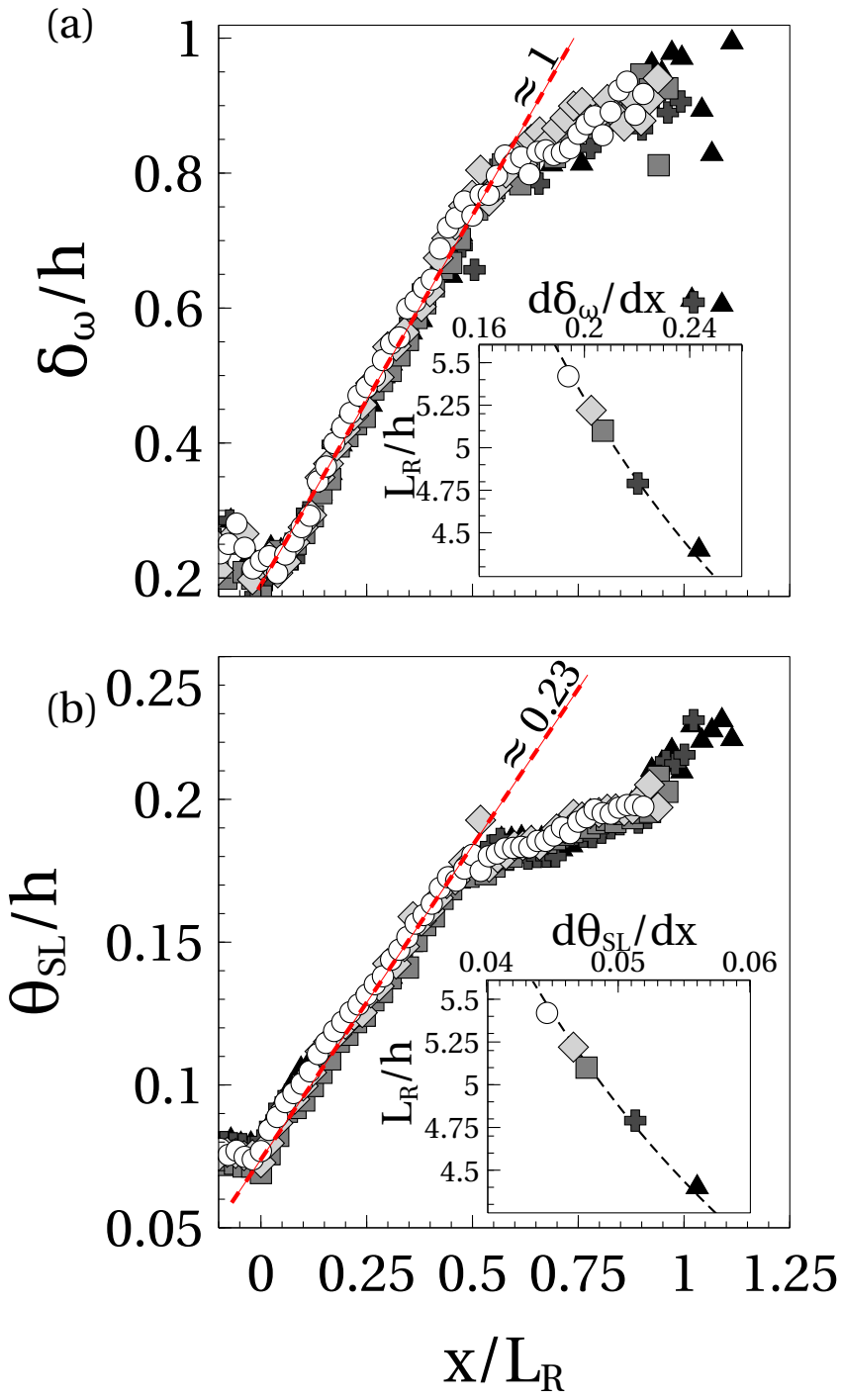

Figure 8.1: Shear layer growth on the R2 ramp. (a) Vorticity thickness δ_ω; (b) Generalised momentum thickness θ_{SL}. Symbols: ◯ $Re_h = 3 \times 10^4$; ◇ $Re_h = 4 \times 10^4$; ■ $Re_h = 5 \times 10^4$; ✚ $Re_h = 6 \times 10^4$; ▲ $Re_h = 7 \times 10^4$. The inserts show the L_R dependency on shear layer growth rate. – – – -1 power law.

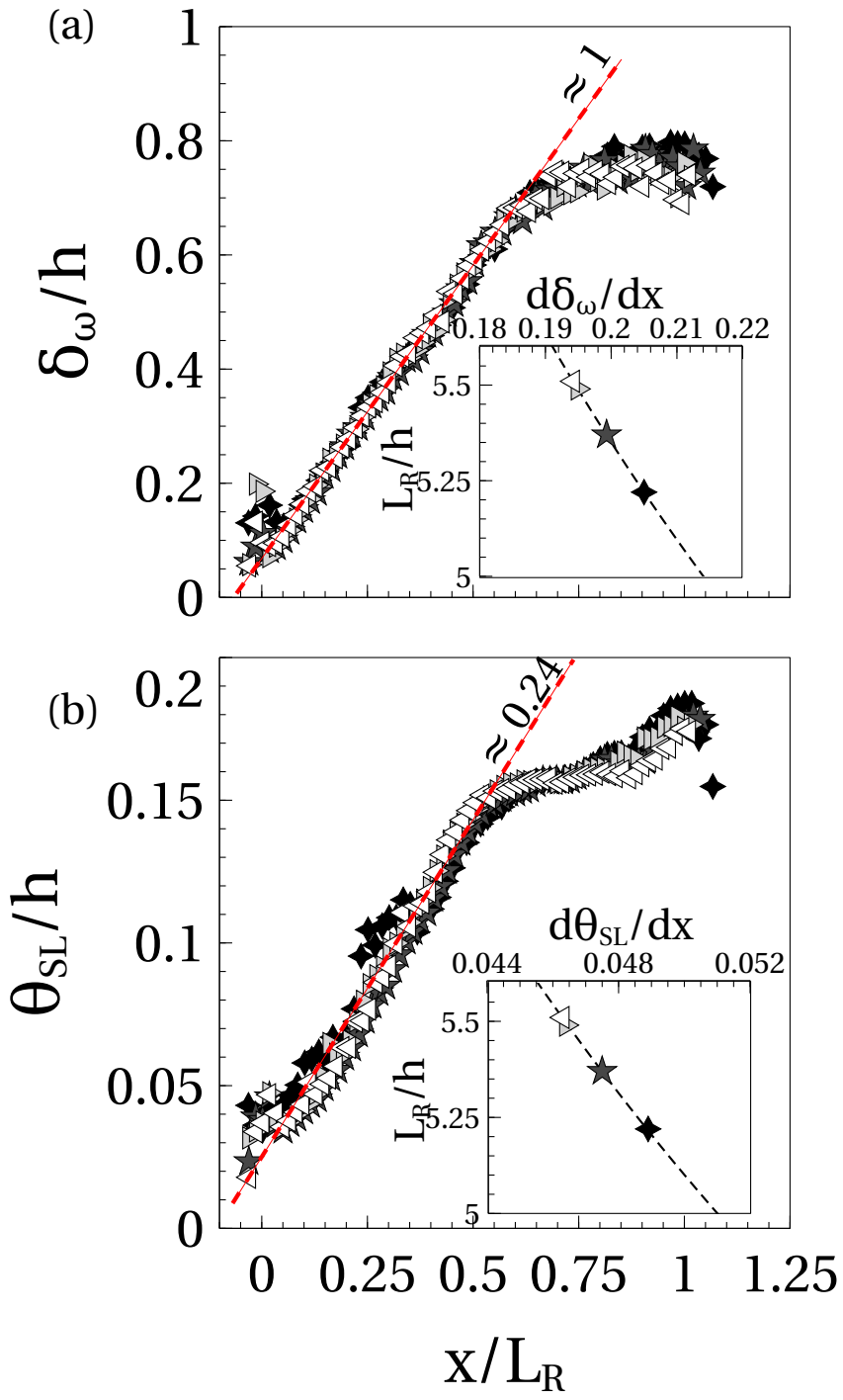

Figure 8.2: Shear layer growth on the GDR ramp. (a) Vorticity thickness δ_ω; (b) Generalised momentum thickness θ_{SL}. Symbols: $\triangleleft$ $Re_h = 10 \times 10^4$; $\triangleright$ $Re_h = 13.3 \times 10^4$; $\bigstar$ Re_h =20×10^4; $\bigstar$ $Re_h = 26.7 \times 10^4$. The inserts show the L_R dependency on shear layer growth rate. – – – -1 power law.

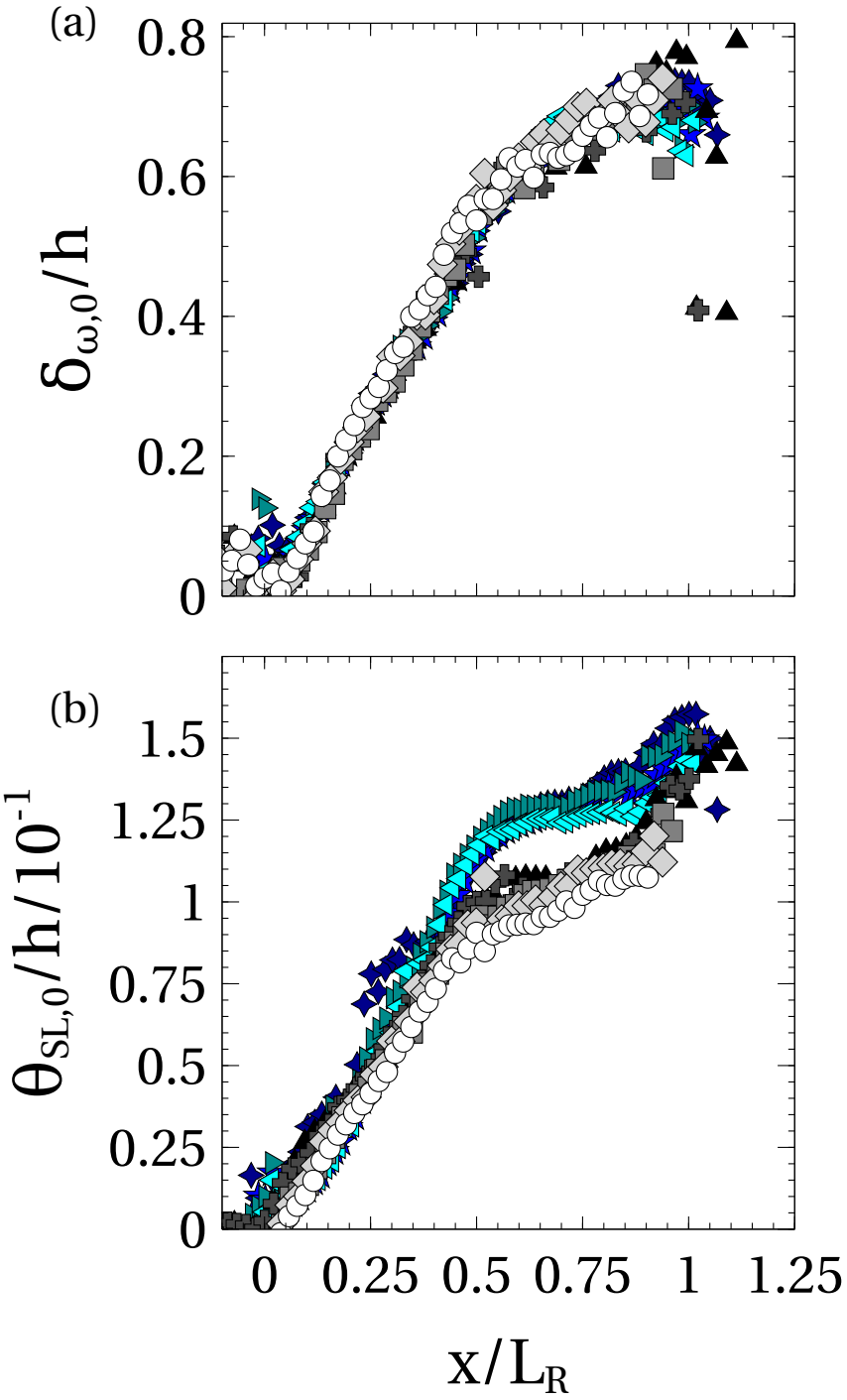

Figure 8.3: Comparison of translated shear layer growths. (a) Vorticity thickness $\theta_{SL,0}$; (b) Generalised momentum thickness $\delta_{\omega,0}$. Symbols as in figure 8.1 (gray shades) and figure 8.2 (blue shades).

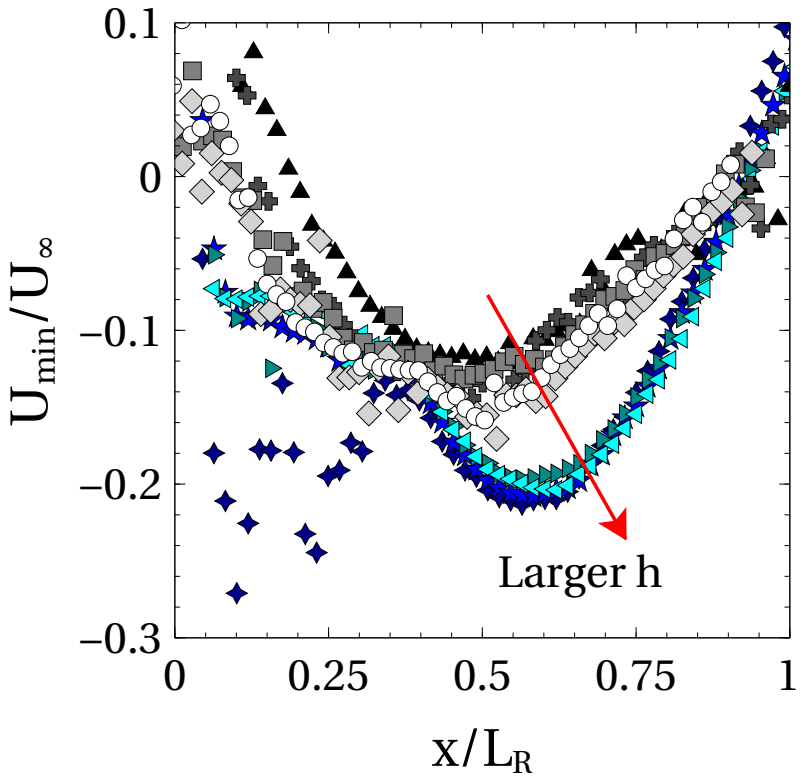

Figure 8.4: Comparison of the evolutions of U_{min}/U_∞ along the separated shear layer. Symbols as in figure 8.3.

For an additional geometric argument in favour of scaling the shear layer with L_R and h, let us now approximate the TNTI and the RRI with simple straight lines, as in figure 8.5. This simplification is rather well supported by figure 5.1. Since the resulting shear layer spreads linearly and mainly toward the wall, it seems reasonable to put:

$$\frac{\mathrm{d}\delta_\omega}{\mathrm{d}x} \sim \tan(\psi) = h/L_R = \left(\frac{L_R}{h}\right)^{-1}. \tag{8.2}$$

It follows immediately that, for geometrically similar ramps, $\mathrm{d}(\delta_\omega/h)/\mathrm{d}(x/L_R) \approx const$, as verified in figure 8.3(a). Similar arguments apply to $\mathrm{d}\theta_{SL}/\mathrm{d}x$, at least for $x/L_R < 0.5$. More importantly, this simple result implies that the faster the separated shear layer grows, the smaller is the recirculation region (also see Adams & Johnston (1988*a*) on this subject), which is well supported by the inserts in figure 8.1 and figure 8.2.

8.2.1 Comparison with a free shear layer

It is generally agreed that the separated shear layer behaves similarly to a free shear layer in a large region downstream of the upper edge of the ramp (Eaton & Johnston (1981), Chandrsuda & Bradshaw (1981)). This would have important implications for the present work, because spreading of free shear layers is driven by entrainment of external fluid (see Pope (2000)). To have some insights into this matter, let us consider spreading rates typical of free turbulent mixing layers, modelled by Browand & Troutt (1985) as follows:

$$\frac{\mathrm{d}\theta_{SL}}{\mathrm{d}x} = 0.034\,\frac{U_\infty(x) - U_{min}(x)}{U_\infty(x) + U_{min}(x)}, \tag{8.3a}$$

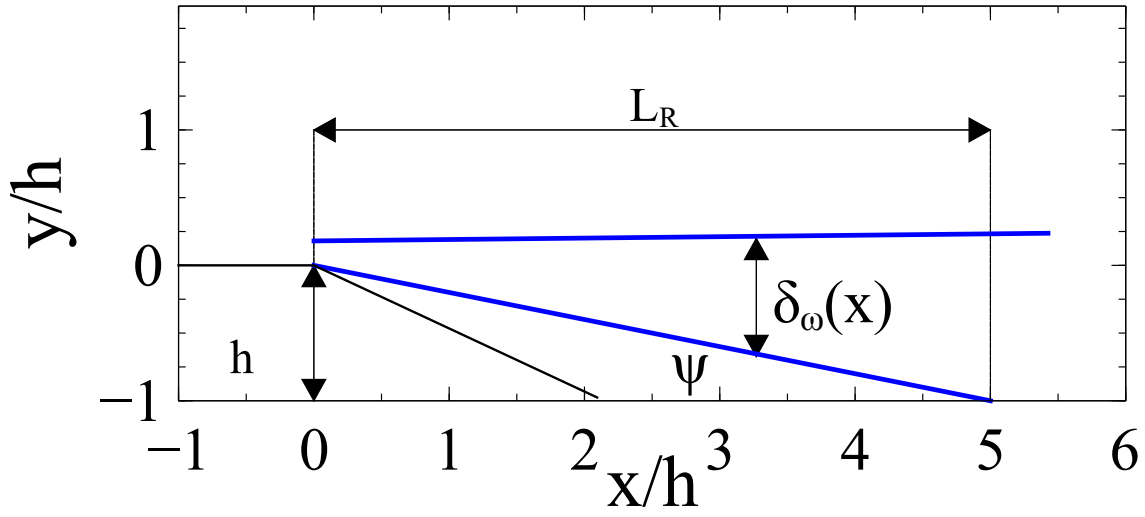

Figure 8.5: Simplified sketch of separated shear layer growth. The mean TNTI and the mean RRI are approximated with straight lines. Ψ is the angle at which the separated shear layer impacts the wall.

$$\frac{\mathrm{d}\delta_\omega}{\mathrm{d}x} = 0.17\,\frac{U_\infty(x) - U_{min}(x)}{U_\infty(x) + U_{min}(x)}. \tag{8.3b}$$

For $x/L_R < 0.5$, the velocity ratio in eq. 8.3 ranges between 1.15 and 1.3. Then, equations 8.3 yield $\mathrm{d}\theta_{SL}/\mathrm{d}x \approx 0.042 \pm 0.003$ and $\mathrm{d}\delta_\omega/\mathrm{d}x \approx 0.205 \pm 0.015$, compared to measured mean values of 0.05 ± 0.006 and 0.22 ± 0.03, respectively. The relatively good agreement of estimated and observed values supports the idea that the separated shear layer develops similarly to a free shear layer, and that its growth is dominated by entrainment. Interestingly, eq. 8.3 are no longer acceptable approximations when the growth rates of θ_{SL}/h and δ_ω/h decrease for $x/L_R > 0.5$. Pressure data shown at § 6.2.1 illustrate that lower spreading rates are correlated with strong pressure recovery. This might be evidence that the shear layer is no longer free: interactions with the wall might play a role in the second half of the flow. However, on both ramps entrainment appears to be the main contributor to spreading of the separated shear layer as a whole, since $75\,\%$ of total shear layer growth takes place within $x/L_R < 0.5$.

8.3 RANS equations in the separated shear layer

Before going any further, it seems wise to build an analytical framework for future investigations, based on the transport equations for mean momentum (eq. 2.10). Putting in evidence the pressure term, one can write:

$$\frac{1}{\rho}\frac{\partial P}{\partial x_i} = -U_j\frac{\partial U_i}{\partial x_j} + \nu\frac{\partial^2 U_i}{\partial x_j^2} - \frac{\partial}{\partial x_j}\langle u_i' u_j'\rangle. \tag{8.4}$$

PIV data give access to all quantities on the right hand side of eq. 8.4. Anyway it will be $i, j = 1, 2$, since only the streamwise (u) and vertical (v) velocity components are available. This approximation should be acceptable because the mean large fields are almost bidimensional, as discussed in section 6.3. For simplicity, a central difference scheme is adopted to approximate derivatives. Before derivation, the fields of U_i and $\langle u_i' u_j'\rangle$ are convoluted with a top-hat filter of kernel side equal to 10 velocity vectors, in order to limit amplification of noise. We limit our discussion to the analysis of each of the two accessible RANS equations along the RRI and the TNTI. Once the two fields of $\partial P/\partial x$ and $\partial P/\partial y$ have been reconstructed, the evolution of the pressure gradients along the TNTI and the RRI are computed by interpolating them at the points that compose the two interfaces. With the same procedure, the trend and the order of magnitude of each term of eq. 8.4 can also be assessed. The results presented at § 6.2.1 and § 8.2 prove that the development of the shear layer is correlated to the longitudinal pressure gradient. Then, we focus on the mean streamwise momentum transport equation first.

8.3.1 Streamwise momentum transport

The streamwise RANS equation is rewritten in explicit form as:

$$\frac{1}{\rho}\frac{\partial P}{\partial x} = -U\frac{\partial U}{\partial x} - V\frac{\partial U}{\partial y} + \nu\left(\frac{\partial^2 U}{\partial x^2} + \frac{\partial^2 U}{\partial y^2}\right) - \frac{\partial}{\partial x}\langle u'^2\rangle - \frac{\partial}{\partial y}\langle u'v'\rangle. \tag{8.5}$$

Figures 8.6 and 8.7 report all terms of eq. 8.5 at $U_\infty = 20\,\mathrm{m\,s^{-1}}$, respectively along the RRI and along the TNTI. On the RRIs, $\partial P/\partial x$ is in good agreement with wall pressure gradients reported in figure 6.1 and figure 6.2. Even if $\partial P/\partial x < 0$ for $x/L_R < 0.5$, the evolution of $\partial P/\partial x$ merges with the streamwise pressure gradient at the wall as the flow approaches reattachment, which is consistent with the definition and shape of the RRI. Similar trends can also be observed along the TNTI. It is now $\partial P/\partial x \approx 0$ in correspondence of the pressure plateau ($x/L_R < 0.5$), then $\partial P/\partial x$ increases and reaches a maximum that is located at $x/L_R \approx 0.85 \approx 4.7h/L_R$, which compares well with the peak pressure gradient measured at the wall (figure 6.1(b)). Data from the R2 ramp also suggests that $\partial P/\partial x \to 0$ for $x/L_R \approx 1.5 \approx 7.5h/L_R$, which is once more consistent with figure 6.1(b). Finally, along both interfaces, $\partial P/\partial x$ seems to relate well to shear layer development: generally speaking, slower growth corresponds to positive (i.e. adverse) pressure gradients. Let us now comment the right-hand side of eq. 8.5. It is evident that viscous stresses are always negligible, as it could be reasonably expected far from walls. Further, mean and turbulent shear-stresses appear to be important along both interfaces, while other terms seem to have more specific local roles. Along the RRI (figure 8.6), the streamwise convective term $U\partial U/\partial x$ is zero by definition. In the neighbourhood of the separation point, the convective term $V\partial U/\partial y$, related to the main component of mean shear, provides the dominant contribution to $\partial P/\partial x$, since Reynolds stresses tend to cancel each other out. This is no longer the case in a large neighbourhood of the reattachment point ($x/L_R > 0.7$), where $\partial\langle u'v'\rangle/\partial y$ overweights the other terms and causes $\partial P/\partial x$ to reach its maximum. As for the TNTI (figure 8.7), $V\partial U/\partial y$ and $\partial\langle u'v'\rangle/\partial y$ appear to have opposite effects: this suggests that the contribution of turbulence to momentum transport (partially) compensates for losses due to mean shear. Interestingly, here $U\partial U/\partial x < 0$ gives a sizeable contribution to the increasing streamwise pressure gradient. If we consider that the TNTI is the limit of the potential region of the flow, the inviscid assumption can be applied to 8.5, yielding $P + 1/2\rho U^2 \approx const$ and hence:

$$\frac{\partial P}{\partial x} \approx -\rho U\frac{\partial U}{\partial x}. \tag{8.6}$$

This relation will be of some importance in the discussion of the scaling laws of streamwise pressure gradient (see § 8.4) and of statistical behaviour of the TNTI (see § 10.2.4).

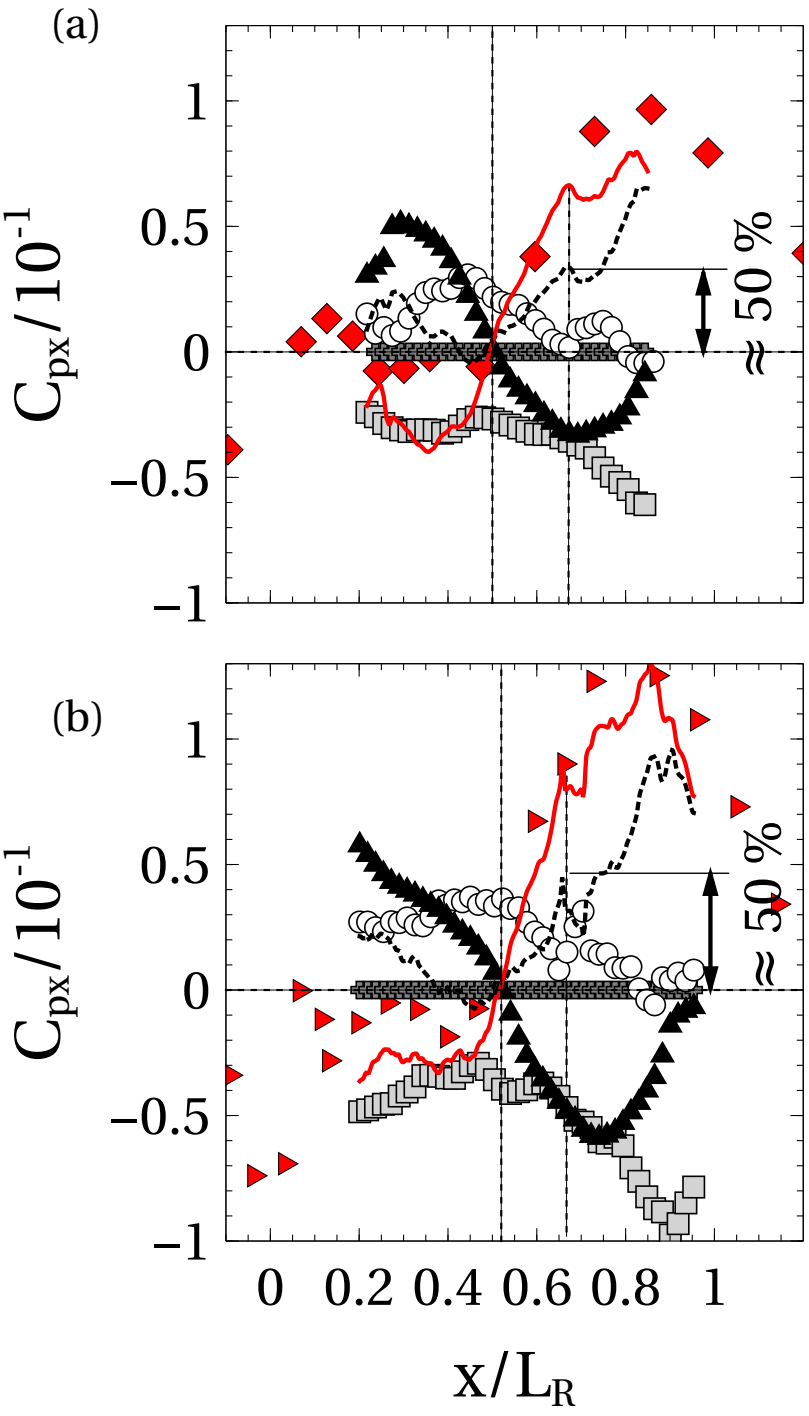

Figure 8.6: Streamwise pressure gradient along the RRI at $U_\infty = 20\,\mathrm{m\,s^{-1}}$ for (a) the R2 ramp ($Re_h = 4 \times 10^4$); (b) the GDR ramp ($Re_h = 13.3 \times 10^4$). Symbols: ◯ $\partial\langle u'^2\rangle/\partial x$; ■ $\partial\langle u'v'\rangle/\partial y$; ▲ $\partial UV/\partial y$; ✚ $\nabla^2 U$; ♦ R2 wall pressure gradient (figure 6.1(b)); ► GDR wall pressure gradient (figure 6.2(b)); – – – $-(\partial\langle u'v'\rangle/\partial y + \partial\langle u'^2\rangle/\partial x)$; ——— $\partial P/\partial x$, computed with eq. 8.5. All curves are normalised on dynamic pressure and step height h.

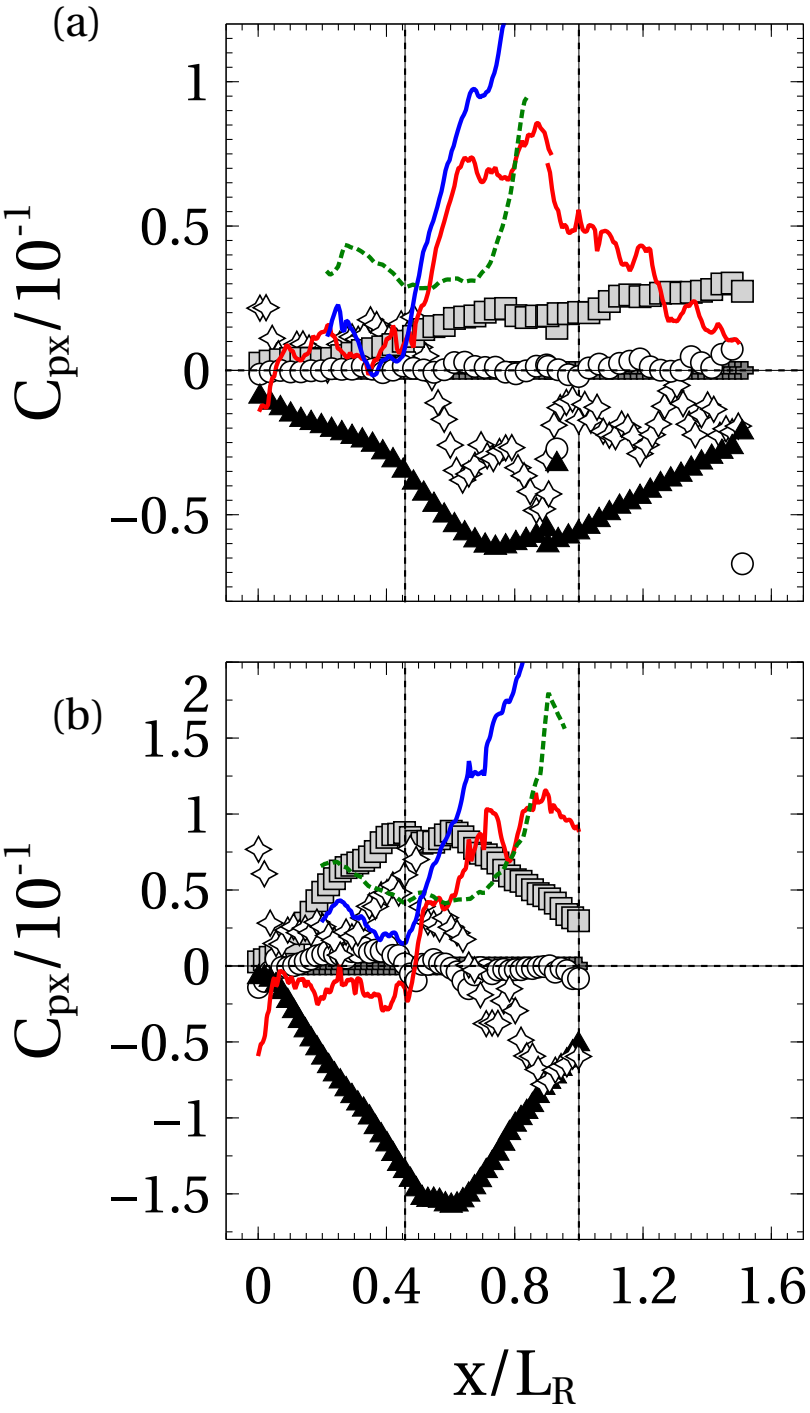

Figure 8.7: Streamwise pressure gradient along the TNTI at $U_\infty = 20\,\mathrm{m\,s^{-1}}$, for (a) the R2 ramp ($Re_h = 4 \times 10^4$); (b) the GDR ramp ($Re_h = 13.3 \times 10^4$). Symbols: ✧ $U\partial U/\partial x$; – – – $\partial\langle v'^2\rangle/\partial x$; ——— $\partial P/\partial x$ computed with Eq. 8.11. Other symbols as in figure 8.6. All curves are normalised on dynamic pressure and step height h.

8.3.2 Vertical momentum transport

We now investigate the RANS equation for the vertical velocity component v, that is:

$$\frac{1}{\rho}\frac{\partial P}{\partial y} = -U\frac{\partial V}{\partial x} - V\frac{\partial V}{\partial y} + \nu\left(\frac{\partial^2 V}{\partial x^2} + \frac{\partial^2 V}{\partial y^2}\right) - \frac{\partial}{\partial x}\langle u'v'\rangle - \frac{\partial}{\partial y}\langle v'^2\rangle. \tag{8.7}$$

Figure 8.8 and figure 8.9 report the vertical pressure gradient $\partial P/\partial y$ along the RRI and the TNTI, respectively. Along the RRI, $\partial P/\partial y$ is essentially determined by normal stresses, as previously observed by Kim *et al.* (1980). It is thought that the strong decreasing trend observed close to reattachment might be, once again, an effect of the interaction with the wall, that tends to stop fluid particles that have acquired some vertical velocity over $x/L_R < 0.5$. In addition, $\partial P/\partial y$ is not particularly well correlated with shear layer growth. Neglecting all smaller terms, along the RRI eq. 8.4 becomes:

$$\frac{\partial P}{\partial y} \approx -\rho\frac{\partial\langle v'^2\rangle}{\partial y}. \tag{8.8}$$

Following Pope (2000), eq. 8.8 can be integrated to:

$$P/\rho = P_0/\rho - \langle v'^2\rangle, \tag{8.9}$$

where P_0 is the mean pressure in the free-stream. The streamwise pressure gradient can then be computed by taking the derivative of eq. 8.9, which gives:

$$\frac{1}{\rho}\frac{\partial P}{\partial x} = \frac{1}{\rho}\frac{\mathrm{d}P_0}{\mathrm{d}x} - \frac{\partial\langle v'^2\rangle}{\partial x}. \tag{8.10}$$

By plugging into eq. 8.5 at the RRI, this yields:

$$\frac{\mathrm{d}P_0}{\mathrm{d}x} \approx -\rho\left(\frac{\partial}{\partial y}\left(UV + \langle u'v'\rangle\right) + \frac{\partial}{\partial x}\left(\langle u'^2\rangle - \langle v'^2\rangle\right)\right). \tag{8.11}$$

Now, if one considers that the mean TNTI bounds the free flow, eq. 8.11 evaluated at the mean RRI should at least approximate the evolution of the pressure gradient along the TNTI. Figure 8.7 also reports the longitudinal pressure gradient along the TNTIs computed with eq. 8.11. Similar results are obtained at all Re_h and are not shown for sake of simplicity. The agreement with the curve of $\partial P/\partial x$ obtained with eq. 8.5 is not completely satisfactory, but tendencies are clearly matched at least up to $x/L_R \approx 0.6$-0.7. After this point, the deviation between the two curves seems to be mainly caused by $\partial\langle v'^2\rangle/\partial x$, but it is not clear if this is a natural tendency of the flow or a problem induced by quality of PIV images close to the wall. In spite of this limitation, this qualitative result suggests that the mean pressure distribution connects the two mean interfaces on scales of the order of L_R.

The interpretation of $\partial P/\partial y$ along the TNTI is less obvious, possibly because of stronger biases due to PIV noise in the derivatives of eq. 8.7. However, it appears quite clearly in figure 8.9 that the vertical pressure gradient reaches its maximum at $x/L_R \approx 0.5$, i.e. at a streamwise position consistent with the change in shear layer growth rate. Further, the main contributions to $\partial P/\partial y$ come from $U\partial V/\partial x$ and $\partial\langle v'^2\rangle/\partial y$, although their relative weights do not evolve in the same fashion over the recirculation region of the two ramps. Interestingly, R2 data suggest that turbulence and the streamwise component of mean shear compensate each other after reattachment, which was not the case up to $x/L_R \approx 1.5$ for streamwise momentum.

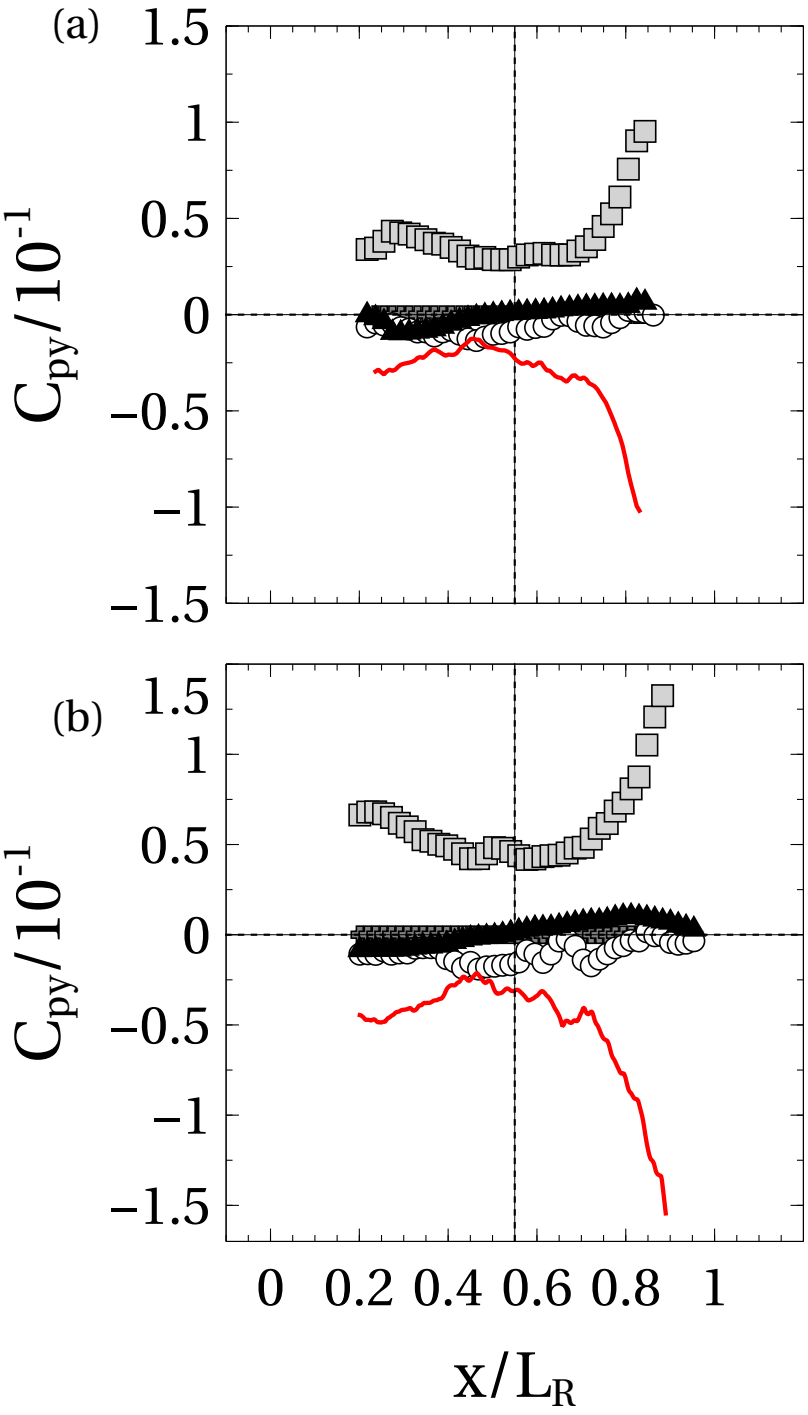

Figure 8.8: Vertical pressure gradient along the RRI at $U_\infty = 20\,\mathrm{m\,s^{-1}}$ for (a) the R2 ramp ($Re_h = 4 \times 10^4$); (b) the GDR ramp ($Re_h = 13.3 \times 10^4$). Symbols: ◯ $\partial\langle u'v'\rangle/\partial x$; ■ $\partial\langle v'^2\rangle/\partial y$; ▲ $V\partial V/\partial y$; ✧ $\partial UV/\partial x$; ✚ $\nabla^2 V$; —— $\partial P/\partial y$, computed with eq. 8.7). All curves are normalised on dynamic pressure and step height h.

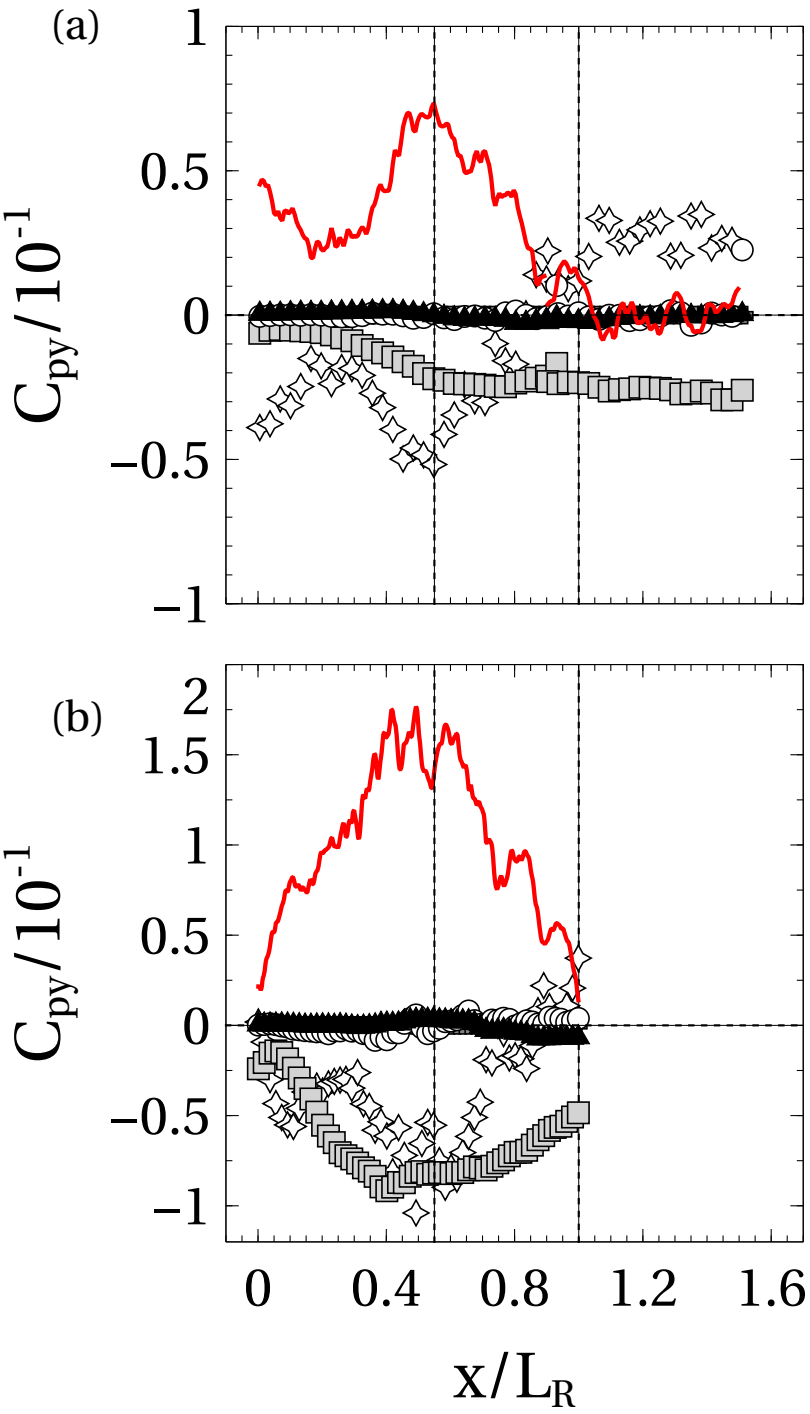

Figure 8.9: Vertical pressure gradient along the TNTI at $U_\infty = 20\,\mathrm{m\,s^{-1}}$ for (a) the R2 ramp ($Re_h = 4 \times 10^4$); (b) the GDR ramp ($Re_h = 13.3 \times 10^4$). Symbols as in figure 8.8.

8.4 Normalisation of pressure gradients: more than one local scale?

It seems now interesting to pay further attention to normalisation of pressure gradients, and in particular of its streamwise component, because results presented at § 8.3.1 and § 8.3.2 suggest that scaling parameters might be different along the two interfaces of the separated shear layer. Let us start from the TNTI, since here the h - L_R scaling appears to be less satisfactory. If such normalisation is relatively acceptable for $\partial P/\partial x$ (figure 8.7), it is visually clear that $\partial P/\partial y$ does not scale with h at all (figure 8.9). Further, the main terms contributing to $\partial P/\partial x$ and $\partial P/\partial y$ do not appear to all share the same scaling, including for what concerns streamwise distance: for example, figure 8.7 shows that $U\partial U/\partial x$ might scale with L_R, but certainly $V\partial U/\partial y$ does not. It was empirically found that some terms of eq. 8.5 and eq. 8.7 are better scaled (at least on part of the available x/L_R range) by the thickness of the incoming boundary layer *at the edge of the ramp*, weighted on a coefficient $C_{h,\delta}$ representing the interplay between such thickness and step height. The same coefficient $C_{h,\delta}$ seems to also correct some of the terms that scale with h, and the streamwise scaling of terms that are not normalised by L_R. We propose the following definition of $C_{h,\delta}$:

$$C_{h,\delta} = (1 + \delta_e/h)\,, \tag{8.12}$$

where, significantly, the ratio δ_e/h appears. It is stressed that the value of δ at the reference section $x/h = -9$ does not seem to correctly scale any term of eq. 8.5 and eq. 8.7. For clarity, the scaling parameters adopted for each term are listed in table 8.2. The resulting, (partially) improved collapse of the main terms of $\partial P/\partial x$ and $\partial P/\partial y$ along the TNTI are reported in figure 8.10 and figure 8.11.

	C_{px}	$U\partial U/\partial x$	$V\partial U/\partial y$	$\partial\langle u'v'\rangle/\partial y$	C_{py}	$U\partial V/\partial x$	$\partial\langle v'^2\rangle/\partial y$
momentum scale	h^{-1}	$(hC_{h,\delta})^{-1}$	$(\delta_e/C_{h,\delta})^{-1}$†	$(\delta_e C_{h,\delta})^{-1}$	n.s.	h^{-1}	$(\delta_e C_{h,\delta})^{-1}$†
x scale	L_R	L_R	$L_R C_{h,\delta}$	$L_R C_{h,\delta}$†	L_R	L_R	$L_R C_{h,\delta}$†

Table 8.2: Scaling parameters for the main terms of the RANS equations at the TNTI. The symbol † stands for a partially successful scaling. The abbreviation *n.s.* indicates that no clear scaling was found.

Eq. 8.5 along the TNTI can be rewritten in non-dimensional form, by using the scaling parameters of table 8.2. It is:

$$\frac{U_\infty^2}{2h}\frac{\partial C_p}{\partial x^*} \approx -\frac{U_\infty^2}{2hC_{h,\delta}}\left(\frac{\partial U^{*2}}{\partial x^*}\right) - \frac{C_{h,\delta}U_\infty^2}{\delta_e}\left(\frac{\partial V^*U^*}{\partial y^*}\right) - \frac{U_\infty^2}{\delta_e C_{h,\delta}}\left(\frac{\partial}{\partial y^*}\langle u'v'\rangle^*\right), \tag{8.13}$$

where smaller terms have been neglected and the superscript * indicates normalisation. Once eq. 8.13 is divided by $U_\infty^2/2h$, one obtains:

$$\frac{\partial C_p}{\partial x^*} \approx -\frac{1}{C_{h,\delta}}\left(\frac{\partial U^{*2}}{\partial x^*}\right) - 2C_{h,\delta}\frac{h}{\delta_e}\left(\frac{\partial V^*U^*}{\partial y^*}\right) - \frac{2}{C_{h,\delta}}\frac{h}{\delta_e}\left(\frac{\partial}{\partial y^*}\langle u'v'\rangle^*\right). \tag{8.14}$$

This latter expression highlights the fact that the main terms of eq. 8.5 do not share the same scaling. The scaling parameters depend both on geometry and on the incoming flow, which is in qualitative agreement with findings of section 8.2: indeed figure 8.3 already showed that a characteristic scale of the incoming boundary layer (e.g. $\delta_\omega(0)$) also influences the development of the separated shear layer. More interestingly, the effect that dominates the scaling parameters in eq. 8.14 (i.e. geometry or the incoming boundary layer) changes according to the value of $C_{h,\delta}$. This matter will be discussed in more details in further sections.

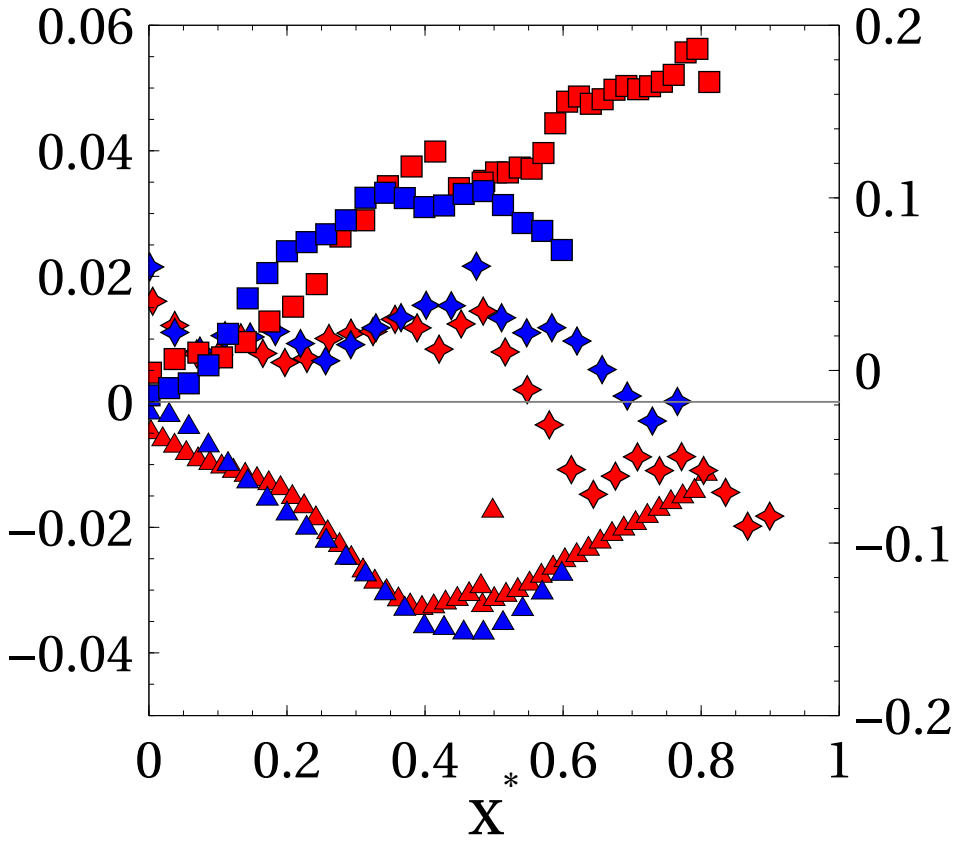

Figure 8.10: Components of the streamwise RANS equation along the TNTI, normalised as in table 8.2. Symbols on the ***left*** vertical axis: ▲ $\partial UV/\partial y$; ■ $\partial\langle u'v'\rangle/\partial y$. Symbols on the ***right*** vertical axis: ✧ $U\partial U/\partial x$. R2 data are in red online, GDR data in blue online. The symbol * indicates normalisation.

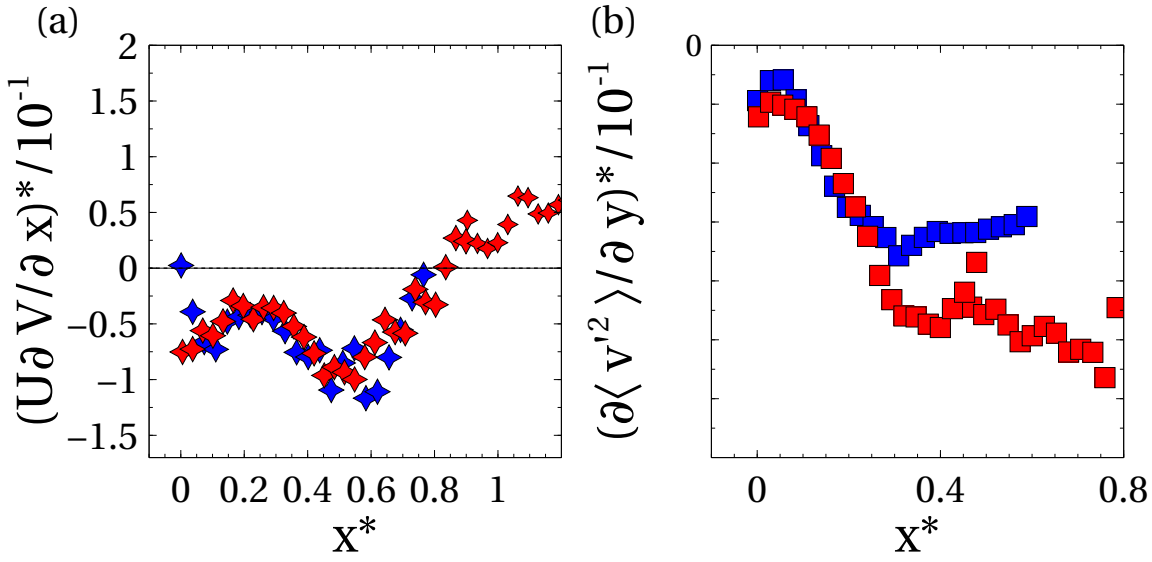

Figure 8.11: Components of the vertical RANS equation along the TNTI, normalised as in table 8.2. (a) ✧ $U\partial V/\partial x$; (b) ■ $\partial\langle v'^2\rangle/\partial y$. R2 data are in red online, GDR data in blue online. The symbol * indicates normalisation.

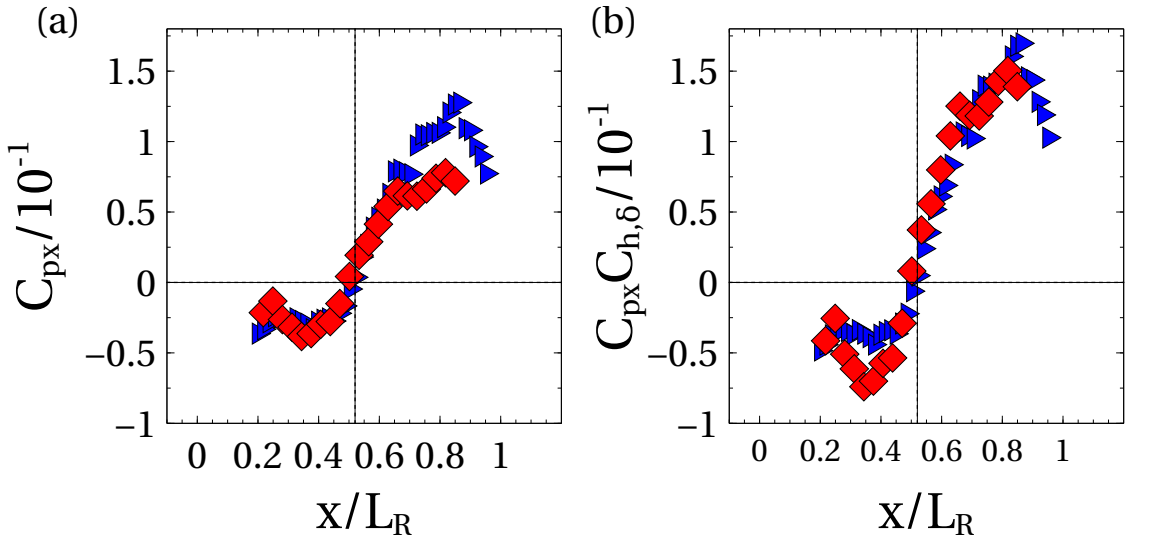

Figure 8.12: Comparison of normalisations of $\partial P/\partial x$ along the RRI: (a) $C_{px} = h\partial C_p/\partial x$; (b) $C_{px}C_{h,\delta}$. Symbols: ♦ R2 ramp; ► GDR ramp.

The identification of $C_{h,\delta}$ and its uses in table 8.2 are data driven and, originally, specific to the TNTI. However, the same factor $C_{h,\delta}$ seems to play a role along the RRI. Figure 8.12(a) directly compares the streamwise pressure gradients along the RRI of the two ramps. For $x/L_R < 0.7$, pressure data are well scaled by dynamic pressure and step height h, while L_R scales streamwise distances as expected. As for the divergence observed on $\partial P/\partial x$ for $x/L_R > 0.7$, it is rather consistent with the δ_e/h dependency of $C^*_{p,r}$ discussed at § 6.2.1. Surprisingly, scaling in this domain is much improved if C_{px} along the RRI is also normalised on $hC_{h,\delta}$, as shown in figure 8.12(b) (streamwise positions, however, still scale with L_R). Figure 8.13 shows the main terms of eq. 8.5 along the RRI, normalised both on h (figure 8.13 (a), (c) and (e)) and $hC_{h,\delta}$ (figure 8.13 (b), (d) and (f)). It appears that Reynolds stresses collapse better when scaled on $hC_{h,\delta}$, over most of the recirculation region. Instead, $V\partial U/\partial y$ seems to change scaling at $x/L_R \approx 0.7$.

	C_{px}	$V\partial U/\partial y$	$\partial\langle u'v'\rangle/\partial y$	$\langle u'^2\rangle/\partial x$
$x/L_R < 0.7$	h^{-1}	h^{-1}		
$x/L_R > 0.7$	$(hC_{h,\delta})^{-1}$	$(hC_{h,\delta})^{-1}$	$(hC_{h,\delta})^{-1}$	$(hC_{h,\delta})^{-1}$

Table 8.3: Scaling parameters for the main terms of the RANS equations at the RRI. The longitudinal scale is L_R for all listed terms.

These observations are consistent with § 8.3.1: $\partial P/\partial x$ scales with h over $x/L_R < 0.7$ because on this domain $V\partial U/\partial y$ dominates the streamwise pressure gradient. Close to reattachment, instead, the $hC_{h,\delta}$ scaling is in qualitative agreement with data by Adams & Johnston (1988*a*): turbulent shear-stresses become dominant, and impose to $\partial P/\partial x$ a dependence on δ_e/h. The retained scaling parameters for the main terms of eq. 8.5 along the RRI are summarised in table 8.3. Making use of this information, eq. 8.5 can be rewritten as:

$$\frac{U_\infty^2}{2h}\frac{\partial C_p}{\partial x^*} \approx -\frac{U_\infty^2}{2h}\left(\frac{\partial V^*U^*}{\partial y^*}\right) - \frac{U_\infty^2}{hC_{h,\delta}}\left(\frac{\partial}{\partial y^*}\langle u'v'\rangle^* + \frac{\partial}{\partial x^*}\langle u'^2\rangle^*\right) \text{ for } x/L_R < 0.7. \tag{8.15a}$$

$$\frac{U_\infty^2}{2hC_{h,\delta}}\frac{\partial C_p}{\partial x^*} \approx -\frac{U_\infty^2}{2hC_{h,\delta}}\left(\frac{\partial V^*U^*}{\partial y^*}\right) - \frac{U_\infty^2}{hC_{h,\delta}}\left(\frac{\partial}{\partial y^*}\langle u'v'\rangle^* + \frac{\partial}{\partial x^*}\langle u'^2\rangle^*\right) \text{ for } x/L_R > 0.7. \tag{8.15b}$$

With simple manipulations, this further yields:

$$\frac{\partial C_p}{\partial x^*} \approx -\left(\frac{\partial V^*U^*}{\partial y^*}\right) - \frac{2}{C_{h,\delta}}\left(\frac{\partial}{\partial y^*}\langle u'v'\rangle^* + \frac{\partial}{\partial x^*}\langle u'^2\rangle^*\right) \text{ for } x/L_R < 0.7. \tag{8.16a}$$

$$\frac{\partial C_p}{\partial x^*} \approx -\left(\frac{\partial V^*U^*}{\partial y^*}\right) - 2\left(\frac{\partial}{\partial y^*}\langle u'v'\rangle^* + \frac{\partial}{\partial x^*}\langle u'^2\rangle^*\right) \text{ for } x/L_R > 0.7. \tag{8.16b}$$

Interestingly, eq. 8.16 predicts that scaling along the RRI might be not homogeneous at separation, depending on the value of δ_e/h, but that it becomes so as the flow approaches reattachment. Anyway, mind that 8.16b tends to hide the fact that the common scaling parameter $U_\infty^2/2hC_{h,\delta}$ is *also* a function of δ_e/h. The next sections propose interpretations of how the weight of the terms of eq. 8.14 and eq. 8.16 may change with δ_e/h.

	$C_{h,\delta}$	$\delta_e C_{h,\delta}$	$\delta_e/C_{h,\delta}$	$hC_{h,\delta}$	$L_R C_{h,\delta}$
$\delta_e/h \ll 1$	1	δ_e	δ_e	h	L_R
$\delta_e/h \gg 1$	δ_e/h	δ_e^2/h	h	δ_e	$\gg L_R$
$\delta_e/h \approx 1$	2	$2\delta_e$	$\delta_e/2$	$2h$	$2L_R$

Table 8.4: Asymptotic evolution with δ_e/h of RANS scaling parameters along the interfaces of the separated shear layer.

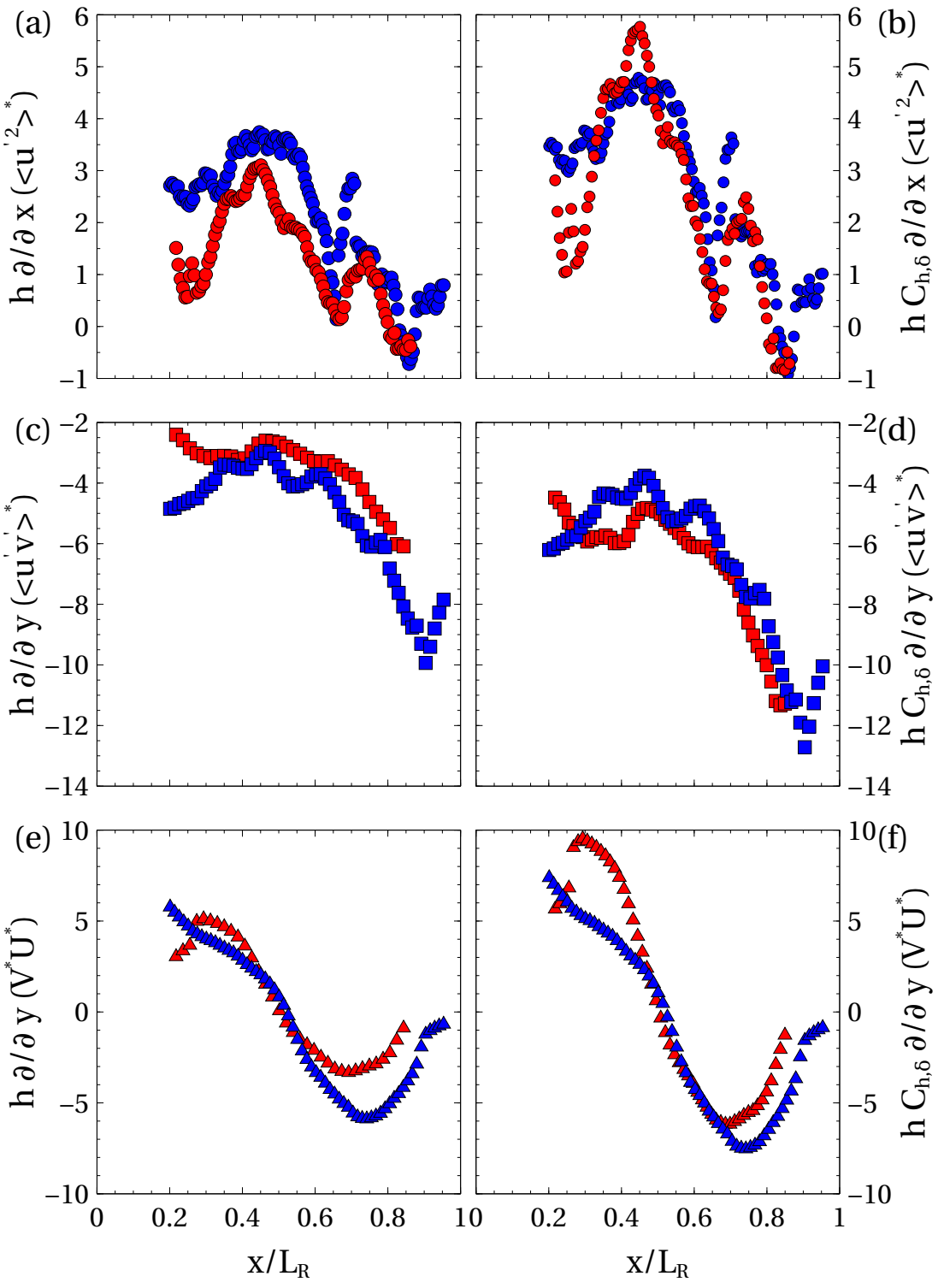

Figure 8.13: Components of the streamwise RANS equation along the RRI, normalised on h and $hC_{h,\delta}$. Symbols: ◯ $\partial\langle u'^2\rangle/\partial x$; □ $\partial\langle u'v'\rangle/\partial y$; △ $\partial UV/\partial y$. R2 data are in red online, GDR data in blue online. The symbol * indicates normalisation.

8.4.1 Case 1: $\delta_e/h \ll 1$

With reference to table 8.4, when $\delta_e/h \ll 1$, it is $C_{h,\delta} \to 1$. It follows that the streamwise scale of all terms becomes L_R. At the TNTI, eq. 8.14 becomes:

$$\frac{\partial C_p}{\partial x^*} \approx -\frac{\partial U^{*2}}{\partial x^*} - \frac{2h}{\delta_e}\left(\frac{\partial V^* U^*}{\partial y^*} + \frac{\partial}{\partial y^*}\langle u'v'\rangle^*\right). \tag{8.17}$$

Interestingly, all *shear stresses* are sized by $(\delta_e/h)^{-1}$, while *normal stresses* vary with h. Shear stresses seem to be the strongest components in eq. 8.13, since $\delta_e \ll h$. However, the pressure gradient scales with h (see table 8.2), which means that, globally, shear stresses tend to cancel each other out. This is quite well verified for the GDR ramp, as shown in figure 8.7(b). In particular, for $x/L_R \to 1$, i.e. approaching the position of maximum pressure gradient, $U\partial U/\partial x$ becomes the main contribution to C_{px}, as predicted by eq. 8.6. For comparison, let us consider the scaling parameters along the RRI. Since $C_{h,\delta} \to 1$, both eq. 8.16a and 8.16b scale uniquely with h over the entire recirculation length, with no effect of boundary layer properties. These observations agree with Bradshaw & Wong (1972), reporting that the structure of a separated flow is independent of δ_e for very low values of δ_e/h, and with wall pressure data by Roshko & Lau (1965) and Adams & Johnston (1988*a*), which show that, provided that ER is not too high, the reduced wall pressure distribution within separation becomes quasi-universal for $\delta_e/h \to 0$ (see figure 6.4). These latter authors also show that, for $ER \leq 1.25$, the condition $\delta_e/h \ll 1$ is already fulfilled at $\delta_e/h < 0.25$: this being so, the GDR ramp should well approximate this first category of flows.

8.4.2 Case 2: $\delta_e/h \gg 1$

Let us now consider the case in which $\delta_e/h \gg 1$, i.e. the incoming boundary layer is much thicker than step height: in this condition $C_{h,\delta} \approx \delta_e/h$. Hence, turbulent stresses can be dropped from eq. 8.14 and the streamwise pressure gradient along the TNTI becomes:

$$\frac{\partial C_p}{\partial x^*} \approx -2\frac{\partial V^* U^*}{\partial y^*}, \tag{8.18}$$

where all terms scale with h. Unlike as in eq. 8.17, mean shear is now determined by geometry, i.e. at the TNTI the scaling parameter of $\partial VU/\partial y$ seems to *change with* δ_e/h.

Similar results are obtained along the RRI, for $x/L_R < 0.7$. Since $C_{h,\delta} \approx \delta_e/h$, eq. 8.16a predicts that Reynolds stresses should once again become vanishingly small as $\delta_e/h \to \infty$. Although we do not dispose of high enough values of δ_e/h to test this hypothesis, comparison of the two ramps is encouraging, since Reynolds stresses seem to become less intense as δ_e/h increases. Then, eq. 8.16a is reduced to eq. 8.18: as expected, in a large neighbourhood of separation geometry scales all terms of the pressure gradient along the RRI. As for $x/L_R > 0.7$, the characteristic scale is now $hC_{h,\delta} \approx \delta_e$. This being so, eq. 8.16b states that pressure gradient at reattachment should evolve as the inverse of δ_e. In the limit of $\delta_e \to \infty$, all terms of eq. 8.16b become vanishingly small. However the h-scaled eq. 8.16a is still valid: this seems to indicate that if δ_e is thick enough, the pressure gradient at the wall is once again determined by geometry. This global picture appears to be well correlated with values of $C^*_{p,r}$ decreasing with larger δ_e/h, as predicted by the theory of Nash (1963), and with the saturation of $C^*_{p,r}$ to an asymptotic value determined by geometry (and in particular ER), as observed by Adams & Johnston (1988*a*) (see figure 6.3). Based on high-ER data by Westphal *et al.* (1984), these authors further suggest that higher values of ER impose their influence on the flow at lower δ_e/h, so that the condition $\delta_e/h \gg 1$ might need to be interpreted just as a limit situation, observed in reality at values of δ_e/h that depend on the actual ER. With $ER = 1.25$, Adams & Johnston (1988*a*) report that saturation is already attained at $\delta_e/h \approx 0.8$. For the R2 ramp it is $ER \approx 1.06$, but $\delta_e/h \approx 0.8$ to 1: then, pressure distributions of this experiment might already be influenced by ER.

Interestingly, if $h \to 0$ (i.e. $ER \to 1$) all terms of eq. 8.16a (and eq. 8.14) vanish, since no geometric perturbance exists to generate a pressure gradient. Instead, the δ_e-scaled eq. 8.16b is still valid. Further, it approximates the equation of a turbulent boundary layer on a flat plate ($h = 0$) far from the wall. According to table 8.2, streamwise scaling along the RRI should always depend on L_R, but the extrapolation to $h \to 0$ does not seem sound, because $L_R \sim h \to 0$. One would intuitively expect that if step height is very small, a streamwise scale $L_x \to \delta$ or $L_x \to \infty$ would appear. Unfortunately this idea could not be tested, because no dataset was found in literature having high δ_e/h and $ER \to 1$ at the same time.

8.4.3 Discussion

All in all, the two experiments analysed in this work seem to tend towards two opposite sides of a spectrum of possible configurations, governed by the parameter δ_e/h. In the GDR datasets, δ_e/h is expected to be low enough so that δ_e affects almost uniquely shear terms at the TNTI, while h sizes the RRI as well as pressure terms throughout the flow. This is not the case for the R2 ramp, over which the two scales are in mutual interplay (e.g. at reattachment). This might explain why comparison of terms of the RANS equations is so complex, in particular for what concerns $\partial P/\partial y$ at the TNTI (eq. 8.7).

Surprisingly, our asymptotic analysis shows that the streamwise pressure distribution (and possibly other correlated quantities) seem to be determined mainly by geometry, for both $\delta_e/h \ll 1$ and for $\delta_e/h \gg 1$, which is supported, at least to some extent, by available data. However, the pressure gradients contributions in eq. 8.14 and in eq. 8.16 do not have the same scaling parameters and relative strengths in the two cases: this suggests that the role of geometry might also differ, as follows. Low values of δ_e/h are associated with a non negligible weight of $U\partial U/\partial x$ along the TNTI and with intense Reynolds shear stresses. More in general, shear terms appear to have a key role throughout the recirculation region: mean and turbulent shear stresses are the strongest terms at the TNTI (although compensating each other) and determine the pressure gradient along the RRI. If it is assumed that the effects of the incoming boundary layer are negligible in these conditions, the scaling observed along the TNTI at § 8.4.1 suggests that the separated flow can be interpreted as the superposition of two simpler flows: a free-like turbulent shear layer (scaling with $(\delta_e/h)^{-1}$) and a potential flow in a diffuser (scaling with h or more likely with ER). Of course h and ER are not independent, but since turbulence is strong (i.e. overall the flow is not potential), it seems reasonable to consider that, for $\delta_e/h \ll 1$, the main effect of h is the development of the turbulent shear layer.

On the contrary, turbulence and normal stresses appear to be negligible (at least in the big picture) when $\delta_e/h \gg 1$. This seems to be due to the strength of the incoming boundary layer (scaling with δ_e or even δ), that is thick enough not to be too perturbed by the size of the step and to overcome the pressure recovery induced by the expanding geometry. The remaining pressure gradient is uniquely determined by mean shear at both interfaces. This suggests to interpret $V\partial U/\partial y$ as a consequence of the local *deviation* of streamlines due to the increased cross section of the flow. Then, the most appropriate geometric parameter to size the flow might be ER rather than h alone. In this respect, h appears to be sufficient to scale eq. 8.14 and eq. 8.16 only because ER is fundamentally constant across the experiments. All in all, if $\delta_e/h \ll 1$ the influence of geometry on the flow is due to both h and ER; if $\delta_e/h \gg 1$, instead, ER seems to be the most important geometric parameter. This view is consistent with (and partially inspired by) previous works on separated shear flows, and in particular with observations reported by Adams & Johnston (1988*a*).

As a conclusion to this section, it seems important to summarise momentum transfer scaling in a few sentences. Firstly, it must be stressed that these results do not answer exaustively to the problem of scaling together separated flows with different geometries, incoming boundary layers or both. Much work is left to test and extend a discussion that, for the moment, is empirically driven. However, our findings appear to highlight some points of great potential relevance, that support and extend previous observations by other researchers. Firstly, separated flows assimilable to the ramps under study seem to be governed by more than one characteristic scale, viz. h, that is the size of the disturbance generating the separation, and δ, that is the thickness of the incoming boundary layer at separation. ER is also expected to be an important parameter, at least if $\delta_e/h \gg 1$. The effects of h and δ might be segregated in different regions of space or they might overlap and be indistinguishible, depending on the relative strength of h and δ. In this work, we have used a coefficient $C_{h,\delta}$ to model the interplay between the two scales. Most interestingly, the terms of the RANS equations can change their scaling parameter (i.e. h or δ) in function of the value of $C_{h,\delta}$. This behaviour is felt to be one of the main reasons of the variety seen in massively separated flows and of their consequent difficult interpretation.

8.5 Dependencies on the incoming boundary layer

The asymptotic results presented in section 8.4 highlight that the streamwise pressure gradient, that is one of the main features of a massively separated flow, scales with geometry for both $\delta_e/h \ll 1$ and $\delta_e/h \gg 1$. However, table 5.1 shows that L_R/h (i.e. the characteristic length of the separated flow) follows a decreasing Re trend, that cannot be explained by geometry alone. This strongly suggest the existence of persisting

dependencies on the incoming flow, an idea that is also supported by many previous works such as those of Adams & Johnston (1988*a*), Adams & Johnston (1988*b*) and Neumann & Wengle (2003) among others. Then, it seems important to investigate more in details the influence of properties of the incoming boundary layer on the separated flow under study. We stress that this work does not consider the possible effects of several other parameters, including the ramp angle α (see Ruck & Makiola (1993)), the salient/rounded ramp edge profile (see Debien *et al.* (2014) among others) and free stream turbulence (see for example Adams & Johnston (1988*b*)).

A first correlation between shear layer and incoming boundary layer is provided by figure 6.3 in terms of δ_e/h (at separation) and C_p^*. However the overlapping effects of δ_e/h, ER and Re_θ (which are all inseparable in our experimental setup) make its interpretation complex. Furthermore, the dimensionless length δ_e/h provides a comparison between the incoming flow and the geometric perturbation, but it tells nothing about turbulence in the incoming flow, which is known to have a huge influence on shear layer development (Isomoto & Honami (1989), Aider & Danet (2006) among others). In this respect, Re_h does not seem an effective choice either, in spite of its widespread use in the literature[1].

Re_θ and L_R/h form an alternative set of parameters that could characterise the upstream dependencies of the shear layer: Re_θ is intended to include some information about the turbulent state of the incoming boundary layer[2] whereas L_R/h relates to shear layer development, normalised, at least in first approximation, on geometry effects. Based on the work of Neumann & Wengle (2003), it appears that shear layer properties are rather influenced by the turbulent state of the boundary layer *at some distance* upstream of separation. Then, Re_θ is evaluated at the reference boundary layer section, that is $x/h = -9$. Using these data, it is found that L_R/h evolves as $C_\theta Re_\theta^m$ (shown in figure 8.14(a)), where m is a negative power and C_θ a constant, at least on the available range of Re_θ. This relationship seems to be robust to δ_e/h, because the same Re_θ^m trend appears with the datasets of both ramps, although with slightly different proportionality constants (their ratio gives $C_\theta|_{R2}/C_\theta|_{GDR} \approx 0.97$). It would be interesting to test if BFS data, in particular L_R/h values reported by Nadge & Govardhan (2014), also fit into this picture: this would help understand if, as it seems from our measurements, Re_θ is a better scaling parameter than Re_h. Unfortunately, Nadge & Govardhan (2014) assessed boundary layer properties at the edge of the step, and did not report values of Re_θ for all their experimental points.

Surprisingly, our measurements on the R2 ramp reveal that m changes abruptly from -0.1 to -0.5 around a critical value $Re_{\theta c} \approx 4100$. Only one point at $Re_\theta > Re_{\theta c}$ is available for the GDR ramp, but its L_R/h seems compatible with a similar faster trend. Qualitatively, this change of exponent appears to be linked to the intensity of the turbulence of the flow (but *not* to transition to its fully turbulent state, at least if the criterion adopted at § 7.3.1 is retained). Figure 8.15 and figure 8.16 present the vertical profiles of Reynolds stresses at $x/L_R \approx 0.25$ and $x/L_R \approx 0.8$ for all available Re, respectively on the R2 ramp and the GDR ramp. The curves are normalised on θ_{SL}[3] and U_∞. Reynolds stress profiles appear to be progressive functions of Re_θ. Similar Re_θ dependencies of turbulent quantities have already been observed in separating/reattaching flows, for example by Song & Eaton (2003). Interestingly, peak values of Reynolds stresses evolve as Re_θ^n, where n is now positive. Once again n changes abruptly around $Re_{\theta c}$. The values of n appear to change in the streamwise direction also, but the Re_θ trends shown in the inserts in figure 8.15 and figure 8.16 are representative. This supports the interpretation suggested by figure 8.14(a), i.e. that, at least for a fixed value of h, L_R decreases with increasing intensity of incoming turbulence. An analytical interpretation of these findings will be discussed at § 8.6. As a final remark, it is pointed out that curves presented in figure 8.15 and figure 8.16 collapse together poorly (not shown). This is not too surprising in the light of the discussion of § 8.4. On the GDR ramp, scaling should depend on δ in the upper part of the flow and on h in the lower one; the effects of h, δ and possibly ER overlap in the case of the R2 ramp, in particular at reattachment. This being so, no effort was made to find a more elaborate common scaling.

[1] Interestingly, Armaly *et al.* (1983) arrives to similar conclusions by comparing data from different experiments.

[2] In addition, Chun & Sung (1996) suggests that θ might be the correct scale to normalise the actuation frequency of a periodic forcing of the flow.

[3] Mind that $\theta_{SL} \sim h$, so that scaling requirements presented in table 8.2 should be well met for the R2 ramp and at least the lower part of the GDR separation.

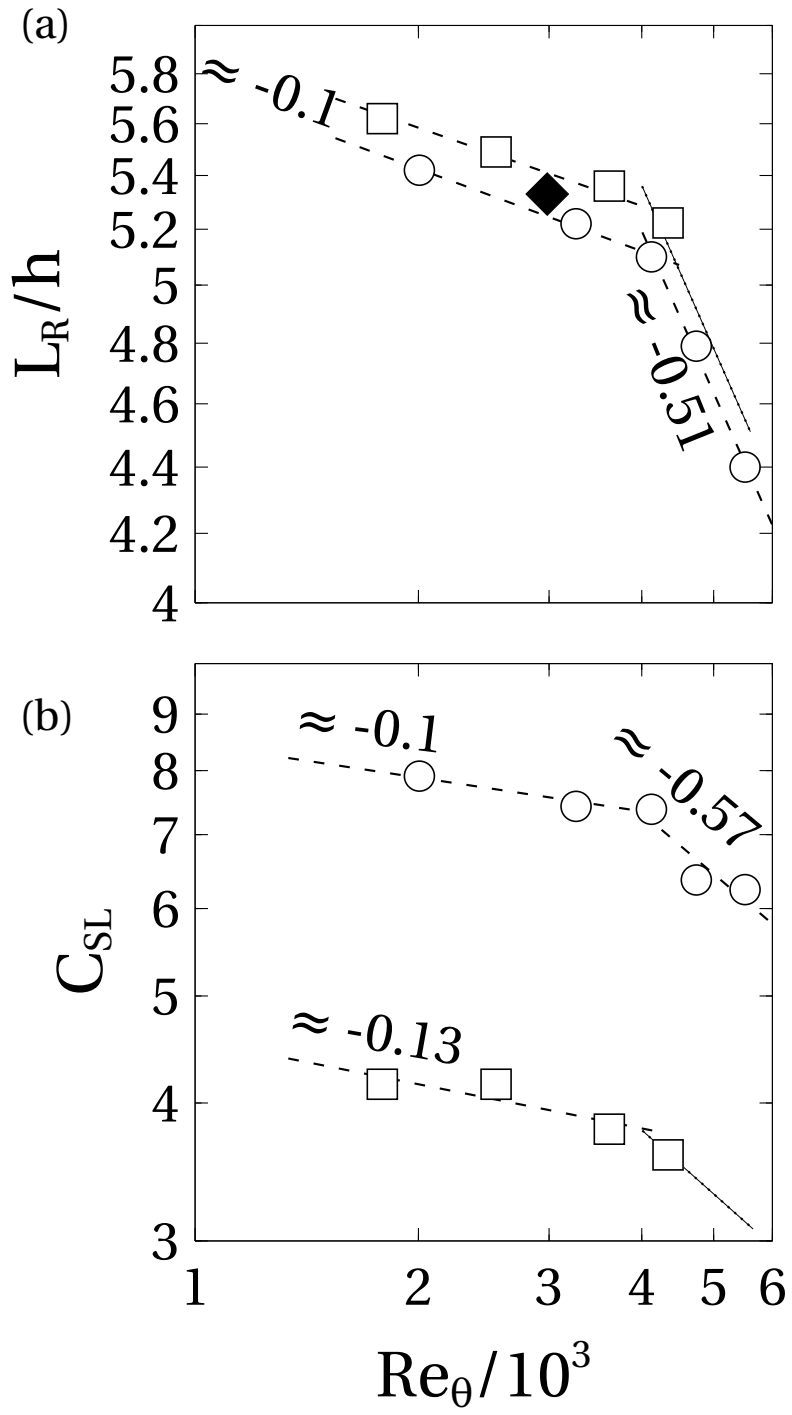

Figure 8.14: Log-log plot in function of Re_θ of (a) L_R/h; (b) C_{SL}. Symbols: ◯ R2 ramp; □ GDR ramp; − − − Power-law fits (in the sense of least-mean square); ····· suggestion of power law at $Re_\theta > Re_{\theta c}$ for the GDR ramp, based on the R2 fit; ♦ Kourta *et al.* (2015), data at $Re_h = 2 \times 10^5$.

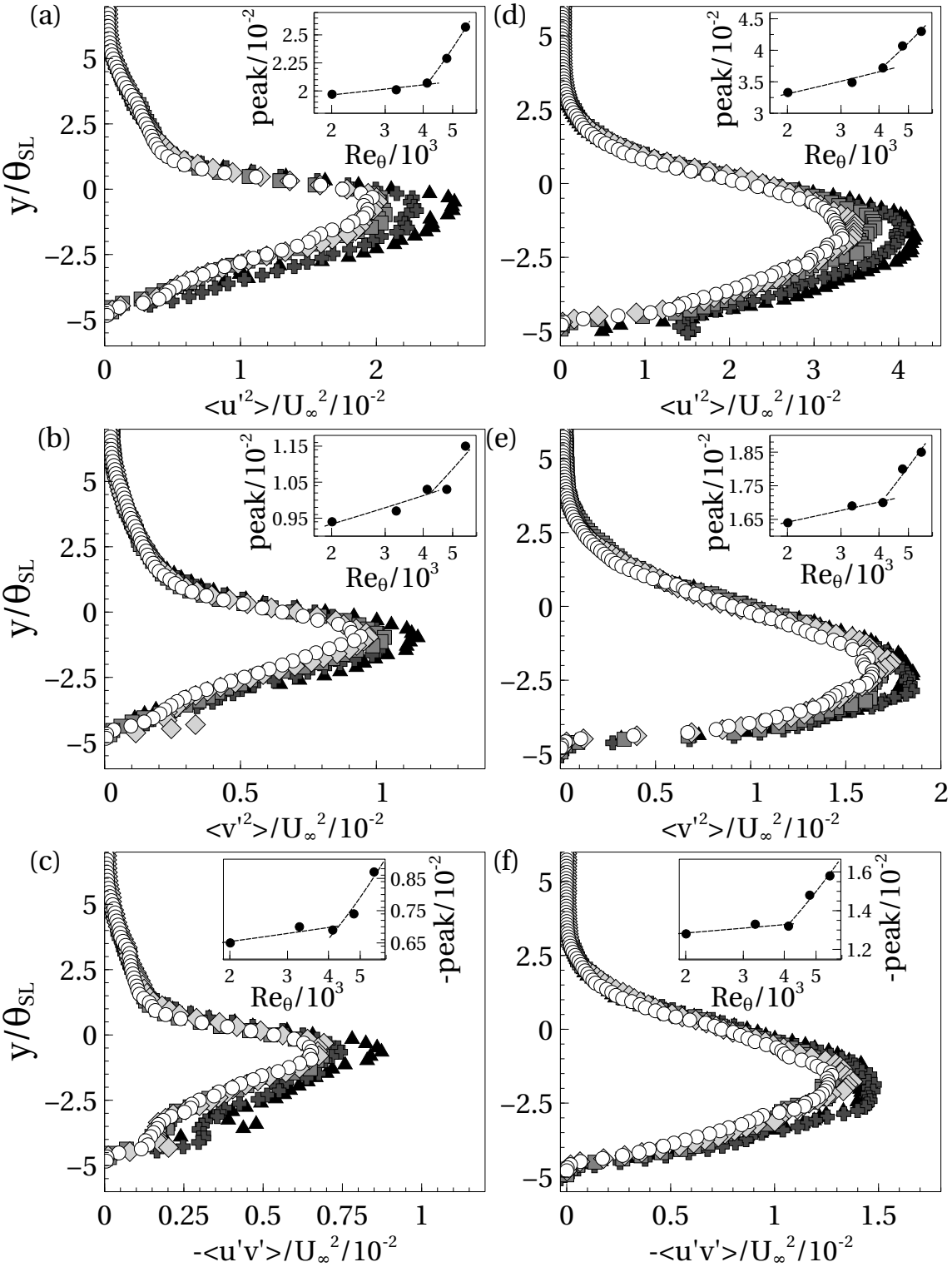

Figure 8.15: Reynold stresses $\langle u'^2 \rangle$, $\langle v'^2 \rangle$ and $-\langle u'v' \rangle$ in the separated shear layer of the R2 ramp at (a), (b), (c) $x/L_R \approx 0.25$ and (d), (e), (f) $x/L_R \approx 0.8$. Inserts show the Re_θ^n evolution of the peak of $\langle u'^2 \rangle$, $\langle v'^2 \rangle$ and $-\langle u'v' \rangle$, respectively. The exponent n passes from 0.05-0.15 to 0.65-0.80. Other symbols as in figure 8.1.

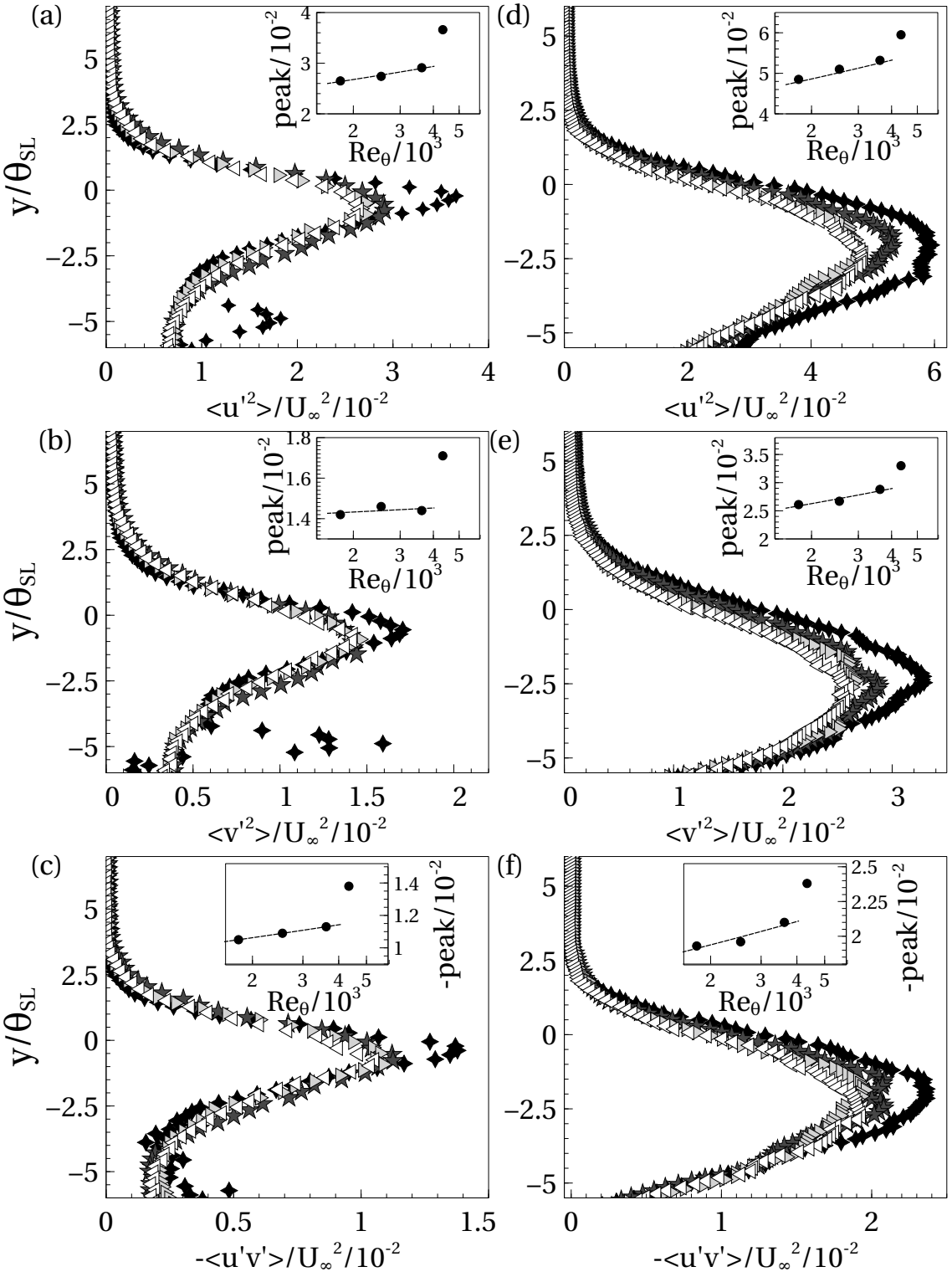

Figure 8.16: Reynold stresses $\langle u'^2 \rangle$, $\langle v'^2 \rangle$ and $-\langle u'v' \rangle$ in the separated shear layer of the GDR ramp at (a), (b), (c) $x/L_R \approx 0.25$ and (d), (e), (f) $x/L_R \approx 0.8$. Inserts show Re_θ^n evolutions of the peaks, as in figure 8.15. The exponent n ranges within 0.1-0.15 for $Re_\theta < Re_{\theta c}$. Other symbols as in figure 8.2.

8.6 On the role of turbulent shear-stresses

It seems now wise to give some physical underpinning to the observations made in section 8.5. The prominent role of turbulent shear stresses in the development of the shear layer is consistent with important past results, that can be invoked to develop the present analysis. In particular, Chapman *et al.* (1958) investigated the properties of the recirculation region for a number of incompressible and compressible, laminar and turbulent flows. Among other results concerning transition and compressibility effects, these authors proposed a theory postulating that the amount of fluid in the recirculation region that is re-entrained by the separated shear layer is balanced by the backflow; and that the pressure distribution within the recirculation region is determined by the interaction of the shear layer with the wall. These views have a central role in this work and, more in general, in the understanding of the recirculation region. Following Chapman *et al.* (1958) and the further developments by Adams & Johnston (1988*a*), close to reattachment one can write:

$$\frac{\partial P}{\partial x} \approx -\rho \frac{\partial \langle u'v' \rangle}{\partial y}, \tag{8.19}$$

which is well supported by our own observations in figure 8.6. Figures 8.15 and 8.16 suggest that $\langle u'v' \rangle \sim R^*_{uv} U^2_\infty$, where R^*_{uv} is a local turbulent shear stress intensity. As for the normalisation of $\partial/\partial y$, many different space scales could be considered within the shear layer, for example θ_{SL}. In this respect, it is pointed out that for similar considerations Chapman *et al.* (1958) suggested to scale the y axis with a displacement thickness δ^*. The two scalings are equivalent in the scope of dimensional analysis. Figure 8.3 shows that $\theta_{SL} \sim h$, at least in first approximation, so that normalising with θ_{SL} near reattachment is consistent with scalings discussed in section 8.4. Normalising all terms of eq. 8.19 gives:

$$\frac{\partial C_p}{\partial x^*} \frac{1/2 \rho U^2_\infty}{X} \approx -\rho \frac{\partial \langle u'v' \rangle^*}{\partial y^*} \frac{R^*_{uv} U^2_\infty}{\theta_{SL}}, \tag{8.20}$$

where X is now a characteristic streamwise scale. On dimensional ground, eq. 8.20 is a valid approximation of the RANS equation if:

$$X \sim -\frac{\theta_{SL,r}}{2R^*_{uv,r}} \approx \begin{cases} 0.2h/0.032 \approx 6.5h \text{ (R2).} \\ \\ 0.2h/0.040 \approx 5h \text{ (GDR).} \end{cases} \sim L_R, \tag{8.21}$$

where empirical values of $\theta_{SL,r}$ and $R^*_{uv,r} = -\langle u'v' \rangle|_{min}/U^2_\infty$ were calculated at the mean reattachment point. The characteristic scale of turbulence-induced pressure gradient is then, once again, of the order of L_R. Further, the agreement between the numerical value of X and the position of $C_{p,r}$ ($\approx 7h$) is impressive, if one considers the relative simplicity of the premises to eq. 8.21. This confirms the idea that the pressure rise is one of the main effects of the interaction of the separated shear layer with the wall, irrespective of the mechanism that determines the final value of $C_{p,r}$. In the framework of this section, however, the most important suggestion given by eq. 8.21 is that L_R should be a function of shear layer properties in a neighbourhood of reattachment. Hence, on both ramps one should verify that at least in the mean:

$$C_{SL} = -\frac{\overline{\theta_{SL}}}{2h\overline{R^*_{uv}}} \sim L_R/h \sim Re_\theta^m \sim \begin{cases} Re_\theta^{-0.1}, & \text{if } Re_\theta < Re_{\theta c}. \\ Re_\theta^{-0.5}, & \text{if } Re_\theta > Re_{\theta c}. \end{cases} \tag{8.22}$$

In eq. 8.22, the overline symbol indicates the average over a streamwise domain within L_R where eq. 8.19 is valid, i.e. $x/L_R \in [0.7, 1]$. The Re_θ trend of C_{SL} is reported in figure 8.14 (b). Very good agreement with data in figure 8.14 (a) and with scaling predicted by eq. 8.22 is obtained both at low and high Re_θ. Figure 8.17 shows that average-based values of the exponent computed on $x/L_R \in [0.7, 1]$ are statistically converged, even if some scatter affects locally computed values (examples are reported in the inserts of figure 8.16). Further, the good collapse with h shown by θ_{SL} (section § 8.2) suggests that $\overline{R^*_{uv}} \sim h/L_R$, so that m would mostly reflect the Re_θ evolution of turbulent shear-stresses. Since it is also $(\mathrm{d}\theta_{SL}/\mathrm{d}x) \sim L_R/h^{-1}$ (§ 8.5), higher free shear layer growth rates at separation are linked to enhanced turbulent mixing close to reattachment. This is in agreement with the views expressed by Adams & Johnston (1988*a*) (although these

authors rather put forward the connection with $C_{p,r}$) and with the flow control experiments by Chun & Sung (1996). In addition, this result qualitatively anticipates that the backflow must balance entrainment from the recirculation region to the separated shear layer, as discussed in chapter § 11.

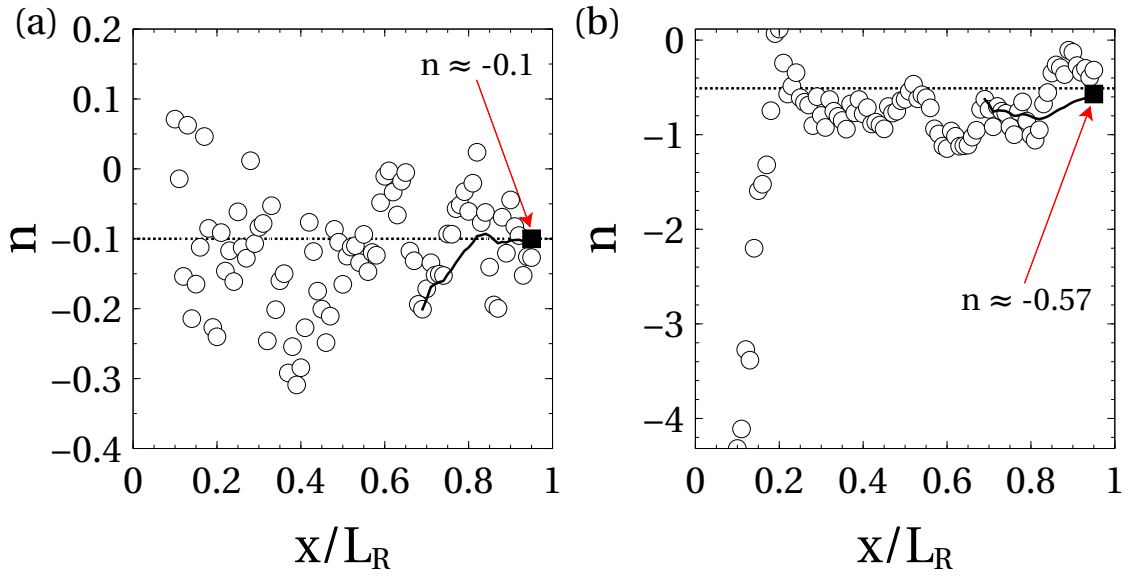

Figure 8.17: Streamwise evolution of the exponent n, obtained by fitting a power law Re_θ^n on local values of parameter C_{SL} computed at many different streamwise positions. (a) $Re_\theta < 4100$; (b) $Re_\theta > 4100$. Symbols: ◯ datapoints; ····· reference value from figure 8.14; ——— running average starting from $x/L_R \approx 0.7$; ■ average on $x/L_R \in [0.7, 0.95]$.

Admittedly, further work is needed to better assess the validity of both correlations presented in figure 8.14. Firstly, the meaning of n should be better understood. Even if it appears reasonable to assume that n expresses the Re_θ behaviour of Reynolds shear-stresses only, in principle the relationship between θ_{SL} and R^*_{uv} might also be a function of Re_θ. This is not secondary matter: indeed, if $\overline{R^*_{uv}} \sim h/L_R$ then $\overline{R^*_{uv}} \sim \mathrm{d}\theta_{SL}/\mathrm{d}x$ and hence there is a linear relationship between (mean) turbulent shear stresses at reattachment and shear layer entrainment at separation (see Pope (2000) and our results at § 11.5.2). Unfortunately, it is not possible to answer to this question definitely with available data, because for such narrow Re_θ ranges they are not precise enough to reliably tell if eq. 8.22 induces separate, small variations of θ_{SL} and R^*_{uv}. Secondly, it appears that the GDR ramp has higher values of L_R/h but lower values of C_{SL} than the R2, even if the ranges of Re_θ spanned in the two experiments are comparable and the ramps geometrically similar. Analytically, this is due to the fact that the GDR shear layer has higher R^*_{uv} all along separation (see figure 8.15 and figure 8.16). This is slightly counterintuitive, if one considers Re_θ as a comprehensive indicator of the turbulent state of the incoming flow, but it is consistent with the scaling on $(\delta_e/h)^{-1}$ shown by shear stresses along the TNTI, for $\delta_e/h \ll 1$. Such observation might imply that the multiscale nature of the flow highlighted in § 8.4 is not adequately taken into account in the dimensional analysis of the present section. However this should only impact the *collapse* of data from different ramps onto a single curve, rather than observations on their Re_θ dependency.

In spite of these limitations, the importance of this result must be stressed, since it provides new insight in the functionning and possible control of separating/reattaching shear layers, as follows. Although the overall topology seems determined by geometry (at least for values of δ_e/h observed in our experiments), the size of the recirculation region *relative to step height* is strongly influenced by the growth rate of the separated shear layer. The latter depends on the turbulent properties of the shear layer, in particular in the neighbourhood of reattachment. It is pointed out that this relationship might not be specific to the present flow, as suggested by results reported by Parezanović & Cadot (2012). These authors investigated the sentivity of the separated flow behind a D-shaped cylinder to the perturbation induced by round cylinders, the latter having a diameter

inferior to the thickness of the separated shear layers. Among other results, Parezanović & Cadot (2012) showed a very good correlation between damping of Reynolds stresses and increased values of L_R, in particular when the round cylinders are placed in the middle of the separated shear layers. This matter will be further investigated in future works. In separated flows originating from a turbulent boundary layer, as the one under study, turbulent properties of the shear layer are correlated to the intensity of turbulence in the incoming boundary layer. Since the pressure rise at reattachment seems to be linked to shear layer impingment, in the mean the fluidic system composed by the incoming boundary layer, the separated shear layer and the wall might behave like a closed loop, in which the (favourable) pressure gradient induced upstream of separation (see figure 6.1(b) and figure 6.2(b)) acts as a feedback branch, influencing properties of the incoming boundary layer. This might explain why boundary layer quantities (e.g. Re_θ) estimated far upstream of separation show some degree of correlation with properties of the separated shear layer (see Neumann & Wengle (2003)). Also, it appears that enhancing free shear layer entrainment by controlling turbulent shear-stress intensity within the shear layer or even within the incoming boundary layer could be an efficient strategy to vary L_R, at least for a given geometry. However, it seems that control actions upstream of separation would have to be calibrated with great care, in order to avoid large variations of δ_e: indeed, this could change the governing scales of the flow and potentially skew the intended effect of control.

8.7 On the role of mean shear

Many pressure and shear layer quantities investigated so far show sharp discontinuities at $x/L_R \approx 0.5$. Notable examples are shear layer growth rates (figure 8.3) and streamwise pressure gradients (figure 8.6 and figure 8.7). One possible explanation of this phenomenon is found by extending the approach of Chapman *et al.* (1958) to the investigation of a neighbourhood of the separation point. Figure 8.6 shows that along the RRI the convective term $\partial UV/\partial y$ is predominant in this region, since Reynolds stresses tend to roughly balance each other. Then, eq. 8.5 can be rewritten as:

$$\frac{\partial P}{\partial x} \approx -\rho \frac{\partial UV}{\partial y}. \tag{8.23}$$

Of course, one can put $U \sim U_\infty$. Since the mean flow is almost bidimensional (see § 6.3), by applying the continuity equation to the recirculation region one obtains $V \sim U_\infty Y/L_R$, where Y is a suitable vertical scale of the recirculation region (for example h). Then, normalising eq. 8.23 along the RRI gives:

$$\frac{\partial C_p}{\partial x^*} \frac{1/2\rho U_\infty^2}{X} \approx -\rho \frac{\partial U^* V^*}{\partial y^*} \frac{U_\infty^2 Y}{Y L_R}, \tag{8.24}$$

where the same notation as in eq. 8.19 applies. Dimensional analysis then yields:

$$X \sim \frac{L_R}{2}, \tag{8.25}$$

which is still consistent with scalings discussed at § 8.4. If it is accepted that eq. 8.23 represents at least the dominant feature of a free shear layer, eq. 8.25 states that in presence of a wall a free shear layer approximation holds just up to $x/L_R \approx 0.5$. This is pleasingly consistent with the findings of the previous sections.

8.8 Some implications for separation control

Findings at § 8.2 show that the relation between L_R/h and the growth rate of the separated shear layer (say $\mathrm{d}\theta_{SL}/\mathrm{d}x$) is a simple inverse proportionality, at least for $x/L_R \in (0, 0.5)$. This suggests that $\mathrm{d}\theta_{SL}/\mathrm{d}x$ might simply and effectively relate the effects of an external forcing on the separated flow. Since in this region $\mathrm{d}\theta_{SL}/\mathrm{d}x$ is determined by entrainment of external fluid (see also § 11.5.2), this supports the idea that entrainment is one of the fundamental variables to be considered in separation control. The work of Berk *et al.* (2017) agrees with this view. These authors apply a periodic forcing to a BFS flow and show that the consequent variation of L_R can be explained more elegantly and predicted more simply in terms

of entrainment than in terms of Strouhal number, that is often used for these purposes (see for example Sigurdson (1995))[1].

Of course, measuring entrainment through the separated shear layer might prove difficult in real-time applications. However, findings at § 8.5 and at § 8.6 suggest that simpler observers might be available both in the incoming boundary layer (Re_θ) and in the recirculation region (C_{SL} and in particular $\langle u'v' \rangle$). Dependencies on Re_θ contribute to explain the effectiveness of control solutions acting on turbulence within the incoming boundary layer (e.g. Chun & Sung (1996)), possibly much upstream of separation (see for example Neumann & Wengle (2003)). They also encourage further work on feed-forward separation control concepts, based on large-scale properties of the incoming flow. As for the correlation between L_R/h and $\langle u'v' \rangle$, it supports a more classical feedback approach, with the notable advantage of offering a seemingly linear relationship between $\langle u'v' \rangle$ and entrainment in the separated shear layer. In this respect, results by Adams & Johnston (1988*a*) suggest that valuable predictions of $\langle u'v' \rangle$ might be obtained from pressure measurement at the wall: then, entrainment-based, closed loop control strategies might be relatively accessible.

There might be very interesting perspectives in choosing control strategies based on $\langle u'v' \rangle$. Eq. 8.11 shows that the pressure recovery in the potential flow depends on total shear along the RRI, but also on a term representing anisotropy of turbulence. According to figure 8.6 and figure 8.7, the anisotropy term might substantially contribute to the adverse pressure gradient. Then, acting on the degree of anisotropy of turbulence might be one further way to control the effects of separation (for instance, pressure drag). In this respect, $\langle u'v' \rangle$ could indeed be a powerful term on which to focus future efforts, because it can be used both to tune shear and to redistribute turbulent momentum along the X and Y direction.

[1] It would be interesting to compare our study to Berk *et al.* (2017) in further details, in particular for what concerns the role of turbulent shear stresses. Unfortunately this is not an easy task, even if the two works provide similar messages on the importance of entrainment. For example, Berk *et al.* (2017) computes entrainment through an arbitrary horizontal line on a fixed length $6h$, for one single value of Re_h. It does not assess the growth rate of the separated shear layer nor the evolution of turbulent shear stresses, which are instead at the core of this work.

Part IV

Mass entrainment through the shear layer

9

Interfaces of the shear layer: choice and detection

Choix et détection des interfaces de la couche cisaillée

Ce chapitre donne les définitions des interfaces instantanées bornant la couche cisaillée, à savoir la TNTI et la RRI, et décrit la manière dont elles sont détectées.

Dans une phase préliminaire, les propriétés statistiques de la TNTI de la couche limite à l'amont sont étudiées à l'aide de mesures au fil chaud (Townsend (1948)). On construit une fonction détecteur Q, définie par Chauhan *et al.* (2014*a*) à partir de l'énergie cinétique turbulente (éq. 9.2). Ensuite, on choisit sur Q un seuil qui discrimine les périodes où le fil chaud était dans l'écoulement turbulent et les périodes où il était dans l'écoulement laminaire (figure 9.1). La fraction de temps passée dans la turbulence est représentée par le facteur d'intermittence γ. Au moins depuis Townsend (1948), on considère que le profil de γ décrit bien la distribution cumulative de la loi de probabilité (indiquée avec l'acronyme anglais *p.d.f.*) de la position de la TNTI. Comme dans Corrsin & Kistler (1955), on trouve que la distribution de γ le long d'une normale à la paroi (à $x/h = -9$) est approximée par une fonction d'erreur (figure 9.2) : la p.d.f. de la TNTI est donc approximativement gaussienne. La p.d.f. est comprise dans l'épaisseur de la couche limite δ. En fait, la position moyenne de la TNTI est $Y_T \approx 0.60\,\delta$ et l'écart type est $\sigma_T \approx 0.12\,\delta$. Ces valeurs sont proches de celles trouvées dans la littérature pour des couches limites turbulentes (tableau 9.1).

Sur les champs PIV, la TNTI est identifiée par un seuil sur le champ d'une énergie cinétique adimensionnée $\tilde{k}$ (éq. 9.3. En suivant l'approche de de Silva *et al.* (2013) et Chauhan *et al.* (2014*c*), le seuil $\tilde{k}_{th}$ est choisi en se basant sur les données PIV de la couche limite incidente, de sorte que la largeur de la p.d.f. de la TNTI corresponde à δ (éq. 9.4). L'algorithme itératif utilisé pour cette opération est détaillé dans la figure 9.8. Une valeur de $\tilde{k}_{th}$ est calculée pour chaque jeu de données des deux rampes, mais $\tilde{k}_{th}$ ne semble pas dépendre de Re_h ou Re_θ (tableau 9.2). La p.d.f. de la TNTI obtenue avec les données PIV est en excellent accord avec celle obtenue à partir des mesures au fil chaud (figure 9.9, figure 9.10 et tableau 9.3). Ensuite, $\tilde{k}_{th}$ est appliqué aux champs PIV du décollement massif. Cette opération est justifiée par le fait que la TNTI est continue, parce qu'il n'y a pas de relaminarisation complète de l'écoulement. De plus, on retrouve les valeurs de $\tilde{k}_{th}$ (au moins comme ordre de grandeur) avec une étude de sensibilité au seuil, effectuée uniquement sur l'écoulement décollé, en s'inspirant des travaux de Prasad & Sreenivasan (1989). Des exemples des TNTI obtenues sur les deux rampes sont présentés dans les figures 9.5 à 9.7. La figure 9.11 montre que les TNTI obtenues semblent être relativement robustes à la résolution de la PIV et à des variations relativement larges de $\tilde{k}_{th}$. Par contre, le bruit de mesure dans les champs larges de la rampe GDR détériore très rapidement la qualité des TNTI détectées avec $\tilde{k}_{th}$ (figure 9.6).

Les RRI instantanées sont identifiées par la condition $u = 0$. La bulle de recirculation instantanée pouvant être composée de plusieurs domaines non connectés, des précautions sont prises pour concaténer tous leurs contours en une interface unique, comprenant des segments de paroi. Le résultat est validé par la

comparaison de la distribution cumulative de la RRI avec les profils du coefficient de *backflow* χ, montrée en figure 9.14.

Dans la partie finale de ce chapitre, nous proposons une technique qui semble pouvoir fournir les TNTI et les RRI instantanées dans un cadre unique. En se basant sur les travaux concernant les *régions à quantité de mouvement uniforme* de Meinhart & Adrian (1995), Kwon *et al.* (2014) et Eisma *et al.* (2015), nous montrons que la bulle de recirculation et l'écoulement irrotationnel peuvent être associés à des régions de la distribution instantanée de la vitesse longitudinale u/U_∞, appelées *modes* (figure 9.15). De ce fait, il est relativement facile de trouver une *vitesse limite* qui marque la frontière de chaque mode et donc une interface séparant chacune des deux régions de l'écoulement de la couche cisaillée. En principe, les vitesses limites sont spécifiques à chaque champ instantané, mais la figure 9.17 montre que leur distribution sur un jeu de données PIV de 2000 images est plutôt étroite : cela suggère que les vitesses limites sont des marqueurs robustes des interfaces de la couche cisaillée décollée. Les figures 9.5 et 9.7 comparent les interfaces obtenues avec cette méthode aux TNTI et aux RRI de la rampe R2, montrant que les résultats sont fondamentalement équivalents, au moins d'un point de vue macroscopique. Dans le cas de la rampe GDR, la pseudo-TNTI identifiée au moyen d'une vitesse limite semble être remarquablement moins déformée par le bruit que la TNTI basée sur $\tilde{k}$. Pour cette raison, dans le cas des jeux de données GDR, les TNTI sont identifiées exclusivement avec la méthode des vitesses limites.

9.1 Introduction

One of the main findings of Part II is the link between size of the recirculation region, intensity of turbulent shear stresses at reattachment and growth rate of the separated shear layer in a large neighbourhood of separation, as well as their dependence on properties of the incoming boundary layer. It was also remarked that entrainment of external fluid drives shear layer growth, while the backflow is one of the dominant features of the region close to reattachment. This being so, it seems now important to gain further insight into the exchanges between the recirculation region and the separated shear layer, and between the latter and the free stream. This is one of the main objectives of Part III of this work, which will do so by computing the mass budget of the separated shear layer and by analysing the involved transfer mechanisms.

As already anticipated, in this work we consider that the mean RRI and the mean TNTI are the lower and the upper boundaries, respectively, of the separated shear layer. In previous sections, the mean TNTI was only invoked as a reference curve, along which local properties of the flow far from the wall were studied: accordingly, only a qualitative definition was given in chapter 5. However, many works have shown that the TNTI has a particular role in transfer problems, so that a thorough definition and an adequate statistical characterisation of the TNTI seem now necessary. Surprisingly, these appear to be open issues for the instantaneous RRI too, even if the mean RRI is a well known, widely considered feature of separated flows. Indeed, improved understanding of the statistical behaviour of the RRI appears to be of great interest, since the size and the shape of the recirculation region vary continuously.

The present chapter addresses the definition of the two instantaneous interfaces. It describes how the TNTI and the RRI are detected on instantaneous PIV fields, prior to their statistical analysis and the investigation of (mean) entrainment. A rich literature exists on the instantaneous TNTI, providing both theoretical underpinning and practical ideas for detection. This is not the case for the instantaneous RRI, that in the past has seldom been considered as a turbulent feature in its own right (interesting numerical examples are reported by Friedrich & Arnal (1990) and Le *et al.* (1997)). Fortunately, the definition of the mean RRI is well known, and can be extended to the detection of instantaneous interfaces with little effort. In spite of their different definitions, both the TNTI and the RRI can be interpreted as constant-property lines and, as such, they are turbulent surfaces in the sense of Pope (1988). Based on this common nature, the final part of this chapter discusses some ideas to investigate the TNTI and the RRI in a single, simple framework.

9.2 TNTI detection

Many strategies have been proposed to detect the TNTI, depending on the characteristics of the flow and the technique chosen to observe it. Single point techniques, such as hot wire anemometry, generally allow to discriminate the turbulent sections of a signal based on a threshold on velocity fluctuations. Historically, these tools provided input to the first important advancements in the understanding of the TNTI (the reader is referred to Corrsin & Kistler (1955) for one impressive example), notwithstanding their relative inability to precisely locate the TNTI in space. In this research, the contribution of hot-wire data to the detection of the TNTI is limited to the investigation of its statistical distribution in the incoming boundary layer, which is discussed in section 9.2.1. Instead, the bulk of TNTI investigations relies on PIV images. With PIV and other image-based techniques, the TNTI is better identified by detecting gradients in a scalar field, or by marking the rotational parts of the flow (Prasad & Sreenivasan (1989), Westerweel *et al.* (2009)). To this end, PIV is often coupled to PLIF. With PLIF, the rotational regions of a flow are contaminated with a fluorescent dye, sensitive to the wavelength of a laser beam. Even though this technique provides high TNTI resolutions, it generally requires adding extra laser units, cameras and wavelength filters to the typical PIV experimental set-up, with increased operative complexity and cost. Moreover, PLIF is usually more reliable if the Schmidt number of the flow is high enough so that the dye diffuses poorly into irrotational regions, which is generally not the case for experiments conducted in air, as far as turbulence is concerned. In this respect, recent works present promising alternatives to PIV/PLIF approaches. For example, Gan (2016) uses different seeding densities to detect the TNTI of a turbulent jet directly from PIV data, with uncertainties and resolutions comparable to those of coupled PIV and PLIF. This solution suppresses the need for PLIF, thus reducing both cost and complexity of the experimental set-up, but it still requires high Schmidt numbers to yield dependable results. To avoid this constraint, some researchers proposed to detect

TNTIs based exclusively on flow properties that can be retrieved from conventional PIV experiments. de Silva *et al.* (2013) and Chauhan *et al.* (2014*c*) show that in turbulent boundary layers the TNTI can be efficiently detected using a two component, turbulent kinetic energy (indicated with $\tilde{k}$) as a passive scalar. This study mainly follows their TNTI detection method, as detailed at § 9.2.2, because it allows to indirectly assess the local entrainment velocity through the interface (see chapter 12 and Philip *et al.* (2014)). However this approach has never been tested on separating/reattaching flows before: then, section 9.2.3 reports a more conventional threshold sensitivity study performed on $\tilde{k}$, that validates the extension of the ideas of de Silva *et al.* (2013) and Chauhan *et al.* (2014*c*) to the separated shear layer under study. Alternatively, Kwon *et al.* (2014) suggest that the TNTI is well approximated by the boundary of a region of uniform momentum, which can be identified simply starting from the probability distribution function of streamwise velocity. This technique (see section 9.4) was considered at a late hour and the implications of its output are not fully assessed in this work. In any case, results are fundamentally consistent with $\tilde{k}$-based TNTIs and allow to overcome unexpected problems encountered in the $\tilde{k}$ distribution over the GDR large field. All in all, TNTIs detected over the separated shear layer were cross checked with three independent techniques, which should insure reliable bases for the analysis of entrainment from the free flow to the separated shear layer.

9.2.1 HW-based TNTI detection: intermittency profiles in the boundary layer

In this work, hot-wire data are used to study the statistical distribution of TNTI position in the incoming boundary layer, at the reference position $x/h = -9$. In turn, this information allows to validate the results of one of the PIV-based TNTI detection method (see § 9.2.2).

Historically, analysis of hot-wire signals provided the first evidences of the existence of the TNTI. In his study of turbulent jets, Corrsin (1943) reported of a *transition* region between the turbulent core of the jets and the field of still fluid, where hot-wire signals appeared to alternate burst of turbulent fluctuations with increasingly long periods of unperturbed motion. Similar observations were made in the wake of a cylinder by Townsend (1948), which ascribed them to the hot-wire being hit by a sharp but instationary and irregular *turbulent front*, separating turbulence from irrotational fluid. Townsend (1948) characterised the resulting intermittent behavior of the signal with an *intermittency factor* (or simply intermittency) γ, which is the fraction of time during which the flow is turbulent. γ represents the probability that the flow is turbulent at a given crossflow position: it is $\gamma = 1$ in the turbulent core of the flow and $\gamma = 0$ in the irrotational, external regions. One of the main interests of γ is that it also represents the cumulative distribution function (c.d.f.) of TNTI position (indicated with C_T). Starting from this information, the TNTI can be characterised in terms of its probability density function (p.d.f., indicated with N_T). In their pioneering work, Corrsin & Kistler (1955) found that in an equilibrated turbulent boundary layer the wall-normal evolution of γ (the so called *intermittency profile*) is well approximated by the error function:

$$C_T = \frac{1}{2}\left[1 + erf\left(\frac{y_T - Y_T}{\sigma_T\sqrt{2}}\right)\right], \tag{9.1}$$

where y_T is the position of the TNTI above the wall and Y_T and σ_T are respectively the mean and the standard deviation of y_T. Then, N_T can be modelled with a normal distribution, centered in Y_T and with standard deviation σ_T. These observations, common to many turbulent flows, were later confirmed by other works (for example Fiedler & Head (1966), Hedley & Keffer (1974*a*) and Chauhan *et al.* (2014*a*)). This property is also verified in the incoming boundary layers of the present experiments, as detailed in the following paragraphs.

Most hot-wire based γ measurement techniques derive from the approach of Townsend (1949), which can be summarised as follows. A suitable detector quantity is chosen, that emphasises turbulent bursts (e.g. velocity fluctuations). Then, a threshold value is set, above which the detector function can be considered turbulent. The detector function is compared to the threshold and hence transformed in an *on-off* binary signal. Finally, segments wherein the binary signal is *on* are counted and compared to the total length of the signal. The reader is referred to the review by Hedley & Keffer (1974*b*) for a discussion of features and limitations of this type of approach. Here we follow a derived criterion by Chauhan *et al.* (2014*a*)), that is an assessment of turbulent kinetic energy. Given a hot-wire signal of streamwise velocity u, velocity fluctuations $u - U_\infty$ are usually much stronger in the turbulent field than in the irrotational one. As such, an

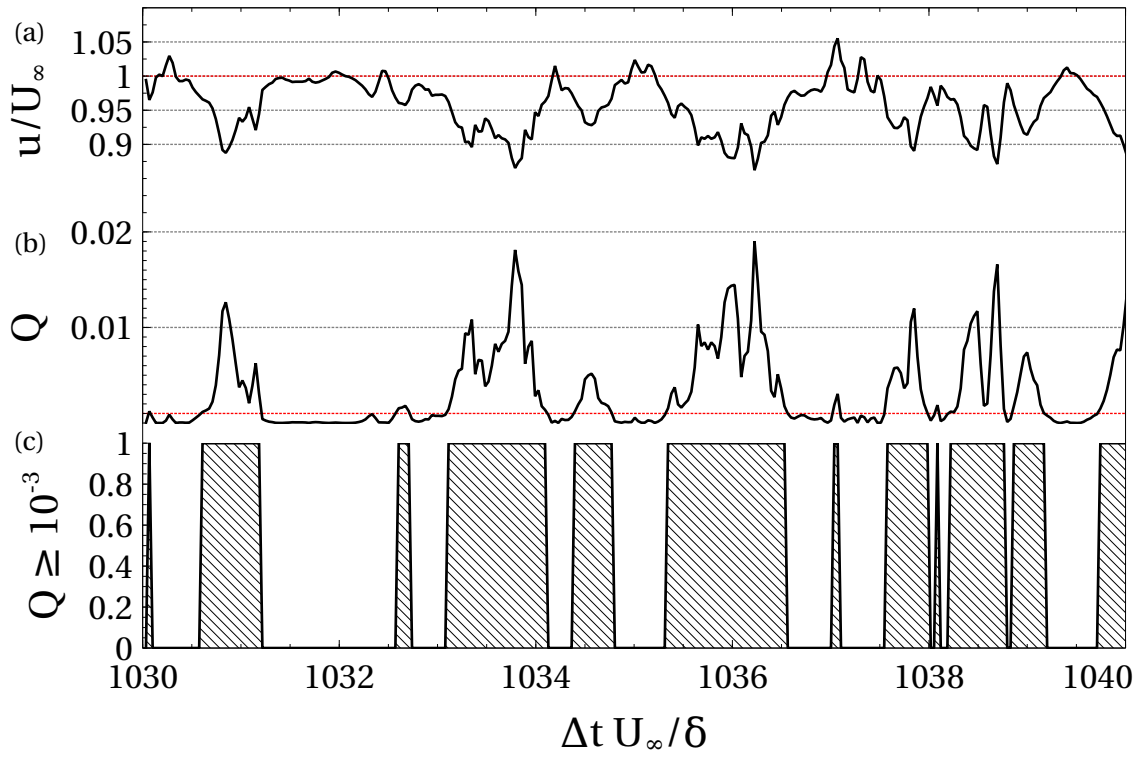

Figure 9.1: A subset of an intermittent hot-wire signal in the incoming boundary layer: (a) u/U_∞; (b) Q; (c) $Q > 1 \times 10^{-3}$, with turbulent periods marked by shaded areas. ····· reference values $u/U_\infty = 1$ and $Q = 1 \times 10^{-3}$.

energy detector function can be defined in the form:

$$Q = [1 - u/U_\infty]^2 . \tag{9.2}$$

Q is essentially zero in the free stream, but highly positive within turbulence. Based on the values of free stream turbulence and on the visual comparison of Q with the original streamwise velocity signals (see figure 9.1), a threshold $Q = 1 \times 10^{-3}$ was chosen to mark the TNTI in both wind tunnels. The resulting boundary layer intermittency profiles are reported in figure 9.2. It appears that intermittency profiles are completely contained within the full boundary layer thickness δ. In most cases they also agree very well with error functions: estimations of Y_T and σ_T can be obtained by least-mean square fitting eq. 9.1 on intermittency data. Table 9.1 shows that both Y_T and σ_T are consistent with values found in comparable past experiments. It is then reasonable to deduce that at $x/h = -9$ the p.d.f. of TNTI position within the boundary layer is gaussian.

9.2.2 PIV-based TNTI detection: turbulent kinetic energy $\tilde{k}$

de Silva *et al.* (2013) and Chauhan *et al.* (2014*c*) used a dimensionless, turbulent kinetic energy $\tilde{k}$ as a passive scalar to mark the position of the TNTI within a turbulent boundary layer, in a fashion that is conceptually equivalent to the hot-wire TNTI detection criterion used by Chauhan *et al.* (2014*a*) (see § 9.2.1). $\tilde{k}$ is defined in percentage of mean free stream energy, as follows:

$$\tilde{k} = \frac{100}{9(U_\infty^2 + V_\infty^2)} \sum_{m,n=-1}^{1} [(u_{m,n} - U_\infty)^2 + (v_{m,n} - V_\infty)^2], \tag{9.3}$$

where U_∞ and V_∞ are respectively the streamwise and the wall-normal components of the local, free-stream velocity.

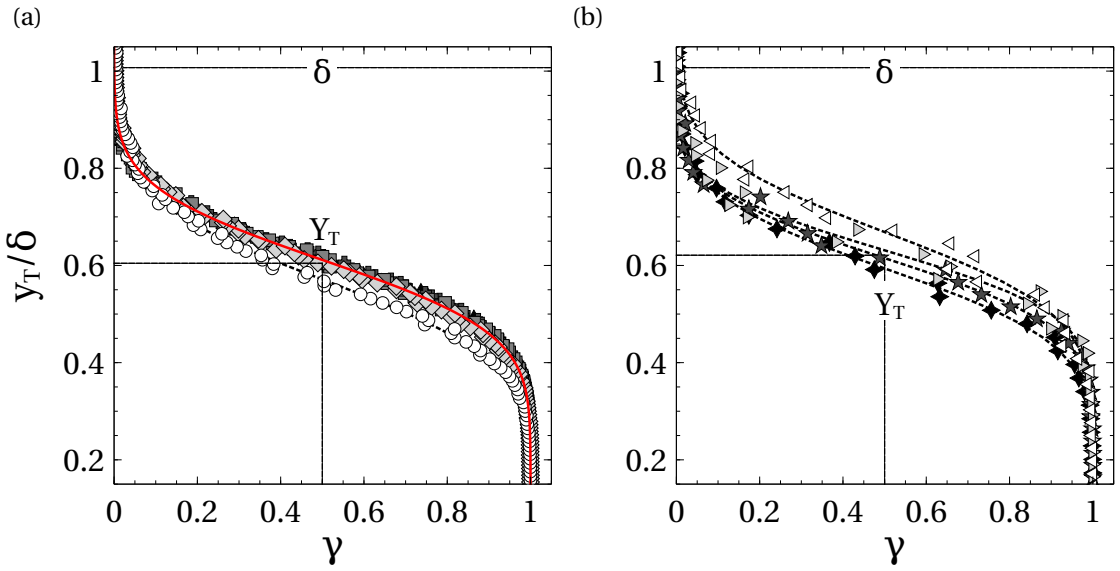

Figure 9.2: Intermittency profiles in the incoming boundary layer. (a) R2 ramp. Symbols: ◯ $Re_h = 3 \times 10^4$; ◇ $Re_h = 4 \times 10^4$; ■ $Re_h = 5 \times 10^4$; ✚ $Re_h = 6 \times 10^4$; ▲ $Re_h = 7 \times 10^4$; for reference, ——— highlights the best fit error function at $Re_h = 5 \times 10^4$. (b) GDR ramp. Symbols: ◁ $Re_h = 10 \times 10^4$; ▷ $Re_h = 13.3 \times 10^4$; ★ Re_h =20×10^4; ✦ $Re_h = 26.7 \times 10^4$; ····· best-fit error functions.

	$Re_h/10^4$	Re_τ	Y_T/δ	σ_T/δ
Corrsin & Kistler (1955)	-	<2000	0.80	0.16
Hedley & Keffer (1974*a*)	-	5100	0.75	0.24
Chauhan *et al.* (2014*a*)	-	8000 to 20 000	$\approx 2/3$	$\approx 1/9$
Chauhan *et al.* (2014*c*)	-	2700	0.64	0.13
	-	22000	0.67	0.11
Present study R2	3	1300	0.57	0.13
	4	1310	0.61	0.12
	5	1750	0.61	0.12
	6	2130	0.62	0.12
	7	2646	0.61	0.12
Present study GDR	10	874	0.67	0.13
	13.3	1128	0.63	0.10
	20	1490	0.62	0.11
	20.7	1883	0.59	0.12

Table 9.1: Comparison of HW-based statistics of TNTI position in the boundary layer.

In eq. 9.3, turbulent kinetic energy is locally averaged on a square kernel to smooth out possible PIV noise. The side of the kernel is equal to 3 correlation windows and the indexes m and n allow to iterate on the two dimensions of the kernel. For the sake of clarity, the dependencies on (x) of U_∞ and V_∞ and on (x, y) of $u_{m,n}$ and $v_{m,n}$ were omitted. Mind that in the original works of de Silva *et al.* (2013) and Chauhan *et al.* (2014*c*) it is $\partial U_\infty/\partial x \approx 0$ and $V_\infty = 0$. Since velocity fluctuations are much more intense in turbulent regions, $\tilde{k}$ is discontinuous at the TNTI: it is practically zero on the external side of the TNTI, but it is sizeable within it. Then, a suitable threshold value $\tilde{k}_{th}$ can efficiently identify the TNTI. de Silva *et al.* (2013) and Chauhan *et al.* (2014*c*) proposed a robust approach to select $\tilde{k}_{th}$ in turbulent boundary layers, based on statistics of the TNTI. As discussed at § 9.2.1, y_T can be approximated by a gaussian distribution, with the entire N_T included within the thickness of the boundary layer δ (see figure 9.3). This being so, de Silva *et al.* (2013) and Chauhan *et al.* (2014*c*) retained a $\tilde{k}_{th}$ value for which N_T is normal and the following criterion is fulfilled:

$$Y_T + 3\sigma_T \approx \delta, \tag{9.4}$$

where δ is estimated with the composite boundary layer profile conceived by Chauhan *et al.* (2009) (see § 7.3.4).

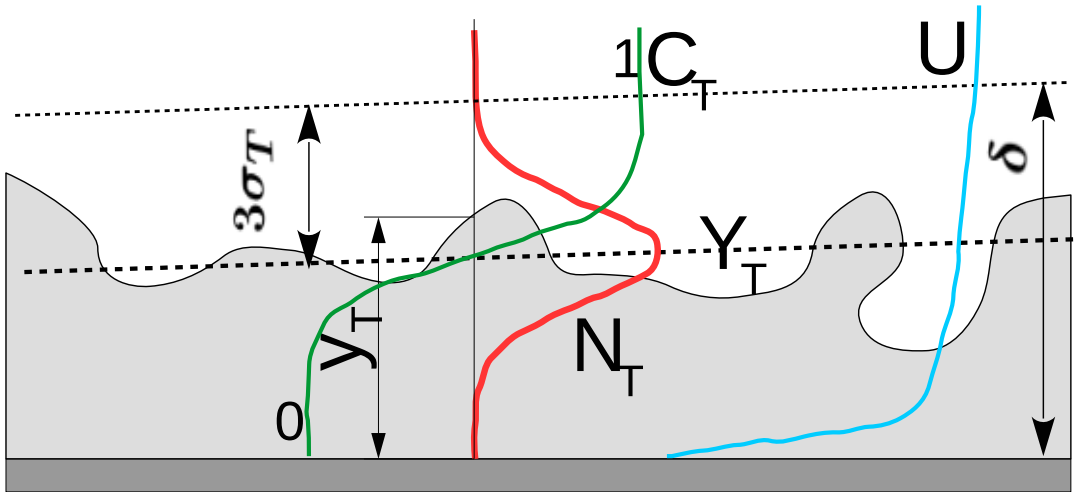

Figure 9.3: Schematic view of the TNTI distribution in the boundary layer. Symbols: —— N_T; —— C_T; —— U profile. The gray shade indicates the turbulent region of the flow.

This TNTI detection criterion is attractive because it can be applied with virtually no extra experimental cost compared to usual PIV measurements, and with reasonable extra post-processing. Its obvious drawback is that eq. 9.4 cannot be directly utilized on the separated shear layer. An equivalent convergence criterion could not be established simply, although some similarities exist between δ and δ_ω. Hence, $\tilde{k}_{th}$ was computed on the boundary layer images provided by the auxiliary fields and then applied to the other PIV fields, to detect the TNTI above the separated shear layers. This operation is justified by the fact that the TNTI is a continuous boundary unless complete relaminarisation occours, which is not the case for the experiments presented in this work (see for example figure 8.15 and figure 8.16). A successive threshold sensitivy study on velocity fields of the R2 ramp also quantitatively validated this choice (see 9.2.3). Examples of instantaneous TNTIs detected in such way are reported in figures 9.4 to 9.7. Figure 9.4 shows the instantaneous TNTI over the boundary layer of the R2 ramp, both on the field of $\tilde{k}$ and on the field of streamwise velocity u. Similar interfaces were obtained for the GDR ramp and are not reported. The TNTI is convoluted by large bulges and valleys, and it may show multiple positions above the wall for the same streamwise position. However, finite PIV resolution (and to some extent the local averaging of $\tilde{k}$) has a smoothing effect on instantaneous TNTIs: wrinkles that are smaller than a cut-off value related to λ_c (see § 4.3.5) are not resolved. Comparable, relatively smooth TNTIs are found on the large fields (figure 9.5 and figure 9.6 for the R2 ramp and the GDR ramp, respectively), but higher resolution allow to observe much smaller wrinkles on the R2 detailed field (figure 9.7).

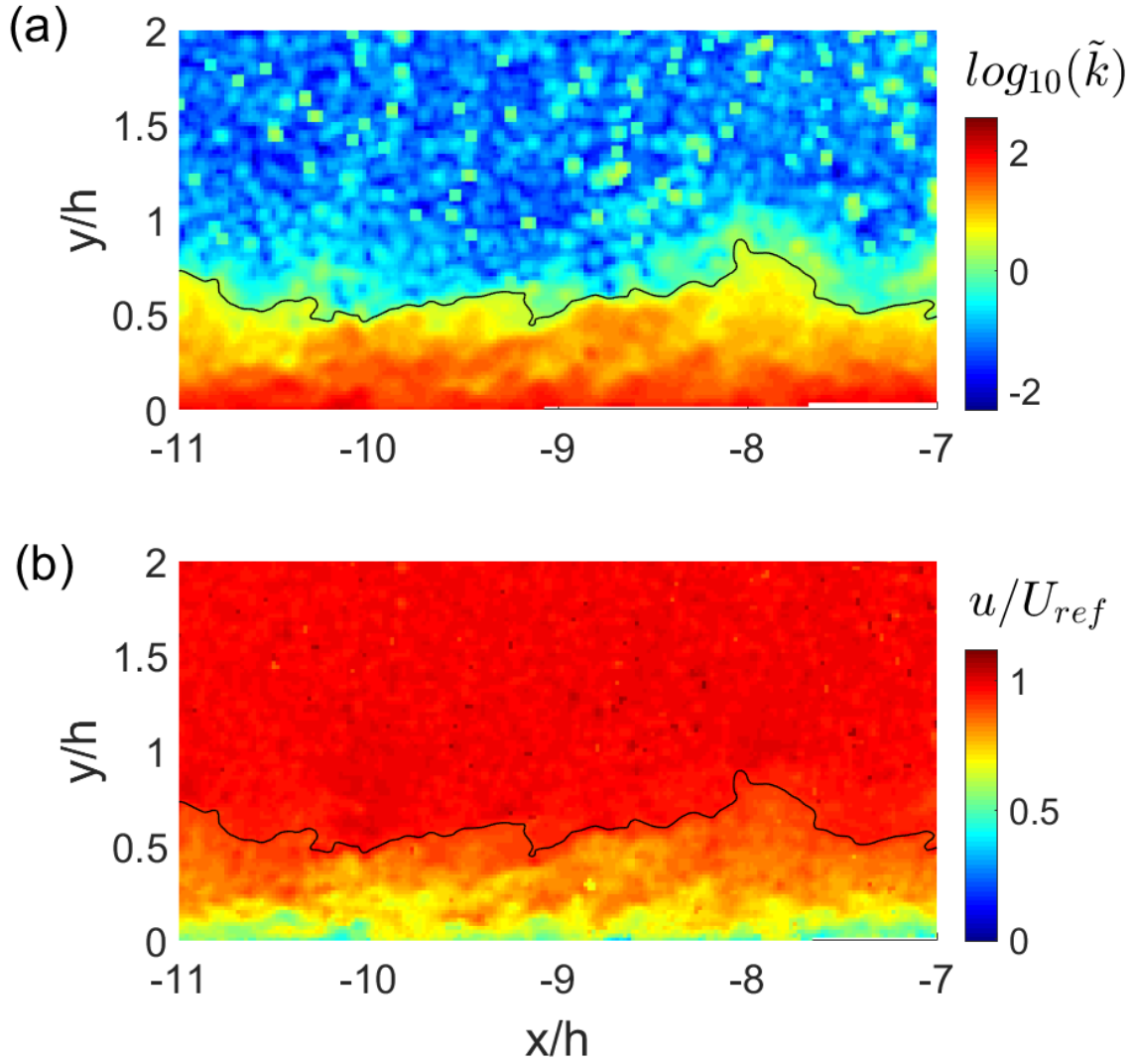

Figure 9.4: Instantaneous TNTI detected on the incoming boundary layer of the R2 ramp, at $Re_h = 4 \times 10^4$ ($U_\infty = 20\,\mathrm{m\,s^{-1}}$), shown on (a) the $\tilde{k}$ field and (b) the streamwise velocity field.

The threshold selection criterion of de Silva *et al.* (2013) and Chauhan *et al.* (2014*c*) was implemented as summarized by the flow chart of figure 9.8. Firstly, instantaneous $\tilde{k}$ fields are computed from PIV velocity fields. Secondly, $\tilde{k}_{th}$ is identified iteratively, as the first value that verifies eq. 9.4 within a given tolerance tol. Then, the instantaneous TNTI is detected on each $\tilde{k}$ field and stored for processing. Finally, the consistency of the PIV-based N_T with a normal distribution is verified. The following sections provide further details on each of these steps.

9.2.2.1 Computation of $\tilde{k}$ fields

Instantaneous $\tilde{k}$ fields are computed from PIV velocity fields by directly applying eq. 9.3. Values of $U_\infty(x)$ and $V_\infty(x)$ are obtained by averaging the 20 most external (i.e. at the highest y positions) points of the mean velocity field for each value of x. Then, they are replicated along y (e.g. with Matlab command *repmat*) as to match the size of u and v. Local averaging is performed by convoluting the unfiltered energy field with the 3×3 square kernel (Matlab command *conv2*). The edges of each field are zero-padded during convolution and successively trimmed to conserve the size of the original velocity fields.

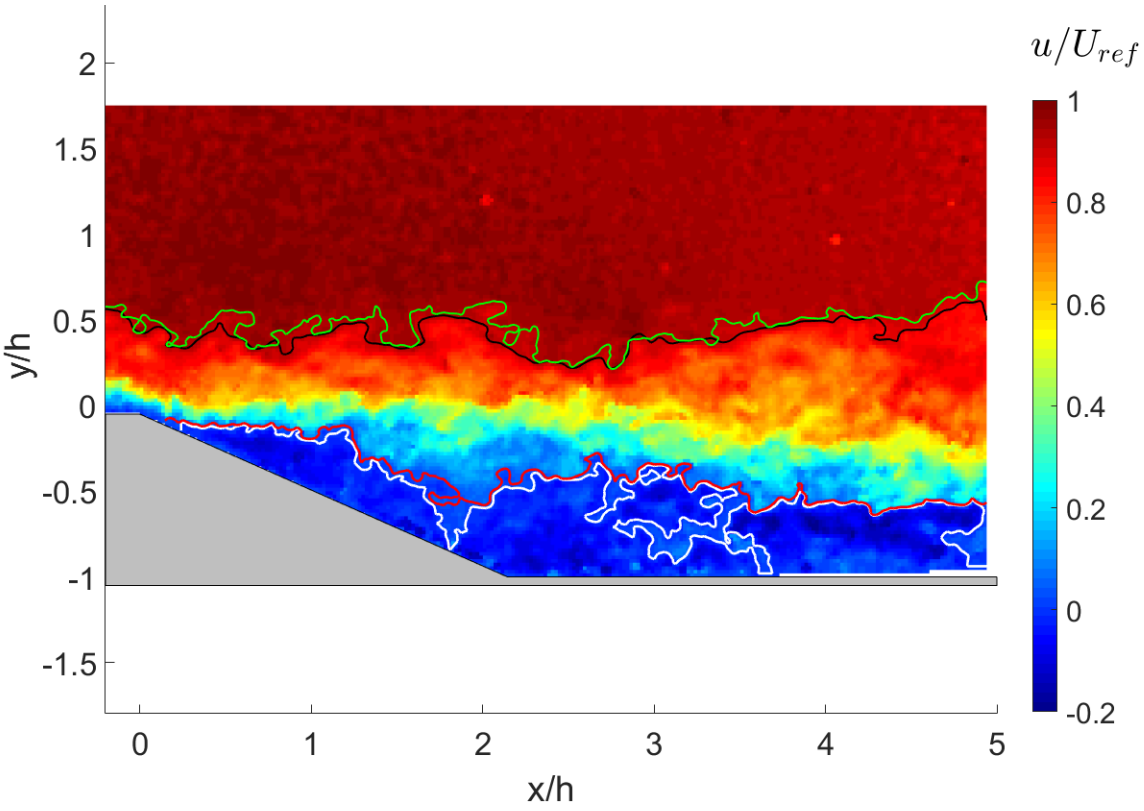

Figure 9.5: Instantaneous TNTI detected on the separated shear layer of the R2 ramp, at $Re_h = 4 \times 10^4$ ($U_\infty = 20\,\mathrm{m\,s^{-1}}$). Symbols: ——— TNTI detected as $\tilde{k}_{th}$ isoline; ——— (white online) RRI detected as $u = 0$ isoline; ——— TNTI and ——— RRI as boundaries of regions of uniform momentum.

9.2.2.2 Iterative computation of the threshold value $\tilde{k}_{th}$

The iterative computation of $\tilde{k}_{th}$ can be assimilated to the minimization of the residual of eq. 9.4, that is:

$$\epsilon_T = 1 - \frac{(Y_T + 3\sigma_T)}{\delta}. \tag{9.5}$$

This minimization problem is solved with a classical bisection algorithm (see figure 9.8), starting from an educated guess of a range $\left[\tilde{k}_{low}, \tilde{k}_{up}\right]$ that should include $\tilde{k}_{th}$. At each iteration, a new value of $\tilde{k}$ is tested, chosen as:

$$\tilde{k}_{test} = \frac{\tilde{k}_{up} + \tilde{k}_{low}}{2}. \tag{9.6}$$

Based on $\tilde{k}_{test}$, instantaneous isocontours are detected on each $\tilde{k}$ field with Matlab function *contourc*, filtered (see § 9.2.2.3) and used to compute Y_T and σ_T. If $|\epsilon_T| > tol$, $\tilde{k}_{test}$ is used to update one value among $\tilde{k}_{low}$ and $\tilde{k}_{up}$, depending on the sign of ϵ_T. Then, a new iteration is launched, and so on untill the convergence criterion is met or a maximum number of iteration is reached. Table 9.2 reports the converged $\tilde{k}_{th}$ values obtained for both ramps, at each tested value of Re_h, with $tol = 10^{-4}$ and a maximum of 20 iterations. Changes in the converged $\tilde{k}_{th}$ appear to be negligible at least for tol within 10^{-5} and 10^{-3}.

9.2.2.3 Filtering of instantaneous TNTIs

It must be stressed that the real TNTI is a three-dimensional surface, of which PIV-based detection only gives access to a section (see also § 4.3.6 for a general discussion of this point). A consequence of this limitation is that 3D protrusions of the TNTI into the irrotational fluid are captured as islands of vorticity in the free

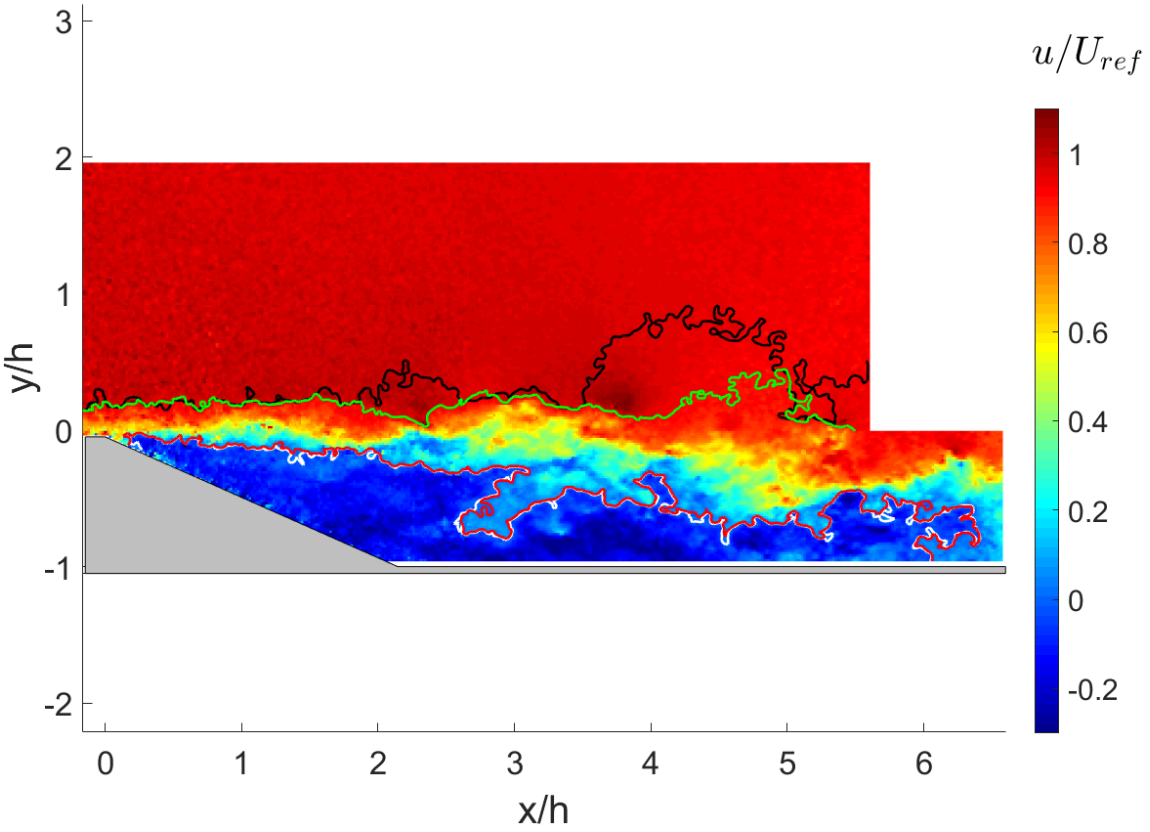

Figure 9.6: Instantaneous TNTI detected on the separated shear layer of the GDR ramp, at $Re_h = 13.3 \times 10^4$ ($U_\infty = 20\,\mathrm{m\,s^{-1}}$). Symbols as in figure 9.5.

	R2 ($h = 30\,\mathrm{mm}$)					GDR ($h = 100\,\mathrm{mm}$)			
$Re_h/10^4$	3	4	5	6	7	10	13.3	20	26.7
$\tilde{k}_{th}$	0.31	0.45	0.36	0.36	0.34	0.25	0.18	0.21	0.17

Table 9.2: Values of $\tilde{k}_{th}$ at different Re_h. Mind that images were correlated at $32 \times 32\,\mathrm{px}^2$ for the GDR ramp, $16 \times 16\,\mathrm{px}^2$ for the R2 ramp.

stream. Conversely, bubbles of external fluid within turbulence are seen as isolated irrotational pockets. The 2D approach of the present work is not relevant to investigate these regions, since no information on their geometry in the azimuthal direction is available. Hence, following Chauhan *et al.* (2014*c*) among others, all islands of rotational (resp. irrotational) fluid that are found in the free stream (resp. in the turbulent flow) are filtered out. This can be done simply, for example by selecting the longest $\tilde{k}_{th}$ isocontour among those detected on an instantaneous $\tilde{k}$ field. Since in our experiments the TNTI does not interact with any wall (see for example figure 9.2 and the TNTI distributions at § 9.2.2.4), this condition is usually sufficient to identify a continuous TNTI outline that divides each $\tilde{k}$ field in two disjoint domains (Borrell & Jiménez (2016)). An equivalent approach was also adopted by Mistry *et al.* (2016).

Admittedly, filtering irrotational bubbles within turbulence prevents any reliable assessment of the large-scale entrainment mechanism called *engulfment*. The relative weight of engulfment and nibbling is, in general, an open problem and, to some extent, a matter of definitions (Borrell & Jiménez (2016)). In many flows, as turbulent jets (Westerweel *et al.* (2005), Taveira *et al.* (2013)) and in particular turbulent boundary layers (Borrell & Jiménez (2016)) the contribution of engulfment to total entrainment was found to be negligible, compared to the one due to nibbling. In other flows like wakes (Bisset *et al.* (2002)) and free shear layers (Brown & Roshko (1974), Dimotakis & Brown (1976)), engulfment seems to predominate. It is

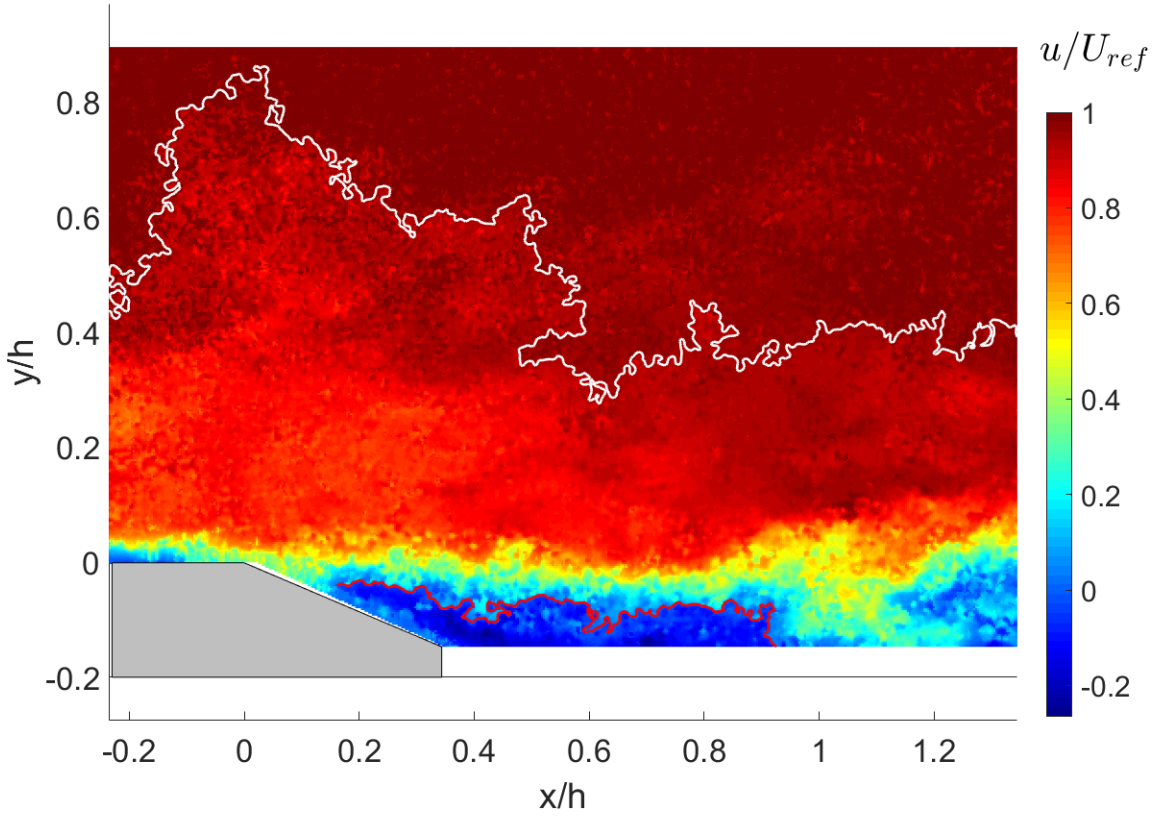

Figure 9.7: Instantaneous TNTI detected in the detailed field of the R2 ramp, at $Re_h = 4 \times 10^4$ ($U_\infty = 20\,\mathrm{m\,s^{-1}}$). Symbols: ——— (white online) TNTI detected as $\tilde{k}_{th}$ isoline; ——— RRI detected as $u = 0$ isoline.

hard to speculate on the prevailing mechanism in the present massively separated flow, since it is influenced by both the incoming boundary layer and the free-like shear layer (see § 8.4). However, this is not a major problem in chapter § 11, because engulfment and nibbling are not relevant to the investigation of mean mass fluxes. The impact on the small-scale analysis of chapter 12 is also expected to be mild. Indeed, it will be shown in chapter 10 that the TNTI keeps the characteristics it has in the incoming boundary layer on the entire extent of the detailed field of the R2 ramp: this being so, it seems reasonable to assume that in this region nibbling will still be the main entrainment mechanism at the TNTI.

9.2.2.4 TNTI distribution in the boundary layer

The computation of $\tilde{k}_{th}$ holds on the assumption that the position of the TNTI above the wall follows a normal distribution (Corrsin & Kistler (1955) among others). This property was already verified with hot-wire data in section 9.2.1, but to assess $\tilde{k}_{th}$ it is important to also test the distribution of PIV-detected instantaneous TNTIs. Figure 9.9 and figure 9.10 show the PIV-based statistical distributions of the TNTI in the incoming boundary layers of the R2 ramp and of the GDR ramp, respectively. N_T and C_T are obtained from all available values of y_T, normalised on the local boundary layer thickness δ. In both cases, N_T is qualitatively similar to a gaussian distribution, centered on $y/\delta \approx 0.6$ to 0.67 ($U/U_\infty \approx 0.95$). As for C_T, it agrees well with γ profiles obtained with hot-wire data, and accordingly with eq. 9.1. To provide a more quantitative assessment, Y_T, σ_T, the skewness coefficient $Sk_T = \mu_{T3}/{\mu_{T2}}^{3/2}$ and the kurtosis coefficient $Kt_T = \mu_{T4}/{\mu_{T2}}^2$ are reported in table 9.3. In these expressions, $\mu_{Tn} = E\left(y_T - E\left(y_T\right)\right)^n$ is the n^{th} central moment of y_T and E is the expected value. At all available Re_h, Y_T and σ_T are consistent with hot-wire estimations of table 9.1 and with Chauhan *et al.* (2014*c*). To the best of our knowledge, higher statistical moments of N_T are not available in the main corpus of works on TNTI. However values of

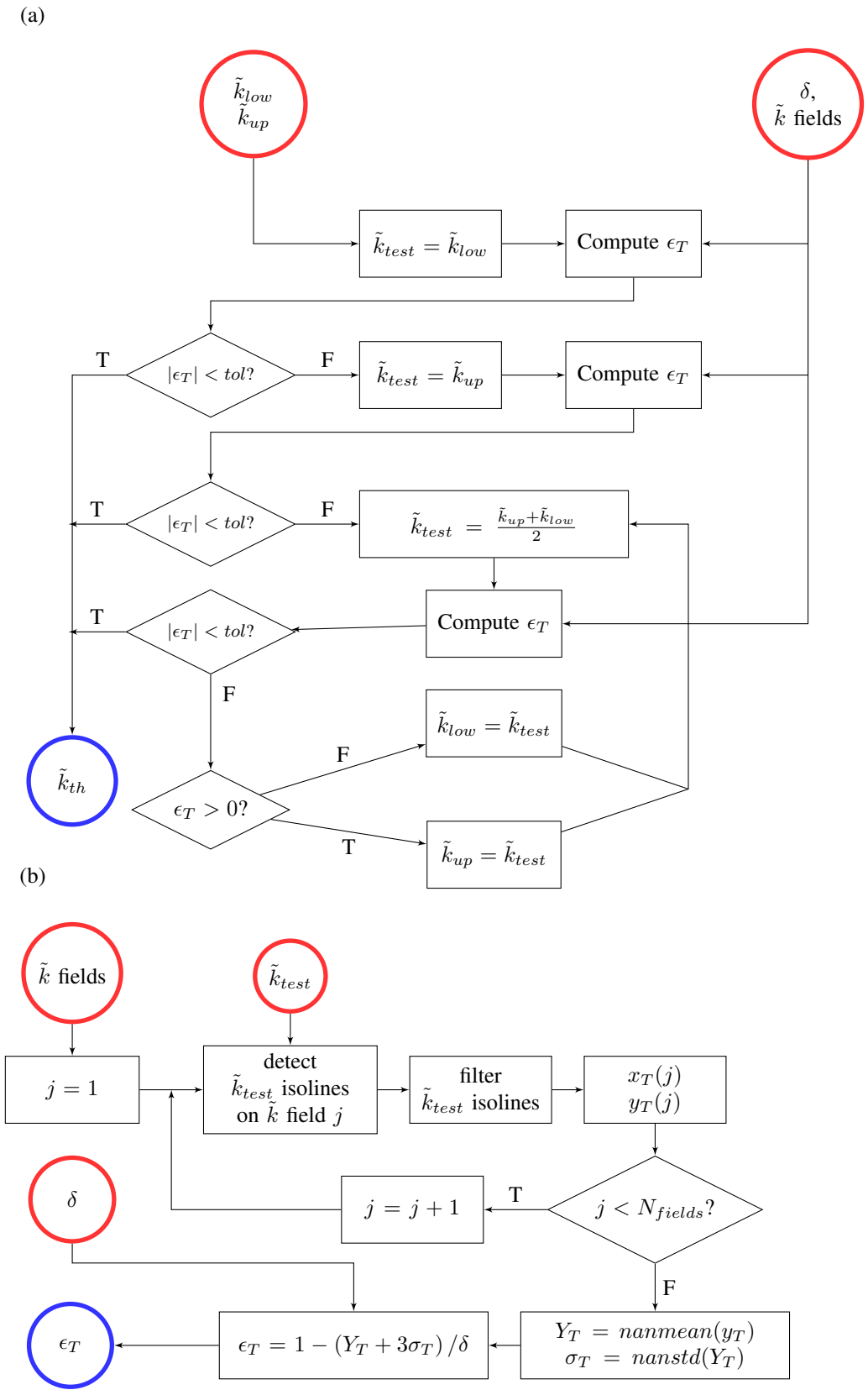

Figure 9.8: Flow charts of (a) $\tilde{k}_{th}$ computation algorithm; (b) block *Compute* ϵ_T, which computes the residual ϵ_T of eq. 9.4. Red circles mark input, blue ones mark output.

Sk_T are, in most cases, reasonably close to 0, which is characteristic of normal distributions. As for Kt_T, Westfall (2014) reminds that its value is essentially determined by the tails of the distribution. In this respect, Corrsin & Kistler (1955) observed that the tails of the TNTI distribution deviate from a normal curve. Tail deviations can also be found in the p.d.f.s reported in many later TNTI studies, for example in Westerweel *et al.* (2009) and Chauhan *et al.* (2014*c*). This being so, differences with respect to the value expected for a normal distribution (i.e. $Kt_T = 3$) are not too surprising. On the contrary, values of Kt_T observed on the R2 ramp suggest very good agreement with a normal distribution. As for the GDR ramp, higher Kt_T deviations are probably due to the presence of outliers. For example, at $Re_h = 13.3 \times 10^4$ it is $C_T(\delta) = 0.992$, i.e. $0.8\,\%$ of TNTI points lies outside of the estitmated δ, in comparison to $C_T(\delta) = 0.999$ obtained at $Re_h = 4 \times 10^4$. The higher number of outliers might in part be a consequence of lower resolution, that increases the minimum distance between resolved TNTI points. In any case, if Kt_T is computed from a subsample $y_T \leq 1.1\delta$ (where a $10\,\%$ tolerance is taken on boundary layer thickness), corrected Kt_T^c values that are obtained are close to 3. A similar correction can be applied to the values of Sk_T (indicated with Sk_T^c) over the GDR ramp. All in all, the PIV-based form of N_T appear to be well approximated by a normal distribution, and the computed $\tilde{k}_{th}$ are acceptable. [1]

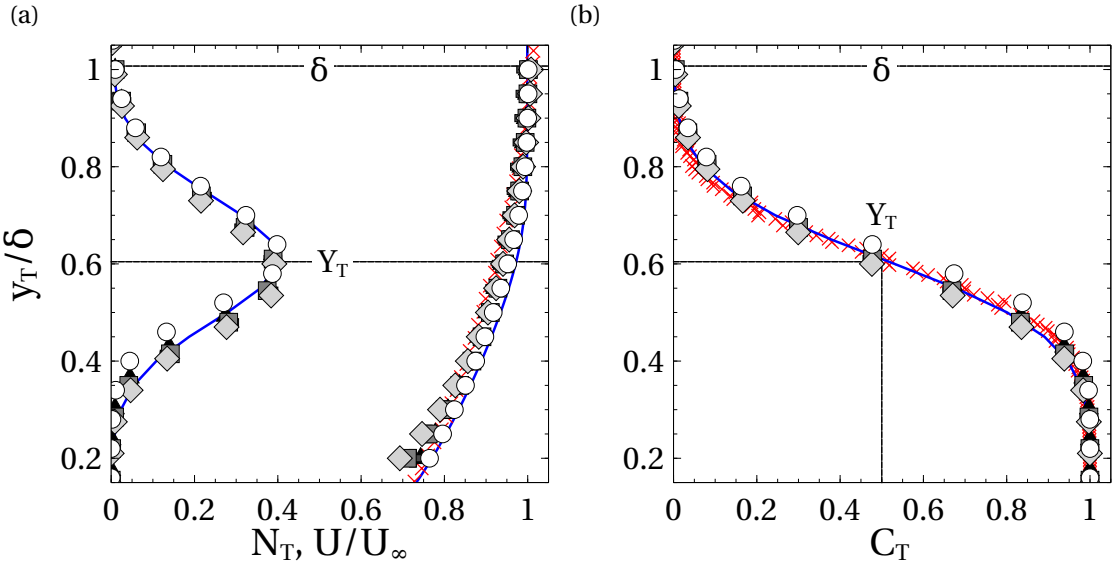

Figure 9.9: Statistical properties of the TNTI distribution in the incoming boundary layer of the R2 ramp. (a) p.d.f. N_T of y_T. Streamwise velocity profiles are also reported for reference. (b) c.d.f. C_T of y_T. Symbols: ◯ $Re_h = 3 \times 10^4$; ◇ $Re_h = 4 \times 10^4$; ■ $Re_h = 5 \times 10^4$; ✚ $Re_h = 6 \times 10^4$; ▲ $Re_h = 7 \times 10^4$; × velocity and intermittency profiles at $Re_h = 5 \times 10^4$, obtained from hot-wire signals; —— reference curves for (a) the p.d.f of a normal distribution and the streamwise velocity profile from DNS of Schlatter & Örlü (2010) ($Re_\theta = 3270$); (b) c.d.f. of a normal distribution.

9.2.2.5 Considerations on robustness of $\tilde{k}_{th}$

Although the choice of $\tilde{k}_{th}$ is data-driven and consistent with experimental conditions (in particular Re_h), no particular trend is found with respect to Re_h. Table 9.2 shows that in most cases one can put $\tilde{k}_{th} \approx 0.20$ on the GDR ramp and $\tilde{k}_{th} \approx 0.35$ on the R2 ramp. These $\tilde{k}_{th}$ values are of the same order of magnitude as the one reported by de Silva *et al.* (2013) and Chauhan *et al.* (2014*c*) (≈ 0.12). Even though exact quantitative comparison with such different experiments seems inappropriate, this element is reassuring if one keeps in mind that the wind tunnels at Prisme Laboratory and the facility used in those studies have comparable levels

[1] It is pointed out that N_T fails common normality tests as the Kolmogorov-Smirnov test (Massey (1951)) or the Jarque-Bera test (Jarque & Bera (1987)). However, it seems that these statistical tools might be too stringent in the framework of this discussion, so that the heuristic assessment utilized above was preferred.

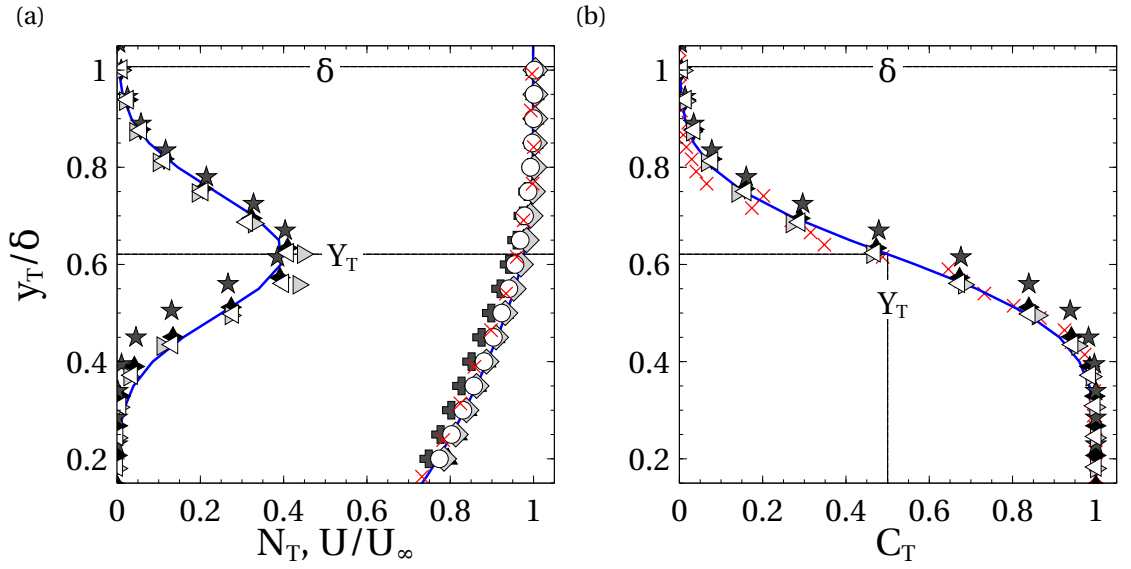

Figure 9.10: Statistical properties of the TNTI distribution in the incoming boundary layer of the GDR ramp. (a) p.d.f. N_T of y_T and U/U_∞ velocity profiles. (b) c.d.f. C_T of y_T. Symbols: $\triangleleft$ $Re_h = 10 \times 10^4$; $\triangleright$ $Re_h = 13.3 \times 10^4$; $\bigstar$ $Re_h = 20 \times 10^4$; $\blacklozenge$ $Re_h = 26.7 \times 10^4$; $\times$ velocity and intermittency profiles at $Re_h = 20 \times 10^4$, obtained from hot-wire signals. Other symbols as in figure 9.9.

of free stream turbulence and PIV noise. Scatter of threshold values, for example at $Re_h = 4 \times 10^4$, appears to be due to slightly different levels of PIV noise and to the quality of the PIV fields in general. Statistics of TNTI position presented in table 9.3 seem just weakly sensitive to these issues, suggesting that noise mostly affects the value of $\tilde{k}_{th}$, rather than the position of the detected TNTI. PIV resolution has a sizeable effect on the value of $\tilde{k}_{th}$: for example, in the case of the R2 ramp a reduction of 30 % is observed if the size of the PIV correlation window is increased from $16 \times 16\,\mathrm{px}^2$ to $48 \times 48\,\mathrm{px}^2$. This seems to be due to the higher signal to noise ratio produced by larger correlation windows. In any case, instantaneous TNTIs prove to be qualitatively robust to resolution and more in general to the choice of $\tilde{k}_{th}$ (see figure 9.11). This supports the choice of also applying the values of $\tilde{k}_{th}$ computed on the auxiliary field to the finer images of the detailed field, and allows comparison between the latter and the large field.

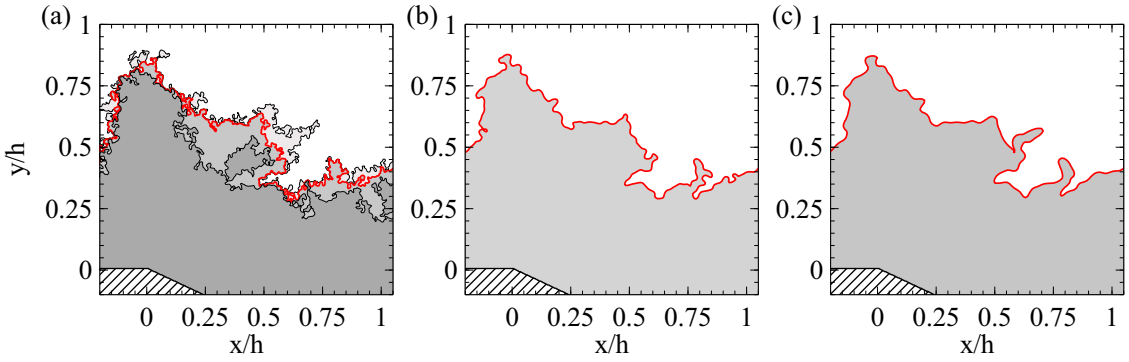

Figure 9.11: Instantaneous TNTI detected on the R2 detailed field at $Re_h = 5 \times 10^4$ (———), at different spatial resolutions. (a) $\Delta/h = 6.4 \times 10^{-3}$ ($16 \times 16\,\mathrm{px}^2$). The grayscale highlights the evolution of the detected turbulent region if the threshold value is tuned within $\tilde{k}_{th} \pm 50\,\%$. Darker shades of gray are used for higher threshold values; (b) $\Delta/h = 1.3 \times 10^{-2}$ ($32 \times 32\,\mathrm{px}^2$); (c) $\Delta/h = 1.9 \times 10^{-2}$ ($48 \times 48\,\mathrm{px}^2$).

	$Re_h/10^4$	Re_τ	Y_T/δ	σ_T/δ	Sk_T	Sk_T^c	Kt_T	Kt_T^c
Chauhan *et al.* (2014*c*)	-	14500	0.67	0.11	-	-	-	-
Present study R2	3	1300	0.64	0.12	0.36	-	3.32	-
	4	1310	0.60	0.13	0.34	-	3.12	-
	5	1750	0.61	0.13	0.36	-	3.12	-
	6	2130	0.61	0.13	0.38	-	3.17	-
	7	2646	0.62	0.12	0.34	-	3.16	-
Present study GDR	10	874	0.62	0.13	0.65	0.32	6.43	3.58
	13.3	1128	0.62	0.13	1.83	0.34	18.57	3.20
	20	1490	0.67	0.11	0.48	0.23	5.64	3.10
	20.7	1883	0.63	0.12	0.80	0.25	9.09	3.00

Table 9.3: Comparison of PIV-based statistics of TNTI position in the boundary layer. $Sk_T = \mu_{T3}/{\mu_{T2}}^{3/2}$ and $Kt_T = \mu_{T4}/{\mu_{T2}}^2$ are the skewness and the kurtosis of the TNTI distribution N_T, respectively, and $\mu_{Tn} = E\left(y_T - E\left(y_T\right)\right)^n$ is the n^{th} central moment of y_T. Expected values for a normal distribution are $Sk_T = 0$ and $Kt_T = 3$. On the GDR ramp, corrected values are obtained by computing Sk_T^c and Kt_T^c on $y_T \leq 1.1\delta$ exclusively.

9.2.2.6 Effects of finite PIV resolution on detected instantaneous TNTIs

Small wrinkles have a primary role in the local, instantaneous transfer of fluid quantities (Westerweel *et al.* (2009), Chauhan *et al.* (2014*c*)), so that it is important to resolve them to correctly assess instantaneous entrainment. Unfortunately, PIV datasets available for this study are under resolved with respect to the smallest time and spatial scales of the flow (see 4.3.5) and direct investigation of instantaneous fluxes is impossible. Indirect, partial solutions to this problem are discussed at § 12.3. In any case, the investigation of transfer through the mean interfaces of the shear layer (see chapter 11) should not be too impacted by finite PIV resolution.

9.2.2.7 A note on the GDR large field

Surprisingly, the $\tilde{k}$-based detection of TNTIs on the GDR large field was not as reliable as in the case of the R2 ramp. Figure 9.6 shows a representative example of detected TNTIs: the interface features unexpected, large *bursts* toward the free flow for x/h within 2 to 2.5 and, more evidently, x/h within 4 to 5. The physical nature of these bursts is questionable. Indeed, the GDR data appears to be very noisy in the free stream, which might significantly corrupt the distribution of turbulent fluctuations and consequently cause artificial *spills* of $\tilde{k}$ into the free stream (for comparison, see the distribution of k in figure 5.5). Such high levels of noise are probably the effect of an image-warping processing (applied before PIV data were made available for this project), of poor illumination of the most downstream half of the flow, or both. TNTI bursts are common enough to produce a mean TNTI that compares poorly to the R2 large field (see § 10.2.1.2), and that does not agree well with other, related features of the GDR flow as the streamwise evolution of θ_{SL} and δ_ω (see 8.2). This being so, on the GDR large field TNTIs were detected with the alternative approach described at § 9.4[1]. As it will be shown in the following chapters, this solution yields results that appear consistent within the GDR flow and with the R2 flow at least up to $x/h \approx 4.5$.

[1] A threshold sensitivity study was avoided because it also seemed exposed to the effects of strong noise.

9.2.3 Threshold sensitivity of the $\tilde{k}$ field

The detection method discussed at § 9.2.2 was cross checked independently of boundary layer properties, by means of a threshold sensitivity study on $\tilde{k}$ performed on the PIV datasets recorded on the R2 ramp. The central idea is that (at least some) properties of the *detected* turbulent field are functions of the *tested* threshold value, and might show a change in behavior when the optimal value is crossed. Prasad & Sreenivasan (1989) developed one such threshold sensitivity approach for detecting the TNTI on PLIF images, which is still largely utilized (e.g. Westerweel *et al.* (2002), Westerweel *et al.* (2009), Anand *et al.* (2009)). Given a flow quantity Q which features a sharp change across the TNTI, Q^+ is the average of all points where Q is above an arbitrary threshold. In some flows, the evolution of Q^+ in function of the chosen threshold shows one sharp change of slope at a value that adequately identifies the TNTI. In the original work of Prasad & Sreenivasan (1989), Q is, quite naturally, the intensity of the light reflected by the fluorescent dye. However, Anand *et al.* (2009) applied this technique to other flow quantities, including vorticity and instantaneous streamwise velocity. They obtained different instantaneous TNTIs, but interface statistics were shown to be independent of the flow quantity used for detection. These results allow to apply the same technique to $\tilde{k}$ with good confidence, in order to obtain alternative estimations of $\tilde{k}_{th}$. Firstly, a set of candidate threshold values $\tilde{k}^*$ is chosen. Secondly, $\tilde{k}^+$ is independently computed on $\tilde{k}^*$ for each PIV image within a dataset. Then, all $\tilde{k}^+$ curves are ensemble averaged to smooth noise out. Finally, $\tilde{k}_{th}$ is chosen at a value among $\tilde{k}^*$ for which $\tilde{k}^+$ changes of slope. Figure 9.12 reports one example of $\langle\tilde{k}^+\rangle$, obtained in the incoming boundary layer of the R2 ramp, at $Re_h = 5 \times 10^4$. The curve changes of slope twice: a first *elbow* is at $\tilde{k}^* \approx 0.08$, while a second one falls in a reassuring range between 0.3 to 0.4. This difference with respect to the jets investigated by Prasad & Sreenivasan (1989), where Q^+ showed only one change of slope, is not too surprising, because their jet was surrounded by still fluid and PLIF images were much more contrasted than our energy fields. The first elbow cannot represent the RRI, because it corresponds to a value of $\tilde{k}^+$ that is lower than (and hence external to) $\tilde{k}_{th}$. It is thought that the first elbow in our datasets might be due to the transition from the truly unperturbed external flow, where velocity fluctuations are of the order of the residual turbulence of the test section, to regions where stronger irrotational velocity fluctuations exist, induced by the interaction with turbulence. The second elbow should then correspond to the TNTI. In this respect, a straightforward choice of $\tilde{k}_{th}$ is the $\tilde{k}^*$ that corresponds to the intersection of the two tangents to $\langle\tilde{k}^+\rangle$ around this elbow (shown in figure 9.12). Alternatively, Prasad & Sreenivasan (1989) suggests to adopt the zero crossing of the second derivative of $\langle\tilde{k}^+\rangle$ as optimal threshold value. In our datasets, $\nabla^2\left(\langle\tilde{k}^+\rangle\right)$ does not seem to cross the zero line at points that are significant to the detection of the TNTI (see figure 9.13). However, $\langle\tilde{k}^+\rangle$ appears close to a straight line within turbulence, so that $\nabla^2\left(\langle\tilde{k}^+\rangle\right)$ should tend to zero for high enough $\tilde{k}^*$. Then, $\tilde{k}_{th}$ can be taken as the value for which $\nabla^2\left(\langle\tilde{k}^+\rangle\right)$ reaches zero. Strictly speaking, these two methods are not equivalent: indeed, by geometrical construction the tangent method must yield lower values of $\tilde{k}_{th}$. Table 9.4 lists the $\tilde{k}_{th}$ obtained with both methods in the incoming boundary layer of the R2 ramp. All values are comparable to those computed at § 9.2.2. In principle, threshold sensitivity can also be directly studied on the large field. In this case, however, only the approach based on $\nabla^2\left(\langle\tilde{k}^+\rangle\right)$ allowed to identify $\tilde{k}_{th}$ easily. Indeed, here the changes of slope of $\langle\tilde{k}^+\rangle$ appear to be too gentle to clearly define elbows. This might be an effect of the ramp: the deviation of the external, irrotational flow over the descending ramp might impact the computation of the $\tilde{k}$ field and smooth the shape of $\langle\tilde{k}^+\rangle$. The $\tilde{k}_{th}$ computed in the large field are also reported in table 9.4. All in all, threshold values provided by the threshold sensitivity study are consistent with those reported in table 9.2, even when directly computed on the separated shear layer. This gives further confidence in the TNTI detection method of de Silva *et al.* (2013) and Chauhan *et al.* (2014*c*) and on the extension of its output to the separated shear layer.

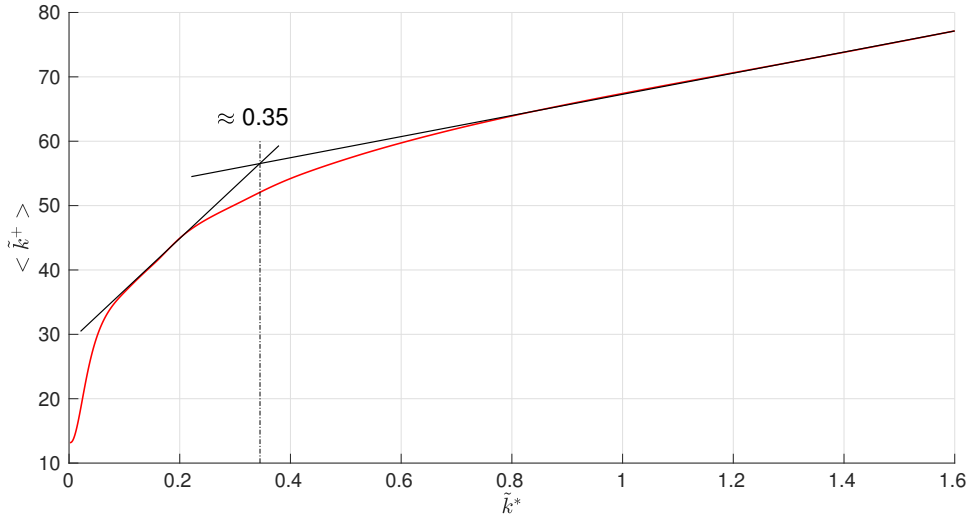

Figure 9.12: Evolution of $\langle \tilde{k}^+ \rangle$ with $\tilde{k}^*$ in the incoming boundary layer of the R2 ramp, at $Re_h = 5 \times 10^4$.

$Re_h/10^4$			3	4	5	6	7
Auxiliary f.	{	Tangents	0.38	0.35	0.35	0.30	0.31
	{	∇^2	0.45	0.50	0.45	0.35	0.33
Large field		∇^2	0.40	0.38	0.42	0.30	0.33

Table 9.4: Values of $\tilde{k}_{th}$ yielded by a threshold sensitivity study on the R2 ramp. The study was not repeated on the GDR ramp.

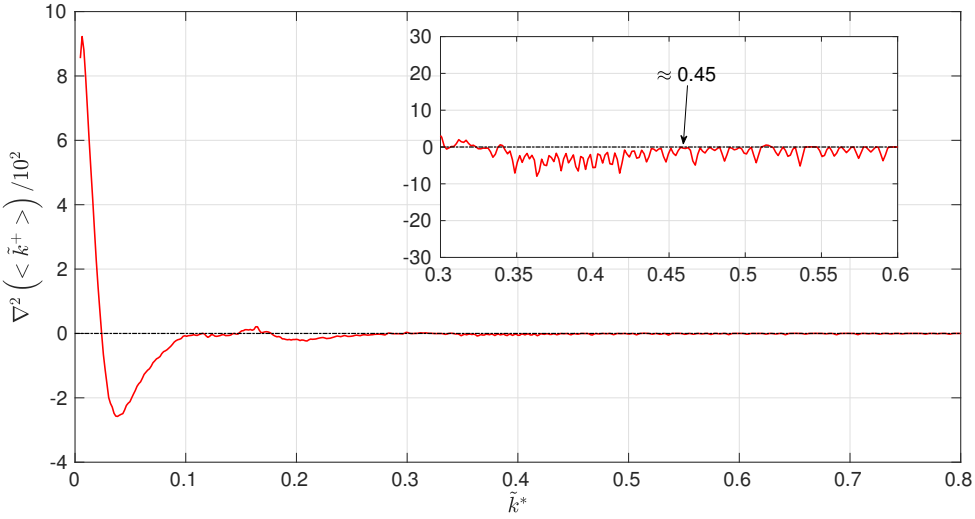

Figure 9.13: Second derivative of $\langle \tilde{k}^+ \rangle$, shown in figure 9.12, in function of $\tilde{k}^*$.

9.3 RRI detection

The detection of instantaneous RRIs is straightforward: based on the definition of mean RRI given at § 5.4, it is sufficient to identify the $u = 0$ isocontour on each instantaneous streamwise velocity field. Isocontours are then filtered, with a procedure that is slightly more complex than the one adopted for the TNTI (see § 9.2.2.3). In principle, indeed, the instantaneous RRI might locally touch the wall before reattachment, as shown by Le *et al.* (1997) (figure 9) and Friedrich & Arnal (1990) (figure 11). If this is the case, the instantaneous recirculation region is composed of more than one subregions where the flow moves upstream. This being so, the filter described at § 9.2.2.3 would incorrectly drop all but the subregion having the longest contour. Then, the following steps are followed to avoid filtering instantaneous RRIs excessively: 1) Closed contours (bubbles) are identified and successively erased. This operation leaves only open contours, that are necessarily in contact with the wall[1]. 2) Open contours that are between the wall and another, more external contour are also erased. Like bubbles, the zones that they delimit could be the 2D projections of 3D protrusions of forward-moving fluid. As already explained in the case of the TNTI, 2D2C-PIV is not relevant to study these regions. 3) Contours that contain less than a minimum number of points are dropped. A threshold of 20 points was chosen, as instantaneous RRIs do not vary much for a wide range of higher values. 4) Remaining RRI segments are concatenated into a single one. Examples of resulting instantaneous RRIs are given in figures 9.5 to 9.7. It is stressed that RRI detection shares many limitations of TNTI detection, in particular for what concerns PIV resolution and the unrecovered third dimension of the flow.

Even without a corpus of previous works to provide references, the detection of the RRI can be validated by comparing profiles of the backflow coefficient χ (defined at § 5.4) with the c.d.f. of the RRI (indicated with C_R). This approach is, by all means, equivalent to the validation of the TNTI distribution in the incoming boundary layer (see 9.2.2.4), but this time no hypothesis whatsoever is made on the form of the distribution, nor on its similarity along the streamwise direction. Figure 9.14 reports the comparison between χ and C_R over the R2 ramp at $Re_h = 5 \times 10^4$. Results at other Re_h are comparable and are not shown. It is found that for $x/h \leq 2$, the two curves agree very well, giving confidence in the detection of the RRI over the first part of the separated shear layer. Further downstream, however, C_R underpredicts the number of instantaneous RRIs that are in proximity of the wall. It should not be surprising that χ does not reach zero at the wall at every streamwise location: due to the buffeting instability, in a neighbourhood of the mean reattachment point, say at x_q/h, the wall can be exposed to a positive streamwise velocity for a fraction of total time. For example, Adams & Johnston (1988*b*) find that $\chi \approx 0.15$ at $x/L_R \approx 0.8$, which compares well with figure 9.14(d). When U is positive at the wall, however, the detection algorithm described above does not find any RRI at x_q/h. Then, since all *detected* RRIs are above the wall, it is $C_{Rq} = 0$ at the wall systematically. To avoid this bias, it is sufficient to concatenate a segment of wall to the detected RRI. Figure 9.14 proves that this simple correction provides a better approximation of χ at all tested streamwise positions. Figure 9.14 also suggests that erroneous filtering of smaller recirculation bubbles has, at most, a weak incidence on the description of the statistical behavior of the RRI given in chapter 10.

[1] Isolines cannot be truncated in the middle of their field: they are either infinite, or closed, or connected to a boundary. Since the RRI is finite by definition and bubbles are filtered, the only remaining possibility is that remaining contours are in contact with the wall.

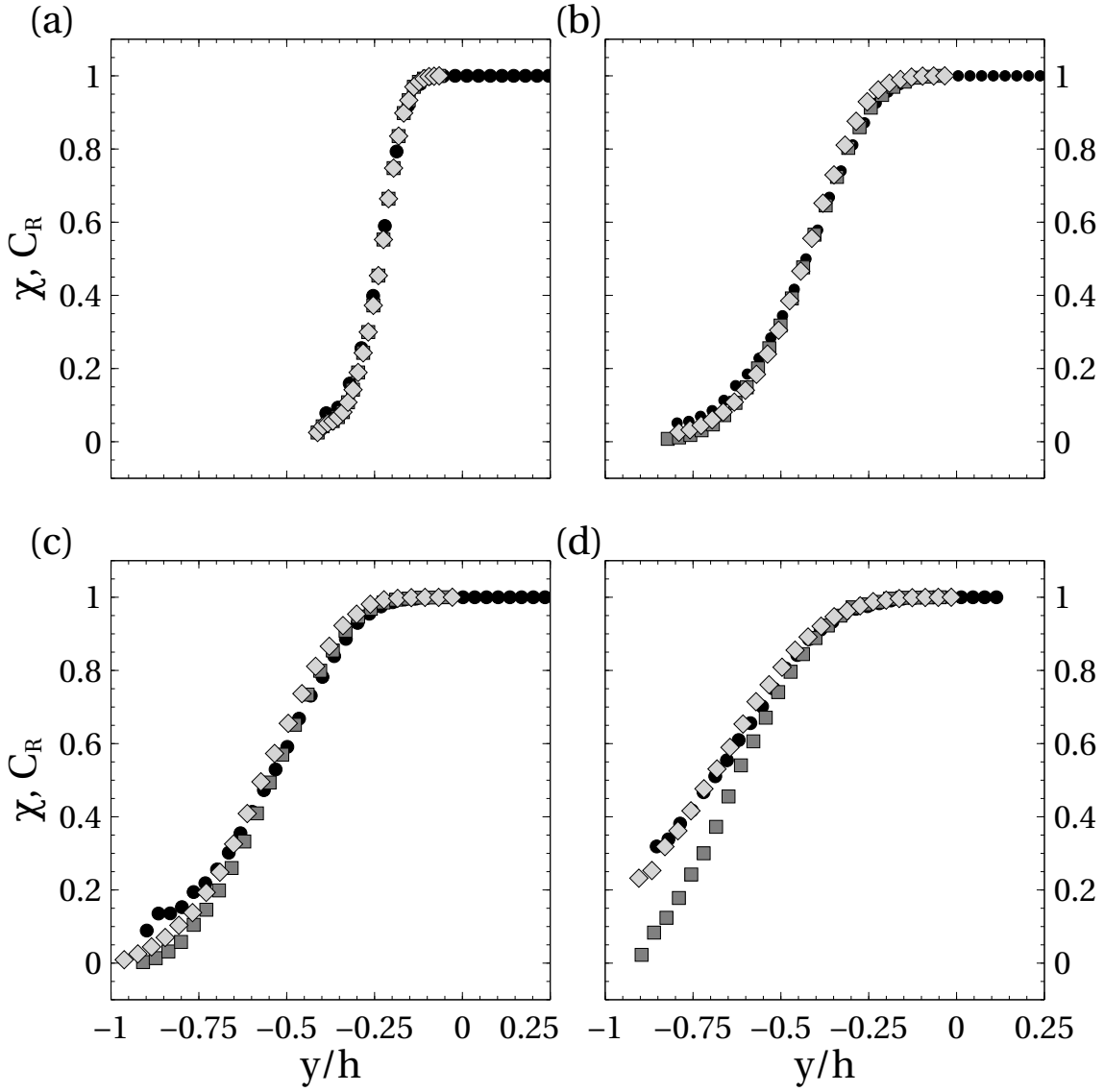

Figure 9.14: Comparison of the c.d.f. of the RRI to the χ profile at four positions within the separated shear layer of the R2 ramp, at $Re_h = 5 \times 10^4$. (a) $x/L_R \approx 0.2$; (b) $x/L_R \approx 0.40$; (b) $x/L_R \approx 0.6$; (b) $x/L_R \approx 0.8$. Symbols: ● χ profile; ■ C_R obtained from unaltered RRIs ; ◆ C_R obtained by adding a segment of wall after the last point of each RRI.

9.4 Regions of uniform momentum: a common detection approach?

In their investigation of turbulent boundary layers, Meinhart & Adrian (1995) reported that within the turbulent flow there exist unsteady, large zones ($l \sim \delta$) where streamwise momentum is almost constant and turbulent fluctuations are low. Such regions are entoured by very thin, strong internal shear layers that share many characteristics of the TNTI, including jumps in conditional velocity, vorticity and turbulent energy profiles (Eisma *et al.* (2015)). Kwon *et al.* (2014) showed that similar regions also exist in channel flows: this led to the description of a surprisingly *quiescent* (i.e. lowly turbulent) core within a fully developed turbulent channel flow. Furthermore, these authors reported that boundaries of the quiescent core agree well with instantaneous isocontours of $\tilde{k}$. These elements suggest that if regions of uniform momentum exist in the separated flow under study, the instantaneous TNTI could be one of their boundaries. Moreover, we argue that the difference in turbulent properties, for example Reynolds stresses and vorticity, that is observed between the recirculation region and the shear layer is qualitatively similar to the one observed by Kwon *et al.* (2014): it should then be possible to also assimilate the RRI, or a very similar lower shear layer boundary, to the boundary of a region of uniform momentum.

The following paragraphs explain how regions of uniform momentum were identified and show that at least two of such zones exist in most PIV fields that were analysed. One of them corresponds roughly to the free flow, which is consistent with Meinhart & Adrian (1995) and Adrian *et al.* (2000): its lower boundary approximates the instantaneous TNTI very well. A new finding is that the recirculation region is also a region of uniform momentum, as speculated, and its upper boundary agrees with the RRI. This means that the interfaces of the shear layer can be conceived and detected in a common framework. Further, this observation casts new light on the physical nature of the RRI (or, more in general, of the lower boundary of the shear layer), in particular by suggesting that the same low scale, instantaneous transfer mechanisms identified at the TNTI and in internal shear layers (Eisma *et al.* (2015) among others) might also act at the RRI. In spite of their potential implications, these findings are not thoroughly exploited in this research. Investigation of regions of uniform momentum was indeed considered at a late hour, when most results had already been obtained with the definitions of TNTI and RRI given in chapter 9.2 and chapter 9.3, respectively. However, instantaneous TNTIs of the GDR large field were identified based on this approach, that appears to be less sensitive to excessive noise in the free stream (see § 9.2.2.7). This should be kept in mind when considering interface statistics presented in chapter 10.

9.4.1 Identification of regions of uniform momentum: modal velocities

Regions of uniform momentum were identified following Adrian *et al.* (2000) and Kwon *et al.* (2014). For each instantaneous PIV field, the probability density function P_u of u over the entire field was plotted, as shown in the example of figure 9.15. In most fields, values of u appear to be grouped in many heaps. Adrian *et al.* (2000) call such heaps *modes*. The u value corresponding to the peak of each mode is called *modal velocity* (indicated with u_m). According to these authors, each mode represents the distribution of u around u_m, within one region of uniform momentum. Even if number and size of modes strongly depend on the extent of the PIV field (Adrian *et al.* (2000)), figure 9.15 suggests that regions of uniform momentum exist in the separated shear layer under study. Moreover, two modes are particularly evident: the first one, M_T, is placed at $u/U_\infty \approx 1$, corresponding to the free flow; the second one, M_R, approximatively covers the range $u/U_\infty < 0$, i.e. the recirculation region. Figure 9.16 presents the distribution of modes found in all instantaneous velocity fields captured on the R2 large field at $Re_h = 4 \times 10^4$. Generally speaking, modes are instantaneous features of the flow (Adrian *et al.* (2000), Eisma *et al.* (2015)): consistently, their corresponding u_m are distributed all over the range of velocities found in this dataset. However, figure 9.16 shows that a modal velocity $u_m/U_\infty \approx 1$, corresponding to M_T, exists in all analysed fields[1]. As for what concerns M_R, $u_m/U_\infty \approx 0$ is the second most common modal velocity, being present in approximately $35\,\%$ of instantaneous fields. If a tolerance of $2\,\%$ is allowed on u_m/U_∞, a modal velocity representing M_R appears in $75\,\%$ of fields. Finally, M_R is found in all fields under the condition $u_m/U_\infty \approx \pm 0.05$. These findings suggest that M_T and M_R correspond to stable (although not necessary stationary) regions of uniform momentum. These observation support the conjecture that the free flow and the recirculation region are the main regions of uniform momentum of a separated shear layer, in a similar fashion as the quiescent

[1] This is not surprising, because the free stream is a flow feature common to all PIV fields.

channel core of Kwon *et al.* (2014). This being so, the values of u that limit such regions can be reasonably expected to identify the boundaries of the shear layer.

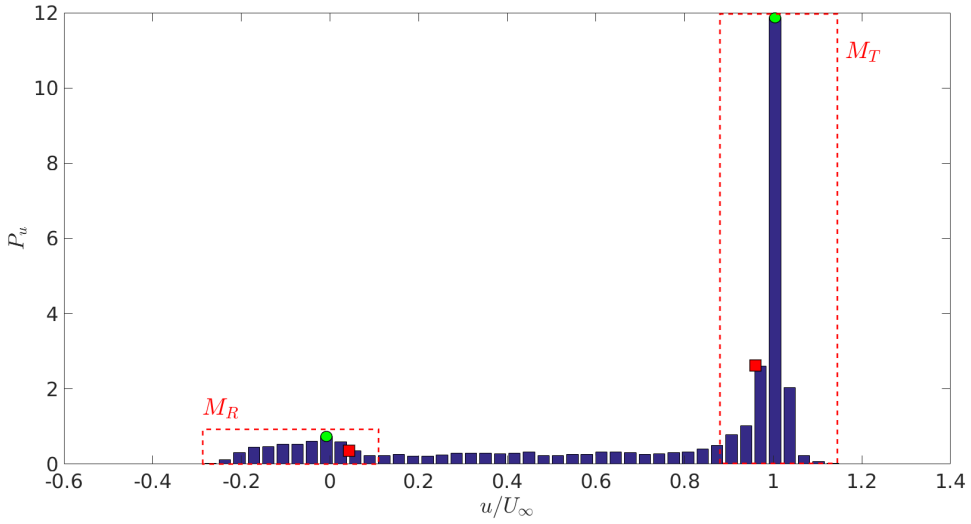

Figure 9.15: P_u, the probability distribution function of u for the instantaneous R2 large field represented in figure 9.5. Symbols: – – – qualitative envelope of the two main modes M_T and M_R; ● modal velocities; ■ boundary velocities.

9.4.2 Boundaries of the regions of uniform momentum

Consistently with the definition of modal velocity, Adrian *et al.* (2000) and Kwon *et al.* (2014) utilised local minima of P_u to identify boundaries between regions of uniform momentum. This simple approach proves very effective in their experiments, but it is often questionable in the present one. Indeed, P_u is often almost uniform between the two main modes and local minima are not always clearly defined, as in the case of figure 9.15. Then, a different convention was adopted, that places the boundaries of each mode at those values of u for which it is:

$$\frac{\mathrm{d}^2 P_u}{\mathrm{d}u^2} = 0. \tag{9.7}$$

Two values of u verify eq. 9.7 for each peak, one on each side of u_m. In the case of M_T, $u < u_m$ was chosen as *boundary velocity*, whereas for M_R, $u > u_m$ was. This method has the advantage of always finding unambigous boundary velocities for every mode, albeit not the same as those identified with the approach adopted by Adrian *et al.* (2000) and Kwon *et al.* (2014). Figure 9.17 shows that boundary velocities of M_T and M_R are distributed over relatively narrow ranges of u, respectively centered at $u/U_\infty = 0.965$ and $u/U_\infty = 0.04$. Interestingly, modal velocities are rare within these same ranges. Unlike modal velocities, boundary velocities appear to depend to some extent on the discretisation (i.e. the number of bins) that is adopted to compute P_u on each instantaneous field. On the large fields of both ramps, it is found that boundary velocities change little if the number of bins varies between 40 and 70, which typically corresponds to discretisations of the u distribution of $0.5\,\mathrm{m\,s^{-1}}$ to $1\,\mathrm{m\,s^{-1}}$. All in all, it seems that the boundary velocities of M_T and M_R can be detected in a robust fashion. In the next section, the corresponding velocity isocontours are compared to the TNTI and the RRI computed as in chapter 9.2 and chapter 9.3.

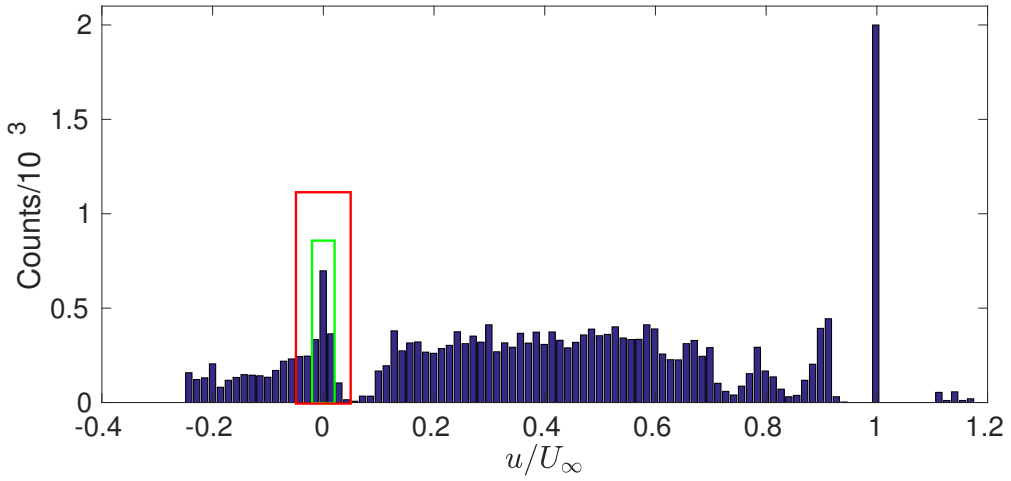

Figure 9.16: Distributions of modal velocities in the R2 large field at $Re_h = 4 \times 10^4$. The mode M_R is identified with ——— (2 % tolerance) or ——— (5 % tolerance).

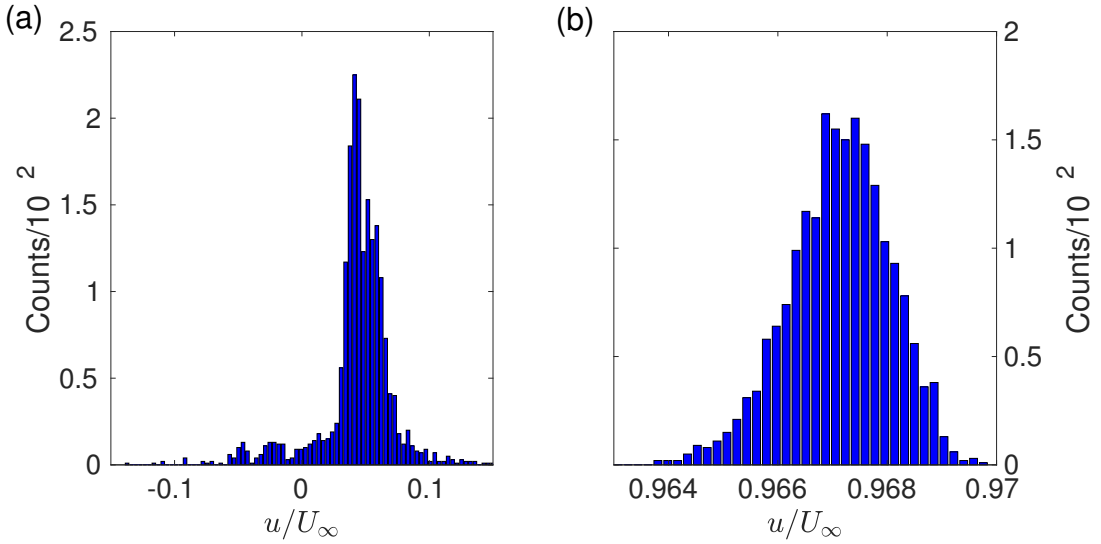

Figure 9.17: Distributions of boundary velocities in the R2 large field at $Re_h = 4 \times 10^4$, for (a) M_T and (b) M_R.

9.4.3 Comparison and discussion

Isocontours corresponding to the boundary velocities of M_T and M_R are reported in figure 9.5 and figure 9.6. On the R2 large field, agreement with both the TNTI and the RRI is good, considering the different identification approaches. In particular, it should not be forgotten that the M_R isocontour is, by definition, not on $u = 0$. As for the TNTI, the local filter applied to the $\tilde{k}$ field might smooth out wrinkles that are instead visible on the velocity-defined M_T isocontour, accentuating local differences between the two curves. In any case, interface statistics presented in chapter 10 will briefly show that such differences between instantaneous realisation do not seem to significantly affect the main streamwise statistical trends and scaling laws. This confirms that the boundaries of M_T and M_R are very good surrogates of the TNTI and the RRI, with statistical properties that are completely equivalent in the framework of investigation of shear layer boundaries. In the light of these results, problems encountered during the detection of the TNTI over the GDR large field (see § 9.2.2.7) do not seem too troubling: even if the reliability of $\tilde{k}$-based TNTI detection is poor, boundaries of M_T seem reliable and can be used in the following steps of this work. In this respect, it is pointed out that if a typical value of the M_T boundary velocity (e.g. 0.97) is plugged into eq. 9.2, one obtains $Q \approx 8 \times 10^{-4}$ to 1.3×10^{-3}, which is comparable to the treshold used at § 9.2.1 to identify turbulent sections of hot-wire signals. This further supports consistency between the TNTI detection methods reviewed in this chapter.

10

One point statistics of interfaces of the shear layer

Statistiques en un point des interfaces de la couche cisaillée

Ce chapitre analyse les statistiques en un point de la position des interfaces (TNTI et RRI) de la couche cisaillée. Dans les deux cas, la position instantanée est calculée dans un repère centré sur l'interface moyenne, comme montré en figure 10.3.

La p.d.f. de la TNTI (symbole N_T) reste proche d'une distribution gaussienne typique de la couche limite turbulente (Corrsin & Kistler (1955)) sur une longueur L_G au-dessus d'une partie de la bulle de recirculation. Ensuite, la p.d.f. devient asymétrique : les TNTI instantanées sont concentrées en dessous de la TNTI moyenne (figure 10.4 et figure 10.5). L'analyse des trois premiers moments statistiques de d_T (représentes par l'écart type σ_T, le coefficient de dissymétrie Sk_T et le coefficient d'aplatissement Kt_T) révèle que L_G est approximativement constante sur la rampe R2 et la rampe GDR, mais que le rapport L_G/L_R est trois fois plus petit dans ce deuxième cas (figure 10.6 et figure 10.7). En fait, on observe que $L_G \sim \delta_e$ (figure 10.8) : étant donné que la normalisation en h n'est pas correcte, la longueur L_G ne dépend pas du décollement. La comparaison de Sk_T et Kt_T avec les principales composantes du gradient de pression longitudinale (figure 10.9) suggère que la déviation vis-à-vis de la distribution de la forme gaussienne de N_T est corrélé à la composante $U\partial U/\partial x$ de l'équation RANS, c'est à dire à l'augmentation de la pression due à ER. Plus à l'aval, Sk_T et Kt_T suivent mieux l'évolution du cisaillement total $\partial/\partial y^* \, (U^*V^* + \langle u'v' \rangle^*)$, normalisé selon les prescriptions du tableau 8.2. Ainsi, L_G semble être le résultat de l'interaction entre la récupération de pression due à ER et la couche limite amont (représentée par δ_e). La hauteur de la rampe h induit, elle, un poids relatif différent de la couche cisaillée décollée : pour un ER donné, plus le rapport δ_e/h est petit, plus la couche limite perd de l'influence sur l'écoulement décollé et $L_G/L_R \to 0$.

La p.d.f. de la RRI n'est jamais gaussienne à cause des interactions de l'interface avec la paroi (figure 10.12 et figure 10.13). L'analyse des moments statistiques montre que le coefficient de dissymétrie Sk_R et le coefficient d' aplatissement Kt_R atteignent une évolution régulière sur L_R, après une phase transitoire qui s'étend sur une longueur L_V (figure 10.14 et figure 10.15). Comme dans le cas de la TNTI, on trouve que L_V est approximativement constante sur les deux rampes et que $L_V \sim \delta_e$ (figure 10.16). De plus, l'écart type σ_R mesuré sur les deux rampes est mis en échelle par l'usage du coefficient $C_{h,\delta}$ (figure 10.19). Ces éléments indiquent que L_V est la longueur sur laquelle la couche limite à l'amont influence l'écoulement décollé. Les évolutions de Sk_R et Kt_R ne sont pas bien corrélées avec le gradient de pression longitudinal (figure 10.17) mais plutôt avec la production turbulente $\mathcal{P}$ mesurée *au centre* de la couche cisaillée (figure 10.18). On interprète cette observation comme la manifestation d'un lien entre les plissements de la RRI et le mélange turbulent qui gouverne les échanges entre la bulle de recirculation et la couche cisaillée.

10.1 Introduction

The mean TNTI and the mean RRI have already been used in the previous chapters of this work, in particular in reference to the study of mean quantities (e.g. the streamwise pressure gradient). Now that the definitions of the *instantaneous* interfaces have been discussed thoroughly, it is possible to go one step further and investigate the statistical behaviour of the boundaries of the shear layer. In the following, one-point statistics are used to highlight that the massive separation appears to be the result of complex interactions between a pressure recovery induced by geometry, the separated shear layer and the incoming boundary layer.

10.2 Statistics of the TNTI

The convergence criterion used to compute $\tilde{k}_{th}$ is based on the observation that in boundary layers the position of the TNTI approximatively follows a gaussian distribution, as it does in many other canonical flows including wakes (Bisset *et al.* (2002)), jets (Westerweel & Scarano (2005)) and free mixing layer (Attili *et al.* (2014)). This motivates us to verify if such statement is also true over the massive separation.

10.2.1 Mean interfaces

Section 9.2 presented different detection techniques for instantaneous TNTIs, highlighting that they give substantially concordant results, if quality of PIV datasets is high enough. In this section we extend those approaches to the detection of the mean TNTIs on the mean fields, and we briefly investigate their behaviour with respect to Re numbers. It is pointed out that Maurice *et al.* (2016) suggests that any mean turbulent interface can also be obtained by averaging the positions of its instantaneous realisations. Generally speaking, this seems reasonable: for what concerns the RRI, for example, the concordance of χ profiles (computed by averaging PIV fields) with C_R (computed from instantaneous interface positions) indicates that the same mean RRI can be retrieved from the mean field as from the average of instantaneous interfaces. However, the implementation proposed by Maurice *et al.* (2016) gave ambiguous results in our study and was not exploited, in particular because detection from the mean field is straightforward.

10.2.1.1 Detection

Conversely to the case of the RRI (see § 9.3), mean TNTIs can be found by applying the approaches given at § 9.2 to the mean field, viz. by detecting the $\tilde{k}_{th}$ isocontour of the mean field, if the energetic approach is retained, or alternatively by identifying the contour of a mean region of uniform momentum (usually at $U/U_\infty \approx 0.96$ to 0.97 in this study). Results obtained at $U_{ref} = 20\,\mathrm{m\,s^{-1}}$ with both techniques are presented in figure 10.1. Comparisons at other velocities give similar results and are not shown for sake of simplicity. As demonstrated by Kwon *et al.* (2014) and anticipated at § 9.2, mean TNTIs agree acceptably well in the case of the R2 ramp. The distance between the two lines is about $0.1h \approx 2\Delta$, which remains reasonable. As for the GDR ramp, it seems safe to conclude that the energetic approach fails at giving a correct estimation of the mean TNTI beyond $x/h \approx 2.5$. Before this point, however, the $\tilde{k}_{th}$ isocontour matches the boundary velocity $U/U_\infty \approx 0.97$ well, suggesting that the surprising shape of the former one is due to local problems within the $\tilde{k}$ distribution. Consistently, the backward folding of the $\tilde{k}_{th}$ isocontour (indicated by an arrow in figure 10.1(b)) occurs in correspondence of the energy spills observed in instantaneous GDR large fields (see § 9.2.2.7). For these reasons, in what follows the energetic approach is not used for investigating TNTI behaviour over the GDR ramp.

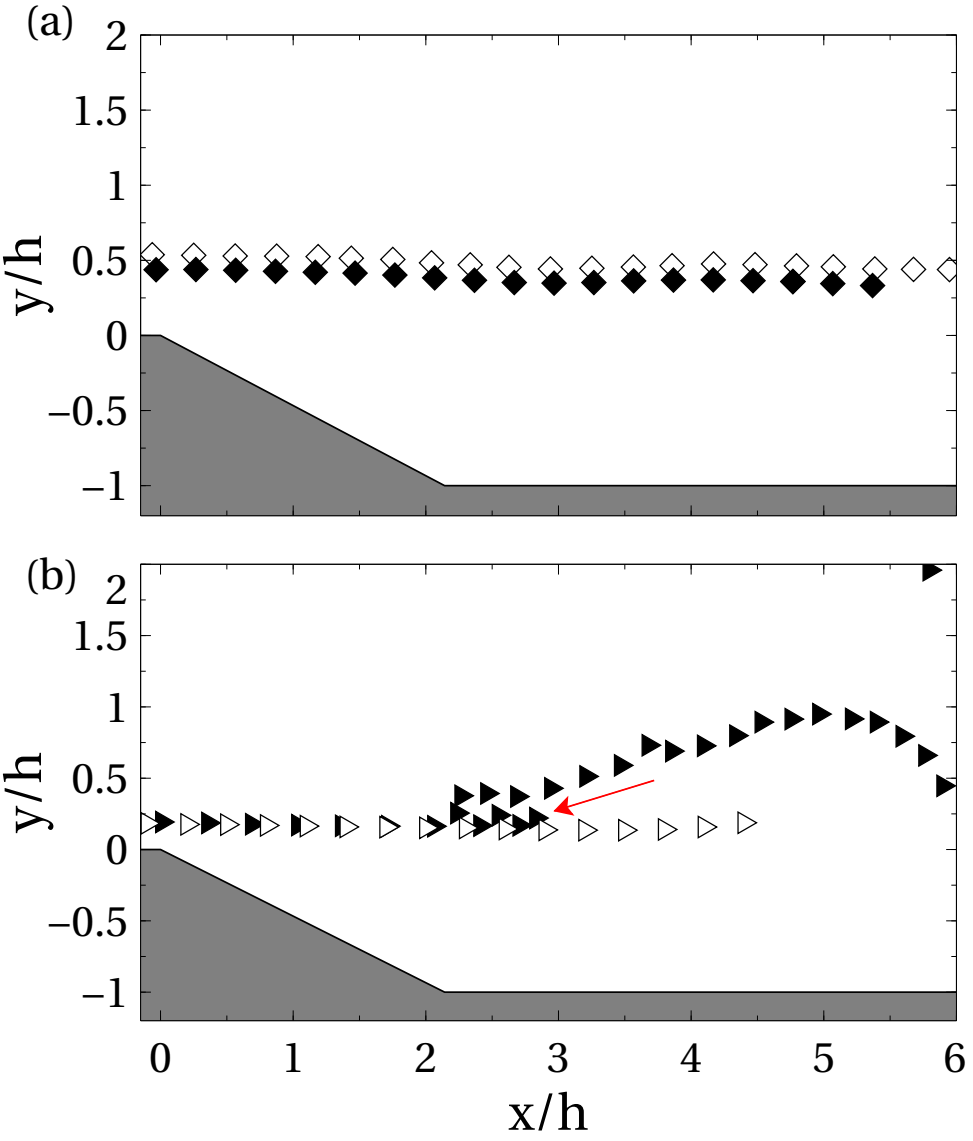

Figure 10.1: Comparisons of mean TNTIs found with different detection techniques at $U/U_{ref} = 20\,\mathrm{m\,s^{-1}}$: (a) R2 ramp ($Re_h = 4 \times 10^4$); (b) GDR ramp ($Re_h = 13.3 \times 10^4$). The color of the symbols indicates the detection technique: white online is used for the boundary velocity criterion, black online for the energetic criterion. The red arrow shows the backward folding of the $\tilde{k}_{th}$ isocontour over the GDR ramp.

10.2.1.2 Comparison at different Re

Figure 10.2 presents the mean TNTIs at all available Re_h, normalised with respect to h. Mean interfaces collapse reasonably well onto a single curve for each ramp. The two sets of curves seem to be roughly parallel to each other, even if an ondulation is visible on interfaces of the R2 ramp, at $x/h \approx 3$. One evident exception to this rule is the rise of the GDR mean TNTIs, indicated by a red arrow in figure 10.2. As already discussed, such behaviour is probably an artifact due to quality of the GDR PIV datasets, that was not completely filtered by the use of the boundary velocity approach. But for these elements, the curves are relatively smooth and can be fitted quite well by straight lines, at least in a large neighbourhood downstream of the mean separation point. The slopes of the fitted lines (indicated with the symbol ϕ_{TNTI}) are reported in table 10.1: interestingly, ϕ_{TNTI} seems to roughly scale with h/L_R and hence with Re_θ^{-m}. This would be consistent with the behaviour of separated shear layer highlighted at § 8.2: when the shear layer grows faster and the recirculation region shrinks, the mean TNTI also leans more toward the wall. In the limit, it can be thought that for a completely attached boundary layer the TNTI would deviate downward rouhly following the slope of the ramp. Admittedly, scaling is not completely satisfactory on the GDR ramp, with a noticeable decrease of the slope for higher Re_θ, but precise numerical values should be taken with caution due to the previously discussed artificial rise of the mean TNTI.

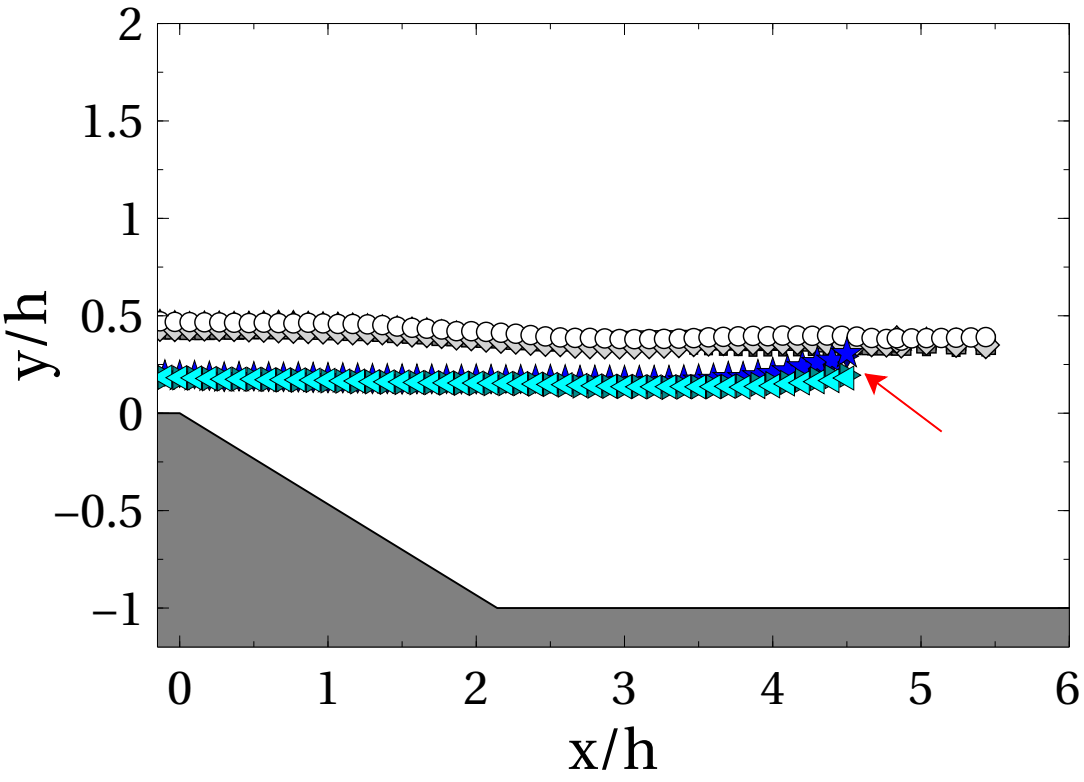

Figure 10.2: Comparison of mean TNTIs at different Re_h. Gray-shade symbols indicate R2 data: ◯ $Re_h = 3 \times 10^4$; ◊ $Re_h = 4 \times 10^4$; ■ $Re_h = 5 \times 10^4$; ✚ $Re_h = 6 \times 10^4$; ▲ $Re_h = 7 \times 10^4$. Blue-shade symbols indicate GDR data: ◁ $Re_h = 10 \times 10^4$; ▷ $Re_h = 13.3 \times 10^4$; ★ Re_h =20 $\times 10^4$; ✦ $Re_h = 26.7 \times 10^4$. The red arrow shows the artificial rise of the mean TNTIs on the GDR ramp. All curves are normalised on h.

$Re_h/10^4$	3	4	5	6	7	10	13.3	20	26.7
δ_e/h	0.92	0.86	0.82	0.82	0.91	0.34	0.28	0.33	0.29
Re_θ	2006	3262	4122	4738	5512	1788	2547	3617	4340
L_R/h	5.42	5.22	5.1	4.79	4.4	5.62	5.49	5.37	5.22
ϕ_{TNTI}	-0.020	-0.020	-0.017	-0.026	-0.026	-0.014	-0.014	-0.007	-0.006
$\phi_{TNTI}\, L_R/h$	-0.11	-0.10	-0.09	-0.12	-0.11	-0.08	-0.08	-0.04	-0.03

Table 10.1: Slopes of the linear fits of mean TNTIs. Values of δ_e/h, Re_θ and L_R/h are also reminded.

10.2.2 A reference frame for interface statistics

For what follows, it is practical to compute the positions of instantaneous TNTIs in the local frame presented in figure 10.3, which is conceptually equivalent to the streamwise-wall normal one used for boundary layers but more convenient for computations over the massive separation.

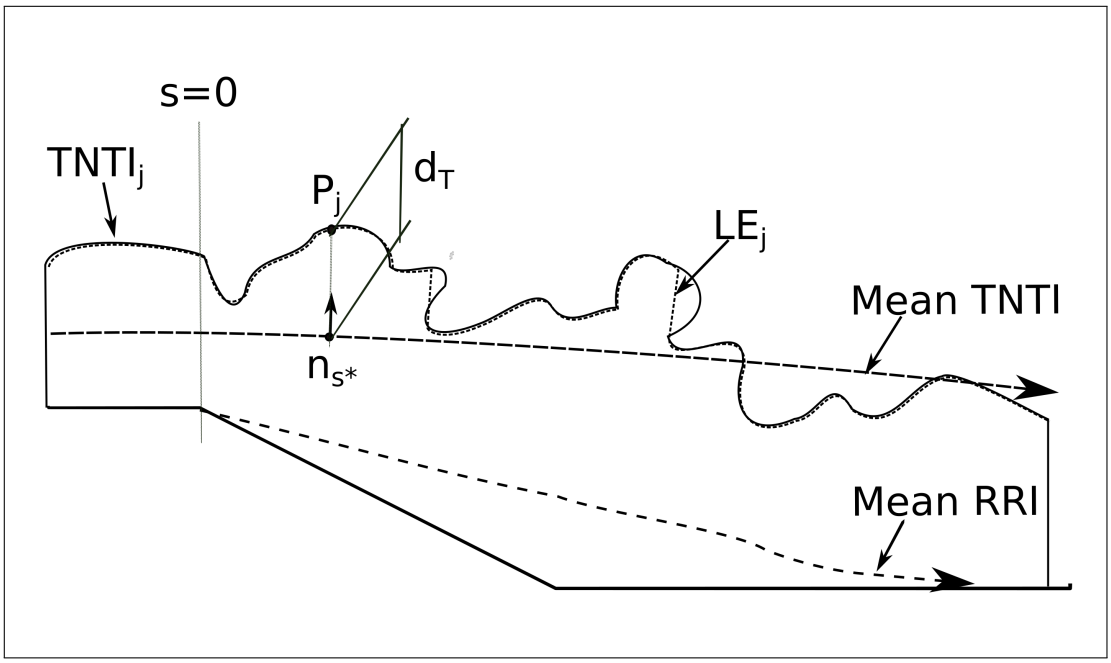

Figure 10.3: Notations and reference frames for the TNTI. $d_T(s^*)$ is the position of the instantaneous TNTI at the curvilinear abscissa s^*.

We define a curvilinear abscissa s along the mean TNTI. For convenience the origin of s is placed at $x = 0$. Let also $\boldsymbol{n}_{s^*}$ be the normal to the mean TNTI for $s = s^*$. The instantaneous TNTI location at s^* is defined by $d_{Tj}(s^*)$, the signed distance (positive up) along $\boldsymbol{n}_{s^*}$ between the j-th instantaneous TNTI and the mean TNTI. .

10.2.3 Statistical distribution

The forms of $N_T(s)$ over the R2 ramp and the GDR ramp are reported in figure 10.4 and figure 10.5, respectively, at several streamwise locations. Figure 10.5 shows $N_T(s)$ at more locations because the length of the R2 large field is comparable to the GDR one, for a much shorter L_R. On both ramps, there exist a neighbourhood of the mean separation point in which the TNTI seems roughly distributed as a gaussian random variable: the statistical properties of the TNTI that are typical of boundary layers seem then to survive to separation, persisting over a part of the recirculation region. Let us call *gaussian length* (noted L_G) this first part of the separated flow. Further downstream, however, $N_T(s)$ deviates progressively from

a gaussian distribution. $N_T(s)$ is more and more skewed: its *inner* (i.e. towards the wall) tail is shortened and the TNTI sample is more concentrated slightly under the mean TNTI. In itself, the streamwise evolution of some TNTI properties is not surprising: indeed, unlike canonical flows studied in previous works, the massive separation under investigation is not equilibrated (since the boundary conditions evolve) nor, in general, self-similar (see for example Song & Eaton (2004)). It is more intriguing that L_G seems to be much shorter on the GDR ramp than on the R2 ramp. In the latter case, deviations from a gaussian distribution do not appear before $x/L_R \approx 0.8$, while in the former one they are already evident at $x/L_R \approx 0.4$. The analysis of the streamwise evolution of statistical moments will allow to better assess L_G and to sketch some possible explanations of its different magnitudes.

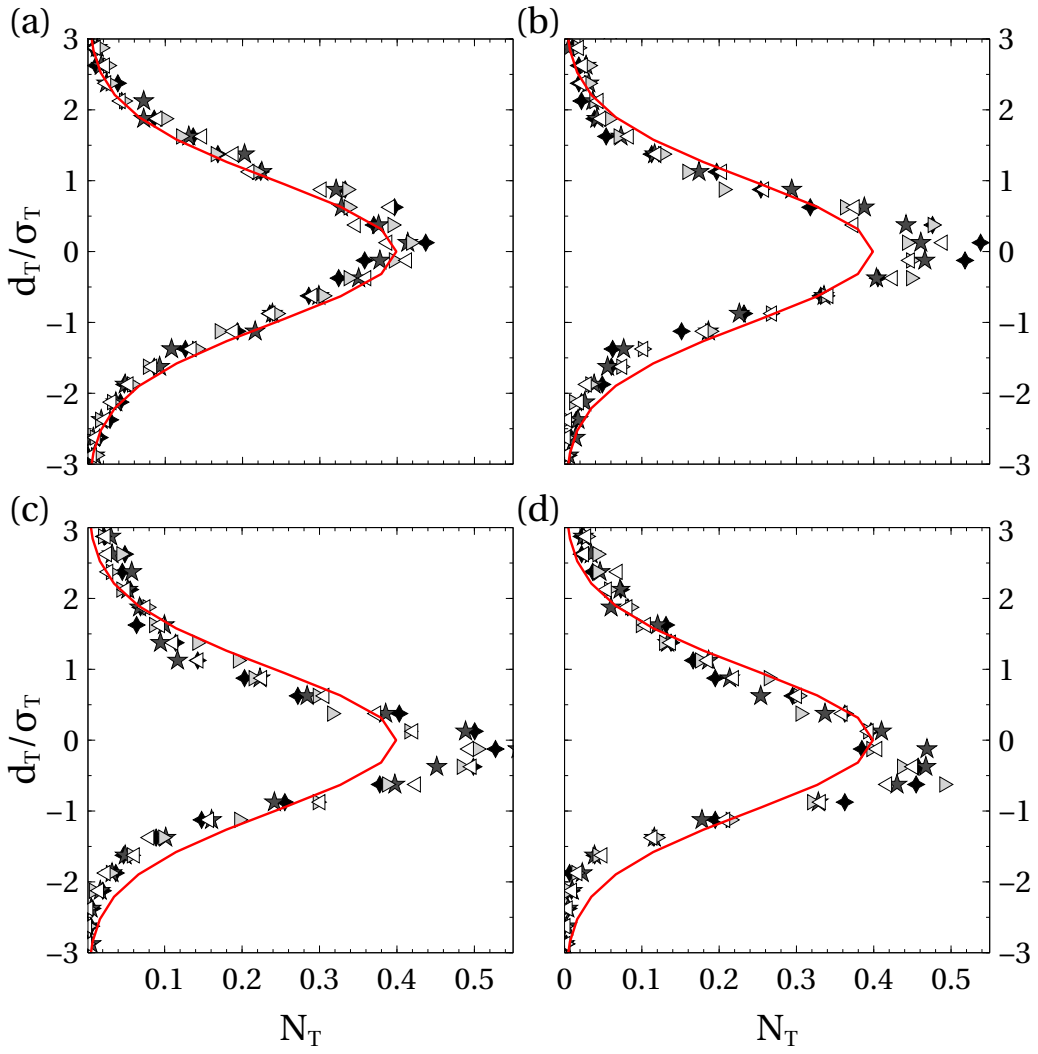

Figure 10.4: Normalised TNTI distribution on the GDR ramp. (a) $x/L_R = 0.2$; (b) $x/L_R = 0.4$; (c) $x/L_R = 0.6$; (d) $x/L_R = 0.8$. $\triangleleft$ $Re_h = 10 \times 10^4$; $\triangleright$ $Re_h = 13.3 \times 10^4$; $\bigstar$ Re_h =20×10^4; $\blacksquare$ $Re_h = 26.7 \times 10^4$. —— gaussian distribution.

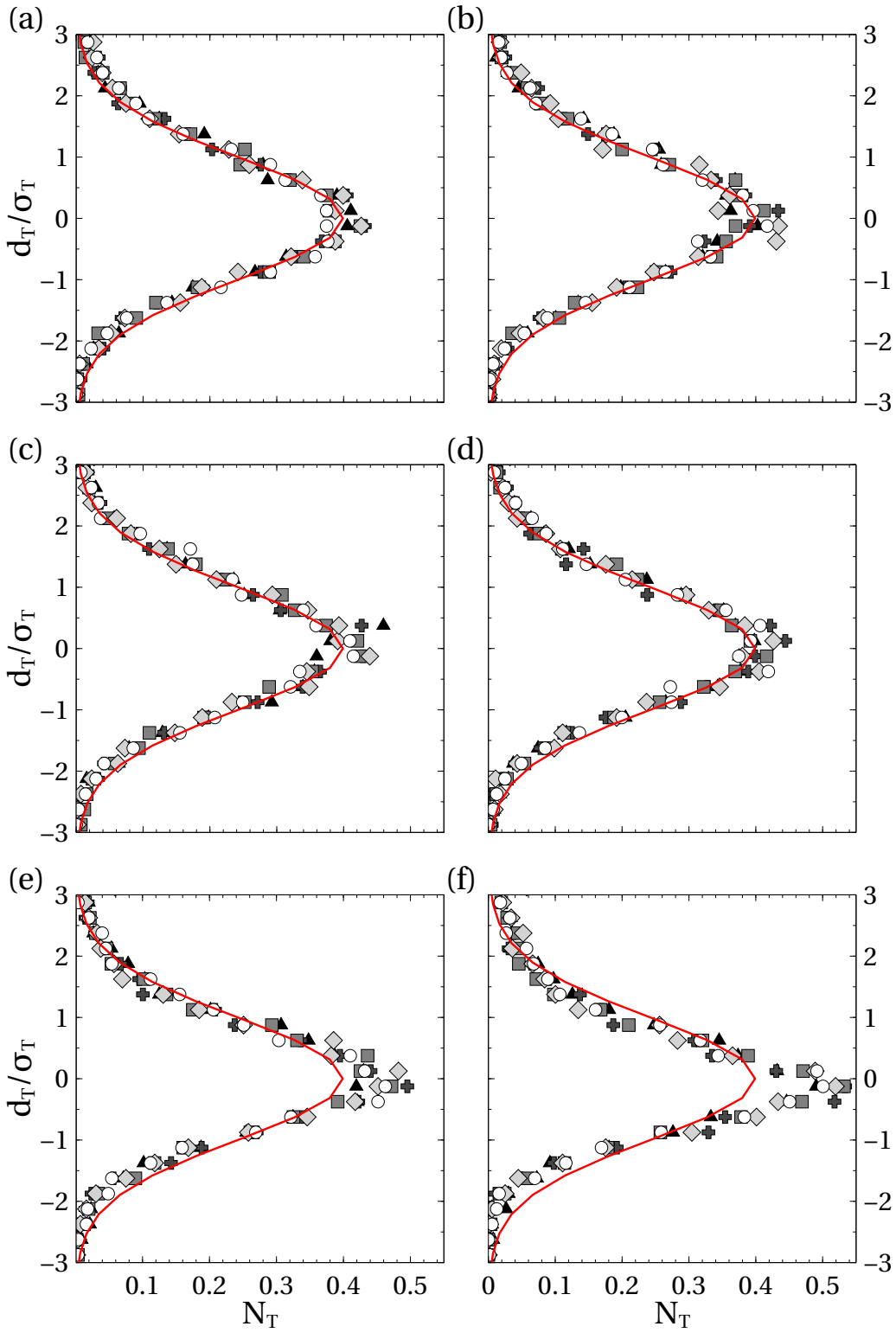

Figure 10.5: Normalised TNTI distribution on the R2 ramp. (a) $x/L_R = 0.2$; (b) $x/L_R = 0.4$; (c) $x/L_R = 0.6$; (d) $x/L_R = 0.8$; (e) $x/L_R = 1.1$; (f) $x/L_R = 1.4$. Symbols: ◯ $Re_h = 3 \times 10^4$; ◇ $Re_h = 4 \times 10^4$; ■ $Re_h = 5 \times 10^4$; ✚ $Re_h = 6 \times 10^4$; ▲ $Re_h = 7 \times 10^4$. —— gaussian distribution.

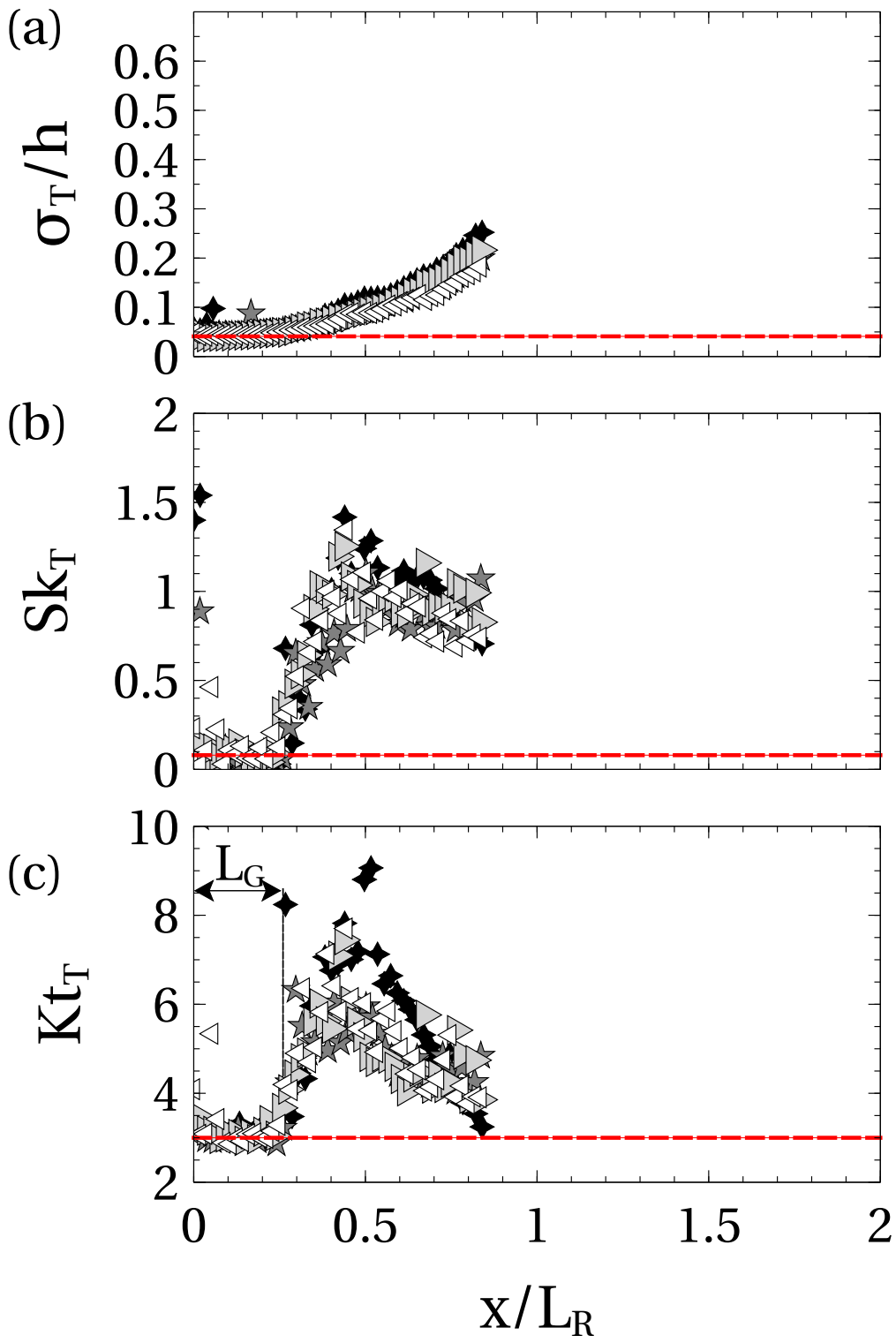

Figure 10.6: Streamwise evolution of TNTI statistics on the GDR ramp: (a) normalised standard deviation σ_T/h; (b) skewness coefficient $Sk_T = {\mu_{T3}}/{\mu_{T2}}^{3/2}$; (c) kurtosis coefficient $Kt_T = {\mu_{T4}}/{\mu_{T2}}^2$. – – – reference value within L_G. Other symbols as in figure 10.4.

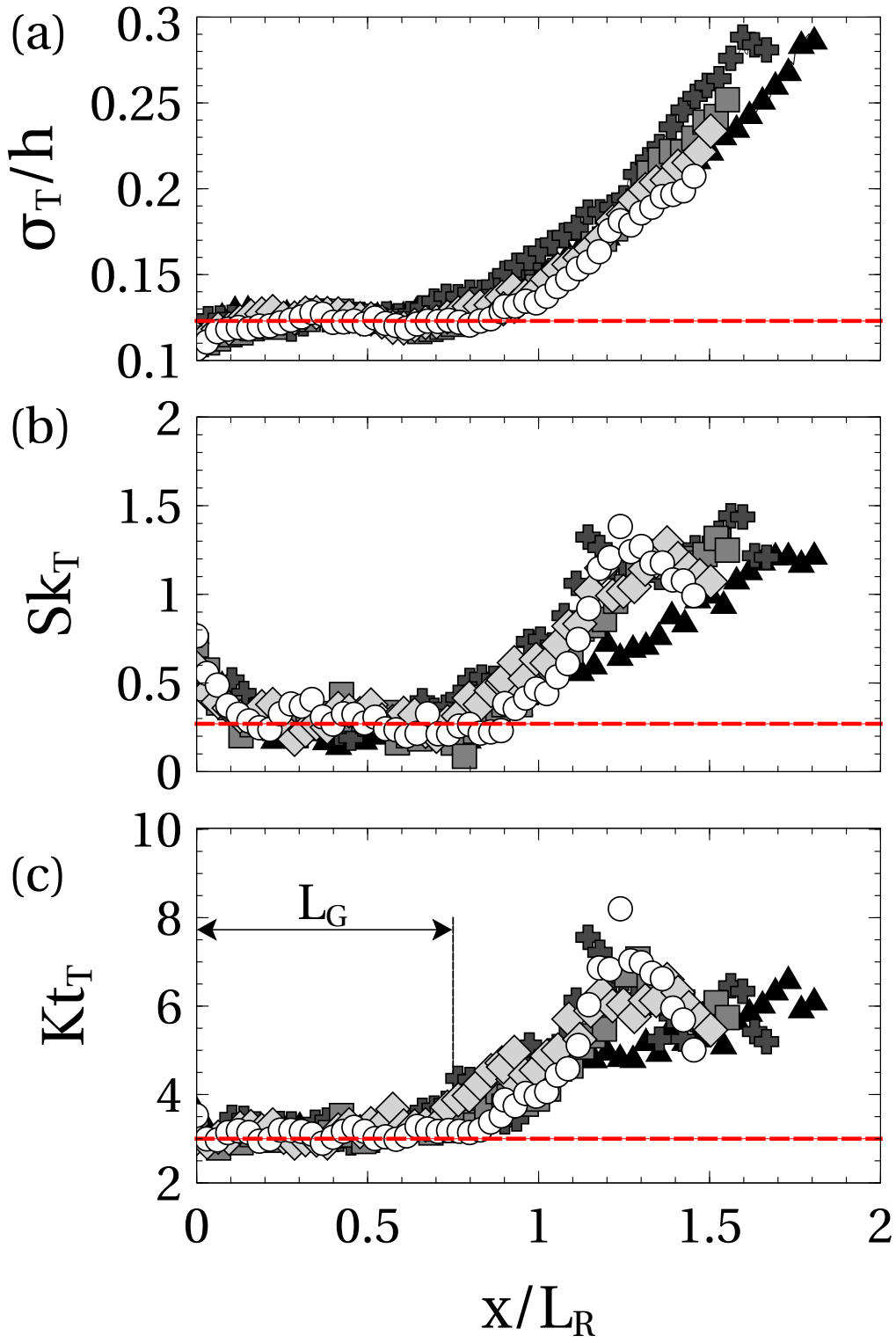

Figure 10.7: Streamwise evolution of TNTI statistics on the R2 ramp: (a) normalised standard deviation σ_T/h; (b) skewness coefficient $Sk_T = \mu_{T3}/{\mu_{T2}}^{3/2}$; (c) kurtosis coefficient $Kt_T = \mu_{T4}/{\mu_{T2}}^2$. – – – reference value within L_G. Other symbols as in figure 10.5.

10.2.4 Streamwise evolution of statistical moments

The streamwise evolutions of the first three statistical moments of N_T are presented in figure 10.6 (GDR ramp) and figure 10.7 (R2 ramp). The standard deviation σ_T is normalised on step height h, while the third and fourth moments are given in the form of the non-dimensional skewness coefficient Sk_T and kurtosis coefficient Kt_T, respectively, that were already introduced at § 9.2.2.4. Statistical moments confirm the suggestions of § 10.2.3. Over a length L_G downstream of separation, N_T is approximatively homogeneous in the streamwise direction. On this range, σ_T is almost constant and it is $Sk_T \approx 0.2$-0.25 and $Kt_T \approx 3$, with substantial agreement among the two ramps. Values of skewness and kurtosis match closely those typical of a gaussian distributions (viz. $Sk_T = 0$ and $Kt_T = 3$) and are consistent with boundary layer properties listed in table 9.3. These elements quantitatively confirm that the gaussian form of N_T persists downstream of separation, over a domain $x \in (0, L_G)$. On the contrary, N_T becomes more scattered for $x > L_G$, as shown by the roughly linear increase of σ_T. Positive skewness coefficients are compatible with a longer *outer* (i.e. toward the free stream) tail and higher values of Kt_T might indicate a stronger presence of outliers. All these elements scatch the picture of a more instable instantaneous TNTI, spread over wider regions of space by the activity of the turbulent flow.

In spite of these qualitative similarities, trends of TNTI statistics are not the same over the two ramps. The most evident difference is the value of L_G, which does not seem to scale with L_R nor with $L_R C_{h,\delta}$. With a simple visual assessment, one can put $L_G/L_R \approx 0.7$ to 0.8 on the R2 ramp, but $L_G/L_R \approx 0.2$ to 0.3 in the case of the GDR ramp. Interestingly, since it is $h_{GDR}/h_{R2} = 3$ and $L_R/h \approx 5$ for both ramps (at least for $Re_\theta < Re_{\theta c}$), L_G has similar *dimensioned* values (e.g. in mm) in the two experiments. This suggests that L_G might scale with quantities that do not vary much from one ramp to the other.

The first candidate is δ_e, which is supported by N_T keeping the form it had in the incoming boundary layer. Figure 10.8 presents the streamwise evolution of σ_T at all Re_h. δ_e is now used to normalise both σ_T and streamwise distance. Indeed, the length L_G is relatively well collapsed. As for σ_T, over L_G collapse is achieved within $5\,\%$ of δ_e, which is quite adequate if one considers that on the large fields PIV resolutions are limited and it is $\Delta_{R2} \approx 0.05\delta_e < \Delta_{GDR}$. Then, at least in first approximation, L_G seems to scale with the incoming boundary layer. Figure 10.8 shows that the δ_e scaling is less satisfactory further downstream, as different experiments do not collapse anymore. Interestingly, with this scaling datasets recorded at $Re_\theta > Re_{\theta c}$ also diverge from those at $Re_\theta < Re_{\theta c}$ (see 10.8(b)): this supports the idea of scaling data at $x > L_G$ *from the same ramp* with L_R, as done in figure 10.7(a) and figure 10.6(a). However, no Re_θ-based scaling was found common to both ramps.

A second candidate quantity that might scale L_G is ER, which is comparable in the two experiments, viz. 1.06 for the R2 ramp and 1.11 for the GDR ramp. Since the longitudinal pressure gradient is a strong function of ER (see for example Adams & Johnston (1988*a*) and considerations at § 8.4), it could be expected that L_G relates to $U\partial U/\partial x$. For simplicity, let us start with the GDR ramp, over which scaling of pressure gradients depends only on geometry throughout the flow. Figure 10.9(a) compares the streamwise evolution of skewness at $U_\infty = 20\,\mathrm{m\,s^{-1}}$ ($Re_h = 13.3 \times 10^4$) to the terms $U^*\partial U^*/\partial x^*$ and $\partial/\partial y^*\,(U^*V^* + \langle u'v'\rangle^*)$ along the TNTI, where the superscript * indicates normalisation according to table 8.2. It is pointed out that the * scaling of the longitudinal coordinate was not used, because it does not improve L_G scaling across different experiments. It appears that Sk_T follows the evolution of $U^*\partial U^*/\partial x^*$ quite faithfully, at least up to $x/L_R \approx 0.6$. Shear stresses are not completely negligible: indeed, Sk_T seems to settle to a constant value as the sum of normalised shear terms does, for $x/L_R > 0.6$. However, departure from the initial, gaussian value of Sk_T is better correlated to a local increase in normal stresses and hence to a geometric, ER-driven effect. An equivalent behaviour was observed on the streamwise evolution of flatness and it is not reported. The comparison of Sk_T with the terms $U^*\partial U^*/\partial x^*$ and $\partial/\partial y^*\,(U^*V^* + \langle u'v'\rangle^*)$ for the R2 ramp is presented in figure 10.9(b). The interpretation is now more ambiguous, since the importance of h and δ_e is comparable on the R2 flow. At first sight, the gaussian TNTI distribution seems to be broken in correspondence of an increase in total shear. However, correlation with $U^*\partial U^*/\partial x^*$ is also quite good for x/L_R between 0.7 and 1. Then, it is at least possible to describe a scenario similar to the GDR one: deviation from the gaussian distribution is triggered by normal stresses, but further downstream the new TNTI distribution is rather correlated to shear stresses. According to this view, L_G is the distance over which the pressure gradient induced by the expanding geometry breaks the spatial organisation that the TNTI had in the incoming boundary layer. We will retain this interpretation in the rest of this work.

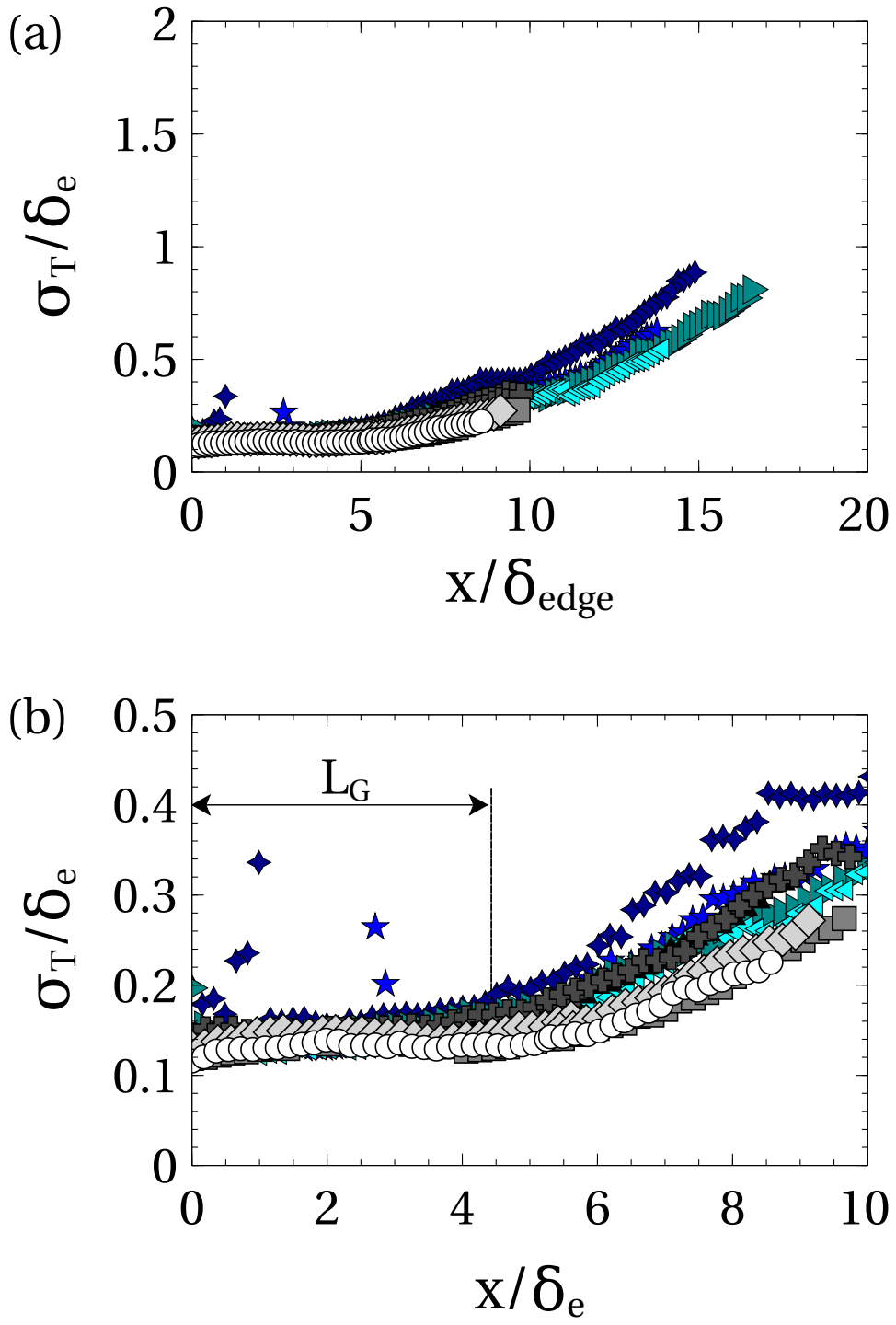

Figure 10.8: Streamwise evolution of σ_T normalised on δ_e. (a) Complete streamwise domains; (b) detailed view of $x/\delta_e \in (0, 10)$. Symbols as in figure 10.2.

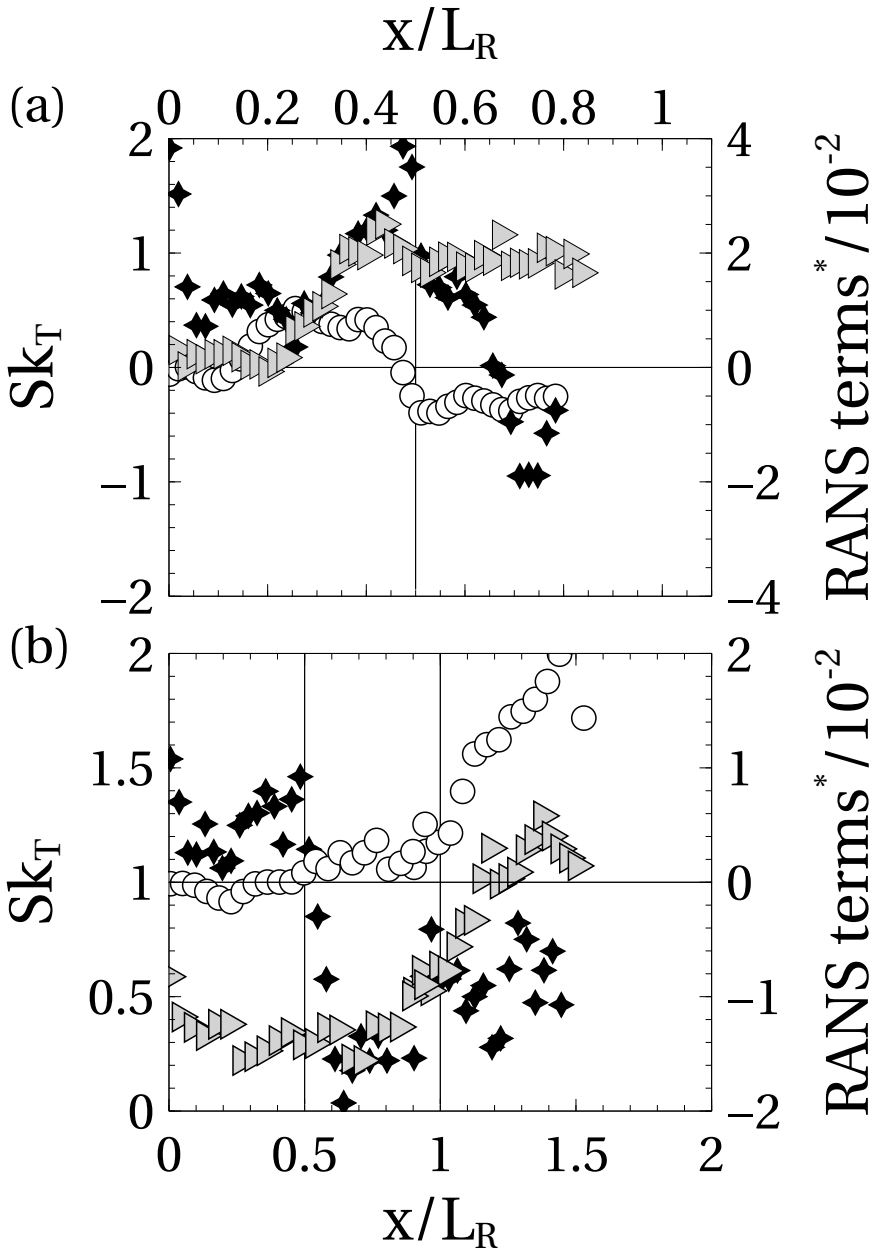

Figure 10.9: Comparison of Sk_T to the main terms of the longitudinal RANS equation along the mean TNTI: (a) GDR ramp; (b) R2 ramp. Symbols: ▶ Sk_T; ◯ $\partial/\partial y^* \, (U^*V^* + \langle u'v' \rangle^*)$; ✦$U^* \partial U^*/\partial x^*$.

10.3 Statistics of the RRI

The mean behaviour of the RRI is quite well known in literature and it has been already characterised (although indirectly) in previous sections. For example, comparison of different detection techniques was presented at § 5.4, as part of computation of L_R. Further, since L_R is defined based on the mean RRI, the discussion on the dependencies of the shear layer (section 8.5) implies that the mean RRI scales with Re_θ and that all mean RRIs collapse if normalised on L_R. The present section, then, will focus on the higher statistical moments of the RRI, which are, to the best of our knowledge, a new contribution to the understanding of separated flows. For reference, mean RRIs are reported in figure 10.10, where normalisation on h was preferred to highlight the Re_θ dependency.

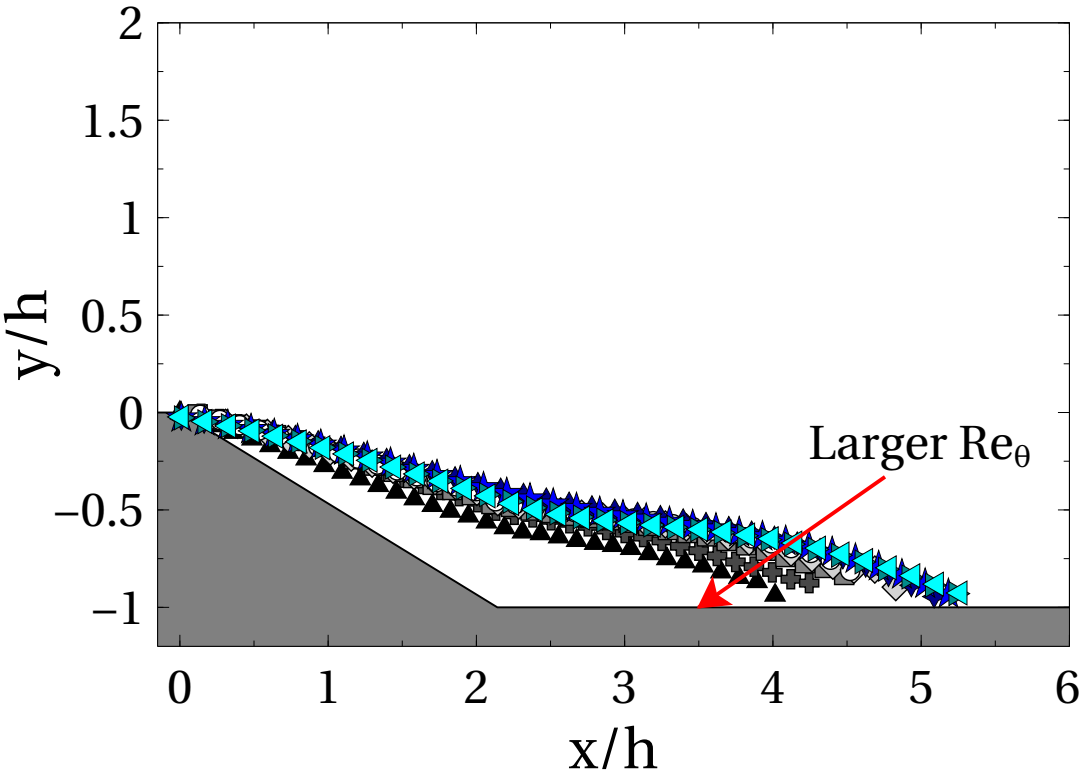

Figure 10.10: Comparison of mean RRIs at different Re_h. All curves are normalised on h. Symbols as in figure 10.2.

10.3.1 Statistical distribution

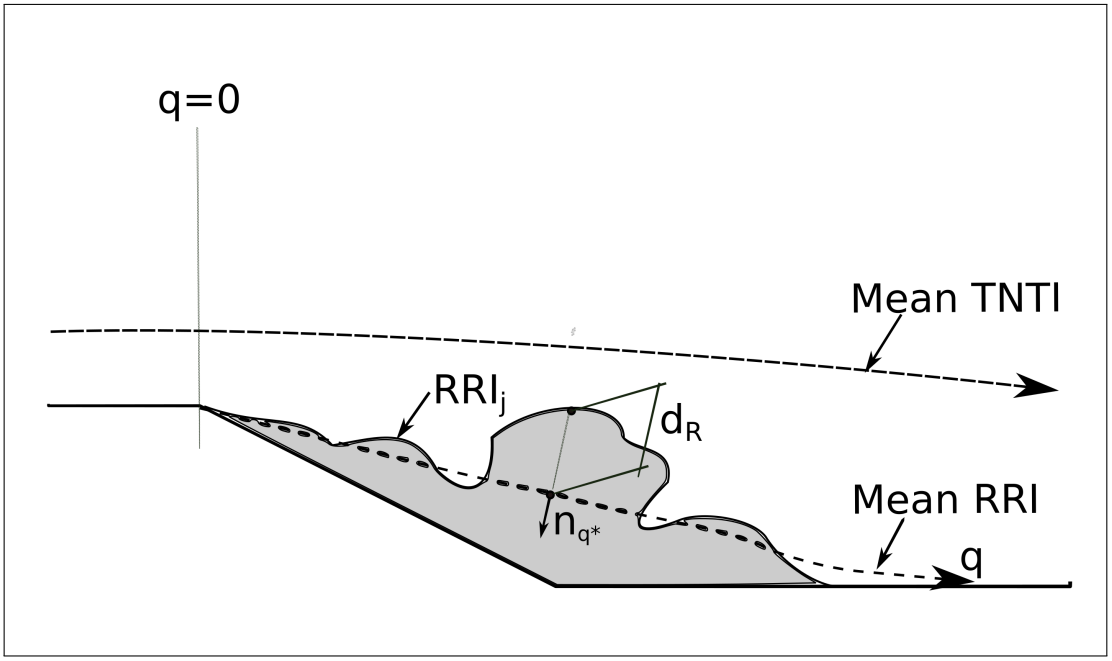

Figure 10.11: Notations and reference frames for the RRI. $d_R(q^*)$ is the position of the instantaneous RRI at the curvilinear abscissa q^*.

To study statistical distributions of the RRI, a similar frame is used as for the TNTI. With reference to figure 10.11, let q be a curvilinear abscissa defined along the mean RRI, with its origin at the mean separation point. The instantaneous position of the RRI $d_{Rj}(q)$ at, say, q^* is given by the signed distance (positive toward the free stream) from the mean RRI, measured along each normal $-\boldsymbol{n}_{q*}$. Let $N_R(q)$ be the probability density function (p.d.f.) of the instantaneous RRI position $d_{Rj}(q)$. The form of $N_R(q)$ is presented in figure 10.12 (GDR ramp) and figure 10.13 (R2 ramp), at four streamwise locations within $x/L_R = 0.2$ and $x/L_R = 0.8$. In neither case $N_R(q)$ agrees with a gaussian distribution. Initially, $N_R(q)$ has a longer inner tail, i.e. the RRI is less scattered toward the mean separated shear layer. Anyway, $N_R(q)$ becomes more symmetrical further downstream and eventually its skewness seems to change sign in a neighbourhood of the mean reattachment point. In addition, $N_R(q)$ appears to be saturated at a limit low position, that changes at different streamwise locations. Clearly, this behaviour is due to the wall, that fixes the maximum lower envelope of instantaneous RRIs.

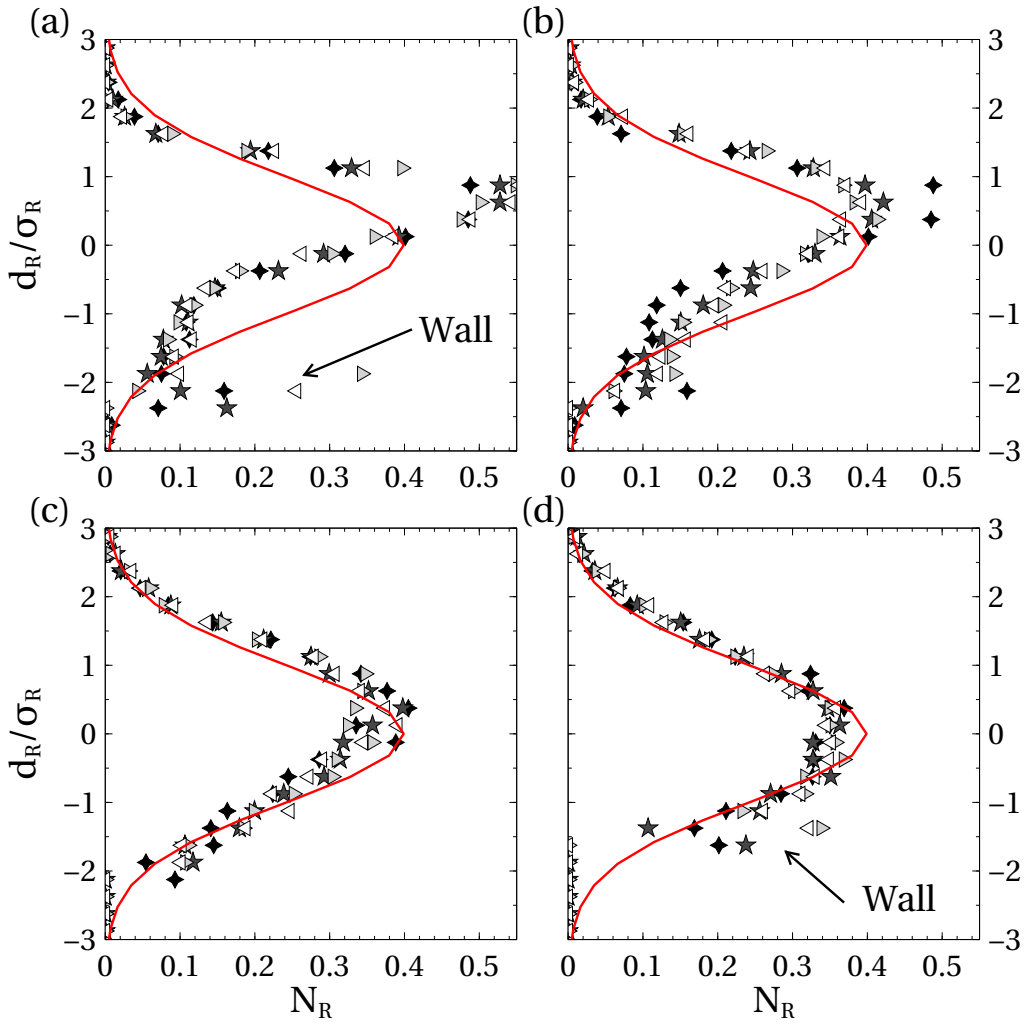

Figure 10.12: Normalised TNTI distribution on the GDR ramp. (a) $x/L_R = 0.2$; (b) $x/L_R = 0.4$; (c) $x/L_R = 0.6$; (d) $x/L_R = 0.8$. Symbols as in figure 10.4.

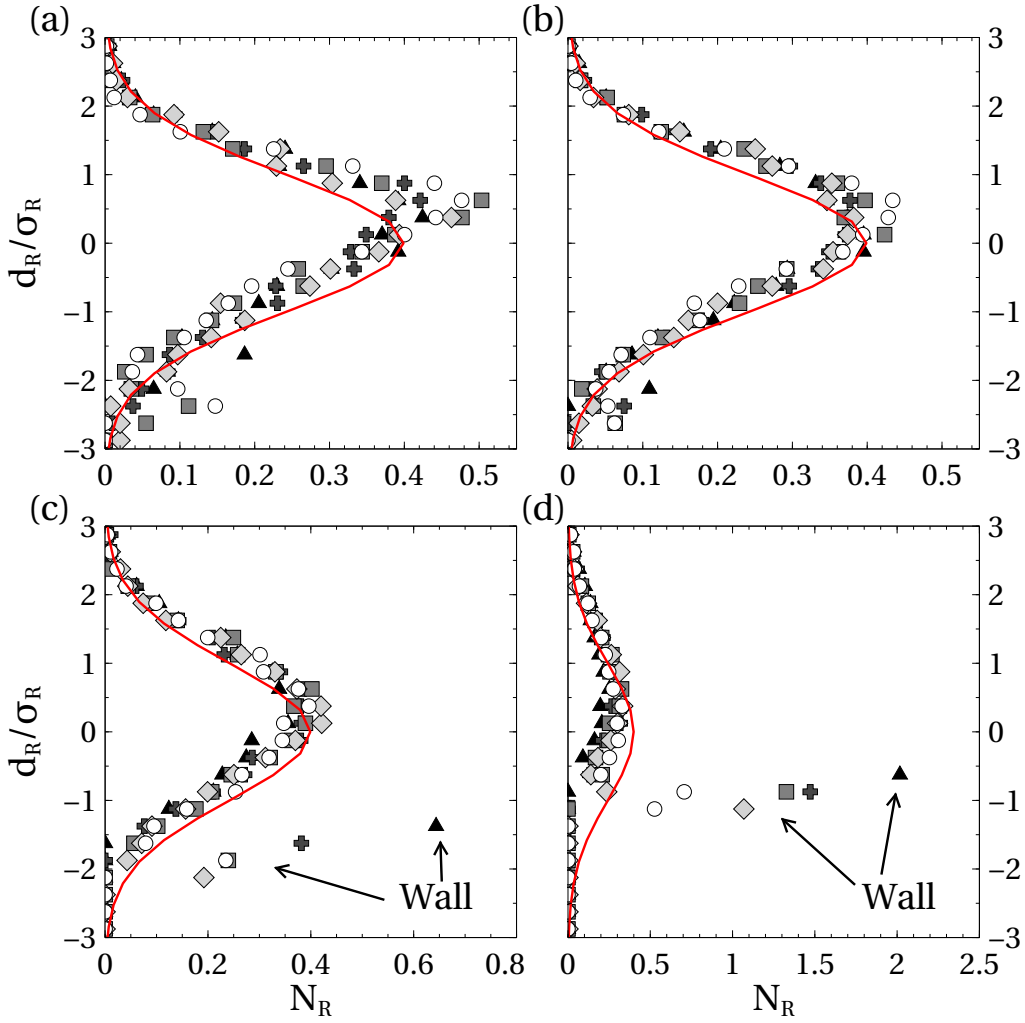

Figure 10.13: Normalised RRI distribution on the R2 ramp. (a) $x/L_R = 0.2$; (b) $x/L_R = 0.4$; (c) $x/L_R = 0.6$; (d) $x/L_R = 0.8$; (e) $x/L_R = 1.1$. Symbols as in figure 10.5.

10.3.2 Streamwise evolution of statistical moments

The streamwise evolutions of standard deviation σ_R, skewness Sk_R and kurtosis Kt_R of d_R are shown in figure 10.14 (GDR ramp) and figure 10.15 (R2 ramp). Qualitatively, statistics are relatively similar across experiments. In both cases the trend of σ_R reminds the development of the separated shear layer (see figure 8.1 and 8.1) and all σ_R curves of each ramp scale nicely with h and L_R. The same L_R scaling is quite successfull for both Sk_R and Kt_R. Sk_R increases surprisingly regularly from about -1 to about 1, while Kt_R attains a constant value of about 2.2 to 2.5. These observations, in particular the inversion of skewness along the mean RRI, confirm the qualitative analysis of N_R (see figure 10.13 and figure 10.12).

The common, regular trends of Sk_R and Kt_R are attained after an initial region marked by larger fluctuations. We indicate this first region with the symbol L_V. L_V appears to increase with the order of the statistical moment. It is $L_V/L_R = 0$ for σ_R on both ramps, even if differences between the two trends are important and will be commented later on; on the GDR ramp (respectively R2 ramp) it is $L_V/L_R \approx 0.1$ to 0.2 (0.3 to 0.4) for Sk_R; it is $L_V/L_R \approx 0.2$ to 0.3 (0.6 to 0.8, with the exception of $Re_h = 7 \times 10^4$) for Kt_R. The extent of L_V is systematically higher for the R2 ramp than for the GDR ramp, but the ratio h_{GDR}/h_{R2} is such that, for each statistical moment, L_V has roughly the same dimensional value in the two experiments. This being so, L_V does not scale with L_R (and hence with h). Instead, it appears that L_V scales well with δ_e, as shown in figure 10.16. These observations supports a parallel between L_V and L_G: both these lengths measure the streamwise range over which interface statistics are still sizeably influenced by the incoming boundary layer. Of course, variation with the order of the statistical moment is a particularity of L_V only. Anyway, in the case of Kt_R it is $L_V \approx L_G$, which seems to imply that the effects of δ_e extend on the same domain at both interfaces, albeit more sensitive statistical tools are necessary to detect them along the RRI. It is pointed out that Kt_R does not collapse with δ_e as well as Sk_R, in particular for some of the highest Re_θ of each experiment. This observation suggests that some Re_θ effects might also exist within L_V. However, such supposed effects do not seem related to $Re_{\theta c}$, nor to another value of Re_θ common to both ramps. For these reasons, deviations from the δ_e scaling seem more probably due to accidents within the datasets, more visible on higher statistical moments, rather than to real flow physics.

In the case of the RRI, it is less straightforward to identify the possible effects of ER, because the term $U\partial U/\partial x$ is null by definition. The comparison of the evolution of higher statistical moments with the remaining terms of the longitudinal RANS equation does not yield definitive results either. Figure 10.17 reports Sk_R, Kt_R and the term $\partial/\partial y^* \left(U^*V^* + \langle u'v' \rangle^*\right)$ along the RRI. The symbol * indicates normalisation in the sense of $\delta_e/h \ll 1$ (see table 8.2), because the correction for boundary layer effects in the neighbourhood of rettachement (for $\delta_e/h \gg 1$) is not essential in the present framework. Over the R2 ramp, some link might exist between the linear trend of Sk_R and the evolution of total shear stresses. This relationship could be extended to Kt_R too, if one considers that the effect of shear includes the entire decreasing trend that brings to $Kt_R \approx 2.5$. Unfortunately, the behaviour of the GDR ramp does not fit in this picture simply. Alternatively, it was found on both ramps that the turbulent production $\mathcal{P}$, evaluated at the centerline of the separated shear layer, seems to be well correlated to Sk_R and in particular to Kt_R (figure 10.18). It is stressed that $\mathcal{P}$ *along the mean RRI* does not compare well with RRI statistics. This finding suggests that the instantaneous behaviour of the RRI (represented here by higher order statistics of N_R) might relate to re-entrainment of low-momentum fluid into the separated shear layer. At separation, this low-momentum fluid rising through the RRI interacts with strong mean shear, to produce turbulent kinetic energy. Further downstream, the persisting fair correlation between statistics of N_R and $\mathcal{P}$ might be due to the backflow which, in average, equilibrates entrainment at separation. However, further work is needed to confirm this idea.

As a final note on this subject, it seems important to stress the striking difference with respect to the TNTI: in particular in the case of the GDR ramp, the breakdown of N_T seems much more abrupt than the process that brings statistical moments of N_R to their regular trends. It is thought that this difference might be explained by the nature of the interaction between different elements of the flow. In the case of the TNTI, the incoming flow encounters an intense, local pressure rise: as for a classical boundary layer in an adverse pressure gradient, the reaction can be rapid and with large consequences on the structure of the flow. As for the RRI, in essence we assist to the transition from one sheared flow to another: it seems reasonable that the reorganisation of the flow takes place more smoothly.

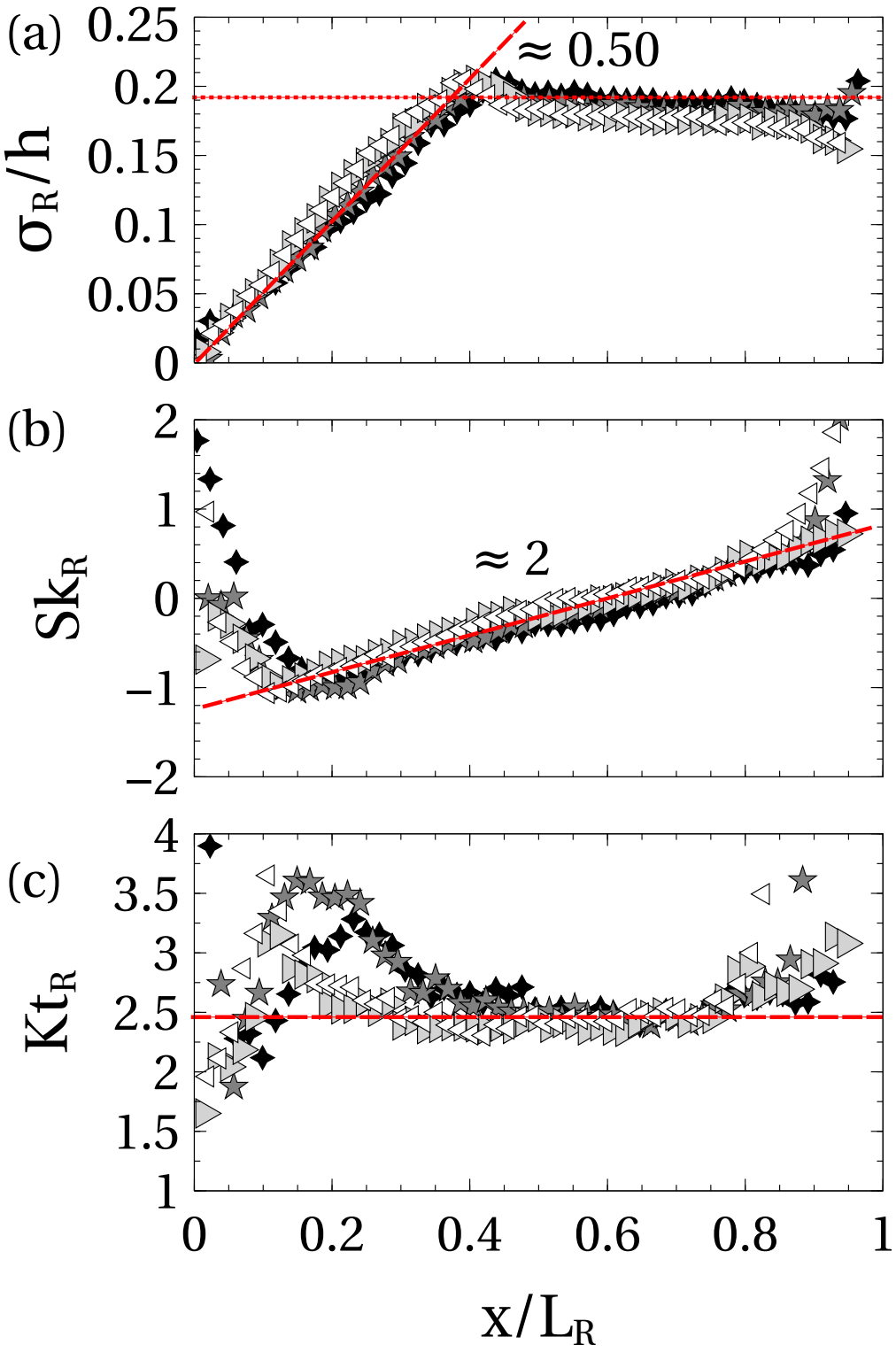

Figure 10.14: Streamwise evolution of RRI statistics on the GDR ramp: (a) normalised standard deviation σ_R/h; (b) skewness coefficient $Sk_R = \mu_{R3}/{\mu_{R2}}^{3/2}$; (c) kurtosis coefficient $Kt_R = \mu_{R4}/{\mu_{R2}}^2$. Other symbols as in figure 10.4.

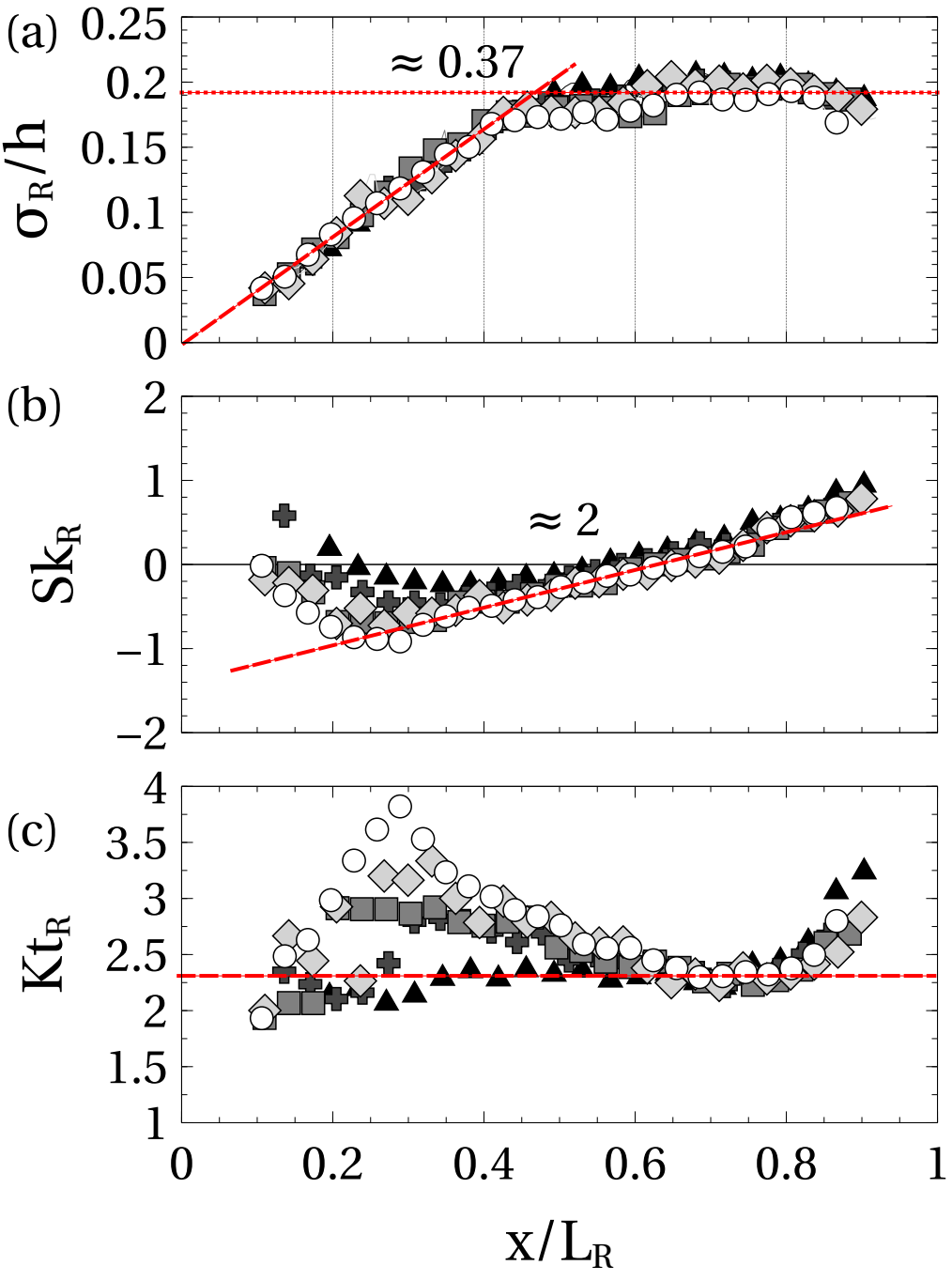

Figure 10.15: Streamwise evolution of RRI statistics on the R2 ramp: (a) normalised standard deviation σ_R/h; (b) skewness coefficient $Sk_R = \mu_{R3}/{\mu_{R2}}^{3/2}$; (c) kurtosis coefficient $Kt_R = \mu_{R4}/{\mu_{R2}}^2$. Other symbols as in figure 10.5.

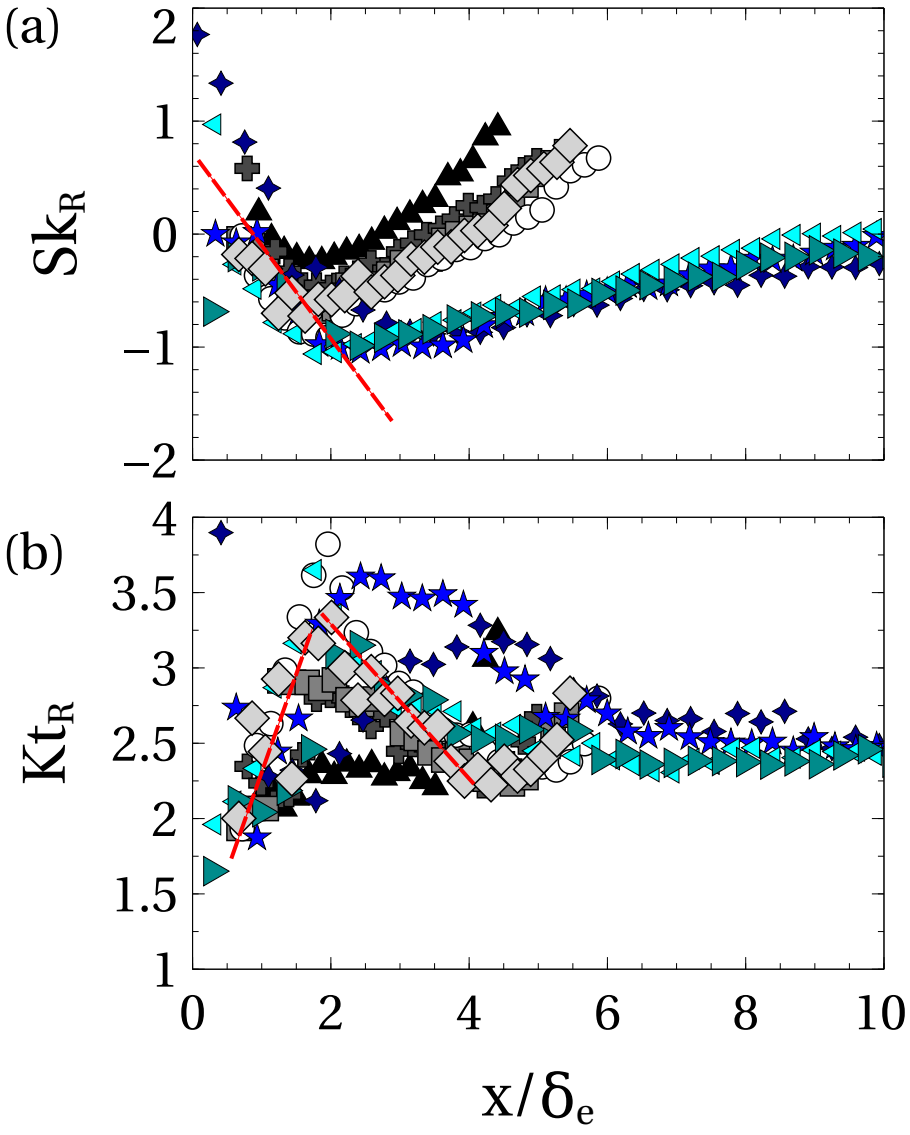

Figure 10.16: Streamwise evolution higher order statistics, normalised on δ at the upper edge of the ramp: (a) Sk_R; (b) Kt_R. Symbols as in figure 10.2.

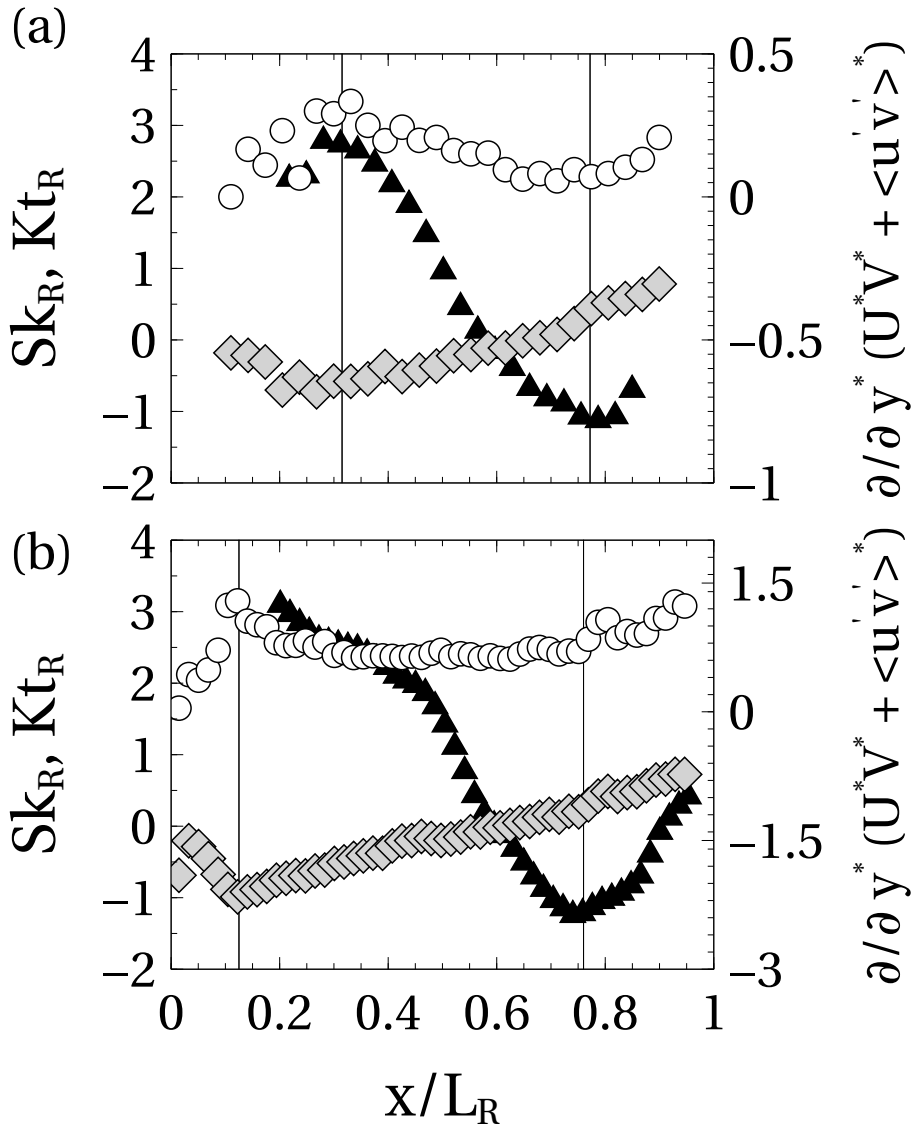

Figure 10.17: Comparison of Sk_R and Kt_R to total shear along the mean RRI: (a) R2 ramp; (b) GDR ramp. Symbols: ◊ Sk_T; ◯ Kt_R; ▲ $\partial/\partial y^* \, (U^*V^* + \langle u'v' \rangle^*)$.

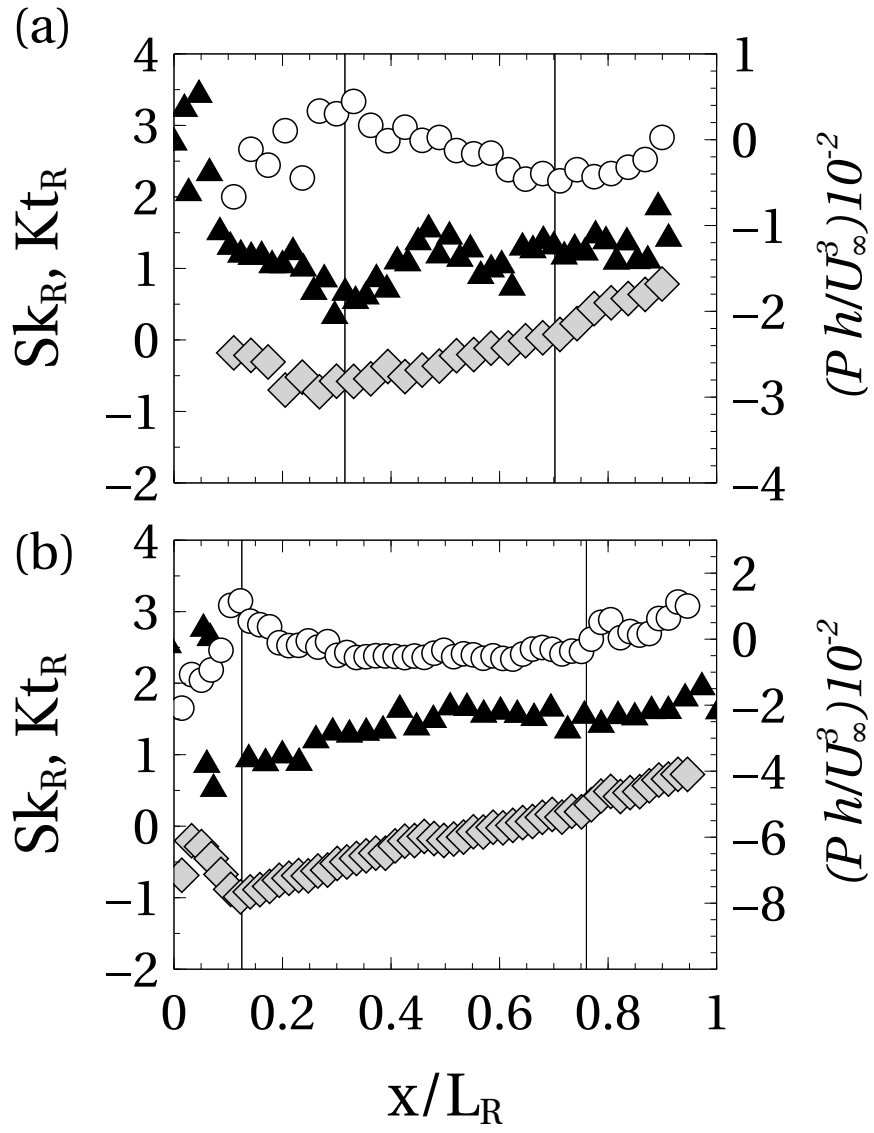

Figure 10.18: Comparison of Sk_R and Kt_R to $\mathcal{P}$ at the centerline of the separated shear layer: (a) R2 ramp; (b) GDR ramp. Symbols: ◊ Sk_T; ○ Kt_R; ▲ $\mathcal{P}$.

We now consider the streamwise evolutions of σ_R, reported in figure 10.14(a) (GDR ramp) and figure 10.15(a) (R2 ramp). As already mentioned, both sets of curves scale well with h and reach similar maximum values, which are also quantitatively comparable to the thickness θ_{SL} (figure 8.1 and figure 8.2). This suggests that scatter of the RRI is related to the development of the separated shear layer, which is evident by the very choice of the RRI as one of its interfaces. However the growth rate of σ_R is not the same on the two ramps, which implies that σ_R changes in slope earlier on the GDR ramp than on the R2 ramp. Moreover, the growth rate of σ_R is higher than shear layer growth rate (which is approximatively $0.235 \pm 0.05 h/L_R$, see figure 8.3): in particular, it is almost twice as high in the case of the GDR ramp. Significantly, all σ_R curves seem to collapse acceptably well if streamwise distance is scaled on $L_R C_{h,\delta}$, as reported in figure 10.19. This observation implies that the incoming boundary layer has an impact on σ_R too, as on other RRI statistics, and this becomes stronger as δ_e/h increases. In this respect, it is pointed out that with high values of δ_e/h the evolution of σ_R relates more closely to shear layer growth than with low ones. This might be due to the fact that when the incoming boundary layer dominates the flow, the separated shear layer is pushed to the wall: the RRI might then move *with* the separated shear layer, similarly to the edge of a rigid body, rather than folding freely at its lower boundary. Interestingly, none of the RANS terms studied at § 8.4 seems to evolve with $L_R C_{h,\delta}$ along the mean RRI. This suggests that the evolution of σ_R might be linked to turbulent activity within the shear layer, similarly to Sk_R and Kt_R.

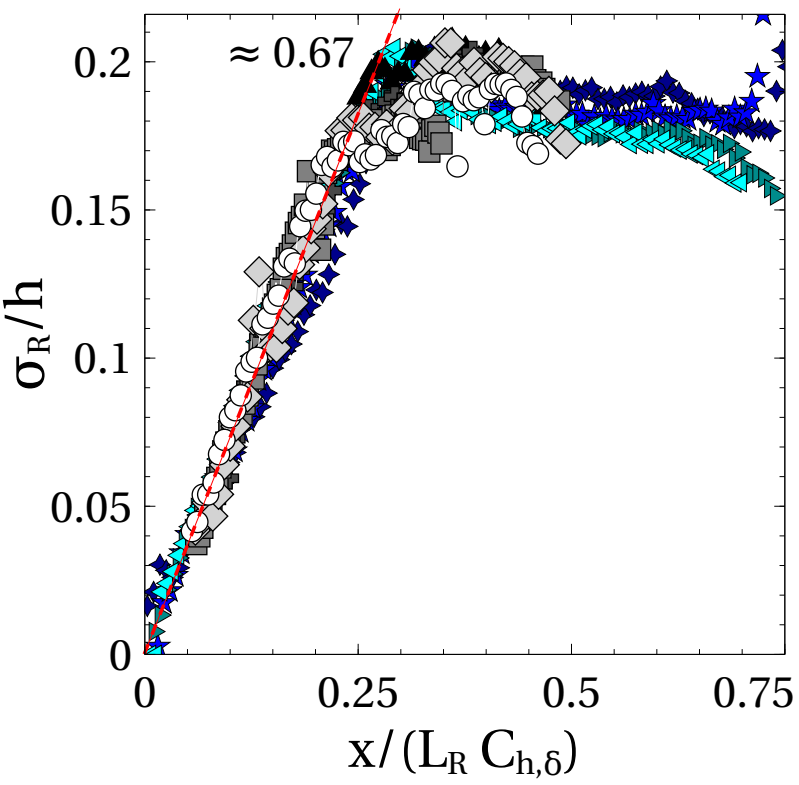

Figure 10.19: Streamwise evolution of σ_R normalised on $L_R C_{h,\delta}$. Symbols as in figure 10.2.

10.4 Discussion

The investigation of one-point statistics of the TNTI and the RRI suggests that the massively separated flow under study might be thought of as the interaction of three simpler flows: a boundary layer, a developing, separated shear layer and a pressure recovery produced by a diffuser. One can associate one parameter to each of these flows, respectively δ_e, h and ER. Of course h and ER are not independent and this distinction is only an ideal one. In this research, δ_e and ER are essentially constant, so that their influence cannot be tested per se. Instead, they form a sort of *background flow*: ER determines the minimum pressure recovery of the separated flow, while δ_e scales properties of the incoming boundary layer. The length L_G gives a measure of relative strength of the incoming boundary layer with respect to the pressure recovery induced by geometry. Accordingly, L_G is independent of h in this study.

For what concers h, available values seem to be sufficiently far apart to highlight different relative weights of the separated shear layer, with respect to the background flow. On the GDR ramp, the separated shear layer dominates the region of the RRI. The influence of the background flow is limited to a neighbourhood of the mean separation point, which is identified by a length $L_V \approx L_G$. Since it is $\delta_e \ll h$, it is also $L_V < L_R$. The discussions at § 6.2.1 and § 8.4 show that for values of δ_e/h similar to those of the GDR ramp (or lower) the wall pressure distribution is almost universal (Roshko & Lau (1965), Bradshaw & Wong (1972) and Adams & Johnston (1988*a*)). This means that the separated shear layer (and hence h) also determines the pressure distribution at the wall. Further, induced wall pressures must always be higher than those imposed by the background flow (see § 6.2.1).

The interaction is much different in the case of the R2 ramp. Overall, the separated shear layer still imposes its topology, but the influence of the background flow persists over most of the separation region. Indeed, this time it is $L_V \approx L_G \approx L_R$. It is important to remind that L_G and L_V do not change with respect to the GDR ramp, but the separated shear layer is *weaker* because h is lower. Accordingly, L_R is also shorter (but L_R/h is roughly constant for a given Re_θ). In this respect, it is interesting to pay further attention to the findings of Song & Eaton (2004). These authors use two-point correlations to investigate the structure of the separated flow behind a smooth ramp. Boundary layer thickness is comparable to our experiments and $ER \approx 1.16$. The ratio δ_e/h ranges between 1.2 and 1.4: such values are sizeably higher than in this study, but they might be well suited to highlight asymptotic behaviours that are already at play over the R2 ramp. Song & Eaton (2004) find that the structure of the separated flow depends on properties of the incoming boundary layer, even within the recirculation region. Song & Eaton (2004) interpret this observation as a sign that large eddies that exist in the outer part of the incoming boundary layer dominate over structures produced by shear-layer separation. This view is consistent with observations on the R2 ramp. As for pressure distribution, it is probably influenced by both flows, with a decreasing effect on $C^*_{p,r}$ (see § 6.2.1 and references therein). In any case, the pressure recovery cannot be lower than the one imposed by ER (Adams & Johnston (1988*a*)).

In the region of the TNTI, the background flow seems to dominate over L_G, with little or no effect of the separated shear layer. This behaviour is clear in the case of the GDR ramp, but also identifiable over the R2 ramp, albeit with some ambiguity due to the similarity of scales involved in the flow. In any case, shear stresses become the most important term further downstream. Once again, results by Song & Eaton (2003) and Song & Eaton (2004) offer very interesting comparison. Indeed, these authors find that turbulent structures generated by the shear layer dominate the recovery region, at least far from the wall. These results agree well with observations on the R2 ramp, as expected based on the relatively *high* ranges of δ_e/h spanned by the two experiments. However, GDR data allow to extend the analysis to *low* δ_e/h, bringing new insight into this matter. In particular, shear stresses can become dominant in the outer region of the flow much upstream of reattachment. This suggests that the structure of the flow observed by Song & Eaton (2003) and Song & Eaton (2004) is not due to shear layer impingment and boundary layer recovery, but to the strength of the separated shear layer relative to the background flow.

11

Mean field mass entrainment

Entraînement de masse du champ moyen

Ce chapitre analyse le transfert de masse au travers des frontières de la couche cisaillé décollée. Ce sujet est d'une importance fondamentale pour la compréhension des écoulements décollés et pour leur contrôle, pour au moins deux raisons. Premièrement, plusieurs études ont montré que l'un des mécanismes moteurs de ces écoulements est l'équilibre dynamique entre le *backflow* et la quantité de fluide qui est réentrainée par la couche cisaillée, dans la région du décollement. Deuxièmement, les résultats présentés à la section 8.2 (et suivantes) ont montré que la taille de la bulle de recirculation est liée au taux d'épaississement de la couche cisaillée. Ce dernier est principalement piloté par l'entraînement de fluide extérieur vers la couche cisaillée. Dans la perspective du contrôle d'écoulement, il semble donc important de mieux comprendre ces phénomènes et d'en étudier les lois d'échelle. Cela peut être fait à partir d'un bilan de masse, calculé sur un volume de contrôle $\mathcal{V}_c$ représentatif de la couche cisaillée, à partir de la formulation intégrale de l'équation de continuité (éq. 11.2). Un choix possible de $\mathcal{V}_c$ est représenté en figure 11.2 : $\mathcal{V}_c$ est délimité par une ligne verticale à l'arête de la rampe descendante, par la RRI moyenne, par une ligne verticale au point de recollement moyen et par la TNTI moyenne. Ces quatre bords sont numérotés de 1 à 4, dans l'ordre donné ci-dessus. Le tableau 11.1 montre les flux de masse moyens à travers des frontières de $\mathcal{V}_c$, normalisés sur $\rho h U_\infty$. La normalisation est indiquée par le symbole *. On a $\dot{m}_2^* \approx 0$, ce qui est expliqué par le fait que la RRI est le seul contour perméable de la bulle de recirculation moyenne, qui est un écoulement bidimensionnel. Au contraire, $\dot{m}_4^* \neq 0$, parce que la TNTI n'est pas une ligne de courant. De plus, on observe que $\dot{m}_4^*$ n'est pas négligeable : sur la rampe R2, il correspond à au moins $30\,\%$ de la masse apportée par la couche limite ($\dot{m}_1^*$) et sa contribution devient même dominante sur la rampe GDR. Ces observations confirment que l'entraînement de fluide irrotationnel a un rôle important dans le fonctionnement de la couche cisaillée décollée.

Malgré la condition $\dot{m}_2^* = 0$, les lois d'échelle du transfert de masse à travers de la RRI peuvent être étudiées à partir des flux de masse locaux (indiqués par $\dot{m}_{x2}^*$), dont la formulation normalisée est donnée en éq. 11.5. L'évolution de $\dot{m}_{x2}^*$ le long de la RRI est montrée en figure 11.4. Dans la direction longitudinale, toutes les courbes sont bien mises en échelle par L_R et $\rho h U_\infty$, sauf dans $x/L_R \in (0.7, 1)$: dans cette région, la couche limite influence les courbes de la rampe R2, comme observé précédemment pour les gradients de pression. La condition $\dot{m}_2^* = 0$ pourrait impliquer une dépendance similaire dans la zone à l'aval du décollement, mais la qualité de nos données PIV à proximité de l'arête ne permet pas de vérifier cette hypothèse. La figure 11.4 montre que $\dot{m}_{x2}^*$ est approximativement antisymétrique, ce qui est cohérent avec $\dot{m}_2^* = 0$. On peut donc étudier séparément le transfert de masse sur $x/L_R < 0.5$ et $x/L_R > 0.5$. La première quantité interessante est la vitesse d'entraînement moyenne v_E^A, qui est calculée avec l'éq. 11.5 pour chacune de deux moitiés de $\dot{m}_{x2}^*$. Le tableau 11.2 montre que $v_E^A/U_\infty \approx 0.0224$, indépendamment du domaine de calcul, de h and Re_θ. Etant donné que la longueur de la RRI évolue comme L_R, ce dernier résultat implique que la masse transférée sur $x/L_R < 0.5$ et $x/L_R > 0.5$ évolue comme Re_θ^m (éq. 11.7). Cette relation est bien vérifiée par les flux de masse calculés sur $x/L_R > 0.5$ (figure 11.4). Cela n'est pas le cas sur $x/L_R < 0.5$, mais ce problème semble être dû, une fois de plus, à la qualité des données PIV.

En conclusion, il semble que l'entraînement au travers de la RRI soit dimensionné par des propriétés de la couche limite amont.

Dans le cas de la TNTI, l'analyse des flux locaux $\dot{m}^*_{x4}$ révèle une claire dépendance en Re_θ de v^A_E/U_∞ (figure 11.5) et une influence marquée de la couche limite à l'amont, si δ_e/h est suffisamment élevé. Ces comportements ont été modélisés dans l'éq. 11.11, à l'aide d'une loi de puissance sous la forme Re_θ^{-m} et par le coefficient $C_{h,\delta}$. L'interprétation physique de l'éq. 11.11 est quelque peu problématique, parce qu'elle semble sous-estimer l'apport de la vitesse verticale V pour $\delta_e/h \to 0$. Pourtant l'accord avec les données est très bon, ce qui autorise à retenir l'éq. 11.11 dans la suite. Pour trouver la loi d'échelle de $\dot{m}^*_4$, il est aussi nécessaire de comprendre le comportement de L^A, qui est la longueur moyenne de la TNTI au dessus de la bulle de recirculation. Les observations du chapitre 10 suggèrent que $L^A \sim L_R \sim hRe^m_\theta$ si $\delta_e/h \ll 1$. En utilisant cette loi d'échelle et l'éq. 11.11, il est aisé de montrer que sur la rampe GDR on a $\dot{m}^*_4 \sim C_{h,\delta}$ (éq. 11.15). Si l'on considère que $C_{h,\delta} \to 1$ sur la rampe GDR, cette expression prédit que lorsque la couche cisaillée domine l'écoulement, on a $\dot{m}^*_4 \sim const$, ce qui est bien vérifié par les données du tableau 11.1 : autrement dit, l'évolution en Re^m_θ de L^A/h est compensée par celle en Re_θ^{-m} de v^A_E/U_∞. Le chapitre 10 montre que $L^A \sim \delta_e$ si $\delta_e/h \gg 1$. Dans ce cas, l'évolution de $\dot{m}^*_4$ ne dépend plus uniquement de $C_{h,\delta}$, mais elle conserve aussi la dépendance en Re_θ^{-m} portée par v^A_E/U_∞. Cela est modélisé dans l'éq. 11.17. Cette relation ne peut pas être vérifiée rigoureusement, parce que les valeurs de δ_e/h disponibles dans nos bases de données ne sont pas assez élevées. Néanmoins, l'approximation de l'éq. 11.17 fournie par les données de la rampe R2 semble prometteuse (éq. 11.18).

Les flux de masse qui traversent la TNTI et la RRI sur $x/L_R \in (0, 0.5)$ contribuent à l'épaississement de la couche cisaillée, selon la relation établie par l'éq. 11.19 (Pope (2000)). On calcule v^A_E/U_∞ pour la TNTI, en appliquant l'éq. 11.5 séparément sur $x/L_R \in (0, 0.5)$ et $x/L_R \in (0.5, 1)$. Cela permet de vérifier relativement bien l'éq. 11.19 sur les deux rampes, comme montré en figure 11.6. La principale contribution à l'éq. 11.19 est fournie par la RRI, en particulier sur la rampe R2 à bas Re_θ.

Il ressort du tableau 11.1 que $\dot{m}_1$ n'est pas correctement normalisé par $\rho h U_\infty$. Il semble plus pertinent d'adopter une normalisation sur $\rho\delta_e U_\infty$, ce qui est en meilleur accord avec les données disponibles (tableau 11.4). Pour ce qui concerne $\dot{m}_3$, l'éq. 11.20 implique que sa loi d'échelle est déterminée par l'influence de δ_e/h sur $\dot{m}_4$. Si $\delta_e/h \ll 1$, l'éq. 11.20 prédit $\dot{m}^*_3 \sim const$. Le tableau 11.1 semble aller dans le sens de cette relation. De plus, dans ce cas, on vérifie que $\dot{m}_1/\dot{m}_3 \approx \delta_e/h$ (tableau 11.5). Au contraire, si $\delta_e/h \gg 1$, l'éq. 11.20 prévoit des dépendances en δ_e/h et Re_θ^{-m}. Une fois encore, les valeurs de δ_e/h disponibles sont trop basses pour vérifier ce comportement, mais le tableau 11.1 montre pour la rampe R2 une claire évolution de $\dot{m}^*_3$ avec Re_θ, ce qui est un élément encourageant.

Les résultats de ce chapitre montrent bien que le *backflow* équilibre la masse de fluide entraînée par la couche cisaillée détachée. De plus, l'équilibre à des valeurs de Re_θ différentes semble être atteint par le changement de la taille de la bulle de recirculation, plutôt que par celui de la vitesse d'entraînement. La normalisation des flux de masse à la TNTI est non trivial en raison d'une influence forte par un fort effet du paramètre δ_e/h, mais généralement des vitesses d'entraînement plus fortes semblent être corrélées à des L_R plus courtes. Les observations au chapitre 8 suggèrent que les comportements à la RRI et à la TNTI semblent être contrôlés par le mélange turbulent au recollement. Il pourrait s'agir d'une caractéristique générale des couches cisaillées décollées, tandis que la dépendance en Re_θ pourrait être une particularité du décollement d'une couche limite turbulente. Cette hypothèse fera l'objet de travaux futurs.

11.1 Introduction

In this chapter we investigate mass entrainment through the separated shear layer. The objective is two fold. In the first place, important previous works, as for example Chapman *et al.* (1958) and Adams & Johnston (1988*a*), stated that one of the main features of massively separated flows is that the backflow balances the amount of mass being re-entrained into the separated shear layer through the RRI. In the perspective of separation control, it seems of great interest to further investigate this behaviour through the analysis of mass entrainment. In the second place, results at § 8.2 (and following) highlighted that the size of the recirculation region is inversely proportional to the rate of growth of the (free-like) shear layer downstream of separation. The latter is determined by entrainment through the boundaries of the shear layer (see Pope (2000)). Then, a fundamental investigation of mass fluxes through the TNTI and the RRI is crucial to provide a strong background to control strategies aiming at tuning the properties of the separated region (e.g. L_R) by modifing the rates of entrainment into the shear layer (among numerous examples, see Sigurdson (1995), Chun & Sung (1996) and more recently Berk *et al.* (2017)). In the analyses presented in this chapter, we will focus on the identification of the scaling parameters of mass fluxes. Other than being of great interest for flow control, scaling parameters are likely to reflect, once again, the competition between the incoming boundary layer (represented by the scale δ_e) and the separated shear (represented by the scale h).

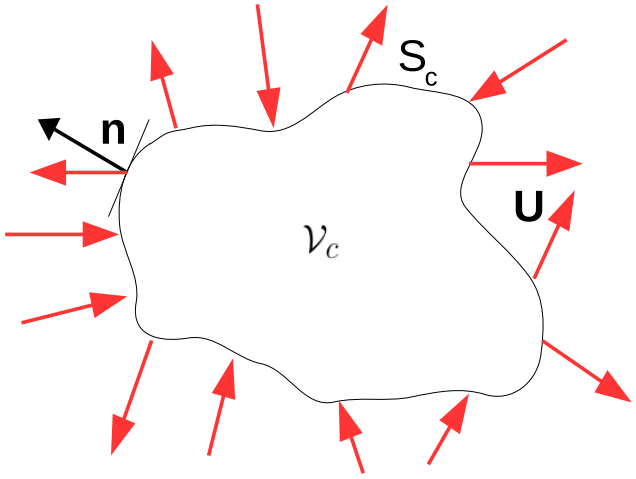

Figure 11.1: Representation of a generic control volume $\mathcal{V}_c$. The symbols $\boldsymbol{n}$ indicates a local normal to S_c, that is the boundary of $\mathcal{V}_c$. The velocity field $\boldsymbol{U}$ along S_c is represented with red arrows.

11.2 Continuity equation in integral form

To begin with, the continuity equation (eq. 2.9) needs to be reformulated in its integral form, which is much more appropriate (and agile) to compute balances. Given a generic control volume $\mathcal{V}_c$ (see figure 11.1), the amount of mass transported by an incompressible flow through $\mathcal{V}_c$ can be obtained by integrating eq. 2.9 over $\mathcal{V}_c$, which gives:

$$\int_{\mathcal{V}_c} \frac{\partial U_i}{\partial x_i} \mathrm{d}V = 0, \tag{11.1}$$

where, as usual, repeated indexes indicate summation. By invoking the Gauss-Green-Ostrogradsky theorem, this integral on the volume $\mathcal{V}_c$ can be reduced to a surface integral on the boundary $\partial\mathcal{V}_c = S_c$, as follows:

$$\oint_{S_c} U_i n_i \mathrm{d}S = 0, \tag{11.2}$$

where n_i is the local normal to S_c, pointing outward of $\mathcal{V}_c$. This expression indicates that in an incompressible flow mass fluxes through the boundary of a volume must balance out, i.e. that no internal mass source or

sink can exist. It is reminded that our PIV data do not resolve the spanwise velocity component. However, since the mean field is bidimensional (see figure 6.5 and figure 6.6), it is justified to compute mass fluxes from PIV images.

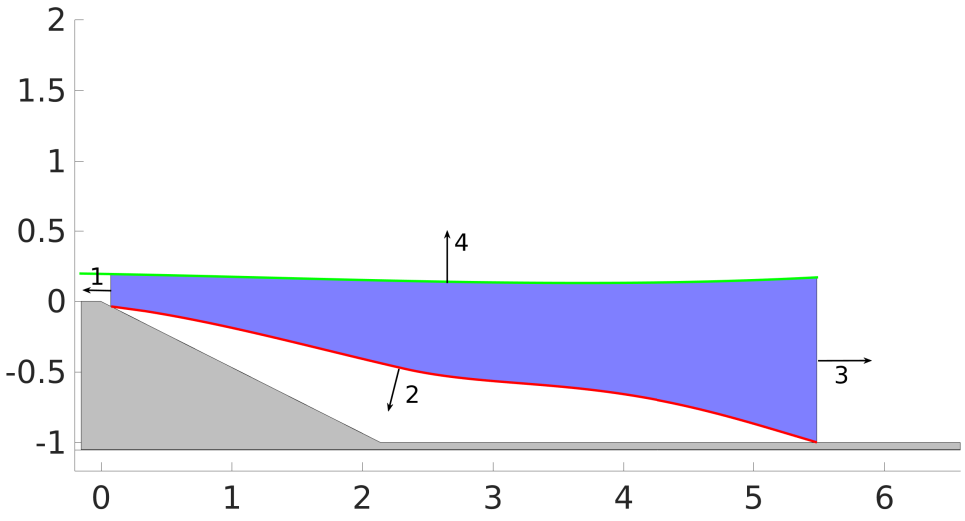

Figure 11.2: Control volume including the separated shear layer at $Re_h = 13.3 \times 10^4$. Mean TNTI. Mean RRI.

11.2.1 Application to the separated shear layer

It is now important to define $\mathcal{V}_c$ as for it to be representative of the separated shear layer. In force of the discussion of chapter 9 and chapter 10, a straightforward choice is a control volume $\mathcal{V}_c$ delimited by the mean RRI, the mean TNTI and two vertical segments, placed at the positions of the mean separation point (called *inlet*) and mean reattachment point (called *outlet*). One example of $\mathcal{V}_c$ at $Re_h = 13.3 \times 10^4$ is given in figure 11.2. Then, starting from eq. 11.2 and considering that the mean field is bidimensional, the total mass flux per spanwise unit length through each of the sides of V_c is given by:

$$\dot{m}_j = -\rho \int_{L_j} U_i(l) n_i(l) \mathrm{d}l = -\rho \int_{L_j} \left(U(l) \sin(\phi(l)) + V(l) \cos(\phi(l)) \right) \mathrm{d}l, \tag{11.3}$$

where L_j is the length of one side, l a curvilinear abscissa and ϕ is the angle between $\boldsymbol{n}(l)$ and the Y axis. The index j goes from 1 to 4. $j = 1$ indicates the inlet at the mean separation point; then, j increases counterclockwise, so that $j = 4$ identifies the mean TNTI. Of course, eq. 11.2 implies that $\sum m_j = 0$. For all RRIs, it is $\boldsymbol{n}(l) = -\boldsymbol{\nabla} U / |\boldsymbol{\nabla} U|$. In the case of the TNTI, it is $\boldsymbol{n}(l) = \boldsymbol{\nabla} U / |\boldsymbol{\nabla} U|$ for the GDR ramp. On the R2 ramp, instead, the energy-based definition of the TNTI is retained, and hence the local normal is given by $\boldsymbol{n}(l) = -\boldsymbol{\nabla} \tilde{k} / |\boldsymbol{\nabla} \tilde{k}|$. Indeed, the energy-based TNTI allows a simple approximated assessment of instantaneous local entrainment velocities, by using eq. 12.6. This is an important advantage, enabling a qualitative discussion of small-scale entrainment (see § 12.3) that outweights the inconvenient of different interface definitions. Moreover, comparisons shown in chapter 9 and chapter 10 assure that this inconsistency does not have a major impact on the shape of instantaneous and mean TNTIs, so that the influence on mass balance should be negligible.

11.3 Mean mass balance

Before discussing measured mass fluxes, it is interesting to draw a preliminary, intuitive image of how mass is transported through S_c. Firstly, it is worth noticing that $\dot{m}_2$ must be zero, since the RRI is the only permeable boundary of the recirculation bubble, which is, in average, two-dimensional and stationary. This is consistent with the idea that backflow and shear layer entrainment through the RRI must balance out (Chapman *et al.* (1958), Adams & Johnston (1988*b*)). Scaling of mass entrainment through the RRI, obtained with a local analysis, will be described at § 11.4. The topology of the flow also suggests that $\dot{m}_1$ (at the mean separation point) will be positive and $\dot{m}_3$ (at the mean reattachment point) negative. Since in general the TNTI is not a streamline, it will then be $\dot{m}_4 = -\dot{m}_3 - \dot{m}_1 \neq 0$. Mean mass fluxes measured at each available Re_h are reported in table 11.1, normalised on $\rho h U_\infty$ (symbol *). All measurements fit well in the qualitative description of mass exchanges given above. Uncertainties on the mass balance are mild and they appear to be mainly due to laser reflections, that introduce corrupted velocity vectors near the wall, in particular in a neighbourhood of the mean separation point. In any case, our results evidence that $\dot{m}_4$ is not negligible. On the R2 ramp, the TNTI contributes to the mass balance with at least $30\,\%$ of the mass injected into $\mathcal{V}_c$ by the separating boundary layer. The role of the TNTI is even stronger on the GDR ramp, over which $\dot{m}_4$ becomes the dominant positive mass contribution. This confirms that entrainment of irrotational fluid plays an important role in the functionning of the separated shear layer. This subject will be discussed in detail at § 11.5.

$Re_h/10^4$	3	4	5	6	7	10	13.3	20	26.7
$\dot{m}_1^*$	0.39	0.43	0.41	0.45	0.44	0.17	0.15	0.15	0.14
$\dot{m}_3^*$	-0.53	-0.56	-0.55	-0.64	-0.59	-0.45	-0.47	-0.45	-0.49
$\dot{m}_4^*$	0.14	0.14	0.14	0.20	0.17	0.27	0.28	0.27	0.33
$\epsilon_m^* = (\dot{m}_1^* + \dot{m}_3^* + \dot{m}_4^*)$	0.00	0.00	0.007	0.006	0.019	-0.03	-0.04	-0.03	-0.02
$\dot{m}_2^*$	-0.005	-0.007	-0.007	-0.004	0.005	-0.01	-0.005	0.008	0.014

Table 11.1: Mass fluxes normalized on $\rho h U_\infty$. The error ϵ_m^* does not include $\dot{m}_2^*$ because $\dot{m}_4^*$ should balance the difference between the inlet and the outlet, independently of how well the $\dot{m}_2^* = 0$ condition is met.

11.4 Scaling of RRI fluxes

It is of primary importance to better understand the scaling of mass exchanges across the RRI because, as already mentioned, the (dynamic) equilibrium between backflow and re-entrainment into the separated shear layer seems to be one of the driving mechanisms of massively separated flows. Of course, the condition $\dot{m}_2 = 0$ does not allow us to investigate RRI mass scaling laws at a global level. Instead, valuable information can be retrieved from the analysis of local mean fluxes per unit surface along the mean RRI. According to eq. 11.3, the normalised local flux at each point of the mean RRI can be computed as:

$$\dot{m}_{x2}^* = \frac{1}{\rho U_\infty}\frac{\mathrm{d}\dot{m}_2}{\mathrm{d}l} = -\frac{1}{U_\infty}(U(l)\sin(\phi(l)) + V(l)\cos(\phi(l))). \tag{11.4}$$

This expression extends the 0-dimensional analysis of eq. 11.3 by including the streamwise evolution of local mass fluxes. The streamwise evolution of $\dot{m}_{x2}^*$ is reported in figure 11.3. It appears that all curves collapse under a longitudinal scaling based on L_R, with the exception of the domain $x/L_R > 0.7$. This is in good agreement with findings at § 8.4, that show that in this region the R2 flow is affected by the incoming boundary layer, while the GDR flow depends only on h. Accordingly, it is possible to improve collapse within $x/L_R > 0.7$ by multiplying local fluxes by $C_{h,\delta}$. $\dot{m}_{x2}^*$ is very well correlated with local pressure gradients shown in figure 8.6. In addition, $\dot{m}_{x2}^*$ has an odd shape, with a sign inversion at $x/L_R \approx 0.5$ and almost antisymmetrical peaks, which is compatible with the mean mass flux through the RRI being zero (see § 11.3). In this respect, it seems probable that data from the two ramps might also scale with $C_{h,\delta}$ at the separation point, to compensate for the different amount of mass exchanged over $x/L_R > 0.7$: for example,

a link with the length L_V might exist. In figure 11.3, the initial slopes of $\dot{m}^*_{x2}$ suggest that mass fluxes might indeed evolve differently in a neighbourhood of the separation point. At present, however, our data do not allow to confidently assess mass transport in proximity of the upper edge of the ramp and this observation needs to be taken with some care.

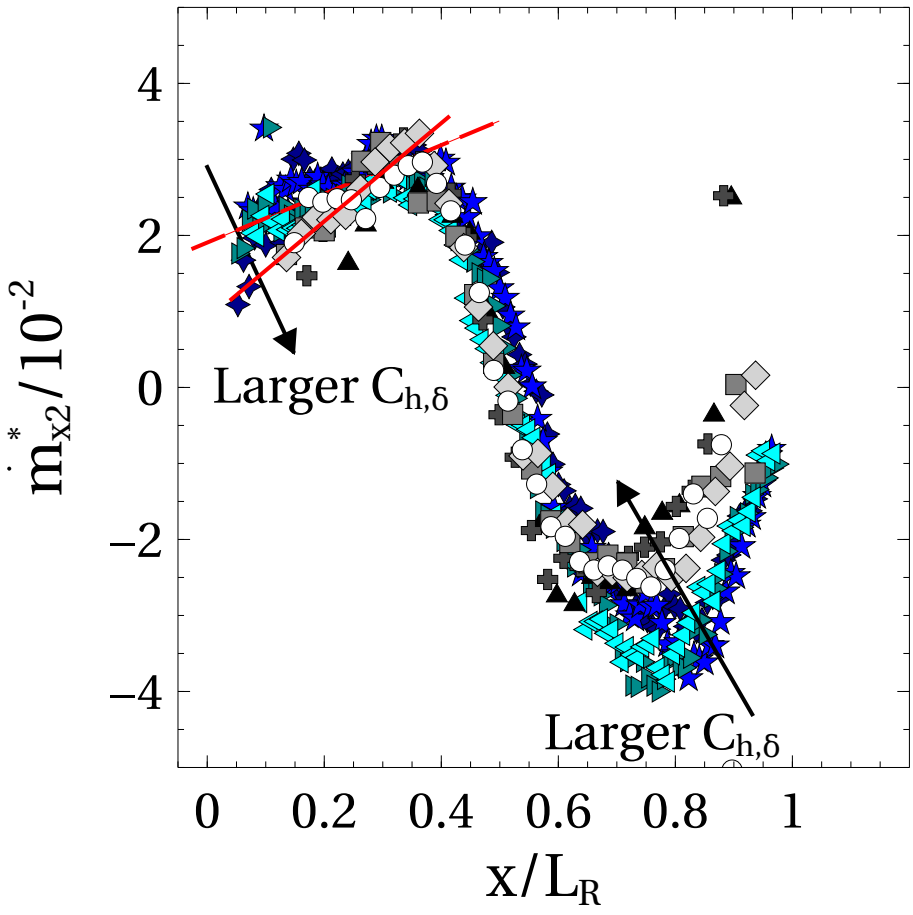

Figure 11.3: Normalized local mass fluxes $\dot{m}^*_{x2}$ along the RRI. Gray-shade symbols indicate R2 data: ◯ $Re_h = 3\times10^4$; ◊ $Re_h = 4\times10^4$; ■ $Re_h = 5\times10^4$; ✚ $Re_h = 6\times10^4$; ▲ $Re_h = 7\times10^4$. Blue-shade symbols indicate GDR data: ◁ $Re_h = 10\times10^4$; ▷ $Re_h = 13.3\times10^4$; ★ Re_h =20 $\times10^4$; ✦ $Re_h = 26.7\times10^4$. ——— slope of $\dot{m}^*_{x2}$ for the R2 ramp. – – – slope of $\dot{m}^*_{x2}$ for the GDR ramp. Black arrows indicate the evolution with increasing values of $C_{h,\delta}$.

According to figure 11.3, $\dot{m}^*_{x2}$ can intuitively be divided in two halfs. On $x/L_R < 0.5$, $\dot{m}^*_{x2}$ injects mass into $\mathcal{V}_c$: we will indicate quantities relative to this domain with the symbol ^{IN}. On the contrary, $\dot{m}^*_{x2}$ extracts mass from $\mathcal{V}_c$ on $x/L_R > 0.5$: quantities relative to this domain will be marked by the symbol ^{OUT}. Considering the scaling of figure 11.3, the integral of $\dot{m}^*_{x2}/L_R$ over, say, $x/L_R < 0.5$ will give:

$$\frac{1}{\rho U_\infty L_R}\int_0^{L_R/2}\frac{\mathrm{d}\dot{m}_i}{\mathrm{d}l}\mathrm{d}l = \frac{1}{U_\infty L_R}\int_0^{L_R/2}\boldsymbol{U}(l)\cdot\boldsymbol{n}(l)\,\mathrm{d}l \approx \frac{v_E^{A,IN}}{U_\infty}, \tag{11.5}$$

where in analogy with eq. 1.1 v_E^A is the mean, large-scale entrainment velocity at the RRI. $v_E^{A,OUT}/U_\infty$ can be computed with a similar expression. Table 11.2 reports both $v_E^{A,IN}/U_\infty$ and $v_E^{A,OUT}/U_\infty$ at all available Re_h, based on data from the large PIV fields. Values are in surprising agreement across experiments: on the available Re_θ range, eq. 11.5 gives $v_E^{A,IN}/U_\infty \approx 0.0224 \pm 0.002$ and $v_E^{A,OUT}/U_\infty \approx -0.0205 \pm 0.0015$ for the R2 ramp; $v_E^{A,IN}/U_\infty \approx 0.0223 \pm 0.002$ and $v_E^{A,OUT}/U_\infty \approx -0.0225 \pm 0.0015$ for the GDR ramp,

independently of Re_θ. This seems to support the idea that v_E^A at the RRI scales mainly with U_∞. If this is so, the mean mass flux that goes through the recirculation region can be computed as:

$$\dot{m}_2^{IN} = -\dot{m}_2^{OUT} \approx \rho v_E^A L_R/2 \sim \rho U_\infty \, h Re_\theta^m, \tag{11.6}$$

and hence:

$$\left(\dot{m}_2^{IN}\right)^* = \left(-\dot{m}_2^{OUT}\right)^* \sim Re_\theta^m. \tag{11.7}$$

Values of $\left(\dot{m}_2^{IN}\right)^*$ and $\left(-\dot{m}_2^{OUT}\right)^*$ are also reported in table 11.2. Differences between the two mass fluxes are, of course, consistent with table 11.1. Figure 11.4 shows that eq. 11.7 is well verified by $\left(-\dot{m}_2^{OUT}\right)^*$ in both experiments, both at low and high Re_θ. Admittedly, this is not the case for $\left(\dot{m}_2^{IN}\right)^*$, which largely deviates from the expected Re_θ, in particular on the GDR ramp. It is thought that such deviations might be due to quality of available data, rather than to a real physical effect, since the region of the separation point is the most impacted by laser reflections on the wall.

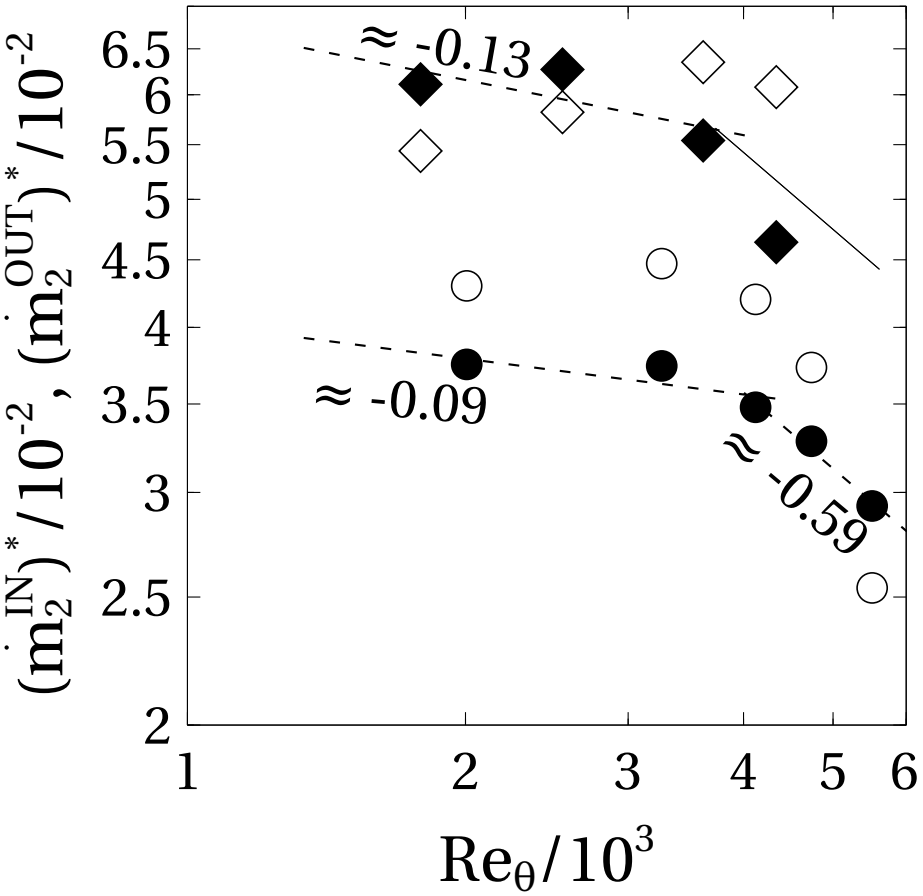

Figure 11.4: Evolution of $\left(\dot{m}_2^{IN}\right)^*$ and $\left(-\dot{m}_2^{OUT}\right)^*$ with Re_θ. Symbols: ◯ R2 ramp; ◊ GDR ramp. White symbols indicate $\left(\dot{m}_2^{IN}\right)^*$, black symbols indicate $\left(\dot{m}_2^{OUT}\right)^*$. – – – fitted power-laws; ——— suggestion of power law at $Re_\theta > Re_{\theta,c}$ for the GDR ramp.

In spite of this problem, the *normalised* mass flux crossing (twice) the RRI appears to evolve with Re_θ^m, i.e. with properties of the separated shear layer. The proportionality constant linking the left-hand side of eq. 11.6 to its right-hand side seems to depend on the experiment. An attempt to scale mass fluxes onto a single Re_θ^m curve was made, by postulating that mass fluxes through the RRI might be affected by the interplay between incoming boundary layer and separated shear layer. As usual, the interplay was represented with

$C_{h,\delta}$, as follows:

$$\left(-\dot{m}_2^{OUT}\right)^* C_{h,\delta} \sim const. \tag{11.8}$$

Unfortunately, available data verify this relationship quite ambiguously. In a way, this is not too surprising, because the $C_{h,\delta}$ correction applies only at reattachment (see § 8.4) and possibly in a neighbourhood of the mean separation point. In any case, if it is admitted that eq. 1.1 might hold for a variety of turbulent interfaces, it is clear that eq. 11.6 provides the scaling of mean large scale mass tranfer $v_E^A L^A$ for the RRI: the backflow decreases as L_R/h for increasing levels of incoming turbulence, because $v_E^{A,OUT}/U_\infty \approx const.$

$Re_h/10^4$	3	4	5	6	7	10	13.3	20	26.7
$v_E^{A,IN}/U_\infty$	2.26	2.24	2.17	2.43	2.11	2.07	2.22	2.40	2.23
$v_E^{A,OUT}/U_\infty$	1.91	1.93	1.93	2.02	2.20	2.19	2.36	2.34	2.11
$\left(\dot{m}_2^{IN}\right)^*$	4.30	4.47	4.20	3.73	2.54	5.44	5.82	6.35	6.08
$\left(\dot{m}_2^{OUT}\right)^*$	3.75	3.74	3.48	3.28	2.93	6.11	6.27	5.54	4.64

Table 11.2: Normalised RRI entrainment velocities and mass fluxes over $x/L_R < 0.5$ (symbol ^{IN}) and $x/L_R > 0.5$ (symbol ^{OUT}). For simplicity, all values are divided by 10^{-2}, with the exception of Re_h.

11.5 Scaling of TNTI fluxes

Section § 11.3 highlighted that entrainment of external fluid through the TNTI is sizeable, and possibly the dominant positive mass contribution to the mass balance of the separated shear layer. We now analyse the behaviour of $\dot{m}_4$ in more details, with focus on its scaling laws.

11.5.1 Global scaling along the entire mean TNTI

It is convenient to start the analysis of entrainment through the TNTI from local mass fluxes. Figure 11.5 presents the streamwise evolution of $\dot{m}^*_{x4}$, obtained by applying eq. 11.4 to the TNTI. As in the case of the RRI, $\dot{m}^*_{x4}$ is very well correlated to the local pressure gradient (figure 8.7). An inflection is evident at $x/L_R \approx 0.4$ to 0.5 and a maximum is reached in the neighbourhood of the reattachment point. The scaling based on U_∞ and L_R is applied once more, but a dependency on Re_θ is now evident, which reminds those observed in figure 8.15 (R2 ramp) and figure 8.16 (GDR ramp). This implies that, unlike along the RRI, v_E^A/U_∞ should be a function of Re_θ along the TNTI. To test this idea, firstly we apply eq. 11.5 to the TNTI of each ramp, over the domain $x/L_R \in (0,1)$. Then, we fit power laws in the form Re_θ^q to its output. The resulting exponents are reported in table 11.3. Over the GDR ramp, it is $q \approx -m$, at least for $Re_\theta < Re_{\theta c}$. Over the R2 ramp, instead, it is $q > -m$, both at low and high values of Re_θ. This difference can be resolved by a common scaling law for v_E^A/U_∞, as follows. Since the angle ϕ is small along the TNTI, from eq. 11.3 v_E^A is approximated by:

$$v_E^A \sim U_\infty \phi_{TNTI} + V. \tag{11.9}$$

It was shown at § 10.2.1.2 that in first approximation $\phi_{TNTI} \sim h/L_R \sim Re_\theta^{-m}$, at least for the present values of h, L_R and δ_e/h (see table 10.1). A suitable scaling of V, instead, is yet to be discussed. For the sake of simplicity, for the moment let us consider the GDR ramp, over which the scaling of the flow should mainly depend on h. Since it is found that $v_E^A/U_\infty \sim Re_\theta^{-m}$, it is also $V \sim U_\infty h/L_R \sim U_\infty Re_\theta^{-m}$, which can be seen as a measure of streamline deviation over the massive separation. Then, for sufficiently low values of δ_e/h eq. 11.9 becomes:

$$\frac{v_E^A}{U_\infty} \sim Re_\theta^{-m}, \tag{11.10}$$

Based on previous results (e.g. the streamwise evolution of statistical properties of the TNTI, see § 10.2.4), it is expected that the extension of eq. 11.10 to the R2 ramp requires to take into account the growing influence of the incoming boundary layer. It is then tempting to simply put:

$$\frac{v_E^A}{U_\infty} \sim Re_\theta^{-m} C_{h,\delta}, \tag{11.11}$$

which of course should still hold for the GDR ramp since $C_{h,\delta} \to 1$ for $\delta_e/h \to 0$. This expression is verified surprisingly well by available data, which for the R2 ramp yield:

$$\frac{v_E^A}{U_\infty C_{h,\delta}} \sim \begin{cases} Re_\theta^{0.15}, & \text{if } Re_\theta < Re_{\theta c}. \\ Re_\theta^{0.58}, & \text{if } Re_\theta > Re_{\theta c}. \end{cases} \tag{11.12}$$

while a reassuring $v_E^A/\left(U_\infty C_{h,\delta}\right) \sim Re_\theta^{0.12}$ is obtained for the GDR ramp, in excellent agreement with previous findings.

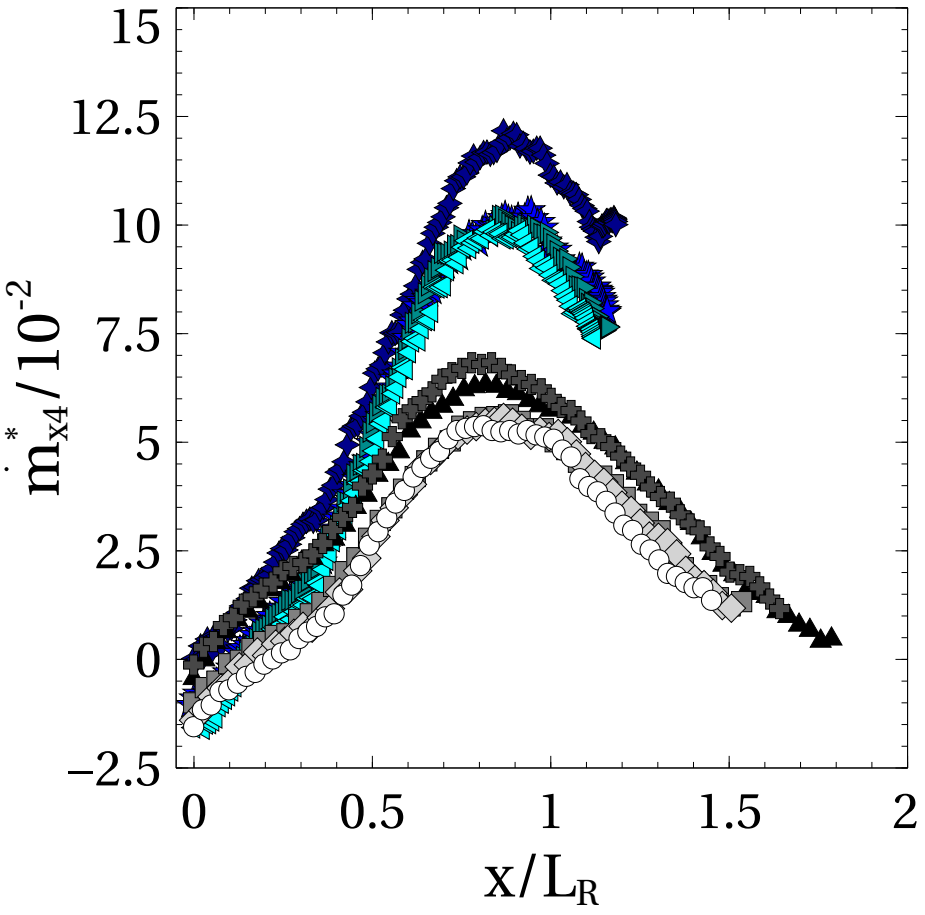

Figure 11.5: Normalized local mass fluxes $\dot{m}^*_{x4}$ along the TNTI. Symbols as in figure 11.3

While eq. 11.11 is supported by these results, its physical interpretation is somehow more ambiguous. Let us rewrite eq. 11.11 by putting in evidence its dependency on δ_e/h, as follows:

$$\frac{v_E^A}{U_\infty} \sim \phi_{TNTI} + \frac{V}{U_\infty} \sim Re_\theta^{-m}\left(1 + \frac{\delta_e}{h}\right). \tag{11.13}$$

Since it seems that $\phi_{TNTI} \sim Re_\theta^{-m}$, it should be $V/U_\infty \sim Re_\theta^{-m}\delta_e/h$, which states that for $\delta_e/h \gg 1$, the vertical velocity component at the TNTI becomes dependent of boundary layer structure and turbulent state (in this respect, the residual dependency on Re_θ^{-m} might not be unreasonable). However, this results also implies that the contribution brought by V wanes for $\delta_e/h \ll 1$, which is not verified on the GDR ramp. This suggests that the dependency on δ_e/h might also apply to ϕ_{TNTI}, in a way that is not adequately highlighted by available data (for example because δ_e/h is not high enough). Further investigations are needed to clarify this point. However, the agreement between experimental data and predictions of eq. 11.11 is such that we will retain this latter expression in what follows.

It is now necessary to look into the scaling of the mean TNTI length, indicated with the general symbol L^A (see the right-hand side of eq. 1.1). Findings in chapter 10, as well as the above discussion on v_E^A/U_∞, suggest that L_A might be determined, once more, by the competition between h and δ_e. Indeed, it seems reasonable to put $L^A \sim L_R \sim hRe_\theta^m$ if the separated shear layer dominates the flow (i.e. for $\delta_e/h \ll 1$), but $L^A \sim L_G \sim \delta_e$ if so does the incoming boundary layer (i.e. for $\delta_e/h \gg 1$). To test these hypotheses, it is more convenient to directly verify their consequences on the scaling of $\dot{m}_4$. For $\delta_e/h \ll 1$, $\dot{m}_4$ can then be rewritten as:

$$\dot{m}_4 \approx \rho v_E^A L^A \sim \rho U_\infty C_{h,\delta} Re_\theta^{-m} hRe_\theta^m \sim \rho U_\infty h C_{h,\delta}. \tag{11.14}$$

By normalising $\dot{m}_4$ on $\rho h U_\infty$ and reminding that $C_{h,\delta} \to 1$ for $\delta_e/h \ll 1$, this expression yields:

$$\dot{m}_4^* \sim C_{h,\delta} \sim const. \tag{11.15}$$

According to table 11.1, this relationship is quite well verified by the GDR ramp, in particular for $Re_\theta < Re_{\theta,c}$, which supports the proposed L^A scaling. This being so, it appears that the total, large-scale mass flux through the TNTI is constant, if δ_e/h is sufficiently low: in other words, when the separated shear layer dominates the flow the reduction (as L_R) of mean TNTI length is compensated for by higher entrainment velocities. In the case $\delta_e/h \gg 1$, instead, one can put:

$$\dot{m}_4 \sim \rho U_\infty C_{h,\delta} Re_\theta^{-m} L_G \sim \rho U_\infty C_{h,\delta} Re_\theta^{-m} \delta_e, \tag{11.16}$$

which leads to:

$$\dot{m}_4^* \sim Re_\theta^{-m} C_{h,\delta} \frac{\delta_e}{h}. \tag{11.17}$$

This expression predicts that the amount of mass entrained by the TNTI will increase with Re_θ^{-m} (i.e. as turbulent shear-stresses in the separated shear layer) if δ_e/h is high enough. Unfortunately, values of δ_e/h measured on the R2 ramp do not seem to fulfill this condition. Indeed since $L_G < L_R$, the mean TNTI length L_A is likely to show a residual Re_θ dependency due to the separated shear layer. This being so, it is expected that $\dot{m}_4^*$ will vary with exponents that are lower than $-m$. Making use of data in table 11.1, it is found:

$$\frac{\dot{m}_4^*}{C_{h,\delta}} \frac{h}{\delta_e} \sim \begin{cases} Re_\theta^{0.08}, & \text{if } Re_\theta < Re_{\theta c}. \\ Re_\theta^{0.35}, & \text{if } Re_\theta > Re_{\theta c}. \end{cases} \tag{11.18}$$

This result is encouraging and seems to support, albeit qualitatively, the idea that the scaling of L^A depends on the incoming boundary layer, if $\delta_e/h \gg 1$. In addition, eq. 11.18 puts into perspective the interpretation proposed in Stella *et al.* (2017). In that work, for which GDR data were not yet available, the scaling of $\dot{m}_4$ over the R2 ramp was approximated with $\dot{m}_4 \sim \rho h U_\infty$, in a similar fashion as in eq. 11.15. The relatively high margin of error ($\pm 10\,\%$) was attributed to a change in the local scaling of v_E^A/U_∞ along the TNTI (see § 11.4). As a whole, results presented in Stella *et al.* (2017) are not questioned by the present, larger work. However, their new interpretation as well as the new scaling laws proposed in this section seem to be more relevant, because they try to take into account the interplay between h and δ_e. With respect to Stella *et al.* (2017), the identification of this phenomenon, largely obscured on the R2 ramp since $\delta_e \approx h$, is probably the most important new element brought by the investigation of GDR data.

		x/L_R			$-m$
		$\in (0,1)$	$\in (0,0.5)$	$\in (0.5,1)$	
GDR	$Re_\theta < Re_{\theta c}$	0.11	0.07	0.05	0.10
R2	$Re_\theta < Re_{\theta c}$	0.2	0.74	0.07	
	$Re_\theta > Re_{\theta c}$	0.7	1.61	0.54	0.55

Table 11.3: Best fit exponents for the relation $v_E^A|_{TNTI}/U_\infty = Re_\theta^q$, tested on the entire L_R and on two domains within it. The expected value $-m$ is also reminded.

11.5.2 TNTI entrainment and shear layer growth

Let us now go back to local mass fluxes through the TNTI and further discuss some of their properties. Interestingly, figure 11.5 suggests that the intensity of transfer is not homogeneous along the TNTI. A simple integration along the TNTI allows us to verify that most mass is transferred over $x/L_R \in (0.5, 1)$. In particular, this region, where turbulent mixing is strong (see figure 5.4), accounts for $80\,\%$ to $90\,\%$ of $\dot{m}_4$, slightly decreasing with Re_θ, on the R2 ramp and for $60\,\%$ to $80\,\%$ of $\dot{m}_4$, once again with a slight decreasing Re_θ trend, on the GDR ramp. The difference between the two experiments is sizeable, and might imply that mass transfer along the TNTI becomes more homogeneous as $\delta_e/h \ll 1$. More importantly, mass entrainment over $x/L_R \in (0, 0.5)$ appears to be constrained by the free shear layer behavior observed in this region, which in particular imposes $\mathrm{d}\theta_{SL}/\mathrm{d}x \sim Re_\theta^{-m}$. Developing from Pope (2000) eq. 5.222, one can put:

$$\frac{\mathrm{d}\theta_{SL}}{\mathrm{d}x} \sim \frac{v_E^A|_{RRI} + v_E^A|_{TNTI}}{U_\infty} \sim Re_\theta^{-m}, \tag{11.19}$$

where $v_E^A|_{RRI}$ and $v_E^A|_{TNTI}$ are, as usual, the values of the mean entrainment velocity at the RRI and at the TNTI, respectively, and eq. 11.19 holds on the domain over which the free shear layer approximation is valid ($x/L_R \in (0, 0.5)$, see § 8.7). To test eq. 11.19, values of v_E^A/U_∞ are obtained with eq. 11.5 on two distinct subregions of the TNTI, defined by the domains $x/L_R \in (0, 0.5)$ and $x/L_R \in (0.5, 1)$. With this information, eq. 11.19 appears to be verified acceptably well on both ramps, as reported in figure 11.6. The RRI contribution is found to be predominant on the R2 ramp, as it accounts for up to $80\,\%$ of $\mathrm{d}\theta_{SL}/\mathrm{d}x$ for $Re_\theta < Re_{\theta c}$ and up to $60\,\%$ for $Re_\theta > Re_{\theta c}$. In the case of the GDR ramp, however, the TNTI accounts for about $45\,\%$ of shear layer growth rate, with a peak of about $60\,\%$ at the only available point for which $Re_\theta > Re_{\theta_c}$. This indicates that the TNTI might contribute at least as much as the RRI to the growth of the shear layer, if δ_e/h is sufficiently low, and possibly become its dominant driver.

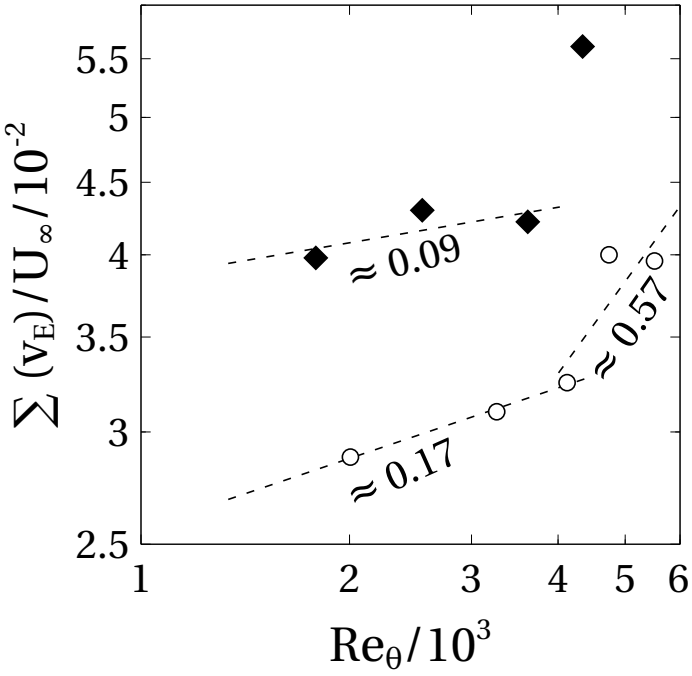

Figure 11.6: Evolution of $\left(v_E^A|_{RRI} + v_E^A|_{TNTI}\right)/U_\infty$ on $x/L_R \in (0, 0.5)$. Symbols as in figure 11.4.

We now investigate the scaling of $v_E^A|_{TNTI}/U_\infty$ on the two halfs on the mean TNTI. As usual, values of $v_E^A|_{TNTI}/U_\infty$ are fitted with power laws in the form Re_θ^q: best-fit exponents are also reported in table 11.3. It is clear that on the R2 ramp v_E^A/U_∞ scales approximately as Re_θ^{-m} on $x/L_R \in (0.5, 1)$, while faster power laws are found on $x/L_R \in (0, 0.5)$. Higher exponents might be due to the fact that the contribution

brought to eq. 11.19 by the TNTI is weak compared to the one due to the RRI: since $v_E^A|_{RRI}/U_\infty$ is constant, the smaller $v_E^A|_{TNTI}/U_\infty$ must grow faster than Re_θ^{-m} for eq. 11.19 to be verified. This strong variation of the exponent q is not observed along the TNTI of the GDR ramp, at least for $Re_\theta < Re_{\theta_c}$. Even if precise values of q might deserve some caution, it seems safe to assume that over the GDR ramp the evolution of $v_E^A|_{TNTI}/U_\infty$ is, on both x/L_R domains, compatible with the Re_θ^{-m} scaling found on the entire TNTI (see eq. 11.15). It is tempting to relate the different behaviours of the exponent to the scales governing the two flows, in accordance with the global view expressed at § 11.5.1. Over the GDR ramp, the separated shear layer dominates the flow: mass entrainment (as well as v_E^A and L^A) is sized by its characteristic scale h along the entire TNTI. On the contrary, in the case of the R2 ramp a large neighbourhood of the mean separation point is still influenced by the incoming boundary layer: this appears to change the local scaling of mass entrainment and in particular of v_E^A. Instead, the h-based scaling is retrieved for $x/L_R \sim 1$, in those regions in which the influence of the boundary layer wanes. At least for what concerns v_E^A, at a global level this change in scaling appears to be well captured by the use of $C_{h,\delta}$, as proposed in eq 11.11.

11.6 Scaling of inlet and outlet fluxes

To complete the picture of mass entrainment, this section investigates scaling of mass fluxes at the inlet and at the outlet of $\mathcal{V}_c$. To begin with, Table 11.1 suggests that the mass flow at the inlet $\dot{m}_1$ does not scale with $\rho h U_\infty$. Of course, a straightforward alternative is scaling $\dot{m}_1$ on $\rho\delta_e U_\infty$, as reported in table 11.4. This second normalisation appears to be more relevant: it is $\dot{m}_1/\rho\delta_e U_\infty \approx 0.5 \pm 0.05$. Although scatter is not always negligible, it seems possible to assume that $\dot{m}_1$ is sized by the outer scales of the incoming boundary layer.

$Re_h/10^4$	3	4	5	6	7	10	13.3	20	26.7
$\dot{m}_1/\rho\delta_e U_\infty$	0.45	0.50	0.50	0.55	0.48	0.48	0.56	0.45	0.54

Table 11.4: Inlet mass fluxes ($\dot{m}_1$) normalized on $\rho\delta_e U_\infty$.

As for what concerns $\dot{m}_3^*$, findings of section 11.5 imply that $\dot{m}_3$ can be Re_θ-dependent, if δ_e/h is high enough. In this respect, let us write:

$$\dot{m}_3 = \dot{m}_1 + \dot{m}_4 \sim \rho\left(\frac{U_\infty\delta_e}{2} + v_E^A L^A\right), \tag{11.20}$$

where we make use of table 11.4 for expressing $\dot{m}_1$ and of general symbols (see eq. 1.1) to rewrite $\dot{m}_4$. By plugging eq. 11.15 and eq. 11.17 into this expression, and normalising on $\rho h U_\infty$ one obtains:

$$\dot{m}_3^* \sim \begin{cases} const, & \text{if } \delta_e/h \ll 1. \\ \delta_e/h\left(\frac{1}{2} + Re_\theta^{-m} C_{h,\delta}\right), & \text{if } \delta_e/h \gg 1. \end{cases} \tag{11.21}$$

It is straightforward to verify eq. 11.21 in the case $\delta_e/h \ll 1$: indeed, table 11.1 reports that on the GDR ramp it is $\dot{m}_3^* \approx -0.47 \pm 0.02$. This also implies that in these conditions $\dot{m}_1/\dot{m}_3 \approx \delta_e/h$ (table 11.5). As usual, on the R2 ramp the value of δ_e/h is not high enough to verify eq. 11.21 in the case

$Re_h/10^4$	3	4	5	6	7	10	13.3	20	26.7
$\dot{m}_1/\dot{m}_3$	0.74	0.76	0.76	0.7	0.72	0.35	0.32	0.33	0.29
δ_e/h	0.92	0.86	0.82	0.82	0.91	0.34	0.28	0.33	0.29

Table 11.5: Ratio between inlet and outlet mass fluxes and comparison with δ_e/h

$\delta_e/h \gg 1$. According to table 11.1, however, Re_θ effects are apparent on $\dot{m}_3^*$, including a larger increase rate at $Re_\theta > Re_{\theta,c}$. In the present framework, this is sufficient to conclude that $\dot{m}_3^*$ becomes independent of Re_θ only if $\delta_e/h \ll 1$. Otherwise, residual Re_θ effects exist, due to the fact that the increase of v_E^A/U_∞ exceeds the reduction of L^A along the TNTI.

11.7 Summary and discussion

In this chapter we investigated mass fluxes through the boundaries of the separated shear layer. The analysis of the RRI proved that the backflow balances the amount of mass that is re-entrained into the separated shear layer in a large neighbourhood downstream of the mean separation point. Interestingly, v_E^A/U_∞ is approximately constant: then, the backflow (normalised on $\rho h U_\infty$) scales as L_R/h and as the inverse of turbulent shear stresses in the separated shear layer at reattachment. This suggests that in an unperturbed separated flow the recirculation region regulates the backflow by varying its size, rather than v_E^A/U_∞. Then, one effective strategy to, say, reduce L_R/h might be to *choke* the recirculation region by hindering the backflow. The picture is more complex at the TNTI, along which a strong effect of the parameter δ_e/h is observed. If $\delta_e/h \ll 1$, the TNTI is not affected by the incoming boundary layer. In this case, the mean mass flux through the TNTI depends only on geometry, represented by h[1]: dependencies on Re_θ cancel out, because the decreasing trend of $L^A \sim L_R$ is compensated for by an inverse trend of v_E^A/U_∞. On the contrary, when $\delta_e/h \gg 1$ it is $L^A \sim L_G \sim \delta_e$: since the scaling of v_E^A/U_∞ is no longer compensated for, the mean mass flux through the TNTI increases as Re_θ^{-m} and, consequently, as $(L_R/h)^{-1}$. In general, anyway, there seems to exist a negative correlation between v_E^A/U_∞ and L_R/h: an excitation increasing v_E^A/U_∞ will correspond to a reduction of L_R/h, and viceversa.

Entrainment behaviours at the RRI and at the TNTI might not be independent. Indeed, results at § 8.6 suggest that their common root cause is the intensity of turbulent mixing in the separated shear layer, in particular at reattachment (where figure 11.5 shows a peak). Higher turbulent shear stresses favour mixing of high-momentum fluid (with positive streamwise velocity) from the free-stream with low-momentum fluid (with negative streamwise velocity) in the recirculation region: in other words, they enhance entrainment through the TNTI and reduce the backflow. In this respect, the dependency on the turbulent state of the incoming boundary layer (represented by Re_θ) might be specific to separated flow originating from a turbulent incoming boundary layer (possibly including the effects of a perturbation upstream of separation, as in Neumann & Wengle (2003)). As already stated, however, it is thought that the role of turbulent mixing in the separated shear layer and its influence on L_R might be a general feature of separated flows.

[1] An effect of ER seems also probable, but cannot be observed with available data in which $ER \approx const.$

12

Some implications for mass transfer at small-scale

Implications pour l'entraînement de masse à petite échelle

Ce chapitre aborde les possibles conséquences que les lois d'échelle de l'entraînement de masse moyen (chapitre 11) pourraient avoir sur la gamme d'échelles turbulentes de l'écoulement. L'existence d'un lien est suggérée par l'éq. 12.1 et par le travail de Mistry *et al.* (2016). Pour cela, il serait nécessaire de calculer la vitesse d'entraînement instantanée $v_E(\Delta)$ le long des interfaces de la couche cisaillée. Nos données n'ayant pas une résolution suffisamment bonne (ni dans le temps, ni dans l'espace) pour ce calcul, $v_E(\Delta)$ est évaluée avec une expression approximée, applicable uniquement le long de la TNTI du champ détaillé de la rampe R2.

Le terme de surface $L(\Delta)$ de l'éq. 12.1 peut être étudié avec les outils de l'analyse fractale des interfaces turbulentes mis au point par Sreenivasan & Meneveau (1986), Sreenivasan *et al.* (1989) et plus récemment Thiesset *et al.* (2016). L'analyse fractale fournit une description de la gamme d'échelles qui plisse la TNTI (comprise entre une échelle de coupure externe η_o et une échelle de coupure intérne η_i) et sur la complexité géométrique de ces plissements (représentée par la codimension fractale β). Ces paramètres sont estimés avec l'éq. 12.2, ajustée sur la courbe de Richardson de la TNTI. Cette courbe est, quant à elle, reconstruite avec la méthode du calibre (Cintosun *et al.* (2007) parmi d'autres). Le tableau 12.1 montre que les valeurs de β sont comparables à celles trouvées dans la littérature (par exemple Sreenivasan *et al.* (1989)). La gamme d'échelles entre $\eta_o \approx 0.2h$ et $\eta_i \sim \eta$ couvre presque 1.5 décade, mais la limite à petite échelle doit être considérée comme qualitative, parce que les données PIV souffrent d'une résolution limitée. Le rapport L_{tot}/L_0 (tableau 12.1) représente une densité de surface, c'est-à-dire la quantité de surface développée par unité de longueur de la TNTI moyenne. L_{tot}/L_0 semble évoluer avec une loi Re_θ^p, avec p variant de 0.17 pour $Re_\theta < Re_{\theta c}$ à 0.46 pour $Re_\theta > Re_{\theta c}$.

Les évolutions avec Re_θ de v_E^A et de L^A sur l'étendue du champ détaillé ont été étudiées respectivement au chapitre 10 ($L^A \sim \delta_e$ pour la rampe R2) et au chapitre 11 (tableau 11.3). Ces résultats conduisent à une estimation du comportement en Re_θ du produit $v_E^A L^A$ (éq. 12.3). Si on suppose que $L(\Delta) \approx L^A\, L_{tot}/L_0$, cela permet d'utiliser l'éq. 12.1 pour prédire l'évolution de $v_E(\Delta)/U_\infty$, qui est la vitesse d'entraînement instantanée normalisée sur U_∞. L'on trouve que $v_E(\Delta)/U_\infty \sim Re_\theta^{q-p}$, où $q - p \approx 0.58$ pour $Re_\theta < Re_{\theta c}$ et $q - p \approx 1.15$ pour $Re_\theta > Re_{\theta c}$ (éq. 12.5). Les données PIV disponibles ne permettent pas de vérifier directement cette prédiction, mais une approximation de $v_E(\Delta)/U_\infty$ peut être obtenue avec l'éq. 12.6, proposée par Philip *et al.* (2014). La loi d'échelle résultante donne $v_E(\Delta)/U_\infty \sim Re_\theta^{0.82}$ pour $Re_\theta < Re_{\theta c}$ et $v_E(\Delta)/U_\infty \sim Re_\theta^{1.89}$ pour $Re_\theta > Re_{\theta c}$ (éq. 12.7). La différence par rapport à la prédiction de l'éq. 12.5 semble être liée à une limitation connue de l'éq. 12.6. Notamment, en filtrant les effets des plus petites échelles qui plissent la TNTI, l'éq. 12.6 tend à sous-estimer $v_E(\Delta)/U_\infty$ (voir Philip *et al.* (2014)). Néanmoins, l'ordre de grandeur des exposants est retrouvé : cela soutient qualitativement l'idée que l'évolution du transfert de masse à petite échelle change à $Re_{\theta c}$ aussi.

Ce dernier résultat encourage à évaluer, au moins de façon qualitative, les contributions au transfert de masse de chaque échelle turbulente. En suivant le travail de Chauhan *et al.* (2014*c*), le transfert *échelle par échelle* peut être représenté par le spectre de Fourier $\Psi_{\mathrm{d}\dot{m}}$ d'une fonction $\mathrm{d}m$, définie par l'éq. 12.8. Dans le cadre de cette discussion qualitative, la longueur de chaque échelle est reconstruite à partir du nombre d'onde k_s en postulant que toute échelle est isotrope, et donc $r = 1/(k_s\pi)$. La figure 12.3 montre que les spectres prémultipliés $\Psi_{\mathrm{d}\dot{m}}k_s$ ont un pic à $r|_{max} \approx \eta_i$, c'est-à-dire à des échelles qui peuvent être associées au mécanisme de transfert visqueux surnommé *nibbling*. Cette idée est confirmée par le fait que, dans la limite de la résolution disponible, $r|_{max}$ est comparable à l'épaisseur de la TNTI δ_ν, qui est souvent considérée comme représentative des échelles visqueuses de l'écoulement (voir Bisset *et al.* (2002), Westerweel *et al.* (2005), da Silva & Pereira (2008) et Chauhan *et al.* (2014*c*)). δ_ν est estimée à partir des profils de $\tilde{k}$ et U (12.5), conditionnés à la position instantanée de la TNTI (Bisset *et al.* (2002)). Ce résultat suggère que l'entraînement de masse à travers la TNTI pourrait être un phénomène multi-échelle : les grandes échelles de l'écoulement imposent les taux de transfert globaux, mais les mécanismes de transfert dominants sont de type visqueux.

Malgré la résolution limitée, on teste s'il existe une loi d'échelle qui normalise les spectres du transfert de masse sur toute leur gamme d'échelles, indépendamment de la valeur de Re_θ. La figure 12.6 montre que les unités internes (u_τ et ν/u_τ) ne constituent pas un bon choix, contrairement à ce qui est suggéré par le travail de Chauhan *et al.* (2014*b*) sur des couches limites turbulentes. Une explication possible est que la présence d'un gradient de pression pourrait imposer une normalisation basée sur des quantités à grande échelle, comme dans la couche limite dans un gradient de pression adverse analysée par Kitsios *et al.* (2015). Sur cette base, on montre avec un procédé semi-empirique qu'il devrait être possible de normaliser tous les spectres en utilisant une loi de puissance $Re_\theta^{2\gamma}$ (au moins dans la gamme de Re_θ disponible) et la longueur L_R (figure 12.7). Ce résultat qualitatif est prometteur, mais doit être confirmé par une étude plus fine sur des données de meilleure résolution.

12.1 Introduction

Results obtained so far suggest that U_∞, L_R, h and θ are the scaling parameters of the flow (and in particular of mass transfer) at large scale. Also, dependencies on Re_θ through the turbulent state of the shear layer were highlighted. In this respect, it is worth reminding the significance of eq. 1.1, which is also reported hereafter for future reference.

$$\boldsymbol{v_E}^\nu L^\nu = \boldsymbol{v_E}(\Delta) L(\Delta) = \boldsymbol{v_E}^A L^A. \tag{12.1}$$

Indeed, eq. 12.1 suggests that these findings might have consequences at small scale, the investigation of which would be the next and last step of this study. This is not a simple task, mainly due to the estimation of $v_E(\Delta)$. The impressive work of Mistry *et al.* (2016) demonstrates that reliable measurements of $v_E(\Delta)$ demand highly accurate information on geometry and time evolution of an instantaneous turbulent interface. Admittedly, our datasets do not fulfil these requirements, since their time and space resolutions are not high enough. However, the detailed field might be sufficient for a qualitative analysis of small-scale behaviours, based on two-point statistics at the boundaries of the shear layer. In spite of their relative simplicity, the approaches developed in what follows require the statistical properties of the interfaces to be homogeneous on a sufficiently large region of the flow. This condition is not verified by the RRI, as proved by the p.d.f. shown in figure 10.12 and figure 10.13. In the case of the TNTI of the R2 ramp, homogeneity is approximated acceptably well over $L_G \approx L_R$. For these reasons, the two-point analysis was restricted to the TNTI of the R2 ramp, by using data provided by the detailed field.

12.2 Fractal analysis

For simplicity, we begin by characterising the term $L(\Delta)$ that appears in eq. 12.1. $L(\Delta)$ can be assessed easily, at least compared to $v_E(\Delta)$, in the well-known framework of fractal analysis. This technique provides information on the range of scales on which a turbulent interface develops and on the complexity of its convolutions (i.e. its roughness). These are key parameters for mass entrainment as for any other transfer problem (e.g. combustion at a turbulent flame or diffusion of chemicals), because the more convoluted is the interface, the larger is the available exchange surface. It is known since the seminal work of Sreenivasan & Meneveau (1986) that the contributions of wrinkles of a turbulent interface to its arclength L are well fitted by a self-similar expression $L(r) \sim r^{-\beta}$, where r is the scale of wrinkles and β is the fractal codimension, at least between an inner scale η_i and an outer scale η_o. This is to say that small-scale wrinkles contribute much more to total interface length than large bulges and valleys. Also, the higher is β, the more the interface is wrinkled. For $r \gg \eta_o$, $L(r)$ is equal to L_0, the average length of the unwrinkled TNTI. L_0 is close to the length of the mean interface. For $r \ll \eta_i$, it is instead $L(r)/L_0 = (\eta_o/\eta_i)^\beta$ (Sreenivasan *et al.* (1989)). The recent work of Thiesset *et al.* (2016) matches these three scalings into the following expression.

$$\frac{L(r)}{L_0} = \left(\frac{\eta_o}{\eta_i}\right)^\beta \left[\frac{1+\left(\frac{r}{\eta_o}\right)^2}{1+\left(\frac{r}{\eta_i}\right)^2}\right]^{\beta/2}. \tag{12.2}$$

Table 12.1 summarises the values of β, η_i, η_o, L_0 and L_{tot}, the total average length of the TNTI, estimated from data collected on the detailed field. To this purpose, each instantaneous interface was processed with the calliper technique (see Cintosun *et al.* (2007) among others), which associates with a scale r the length $n \times r$, where n is the number of r-long segments needed to approximate the entire interface. The operation is repeated for a wide enough range of r. The ensemble-averaged, log-log plot of r versus $n \times r$ is known as the Richardson plot, which gives the cumulative contribution of all scales larger than r to total interface length (figure 12.1). Then, eq. 12.2 is fitted (in a least mean square sense) onto the Richardson plot. This technique to compute fractal parameters is relatively unconventional with respect to more classical methods. Indeed, in most cases fractal parameters are computed by manually identifying the self-similar range of scales on the Richardson plot (which gives estimates of η_o and η_i), and by fitting a power law on it, the exponent of which yields β (Sreenivasan *et al.* (1989), de Silva *et al.* (2013)). However, this type of approach is ambiguous at low Re, as for the flow under study, because the self-similar range is often short and difficult to spot out. On the contrary, the fit of eq. 12.2 is self-constrained: since the three regions of the Richardson plot are blended

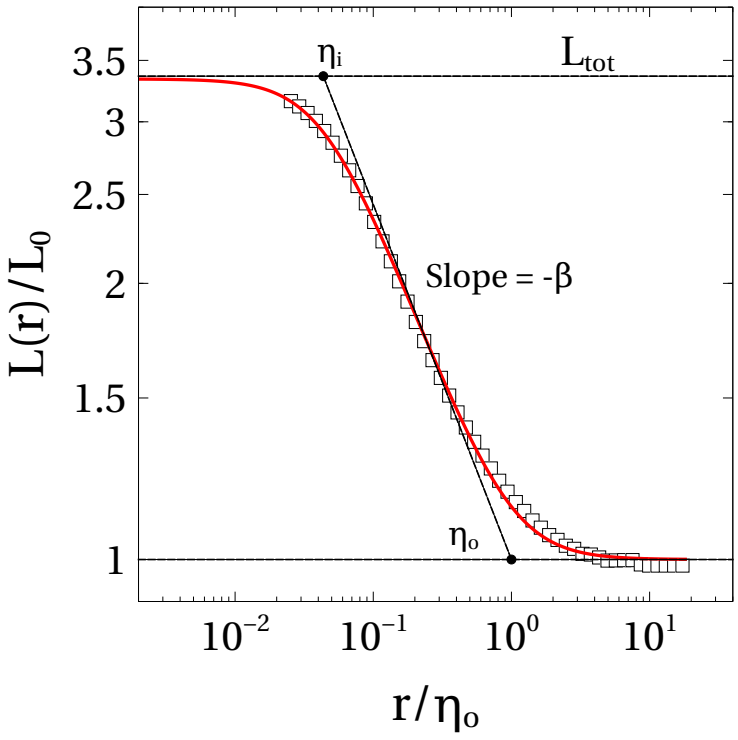

Figure 12.1: Richardson plot of the TNTI, computed on the detailed field. (a) Comparison of data at $Re_h = 5 \times 10^4$ with the best fit of eq. 12.2 (——— shown in red online).

in a unique expression, there is no need to manually identify the self-similar range and fractal parameters are retrieved unambiguously even at low and moderate Re numbers (see Thiesset *et al.* (2016)).

$Re_h/10^4$	β	L_0/h	L_{tot}/h	L_{tot}/L_0	η_o/h	$\eta_i/h/10^{-3}$	η_i/η	$\eta_i/\eta_o/10^{-2}$
3	0.32	1.61	4.80	2.98	0.2052	7.1	1.44	3.4
4	0.37	1.61	5.33	3.31	0.1920	7.8	1.60	4.0
5	0.38	1.61	5.39	3.35	0.1837	8.0	1.80	4.3
6	0.41	1.55	5.53	3.57	0.1856	7.8	1.89	4.4

Table 12.1: Fractal parameters of the TNTI for all available Re_h, computed on the detailed field. β is the fractal dimension, L_{tot} is the total average length of the TNTI, L_0 relates to the length of the visible section of the mean TNTI and η_i and η_o are the inner and the outer scale, respectively. Low values of L_0/h reflect the small size of the detailed field.

Figure 12.2 reports the comparison of experimental data to fits of eq. 12.2 at each Re_h available on the detailed field. It is found that β agrees with previous observations in TNTIs (see Sreenivasan & Meneveau (1986) and Chauhan *et al.* (2014*c*)) and in other turbulent interfaces (Thiesset *et al.* (2016) and references therein). Even if a Re-trend is visible, this does not seem too troubling, because Re are moderate and deviations from theoretical predictions at high Re are to be expected. Indeed, Sreenivasan *et al.* (1989) already showed that $D = 2 + \beta$ evolves with Re between 2 to 2.33 as the flow approaches its fully turbulent state. As for the range of surface-producing scales, it spans almost 1.5 decades, bounded by $\eta_o \approx 0.2h$ and $\eta_i \sim \eta$. This latter result should be considered qualitative, since neither PIV nor hot-wire data are resolved enough to accurately assess the smallest scales of the flow. It is observed that $L(\Delta) \approx L_{tot}$ for the present value of Δ. As for L_0, its length is imposed by the extent of the detailed field. The ratio L_{tot}/L_0 should then be considered as a surface density, i.e. the amount of developed surface per mean unit TNTI length.

L_{tot}/L_0 seems to evolve with Re_θ (see insert in figure 12.1). For convenience, the hypothesis is made that L_{tot}/L_0 also scales with a power law Re_θ^p, with p changing from $p \approx 0.17$ for $Re_\theta < Re_{\theta c}$ to $p \approx 0.46$ for $Re_\theta > Re_{\theta c}$.

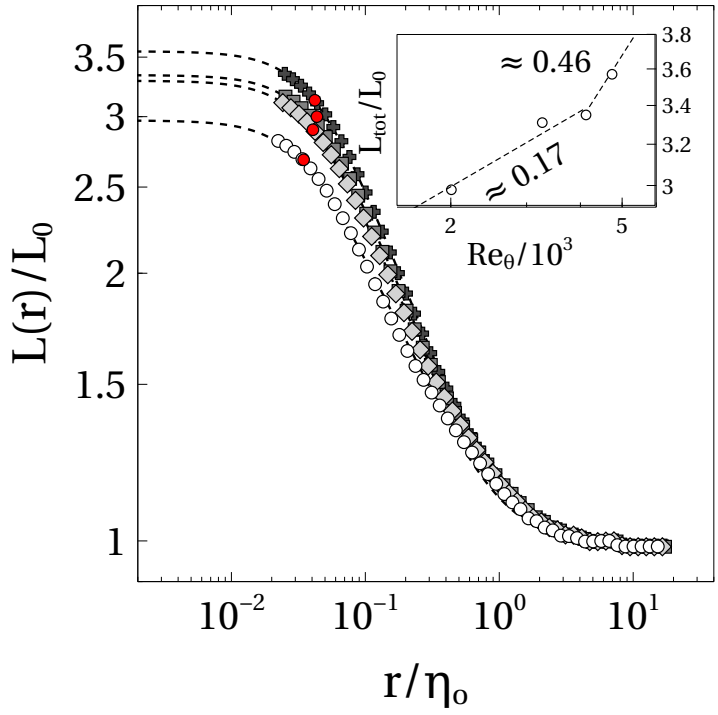

Figure 12.2: Comparison of Richardson plots computed on the detailed field at all available Re_h. Symbols: ◯ $Re_h = 3 \times 10^4$; ◊ $Re_h = 4 \times 10^4$; ■ $Re_h = 5 \times 10^4$; ✚ $Re_h = 6 \times 10^4$. The best fit of eq. 12.2 is also reported for each dataset (− − − in black online). Note that eq. 12.2 attains L_{tot} for values of r that are not resolved in this experiment. Accordingly, Richardson plots are cut-off at a scale r_c, associated to PIV resolution Δ. r_c is computed following the considerations of section 12.3 as $2/k_c$. Red dots mark η_i/η_o. The insert shows the evolution of L_{tot}/L_0 in function of Re_θ.

12.3 Discussion

With these considerations, it is now possible to discuss the implications of eq. 12.1, at least on the extent of the detailed field. Table 11.3 provides a scaling law for $v_E^A|_{TNTI}/U_\infty$ over the domain $x/L_R \in (0, 0.5)$, which includes the detailed field. Then, it is also possible to sketch the evolution of the mean amount of entrained mass (i.e. the right-hand side of eq. 12.1) on $x/L_R \in (0, 0.5)$. For simplicity it is assumed that in this region the length of the mean TNTI L^A scales as δ_e, with no residual Re_θ effect. This is supported by the fact that the streamwise extent of the detailed field is included within L_G (see § 10.2.4). Hence it will be:

$$v_E^A L^A \sim U_\infty \delta_e Re_\theta^q = U_\infty \delta_e \begin{cases} Re_\theta^{0.74}, & \text{if } Re_\theta < Re_{\theta c}. \\ Re_\theta^{1.61}, & \text{if } Re_\theta > Re_{\theta c}. \end{cases} \tag{12.3}$$

As for the small-scale side of eq. 12.1, section § 12.2 provides useful information on the term $L(\Delta)$. In particular, the evolution of surface density L_{tot}/L_0 was modelled with Re_θ^p. Since the physical scaling (i.e. not skewed by the fixed size of the detailed field) of mean TNTI length depends on δ_e, it seems reasonable

to put:

$$L\left(\Delta\right) \sim \frac{L_{tot}}{L_0} L^A \sim \delta_e Re_\theta^p \sim \delta_e \begin{cases} Re_\theta^{0.17}, & \text{if } Re_\theta < Re_{\theta c}. \\ Re_\theta^{0.46}, & \text{if } Re_\theta > Re_{\theta c}. \end{cases} \tag{12.4}$$

Plugging eq. 12.3 and eq. 12.4 into eq. 12.1 allows us to predict a qualitative behavior for $v_E\left(\Delta\right)/U_\infty$. With trivial manipulations, it is found that:

$$\frac{v_E\left(\Delta\right)}{U_\infty} \sim Re_\theta^{q-p} \sim \begin{cases} Re_\theta^{0.57}, & \text{if } Re_\theta < Re_{\theta c}. \\ Re_\theta^{1.15}, & \text{if } Re_\theta > Re_{\theta c}. \end{cases} \tag{12.5}$$

It is pointed out that the same prediction was obtained in Stella *et al.* (2017), where however it was assumed $L^A \sim L_R$ (the role of δ_e being hidden by the fact that $\delta_e \sim h$ on the R2 ramp). Of course, dependencies on L^A in eq. 12.5 cancel out once $L\left(\Delta\right)$ is modelled as in eq. 12.4[1]. In any case, available data do not allow us to verify eq. 12.5 with a direct measurement of $v_E\left(\Delta\right)$. A qualitative assessment is possible by using an indirect estimation, for example by following the method proposed by Philip *et al.* (2014). Based on an energy balance between the turbulent and the non-turbulent parts of the flow and considering that on the detailed field it is $\Delta \sim \eta$, at each point of the TNTI one can put:

$$\boldsymbol{v_E} \cdot \boldsymbol{n} \approx \boldsymbol{v_E}^\nu \cdot \boldsymbol{n} \approx \frac{2\nu}{K_{th}} v_j S_{ji} n_i, \tag{12.6}$$

where $\boldsymbol{v_E}$ is now a local entrainment velocity and $\boldsymbol{n}$ is the local normal to the TNTI. As for other symbols, K_{th} is the dimensional value of $\tilde{k}_{th}$, $\boldsymbol{v} = \boldsymbol{u} - \boldsymbol{U_\infty}$, S_{ji} is the mean strain-rate tensor and all quantities are evaluated at the TNTI. The reader is referred to Philip *et al.* (2014) and to Chauhan *et al.* (2014*c*) for thorough demonstrations of this result. It is worth noticing that, due to insufficient spatial PIV resolution, in Philip *et al.* (2014) eq. 12.6 yielded underestimated values of entrainment velocity, which did not allow to verify a relation for energy equivalent to eq. 12.1. Since our PIV datasets are not fully resolved either, similar limitations are likely to apply. This means that our findings should be taken with caution, in the framework of this qualitative discussion. This being said, the mean entrainment velocity $v_E\left(\Delta\right)$ can be obtained simply by averaging eq. 12.6 on the whole set of instantaneous TNTIs. Then, the best fit of the usual Re_θ power laws gives:

$$\frac{v_E\left(\Delta\right)}{U_\infty} \sim \begin{cases} Re_\theta^{0.82}, & \text{if } Re_\theta < Re_{\theta c}. \\ Re_\theta^{1.89}, & \text{if } Re_\theta > Re_{\theta c}. \end{cases} \tag{12.7}$$

It is clear that the prediction of eq. 12.5 is not well verified, but this result is encouraging, at least with respect to the limitations of the method, if one considers that the order of magnitude of the exponents is approximately recovered. In addition, it seems that the ratios of the exponents in eq. 12.7 ($\approx$2.3) is similar to the one predicted by eq. 12.5 ($\approx$2), which suggests that the scaling of mean entrainment at small scale might also change at $Re_{\theta c}$. In particular, this seems to support the assumption made on the behaviour of surface density at § 12.2. Although not definitive, these findings motivate a further effort. Based on eq. 12.6, it is possible to qualitatively assess the scale-by-scale contributions to mass transfer brought by all turbulent scales, smaller than L_R, that wrinkle the TNTI. Once again we follow the interesting work of Chauhan *et al.* (2014*c*), which proposed to compute the instantaneous local mass flux through the TNTI (or rather its projection on the X-Y plane) as:

$$\mathrm{d}\dot{m} = \rho \boldsymbol{v_E} \cdot \boldsymbol{n}\, \mathrm{d}l, \tag{12.8}$$

where $\mathrm{d}l$ is one element of interface length. Then, the scale-by-scale mass transfer through the TNTI can be estimated with the Fourier spectrum $\Psi_{\mathrm{d}\dot{m}}$ of $\mathrm{d}\dot{m}$. Figure 12.3 shows the premultiplied spectra $\Psi_{\mathrm{d}\dot{m}} k_s$, computed on the detailed field and normalised on U_∞^2 and η_o (symbol ^{F}), with respect to wavelength $\lambda_s = 2\pi/k_s$ along s, k_s being the wavenumber. Following Foucaut *et al.* (2004), the lower bound of each spectrum corresponds to a cutoff wavenumber $k_{s,c}$, computed from PIV resolution as $k_{s,c} = 2.8/\Delta$. Since λ_s represents the arclength of a wrinkle on the interface, it is interesting to estimate the scale r of the turbulent structure that produces it. Generally speaking, it seems reasonable to consider $\lambda_s = C(r)r$, where $C(r)$ is a scale-dependent proportionality factor. For the sake of simplicity and in the context of the present qualitative

[1]However, the change in scaling might have consequences on $L\left(\Delta\right)$, at least if eq. 12.4 is retained. Indeed, since it is $p \approx m$, $L\left(\Delta\right)$ might depend only on h if $L^A \sim L_R$ (see Stella *et al.* (2017)).

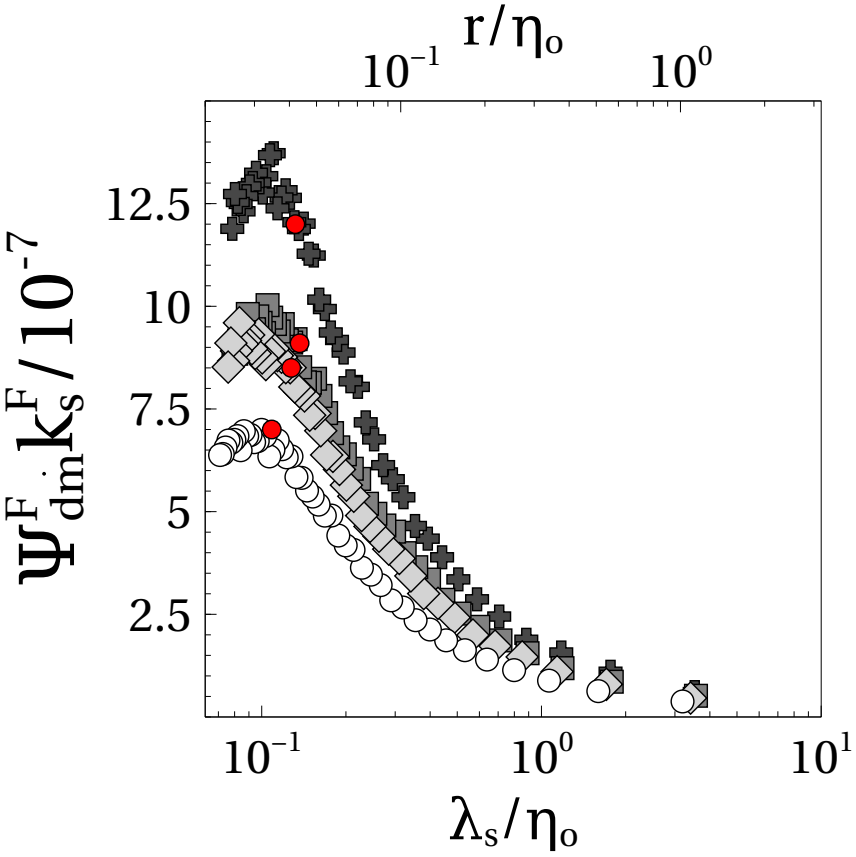

Figure 12.3: Premultiplied spectra of instantaneous mass fluxes computed on the detailed field, normalised based on η_o and U_∞^2. Red dots mark η_i/η_o. Symbols as in figure 12.1.

analysis, isotropy at each scale is assumed, which yields $r = \lambda_s/\pi$. Values of r are reported on the top horizontal axes of figure 12.3.

Within the limit of available resolution, a peak of instantaneous mass transfer appears at $r|_{max}/\eta_o \approx 0.03 \approx \eta_i/\eta_o$ on each spectrum, i.e. at scales that might be associated with viscous transfer mechanisms (nibbling). To test this idea, one can compare $r|_{max}$ to the thickness of the TNTI, noted δ_ν, which is usually related to nibbling (see for example Bisset *et al.* (2002), Westerweel *et al.* (2005), da Silva & Pereira (2008) and Chauhan *et al.* (2014*c*)). In analogy with other works, δ_ν is estimated from the profiles of flow statistics conditioned to the instantaneous TNTI position. With reference to figure 12.4, the conditioned profile of, say, $\tilde{k}$ at s^* is given by the ensemble average of the profiles of $\tilde{k}$ taken in a symmetric neighbourhood of the point $P_j(s^*)$, irrespective of its instantaneous position $d_{Tj}(s^*)$. $P_j(s^*)$ is identified by the intersection between a line along $\boldsymbol{n}_{s^*}$ and the lower envelope LE_j of the j-th instantaneous TNTI. LE_j is obtained by projecting the mean TNTI onto the instantaneous one: it filters gulfs and foldings of the original TNTI$_j$, thus enclosing turbulent fluid exclusively. Conditional profiles of $\tilde{k}$ and U/U_∞ are presented in figure 12.5. Both images yield $\delta_\nu/\eta_o \approx 0.07$ to $0.08 \sim \eta_i/\eta_o$, with minor differences with varying Re_θ. It must be stressed that since $\Delta/\eta_i \approx 1$ these considerations on small scales are just qualitative ones: due to the limited PIV resolution, δ_ν is overestimated, so that $r|_{max} \leq \delta_\nu$ seems to be an acceptable qualitative criterion to relate $r|_{max}$ to nibbling.

These observations support the idea that transfer is a multiscale phenomenon: while instantaneous, local entrainment takes place predominantly at small-scale, global transfer rates in a separating/reattaching flow are set by large scale parameters much upstream of separation (see eq. 12.3). These qualitative findings are consistent with observations on entrainment made in other flows, as turbulent jets (see Westerweel *et al.* (2009)) and in particular turbulent boundary layers (see Chauhan *et al.* (2014*c*)). They also seem to fit into

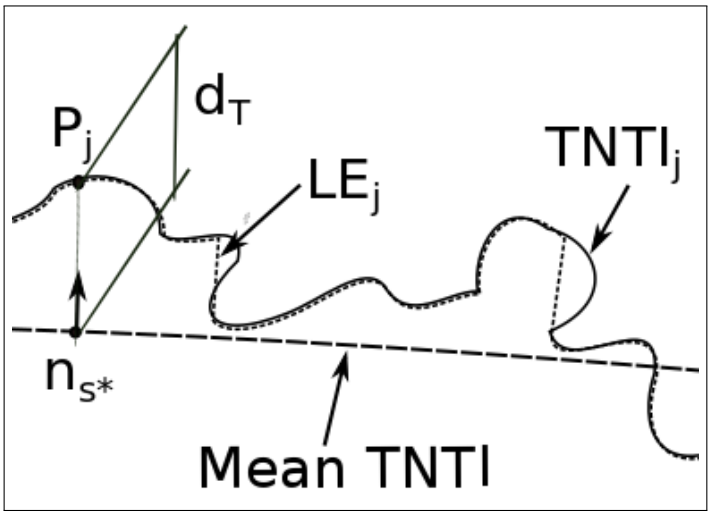

Figure 12.4: Notations and reference frames for computing flow statistics conditioned to TNTI position. LE is the lower envelope of the TNTI (dashed line). $P_j(s^*)$ is a point of the instantanepus TNTI around which profiles of flow quantities (e.g. $\tilde{k}$) are retrieved. $P_j(s^*)$ is identified by the intersection between a line along $\boldsymbol{n_{s^*}}$ and LE_j.

a more general picture of turbulence at moderate Re. In particular, persisting links between large scales and (hence anisotropic) small scales have already been observed in canonical flows by several authors, for example Danaila *et al.* (1999) and Mazellier & Vassilicos (2008). However, it appears important to stress some differences with respect to the work of Chauhan *et al.* (2014*c*) and in particular Chauhan *et al.* (2014*b*). This latter study uses data from four ZPG boundary layers, spanning $Re_\tau \approx 1200$ to $14\,500$, to demonstrate that in these flows δ_ν scales with ν/u_τ and that the mean velocity normal to the TNTI (which is at least similar to v_E^A) scales with u_τ. Such inner scaling was also used by Chauhan *et al.* (2014*c*) to normalise their mass spectra. Since the detailed field is within L_G, i.e. in a domain where the influence of the incoming boundary layer is still strong, inner units were tested for scaling of spectra at different Re_θ. Surprisingly, in the present separated flow inner units do not appear to provide appropriate scaling of $\Psi_{\mathrm{d}\dot{m}}k_s$ (figure 12.6). Although the range of Re is not wide enough for general conclusions, this observation fosters the idea that the link between wall boundary conditions and the kinematics of the TNTI is weaker than in ZPG boundary layers, either due to the separation bubble or, equivalently, to the presence of a pressure gradient. In this respect, Kitsios *et al.* (2015) showed that a pressure gradient induces important changes in the turbulent structure of a boundary layer. These authors found that the statistics of a self-similar, adverse pressure gradient boundary layer on the verge of separation collapse under outer scaling (viz. δ_1). In spite of the differences with respect to such a boundary layer, this result further supports a link between the action of the separation-induced pressure gradient and the θ-dependent behaviours observed in the separated flow. This being so, it is tempting to investigate if a normalisation based on power laws in the form $Re_\theta^{2\gamma}$, where γ varies at $Re_{\theta c}$, makes the whole spectra collapse to a single curve, i.e. if instantaneous, local entrainment at all (resolved) scales also depends on large-scale parameters of the incoming boundary layer. The factor 2 is included in the exponent for convenience, since on dimensional basis it is $\Psi_{\mathrm{d}\dot{m}k_s} \sim \mathrm{d}\dot{m}^2$. A qualitative assessment of this hypothesis can be obtained indirectly, as follows. Firstly, peak values of $\Psi^F_{\mathrm{d}\dot{m}}k_s^F$ are collected from figure 12.3. Secondly, $Re_\theta^{2\gamma}$ power laws are best fitted onto them, which yields $\gamma \approx 0.27$ for $Re_\theta < Re_{\theta c}$ and $\gamma \approx 1.27$ for $Re_\theta > Re_{\theta c}$. If the initial scaling assumption holds, by definition these values of γ should make normalised mass spectra collapse. This is quite well verified in figure 12.7, where premultiplied spectra were normalised based on $U_\infty^2 Re_\theta^{2\gamma}$ and, to further test the link with large scales and with Re_θ, on L_R (noted with the symbol ^{R}). This observation fosters the idea that a unique scaling based on Re_θ power laws might exist for the entire mass entrainment spectrum. Such scaling seems rather to depend on large-scale parameters, which would be in agreement with the findings of Holzner & Lüthi

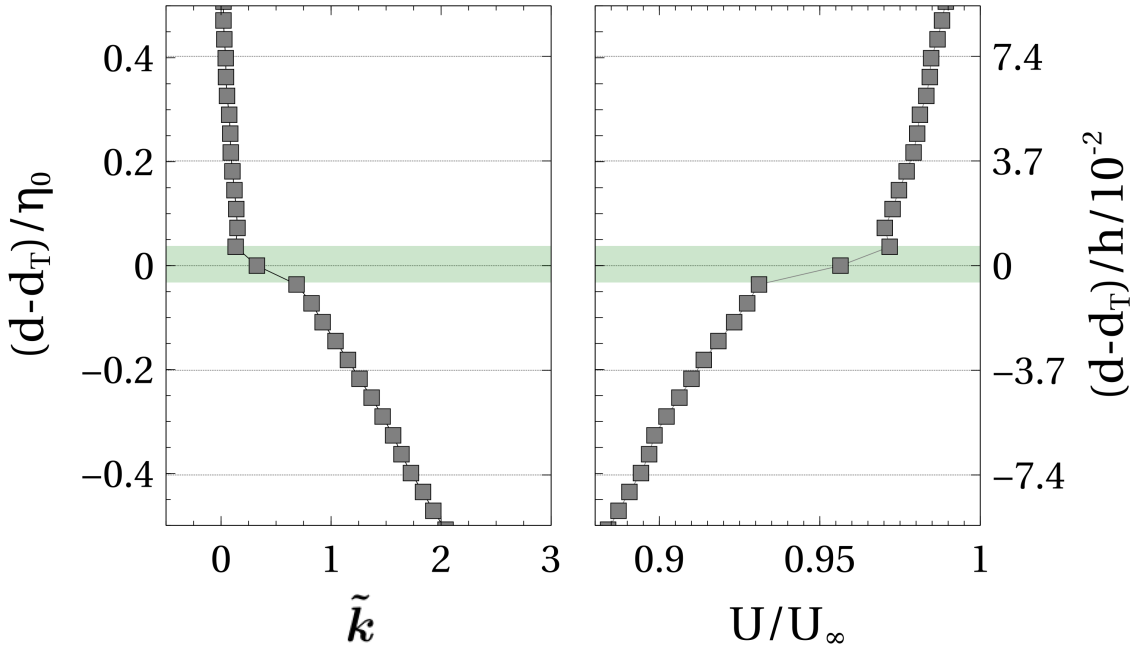

Figure 12.5: Conditionally averaged profiles of (a) $\tilde{k}$ and (b) U/U_∞ at $Re_h = 7 \times 10^4$. The green, shaded area indicates TNTI thickness.

(2011), showing that local entrainment velocities at the TNTI are poorly correlated to local dissipation, and also broadly consistent with the big picture sketched by the theory of Meneveau & Sreenivasan (1990) and the experimental results of Mistry *et al.* (2016).

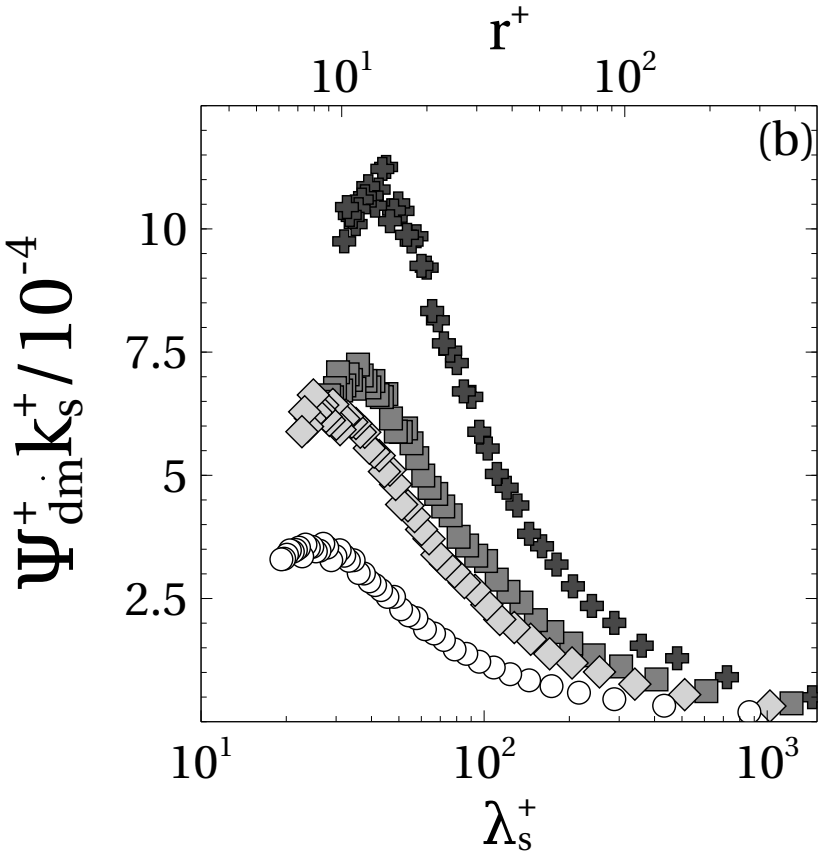

Figure 12.6: Premultiplied spectra of instantaneous mass fluxes normalised on inner units u_τ and ν/u_τ. Symbols as in figure 12.1.

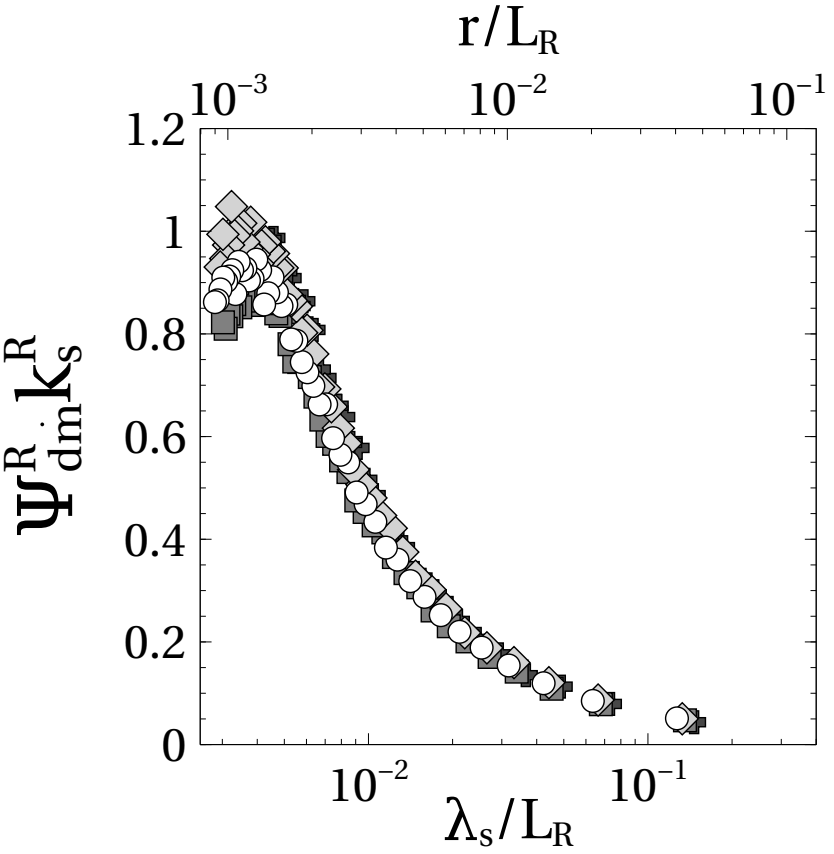

Figure 12.7: Premultiplied spectra of instantaneous mass fluxes computed on the detailed field, normalised based on L_R and $U_\infty^2\, Re_\theta^{2\gamma}$, where $\gamma \approx 0.27$ for $Re_\theta < Re_{\theta c}$ and $\gamma \approx 1.27$ for $Re_\theta > Re_{\theta c}$. Symbols as in figure 12.1.

Part V

Conclusions

Conclusions et perspectives

Ce travail propose une étude expérimentale de la phénoménologie d'un décollement turbulent massif, dans l'optique d'améliorer les performances et la robustesse des systèmes de contrôle du décollement, ainsi que des modèles numériques visant une simulation rapide et économique de ces écoulements dans des conditions industrielles. Notre premier objectif était de mieux comprendre les lois d'échelle des décollements massifs, notamment en ce qui concerne les effets des conditions initiales et aux limites établies par l'écoulement à l'amont du décollement. Deuxièmement, nous voulions étudier les mécanismes de transport de fluide, aussi bien à grande qu'à petite échelle, qui sont censés piloter le fonctionnement des décollements massifs. Compte tenu du temps imparti, nous nous sommes concentrés pour l'instant sur l'analyse du transport de masse. Pour atteindre ces objectifs, nous avons proposé une approche originale, basée sur une description expérimentale et analytique de la couche cisaillée décollée (une des caractéristiques majeures des décollements massifs) et de ses interfaces turbulentes. Ces dernières sont l'interface entre l'écoulement potentiel et la turbulence (*Turbulent/Non Turbulent Interface*, TNTI), qui borne la partie supérieure de la couche cisaillée, et la ligne de séparation instantanée (*Recirculation Region Interface*, RRI) qui borne la partie inférieure. Un large corpus de travaux montre que les interfaces turbulentes jouent un rôle majeur dans les problèmes de transport, mais notre travail est parmi les premiers à les considérer dans le cadre des décollements turbulents massifs.

Nous avons étudié le décollement turbulent massif déclenché par une rampe descendante inclinée à $25°$. Un atout de ce travail est que l'analyse a pu s'appuyer sur deux maquettes géométriquement similaires, qui présentent des hauteurs de rampe différentes (leur rapport étant de 1:3) mais dont les couches limites amont possèdent les mêmes propriétés. De ce fait, nous avons pu observer comment les caractéristiques du décollement varient avec h, et étudier l'écoulement sur 1.5 décade de Re_h, qui est souvent utilisé comme paramètre de similitude aérodynamique dans la littérature. Une large base de données a été créée, contenant des mesures de pression à la paroi, des signaux de vitesse au fil chaud et des champs de vitesse PIV. Ces ressources complémentaires permettent de décrire de façon relativement complète l'écoulement à grande échelle, à l'aval du point de décollement ainsi que dans la couche limite à l'amont. De plus, nous avons mesuré le champ de vitesse dans la région autour de l'arête de la rampe avec un réglage PIV à résolution plus élevée : l'exploitation de ces données permet d'étudier environ 2 décades d'échelles turbulentes qui existent au point de décollement.

En analysant l'écoulement le long de la TNTI moyenne et de la RRI moyenne, nous avons montré que les décollements turbulents massifs proches du nôtre résultent de la compétition de trois écoulements plus simples : la couche limite amont, une couche cisaillée décollée qui trouve son origine à l'arête de la rampe, et un écoulement potentiel dans un diffuseur. En première approximation, on peut associer un paramètre caractéristique à chacun de ces écoulements : il s'agit respectivement de δ_e, h et ER. En règle générale, les lois d'échelle du décollement semblent varier de façon importante en fonction de la combinaison des valeurs de ces trois paramètres. Dans ce travail, nous avons mis en évidence les effets d'une variation de h, tandis que δ_e et ER étaient approximativement constants. Quand $\delta_e/h \ll 1$, tout l'écoulement est dominé par la couche cisaillée décollée et dimensionné par h. En dehors de cette condition, la couche limite amont garde une influence considérable sur le décollement : les lois d'échelles dépendent de δ_e aussi bien que de h. Nous avons représenté l'interaction de ces échelles différentes avec le coefficient $C_{h,\delta} = (1 + \delta_e/h)$. Ce modèle simple nous a permis de mettre en échelle plusieurs quantités qui montraient des comportements discordants sur les deux rampes. La liste inclut toutes les composantes de l'équation RANS longitudinale (le long de la TNTI ainsi que de la RRI), les statistiques en un point des deux interfaces et les vitesses moyennes

d'entraînement à la TNTI. En outre, nous avons pu prédire le comportement de l'écoulement pour $\delta_e/h \gg 1$, une condition qui n'est pas bien représentée dans notre base de données. De façon inattendue, dans ce cas, l'écoulement devrait être dominé par ER (donc une nouvelle fois par la géométrie de la rampe), ce qui concorde avec les résultats expérimentaux trouvés dans la littérature.

La taille de la bulle de recirculation, L_R, est l'échelle caractéristique du décollement massif et elle est souvent utilisée pour évaluer les effets des systèmes de contrôle. Nous nous sommes appuyés sur la théorie de Chapman *et al.* (1958) pour montrer que le rapport L_R/h varie comme l'inverse du coefficient $R^*_{uv,r}$, qui représente l'intensité des efforts de cisaillement turbulents dans la région du recollement de la couche cisaillée. Dans le même temps, le taux d'épaississement de la couche cisaillée est directement proportionnel à $R^*_{uv,r}$, au moins dans une large zone autour du point de décollement moyen. Cette observation suggère que le mélange turbulent au recollement pourrait piloter le fonctionnement de toute la bulle de recirculation. En outre, les efforts de cisaillement turbulents au recollement semblent être dimensionnés par la turbulence de la couche limite amont. Cette dépendance peut être modélisée avec une loi de puissance de forme Re_θ^{-m}, où Re_θ est utilisé pour représenter l'intensité de la turbulence incidente. L'exposant m est négatif et décroît nettement à une valeur critique de Re_θ (dans nos expériences, on trouve $Re_{\theta c} = 4100$). Notons que dans ce travail, Re_θ est mesuré bien à l'amont du point de décollement, à $x/h = -9$. Cette observation pourrait avoir des implications importantes pour le contrôle du décollement. Premièrement, elle contribue à expliquer les résultats encourageants qui ont été atteints avec des systèmes de contrôle qui intensifient le mélange turbulent dans la couche limite amont. Deuxièmement, elle suggère la faisabilité de systèmes de *feed-forward* basés sur des paramètres à grande échelle, mesurables de façon relativement simple, de l'écoulement à l'amont.

L'analyse de l'entraînement de masse étaye ce point de vue. De façon générale, les flux de masse moyens qui traversent la RRI et la TNTI sont bien corrélés avec les principales caractéristiques de la couche cisaillée (en particulier, avec la distribution de pression qu'elle induit et son taux d'épaississement). A l'image de ces dernières, ils varient avec h, δ_e ou les deux (selon la valeur de δ_e/h), avec L_R et avec Re_θ. Dans le cas de la RRI, nous avons vérifié que la quantité de masse qui est transportée par le *backflow* au recollement est égale à celle qui est réentraînée par la couche cisaillée dans la région du décollement. De plus, ces deux flux varient comme L_R/h, c'est-à-dire comme l'inverse des efforts de cisaillement turbulents au recollement. Cela suggère que la bulle de recirculation règle le *backflow* en ajustant sa taille : modifier artificiellement le *backflow* pourrait être un moyen efficace de contrôler L_R. Les flux de masse à travers la TNTI sont quantitativement importants (au moins $35\,\%$ à $40\,\%$ de la masse sortant de la couche cisaillée), ce qui indique que l'entraînement de fluide irrotationnel depuis l'écoulement potentiel est un élément structurant du fonctionnement global de la couché cisaillée décollée. En outre, des taux d'entraînement à la TNTI plus élevés sont corrélés avec des valeurs de $R^*_{uv,r}$ également plus élevées : cela nous indique qu'ils accélèrent l'épaississement de la couche cisaillée et qu'ils contribuent à réduire L_R.

Nous avons ensuite étudié de façon qualitative les mécanismes de transfert à petite échelle, pour l'instant en nous concentrant seulement sur la TNTI. Nôtre étude est limitée par la résolution des données, mais nos résultats suggèrent que l'entraînement est un processus multi-échelle : les paramètres de l'écoulement à grande échelle déterminent les flux moyens de masse, tandis que les échelles visqueuses contribuent de façon prépondérante à l'entraînement local. Cette conception concorde avec les observations faites dans d'autres écoulements, par exemple des jets ou des couches limites turbulentes. En outre, les lois d'échelle de l'écoulement moyen (y compris la dépendance de Re_θ sous forme de loi de puissance) pourraient être valides sur toute la gamme d'échelles qui plisse la TNTI.

Globalement, nos résultats promeuvent les systèmes de contrôle qui agissent sur l'intensité des efforts de cisaillement turbulents dans la couche cisaillée, en particulier au recollement. Une excitation de ce type pourrait être efficace, parce qu'elle affecterait l'entraînement à la RRI et à la TNTI de façon concordante. Le développement de stratégies de contrôle en boucle fermée basées sur les efforts de cisaillement turbulents semble faisable : en effet, les observations de Adams & Johnston (1988*a*) indiquent que de simples mesures de gradient de pression à la paroi pourraient suffire à reconstruire $R^*_{uv,r}$. En outre, des stratégies de type *feed-forward* semblent aussi envisageables, parce que les efforts de cisaillement turbulents dans la couche cisaillée semblent être liés à la turbulence dans la couche limite à l'amont et en particulier à des propriétés turbulentes à grande échelle relativement accessibles. En ce qui concerne la simulation numérique des décollements turbulents massifs, nos résultats montrent qu'il est nécessaire de prédire très précisément les

flux de masse qui traversent la TNTI et la RRI. Par contre, on peut espérer que l'importante contribution due aux mécanismes visqueux pourra être modélisée (et donc ne pas être calculée explicitement) à partir des grandes échelles de l'écoulement, parce que les lois qui décrivent la variation de ces dernières semblent s'appliquer à toute la gamme d'échelles spatiales de la TNTI.

Notre travail n'épuise pas le sujet de l'entraînement dans les décollements massifs, et ouvre des perspectives très riches pour des travaux futurs. Premièrement, il semble important de compléter la caractérisation des mécanismes de transport de la couche cisaillée en étendant l'étude à la quantité de mouvement et à l'énergie cinétique. Une analyse détaillée de ces quantités demande des données à haute résolution, mais notre base de données expérimentale semble être un bon point de départ au moins pour une compréhension générale des principaux mécanismes du champ moyen. Une fois le fonctionnement de l'écoulement naturel bien caractérisé, il serait intéressant d'appliquer l'approche développée dans ce travail à l'analyse d'un décollement sous l'action d'une excitation extérieure. Des résultats préliminaires indiquent que cette démarche pourrait fournir des descriptions très détaillées des interactions de l'écoulement avec un système de contrôle.

L'analyse et la modélisation des interactions entre h, δ_e et ER méritent également d'être affinées. Les lois d'échelle basées sur $C_{h,\delta}$ devraient être testées plus largement, en particulier pour des valeurs élevées du paramètre δ_e/h, et étendues aux effets éventuels de ER. Pour une étude paramétrique de ce type, il pourrait être plus facile de s'appuyer sur la LES que sur des expériences : en fait, une approche numérique (avec un maillage suffisamment fine) permettrait d'obtenir des données relativement fiables, à un coût moindre qu'une campagne expérimentale d'envergure similaire.

Enfin, ce travail ouvre la voie vers d'autres études voire d'autres types d'écoulements. Premièrement, la théorie de Chapman *et al.* (1958) suggère que le rôle des efforts de cisaillement turbulents au recollement pourrait être une caractéristique générique des écoulements décollés, même si cela ne semble pas être possible pour leur dépendance de Re_θ. Il serait intéressant de vérifier cette hypothèse dans d'autres écoulements décollés. Deuxièmement, plusieurs observations indiquent que la RRI pourrait partager plusieurs caractéristiques de la TNTI, en particulier sa nature de *couche cisaillée mince* (Hunt *et al.* (2010)), c'est-à-dire une interface impliquée dans l'entraînement de fluide et marquée par de forts gradients de quantités turbulentes. Les propriétés de la RRI, et notamment les lois d'échelle de son épaisseur, pourraient être un sujet d'étude à part entière. En troisième lieu, la valeur critique $Re_{\theta,c} \approx 4100$ n'est pas en accord avec les seuils de Re_θ pour lesquels la turbulence est communément considérée comme complètement développée. Il serait donc intéressant de mieux saisir la signification de $Re_{\theta,c}$ en termes d'état de la turbulence.

Conclusions and perspectives

In this work we experimentally investigated the phenomenology of massively separated turbulent flows, in the perspective of improving performances and robustness of separation control systems and of enhancing numerical models for fast, affordable simulations of industrial flows. In the first place, we aimed at better understanding the scaling laws of massive separations, and in particular their dependencies on upstream initial and boundary conditions. In the second place, we wanted to shed new light on the mechanisms of fluid entrainment, both at large and small scale, that have been shown (or assumed) to drive many behaviours of separated flows. For a matter of time constraints, this work only treats mass entrainment. A new approach was proposed to attain these objectives, centered on the experimental and analytical description of the separated shear layer (which is one of the marking features of massively separated flows) and of its turbulent interfaces. These are the Turbulent/Non Turbulent Interface (TNTI) and the Recirculation Region Interface (RRI): they bound the separated shear layer respectively from the free-stream and from the recirculation region. A large corpus of literature shows that turbulent interfaces have a major role in entrainment, but this is one of the first works that considers them in a massively separated flow.

The chosen study case was the massively separated turbulent flow generated by a sharp edge, 25° descending ramp. Significantly, this work could rely on two experimental models with sizeably different values of ramp height h (their ratio was 1:3), but otherwise substantially similar geometries and incoming flows. This allowed us to compare two very different h-driven flow configurations and to span one decade of the commonly used similitude parameter Re_h. Wall pressure measurements, hot-wire velocity signals and 2D2C-PIV velocity fields were collected in one large database: these complementary resources allow a relatively complete large-scale description of the separated ramp flow and of its incoming boundary layer. In addition, 2D2C-PIV fields of higher spatial resolution are available for the neighbourhood of the upper edge of one of the two ramps: these data cover approximately 2 decades of the turbulent length scales that are present at separation.

By analysing the flow along the mean TNTI and the mean RRI, we showed that massively separated turbulent flows assimilable to the one under study can be represented as the competition between three simpler flows: the incoming boundary layer, a shear layer originating from the edge of the ramp and a potential flow in a diffuser. In first approximation, each of these flows can be associated to a characteristic parameter, respectively δ_e, h and ER. In general, the scaling laws of the flow seem to vary greatly in function of the combination of the values of these three parameters. In this work we highlighted the effects of varying h for approximately constant δ_e and ER. When $\delta_e/h \ll 1$, the entire flow is dominated by the separated shear layer and scaled by h. Otherwise, sizeable boundary layer effects are found in the separated flow: scaling depends now on both δ_e and h. We have represented this complex interplay of different scales with a coefficient $C_{h,\delta} = (1 + \delta_e/h)$. This simple model allowed us to collapse together many quantities that showed discording behaviours on the two ramps. The list includes all components of the streamwise RANS equation along both the TNTI and the RRI, one-point statistics of interface positions and mean entrainment velocities at the mean TNTI. In addition, we were able to predict the behaviour of the flow at $\delta_e/h \gg 1$, which is not well represented in our experimental database, by extrapolating the $C_{h,\delta}$-based scaling of the streamwise RANS equation. Interestingly, it is found that in this condition the flow should be largely determined by ER (then, once again, by geometry), which is in good agreement with experimental results found in the literature.

The size of the recirculation region, L_R, is the characteristic streamwise scale of separated flows and it is often used to assess the effects of control systems. We made use of the theory of Chapman *et al.*

(1958) to show that the ratio L_R/h scales as the inverse of the intensity of turbulent shear stresses in the reattachment region, that was represented with a non-dimensional coefficient $R^*_{uv,r}$. At the same time, the growth rate of the shear layer in a large neighbourhood of the separation point is directly proportional to $R^*_{uv,r}$. This suggests that turbulent mixing at reattachment might govern the functioning of the entire recirculation region. Moreover, we observed that turbulent shear stresses at reattachment seem to scale with the incoming turbulence. This dependency can be modelled with a power law in the form Re_θ^{-m}, where Re_θ represents the intensity of incoming turbulence. The exponent m is negative and decreases sharply at a critical Re_θ value (in these experiments, it is observed $Re_{\theta c} = 4100$). Significantly, Re_θ is assessed as far upstream as $9h$. This result might have important implications for separation control. On one side, it contributes to explain the encouraging results obtained by control systems that enhance turbulent mixing in the incoming boundary layer. On the other end, it supports the feasibility of feed-forward control systems, based on relatively accessible, large-scale parameters of the incoming flow.

The analysis of mean mass entrainment supports these views. Generally speaking, mean mass fluxes through the RRI and through the TNTI are well correlated to the main properties of the separated shear layer, in particular its induced pressure field and its spreading rate, and they scale accordingly with h, δ_e or both (depending on the value of δ_e/h), with L_R and with Re_θ. In the case of the RRI, we verified that the amount of mass transported by the backflow at reattachment is equal to the amount of mass re-entrained by the shear flow at separation and that they both scale as L_R/h, i.e. as the inverse of turbulent shear stress intensity at reattachment. This suggests that the recirculation region regulates the backflow by changing its size: then, artificially forcing the backflow might be an effective way to tune the size of the recirculation region. Mass fluxes through the TNTI are substantial (at least $35\,\%$ to $40\,\%$ of the mass flowing out of the separated shear layer), which indicates that entrainment of external fluid from the free-stream is important in the overall functioning of the separated shear layer. In addition, higher TNTI entrainment rates are correlated with higher turbulent shear stresses at reattachment: then, they favour faster growth of the separated shear layer and reduce L_R.

To gain a deeper view into entrainment mechanisms, we carried out a qualitative study of mass entrainment at small scale (for the moment limited to the TNTI). Although limited by available experimental data, our results suggest that transfer is a multiscale phenomenon: large scale parameters set the mean mass fluxes, but viscous mechanisms seem to contribute the most to local mass entrainment. This is consistent with observations made in other flows, as turbulent boundary layers and turbulent jets. Also, it appears that scaling of large-scale features (including the power law dependency on Re_θ) might extend to the whole range of scales that wrinkle the TNTI.

All in all, our findings support separation control systems that aim at tuning the intensity of turbulent shear stresses in the separated shear layer, in particular at reattachment. A forcing of this type holds promise of effectiveness, because it changes entrainment at the RRI and at the TNTI concurrently. It seems possible to develop closed-loop control strategies based on turbulent shear stresses, since there is evidence that the latter could be reconstructed from simple wall-pressure measurements in the reattachment region (Adams & Johnston (1988*a*)). In addition, feed-forward control strategies seem also within reach, because turbulent shear stresses seem to be related to relatively accessible, large-scale turbulent properties of the incoming boundary layer. As for what concerns numerical simulations of massively separated turbulent flows, our results confirm that it is important to correctly predict shear layer entrainment at both its interfaces. However, they also suggest that the important contribution to transfer due to small turbulent scales could be modelled (i.e. not simulated explicitily) from large scales reliably, because the scaling parameters of large-scale features of the flow appear to be relevant over the entire range of spatial turbulent scales found on the TNTI.

This work does not exhaust the subject of entrainment in separated turbulent flows and many further studies can pick up from where we left off. Firstly, it seems important to complete the characterisation of shear layer entrainment with the analysis of momentum and energy transfer. Although a thorough investigation of these subjects would require well resolved numerical data, our experimental database seems to be a good starting point at least for outlining the main mechanisms of the mean field. Secondly, once such a baseline of mass, momentum and energy transfer is available, it would be interesting to apply the same approach to separated turbulent flows under an external forcing: preliminary results indicate that very detailed descriptions of the interactions of the flow with a control system might be retrieved.

The interplay between h, δ_e and ER also deserves further attention. Scalings based on $C_{h,\delta}$ should be tested extensively, in particular for higher values of the parameter δ_e/h, and possibly completed as to include the effects of ER. In this respect, LES might be a better investigation tool than experiments: indeed, this approach could allow relatively reliable, comprehensive parametric studies at a fraction of the cost of similar experimental campaigns.

Finally, several independent ideas for original research stem from the bulk of this study. For instance, the theory of Chapman *et al.* (1958) suggests that the role of turbulent shear stresses at reattachment might be a general feature of separating/reattaching flows, although the dependency on incoming turbulence might not. Testing this hypothesis in other flows seems an interesting development of this work. Secondly, many observations hint at the fact that the RRI might share many of the characteristics of the TNTI, and in particular its nature of *thin shear layer* (Hunt *et al.* (2010)), in the sense of a transport boundary with strong local gradients of turbulent quantities. The detailed study of the properties of the RRI, and in particular of the scaling of its thickness, seem then to deserve further attention. Thirdly, the critial value $Re_{\theta,c} \approx 4100$ came as a surprise with respect to Re_θ thresholds for which turbulent flows are commonly considered fully turbulent. Then, the significance of $Re_{\theta,c}$ in terms of turbulence should be further investigated.

Bibliography

ADAMS, E. W. & JOHNSTON, J. P. 1988*a* Effects of the separating shear layer on the reattachment flow structure Part 1: Pressure and turbulence quantities. *Exp. Fluids* **6** (6), 400–408.

ADAMS, E. W. & JOHNSTON, J. P. 1988*b* Effects of the separating shear layer on the reattachment flow structure part 2: Reattachment length and wall shear stress. *Exp. Fluids* **6** (7), 493–499.

ADRIAN, R. J., MEINHART, C.D. & TOMKINS, C.D. 2000 Vortex organization in the outer region of the turbulent boundary layer. *J. Fluid Mech.* **422**, 1–54.

AHN, J. W., PARK, T. S. & SUNG, H. J. 1997 Application of a near-wall turbulence model to the flows over a step with inclined wall. *Int. J. Heat Fluid Fl.* **18** (2), 209–217.

AIDER, J. L. & DANET, A. 2006 Large-eddy simulation study of upstream boundary conditions influence upon a backward-facing step flow. *Comptes Rendus Mécanique* **334** (7), 447–453.

ANAND, R. K., BOERSMA, B. J. & AGRAWAL, A. 2009 Detection of turbulent/non-turbulent interface for an axisymmetric turbulent jet: evaluation of known criteria and proposal of a new criterion. *Exp. Fluids* **47** (6), 995.

ARMALY, B. F., DURST, F., PEREIRA, J. C. F. & SCHÖNUNG, B. 1983 Experimental and theoretical investigation of backward-facing step flow. *J. Fluid Mech.* **127**, 473–496.

ATTILI, A., CRISTANCHO, J. C. & BISETTI, F. 2014 Statistics of the turbulent/non-turbulent interface in a spatially developing mixing layer. *J. Turbul.* **15** (9), 555–568.

AUBRUN, S., KAO, P. L. & BOISSON, H. C. 2000 Experimental coherent structures extraction and numerical semi-deterministic modelling in the turbulent flow behind a backward-facing step. *Exp. Therm. Fluid Sci.* **22** (1), 93–101.

BARROS, D., BORÉE, J., NOACK, B. R., SPOHN, A & RUIZ, T. 2016 Bluff body drag manipulation using pulsed jets and Coanda effect. *J. Fluid Mech.* **805**, 422–459.

BELL, J. H. & MEHTA, R. D. 1988 Contraction design for small low-speed wind tunnels. *NASA STI/Recon Technical Report N* **89**, 13753.

BERK, T., MEDJNOUN, T. & GANAPATHISUBRAMANI, B. 2017 Entrainment effects in periodic forcing of the flow over a backward-facing step. *Phys. Rev. Fluids* **2** (7).

BISSET, D. K., HUNT, J. C. R. & ROGERS, M. M. 2002 The turbulent/non-turbulent interface bounding a far wake. *J. Fluid Mech.* **451**, 383–410.

BORRELL, G. & JIMÉNEZ, J. 2016 Properties of the turbulent/non-turbulent interface in boundary layers. *J. Fluid Mech.* **801**, 554–596.

BRADSHAW, P. & WONG, F. Y. F. 1972 The reattachment and relaxation of a turbulent shear layer. *J. Fluid Mech.* **52** (1), 113–135.

BRASSARD, D. & FERCHICHI, M. 2005 Transformation of a Polynomial for a Contraction Wall Profile. *J. Fluid Eng.* **127** (1), 183–185.

BROWAND, F. K. & TROUTT, T. R. 1985 The turbulent mixing layer: geometry of large vortices. *J. Fluid Mech.* **158**, 489–509.

BROWN, G. L. & ROSHKO, A. 1974 On density effects and large structure in turbulent mixing layers. *J. Fluid Mech.* **64** (04), 775–816.

BRUUN, H.H. 1996 *Hot-Wire Anemometry - Principles and Signal Analysis*. Oxford Science Publications.

CHANDRSUDA, C. & BRADSHAW, P. 1981 Turbulence structure of a reattaching mixing layer. *J. Fluid Mech.* **110**, 171–194.

CHAPMAN, D. R., KUEHN, D. M. & LARSON, H. K. 1958 Investigation of Separated Flows in Supersonic and Subsonic Streams with Emphasis on the Effect of Transition. Technical Report TN-1356. NACA, Washington, DC.

CHAUHAN, K., BAIDYA, R, PHILIP, J, HUTCHINS, N & MARUSIC, I 2014*a* Intermittency in the outer region of turbulent boundary layers. In *Proceedings of the 19th Australasian Fluid Mechanics Conference (AFMC-19)*. AFMS.

CHAUHAN, K., MONKEWITZ, P. A. & NAGIB, H. M. 2009 Criteria for assessing experiments in zero pressure gradient boundary layers. *Fluid Dyn. Res.* **41** (2), 021404.

CHAUHAN, K., PHILIP, J. & MARUSIC, I. 2014*b* Scaling of the turbulent/non-turbulent interface in boundary layers. *J. Fluid Mech.* **751**, 298–328.

CHAUHAN, K., PHILIP, J., DE SILVA, C. M., HUTCHINS, N. & MARUSIC, I. 2014*c* The turbulent/non-turbulent interface and entrainment in a boundary layer. *J. Fluid Mech.* **742**, 119–151.

CHERRY, E. M., ELKINS, C. J. & EATON, J. K. 2008 Geometric sensitivity of three-dimensional separated flows. *Int. J. Heat. Fluid. Fl.* **29** (3), 803–811.

CHERRY, N. J., HILLIER, R. & LATOUR, M. E. M. P. 1984 Unsteady measurements in a separated and reattaching flow. *J. Fluid Mech.* **144**, 13–46.

CHUN, K. B. & SUNG, H. J. 1996 Control of turbulent separated flow over a backward-facing step by local forcing. *Exp. Fluids* **21** (6), 417–426.

CINTOSUN, E., SMALLWOOD, G. J. & GÜLDER, O. L. 2007 Flame Surface Fractal Characteristics in Premixed Turbulent Combustion at High Turbulence Intensities. *AIAA Journal* **45** (11), 2785–2789.

COLLIS, D. C. & WILLIAMS, M. J. 1959 Two-dimensional convection from heated wires at low Reynolds numbers. *J. Fluid Mech.* **6** (3), 357–384.

CORRSIN, STANLEY 1943 Investigation of Flow in an Axially Symmetrical Heated Jet of Air. Technical Report 3L23. NACA, Washington, DC.

CORRSIN, S. & KISTLER, A. L. 1955 Free-Stream Boundaries of Turbulent Flows. Technical Report TN-1244. NACA, Washington, DC.

CUVIER, C. 2012 Active control of a separated turbulent boundary layer in adverse pressure gradient. PhD thesis, École Centrale de Lille, Lille, France.

DA SILVA, C. B. & PEREIRA, J. C. F. 2008 Invariants of the velocity-gradient, rate-of-strain, and rate-of-rotation tensors across the turbulent/nonturbulent interface in jets. *Phys. Fluids* **20** (5), 055101.

DA SILVA, C. B. & DOS REIS, R. J. N. 2011 The role of coherent vortices near the turbulent/non-turbulent interface in a planar jet. *Philos. Trans. R. Soc. Lond. A Math. Phys. Sci.* **369** (1937), 738–753.

DA SILVA, C. B. & TAVEIRA, R. R. 2010 The thickness of the turbulent/nonturbulent interface is equal to the radius of the large vorticity structures near the edge of the shear layer. *Phys. Fluids* **22** (12), 121702.

DANAILA, L., ANSELMET, F., ZHOU, T. & ANTONIA, R. A. 1999 A generalization of Yaglom's equation which accounts for the large-scale forcing in heated decaying turbulence. *J. Fluid Mech.* **391**, 359–372.

DANDOIS, J., GARNIER, E. & SAGAUT, P. 2007 Numerical simulation of active separation control by a synthetic jet. *J. Fluid Mech.* **574**, 25–58.

DE SILVA, C. M., PHILIP, J., CHAUHAN, K., MENEVEAU, C. & MARUSIC, I. 2013 Multiscale Geometry and Scaling of the Turbulent-Nonturbulent Interface in High Reynolds Number Boundary Layers. *Phys. Rev. Lett.* **111** (4), 044501.

DEBIEN, A., AUBRUN, S., MAZELLIER, N. & KOURTA, A. 2014 Salient and smooth edge ramps inducing turbulent boundary layer separation: Flow characterization for control perspective. *Comptes Rendus Mécanique* **342** (6–7), 356–362.

DIMOTAKIS, P. E. & BROWN, G. L. 1976 The mixing layer at high Reynolds number: large-structure dynamics and entrainment. *J. Fluid Mech.* **78** (3), 535–560.

DRIVER, D. M. & SEEGMILLER, H. L. 1985 Features of a reattaching turbulent shear layer in divergent channelflow. *AIAA Journal* **23** (2), 163–171.

DURBIN, P. A. 1995 Separated flow computations with the k-epsilon-v-squared model. *AIAA Journal* **33** (4), 659–664.

DURST, F & TROPEA, C 1981 Turbulent, backward-facing step flows in two-dimensional ducts and channels. In *Proc. 3rd Int. Symp. On Turbulent Shear Flows*, pp. 9–11.

EATON, J. K. & JOHNSTON, J. P. 1981 A Review of Research on Subsonic Turbulent Flow Reattachment. *AIAA Journal* **19** (9), 1093–1100.

EISMA, J., WESTERWEEL, J., OOMS, G. & ELSINGA, G. E. 2015 Interfaces and internal layers in a turbulent boundary layer. *Phys. Fluids* **27**, 055103.

FIEDLER, H. & HEAD, M. R. 1966 Intermittency measurements in the turbulent boundary layer. *J. Fluid Mech.* **25** (04), 719–735.

FISCALETTI, D., ATTILI, A., BISETTI, F. & ELSINGA, G. E. 2016 Scale interactions in a mixing layer – the role of the large-scale gradients. *J. Fluid Mech.* **791**, 154–173.

FOUCAUT, J. M., CARLIER, J. & STANISLAS, M. 2004 PIV optimization for the study of turbulent flow using spectral analysis. *Meas. Sci. Technol.* **15** (6), 1046.

FRIEDRICH, R. & ARNAL, M. 1990 Analysing turbulent backward-facing step flow with the lowpass-filtered navier-stokes equations. *J. Wind Eng. Ind. Aerod.* **35**, 101–128.

GAN, L. 2016 Detection of Passive Scalar Interface Directly from PIV Particle Images in Inhomogeneous Turbulent Flows. *Flow Turbul. Combust.* **97** (1), 141–170.

GARNIER, E., PAMART, P. Y., DANDOIS, J. & SAGAUT, P. 2012 Evaluation of the unsteady RANS capabilities for separated flows control. *Computers & Fluids* **61**, 39–45.

GEORGE, W. K., BEUTHER, P. D. & SHABBIR, A. 1989 Polynomial calibrations for hot wires in thermally varying flows. *Exp. Therm Fluid Sci.* **2 p. 230-235**.

GEORGE, W. K. & CASTILLO, L. 1997 Zero-pressure-gradient turbulent boundary layer. *Appl. Mech. Rev* **50** (12), 689–729.

HEDLEY, T. B. & KEFFER, J. F. 1974*a* Some turbulent/non-turbulent properties of the outer intermittent region of a boundary layer. *J. Fluid Mech.* **64** (4), 645–678.

HEDLEY, T. B. & KEFFER, J. F. 1974*b* Turbulent/non-turbulent decisions in an intermittent flow. *J. Fluid Mech.* **64** (04), 625–644.

HOLZNER, M. & LÜTHI, B. 2011 Laminar Superlayer at the Turbulence Boundary. *Phys. Rev. Lett.* **106** (13), 134503.

HUERRE, P. & MONKEWITZ, P. A. 1990 Local and Global Instabilities in Spatially Developing Flows. *Annu. Rev. Fluid Mech.* **22** (1), 473–537.

HUNT, J. C. R., EAMES, I. & WESTERWEEL, J. 2006 Mechanics of inhomogeneous turbulence and interfacial layers. *J. Fluid Mech.* **554**, 499–519.

HUNT, J. C. R., EAMES, I., WESTERWEEL, J., DAVIDSON, P. A., VOROPAYEV, S., FERNANDO, J. & BRAZA, M. 2010 Thin shear layers – The key to turbulence structure? *J. Hydro-envir. Res.* **4** (2), 75–82.

ISOMOTO, K. & HONAMI, S. 1989 The Effect of Inlet Turbulence Intensity on the Reattachment Process Over a Backward-Facing Step. *J. Fluid Eng.* **111** (1), 87–92.

JARQUE, C. M. & BERA, A. K. 1987 A Test for Normality of Observations and Regression Residuals. *Int. Stat. Rev. / Rev. Int. Stat.* **55** (2), 163–172.

JOSEPH, P., S., LOYER, MAZELLIER, N. & KOURTA, A. 2015 Montage expérimental collaboratif: écoulement sur rampe descendante 2d en soufflerie malavard. Oral communication, Journées du GDR 2502, `http://www.univ-orleans.fr/GDR2502/journees_18_19_11_2015/presentations_191115/Joseph_2015 - 11 - 18 GDR.pdf`.

JOSEPH, P., STELLA, F., MAZELLIER, N. & KOURTA, A. 2016 Flow separation control on a 2d backward facing ramp using synthetic jets. In *Second international conference in numerical and experimental aerodynamics of road vehicles and trains (Aerovehicles 2)*.

JOVIĆ, S. 1998 Recovery of reattached turbulent shear layers. *Exp. Therm. Fluid Sci.* **17** (1–2), 57–62.

KIM, J., KLINE, S. J. & JOHNSTON, J. P. 1980 Investigation of a reattaching turbulent shear layer: Flow over a backward-facing step. *J. Fluids Eng* **102** (3), 302–308.

KING, L. V. 1914 On the Convection of Heat from Small Cylinders in a Stream of Fluid: Determination of the Convection Constants of Small Platinum Wires with Applications to Hot-Wire Anemometry. *Philos. Trans. R. Soc. Lond. A Math. Phys. Sci.* **214**, 373–432.

KITSIOS, V., ATKINSON, C., SILLERO, J. A., BORRELL, G., JIMÉNEZ, J., GUNGOR, A. G. & SORIA, J. 2015 Direct numerical simulation of a self-similar adverse pressure gradient turbulent boundary layer. In *9th. Symp. on Turbulence and Shear Flow Phenomena (TSFP-9). The University of Melbourne, Australia*. Begell House Inc.

KOURTA, A. & LECLERC, C. 2013 Characterization of synthetic jet actuation with application to ahmed body wake. *Sensors Actuators A-Phys* **192**, 13–26.

KOURTA, A., THACKER, A. & JOUSSOT, R. 2015 Analysis and characterization of ramp flow separation. *Exp. Fluids* **56** (5), 1–14.

KRUG, D., HOLZNER, M., LÜTHI, B., WOLF, M., KINZELBACH, W. & TSINOBER, A. 2015 The turbulent/non-turbulent interface in an inclined dense gravity current. *J. Fluid Mech.* **765**, 303–324.

KUBAN, L., LAVAL, J.P., ELSNER, W., TYLISZCZAK, A. & MARQUILLIE, M. 2012 LES modeling of converging-diverging turbulent channel flow. *J. Turbul.* **13**, N11.

KUEHN, D. M. 1980 Effects of Adverse Pressure Gradient on the Incompressible Reattaching Flow over a Rearward-Facing Step. *AIAA Journal* **18** (3), 343–344.

KUMAR, V. & ALVI, F. S. 2005 Efficient control of separation using microjets. *AIAA Paper* **4879**, 6–9.

KWON, Y. S., PHILIP, J., SILVA, C. M. DE, HUTCHINS, N. & MONTY, J. P. 2014 The quiescent core of turbulent channel flow. *J. Fluid Mech.* **751**, 228–254.

LE, H., MOIN, P. & KIM, J. 1997 Direct numerical simulation of turbulent flow over a backward-facing step. *J. Fluid Mech.* **330**, 349–374.

LIGRANI, P. M. & BRADSHAW, P. 1987 Spatial resolution and measurement of turbulence in the viscous sublayer using subminiature hot-wire probes. *Exp. Fluids* **5** (6), 407–417.

MARUSIC, I., MONTY, J. P., HULTMARK, M. & SMITS, A. J. 2013 On the logarithmic region in wall turbulence. *J. Fluid Mech.* **716**.

MASSEY, JR., F. J. 1951 The Kolmogorov-Smirnov Test for Goodness of Fit. *J. Am. Stat. Assoc.* **46** (253), 68–78.

MAURICE, G., THIESSET, F., HALTER, F., MAZELLIER, N., CHAUVEAU, C., GÖKALP, I. & KOURTA, A. 2016 Scale analysis of the flame front in premixed combustion using Proper Orthogonal Decomposition. *Exp. Therm Fluid Sci.* **73**, 109–114.

MAZELLIER, N. & VASSILICOS, J. C. 2008 The turbulence dissipation constant is not universal because of its universal dependence on large-scale flow topology. *Phys. Fluids* **20** (1).

MEINHART, C. D. & ADRIAN, R. J. 1995 On the existence of uniform momentum zones in a turbulent boundary layer. *Phys. Fluids* **7** (4), 694–696.

MENEVEAU, C. & SREENIVASAN, K. R. 1990 Interface dimension in intermittent turbulence. *Phys. Rev. A* **41** (4), 2246–2248.

MISTRY, D., PHILIP, J., DAWSON, J. R. & MARUSIC, I. 2016 Entrainment at multi-scales across the turbulent/non-turbulent interface in an axisymmetric jet. *J. Fluid Mech.* **802**, 690–725.

MOLLICONE, J.-P., BATTISTA, F., GUALTIERI, P. & CASCIOLA, C. M. 2017 Effect of geometry and Reynolds number on the turbulent separated flow behind a bulge in a channel. *J. Fluid Mech.* **823**, 100–133.

MOSS, W. D., BAKER, S. & BRADBURY, L. J. S. 1979 Measurements of Mean Velocity and Reynolds Stresses in Some Regions of Recirculating Flow. In *Turbulent Shear Flows I*, pp. 198–207. Springer, Berlin, Heidelberg.

NA, Y. & MOIN, P. 1998 Direct numerical simulation of a separated turbulent boundary layer. *J. Fluid Mech.* **374**, 379–405.

NADGE, P. M. & GOVARDHAN, R. N. 2014 High Reynolds number flow over a backward-facing step: structure of the mean separation bubble. *Exp. Fluids* **55** (1), 1–22.

NASH, J. F. 1963 *An analysis of two-dimensional turbulent base flow, including the effect of the approaching boundary layer*. HM Stationery Office.

NASH, J. F. 1967 *A discussion of two-dimensional turbulent base flows*. HM Stationery Office.

NEUMANN, J. & WENGLE, H. 2003 DNS and LES of Passively Controlled Turbulent Backward-Facing Step Flow. *Flow Turbul. Combust.* **71** (1-4), 297.

NEUMANN, J. & WENGLE, H. 2004 Coherent structures in controlled separated flow over sharp-edged and rounded steps. *J. Turbul.* **5**, N22.

OBI, S, AOKI, K & MASUDA, S 1993 Experimental and computational study of turbulent separating flow in and asymmetric plane diffuser. In *9th. Symp. of turbulent shear flows. The University of Kyoto, Japan*. Springer-Verlag.

VAN OMMEN, J. R., SCHOUTEN, J. C., VAN DER STAPPEN, M. L. M. & VAN DEN BLEEK, C. M. 1999 Response characteristics of probe–transducer systems for pressure measurements in gas–solid fluidized beds: how to prevent pitfalls in dynamic pressure measurements. *Powder Technol.* **106** (3), 199–218.

ÖRLÜ, R. & ALFREDSSON, P. H. 2010 On spatial resolution issues related to time-averaged quantities using hot-wire anemometry. *Exp. Fluids* **49** (1), 101–110.

PAREZANOVIĆ, V. & CADOT, O. 2012 Experimental sensitivity analysis of the global properties of a two-dimensional turbulent wake. *J. Fluid Mech.* **693**, 115–149.

PAREZANOVIĆ, V., LAURENTIE, J.-C., FOURMENT, C., DELVILLE, J., BONNET, J.-P., SPOHN, A., DURIEZ, T., CORDIER, L., NOACK, B. R., ABEL, M., SEGOND, M., SHAQARIN, T. & BRUNTON, S. L. 2015 Mixing Layer Manipulation Experiment. *Flow Turbul. Combust.* **94** (1), 155–173.

PHILIP, J., HUTCHINS, N., MONTY, J. P. & MARUSIC, I. 2013 Spatial averaging of velocity measurements in wall-bounded turbulence: single hot-wires. *Meas. Sci. Technol.* **24** (11), 115301.

PHILIP, J. & MARUSIC, I. 2012 Large-scale eddies and their role in entrainment in turbulent jets and wakes. *Phys. Fluids* **24** (5), 055108.

PHILIP, J., MENEVEAU, C., SILVA, C. M. DE & MARUSIC, I. 2014 Multiscale analysis of fluxes at the turbulent/non-turbulent interface in high Reynolds number boundary layers. *Phys. Fluids* **26** (1), 015105.

POPE, S. B. 1988 The evolution of surfaces in turbulence. *Int. J. Eng. Sc.* **26** (5), 445–469.

POPE, S. B. 2000 *Turbulent flows*. Cambridge University Press.

PRASAD, R. R. & SREENIVASAN, K. R. 1989 Scalar interfaces in digital images of turbulent flows. *Exp. Fluids* **7** (4), 259–264.

RAFFEL, M., WILLERT, C. E., WERELEY, S. & KOMPENHANS, J. 2007 *Particle Image Velocimetry: A Practical Guide*. Springer.

ROSHKO, A. & LAU, J. C. 1965 Some observations on transition and reattachment of a free shear layer in incompressible flow. In *Proceedings of the Heat Transfer and Fluid Mechanics Institute*, , vol. 18, p. 157. Stanford University Press.

RUCK, B. & MAKIOLA, B. 1993 Flow Separation over the Inclined Step. In *Physics of Separated Flows — Numerical, Experimental, and Theoretical Aspects*, *Notes on Numerical Fluid Mechanics (NNFM)*, vol. 40, pp. 47–55. Vieweg+Teubner Verlag, Wiesbaden.

ŠARIĆ, S., JAKIRLIĆ, S., BREUER, M., JAFFRÉZIC, B., DENG, G., CHIKHAOUI, O., FRÖHLICH, J., TERZI, D. VON, MANHART, M. & PELLER, N. 2007 Evaluation of Detached Eddy Simulations for predicting the flow over periodic hills. *ESAIM: Proceedings* **16**, 133–145.

SCHLATTER, P. & ÖRLÜ, R. 2010 Assessment of direct numerical simulation data of turbulent boundary layers. *J. Fluid Mech.* **659**, 116–126.

SCHLICHTING, H., GERSTEN, K., KRAUSE, E., OERTEL, H. & MAYES, K. 1968 *Boundary-layer theory*, 6th edn. Springer.

SELBY, G. V., LIN, J. C. & HOWARD, F. G. 1992 Control of low-speed turbulent separated flow using jet vortex generators. *Exp. Fluids* **12** (6), 394–400.

SIGURDSON, L. W. 1995 The structure and control of a turbulent reattaching flow. *J. Fluid Mech.* **298**, 139–165.

SIMPSON, R. L. 1989 Turbulent boundary-layer separation. *Annu. Rev. Fluid Mech.* **21** (1), 205–232.

SONG, S. & EATON, J. K. 2003 Reynolds number effects on a turbulent boundary layer with separation, reattachment, and recovery. *Exp. Fluids* **36** (2), 246–258.

SONG, S. & EATON, J. K. 2004 Flow structures of a separating, reattaching, and recovering boundary layer for a large range of Reynolds number. *Exp. Fluids* **36** (4), 642–653.

SREENIVASAN, K. R. & MENEVEAU, C. 1986 The fractal facets of turbulence. *J. Fluid Mech.* **173**, 357–386.

SREENIVASAN, K. R., RAMSHANKAR, R. & MENEVEAU, C. 1989 Mixing, Entrainment and Fractal Dimensions of Surfaces in Turbulent Flows. *Proc. R. Soc. Lond. A* **421** (1860), 79–108.

STELLA, F., MAZELLIER, N. & KOURTA, A. 2017 Scaling of separated shear layers: an investigation of mass entrainment. *J. Fluid Mech.* **826**, 851–887.

TANI, I., IUCHI, M. & KOMODA, H. 1961 Experimental Investigation of Flow Separation Associated with a Step or a Groove. In *Report/Aeronautical Research Institute, University of Tokyo*. Aeronautical Research Institute, University of Tokyo.

TAVEIRA, R. R., DIOGO, J. S., LOPES, D. C. & DA SILVA, C. B. 2013 Lagrangian statistics across the turbulent-nonturbulent interface in a turbulent plane jet. *Phys. Rev. E* **88**, 043001.

TEMMERMAN, L., LESCHZINER, M. A., MELLEN, C. P. & FRÖHLICH, J. 2003 Investigation of wall-function approximations and subgrid-scale models in large eddy simulation of separated flow in a channel with streamwise periodic constrictions. *Int. J. Heat. Fluid. Fl.* **24** (2), 157–180.

TENNEKES, H. & LUMLEY, J. L. 1972 *A first course in turbulence*. MIT press.

THACKER, A., AUBRUN, S., LEROY, A. & DEVINANT, P. 2013 Experimental characterization of flow unsteadiness in the centerline plane of an ahmed body rear slant. *Exp Fluids* **54** (3), 1–16.

THIESSET, F., MAURICE, G., HALTER, F., MAZELLIER, N., CHAUVEAU, C. & GÖKALP, I. 2016 Geometrical properties of turbulent premixed flames and other corrugated interfaces. *Phys. Rev. E* **93**, 013116.

TOWNSEND, A. A. 1948 Local Isotropy in the Turbulent Wake of a Cylinder. *Aust. J. Chem.* **1** (2), 161–174.

TOWNSEND, A. A. 1949 The Fully Developed Wake of a Circular Cylinder. *Aust. J. Chem.* **2** (4), 451–468.

TOWNSEND, A. A. 1966 The mechanism of entrainment in free turbulent flows. *J. Fluid Mech.* **26** (04), 689–715.

TROPEA, C., YARIN, A. L. & FOSS, J.F. 2007 *Springer Handbook of Experimental Fluid Mechanics*. Springer Science & Business Media.

VEYNANTE, D., LODATO, G., DOMINGO, P., VERVISCH, L. & HAWKES, E. R. 2010 Estimation of three-dimensional flame surface densities from planar images in turbulent premixed combustion. *Exp. Fluids* **49** (1), 267–278.

WEI, T., SCHMIDT, R. & MCMURTRY, P. 2005 Comment on the Clauser chart method for determining the friction velocity. *Exp. Fluids* **38** (5), 695–699.

WESTERWEEL, J., FUKUSHIMA, C., PEDERSEN, J. M. & HUNT, J. C. R. 2005 Mechanics of the Turbulent-Nonturbulent Interface of a Jet. *Phys. Rev. Lett.* **95** (17), 174501.

WESTERWEEL, J., FUKUSHIMA, C., PEDERSEN, J. M. & HUNT, J. C. R. 2009 Momentum and scalar transport at the turbulent/non-turbulent interface of a jet. *J. Fluid Mech.* **631**, 199–230.

WESTERWEEL, J., HOFMANN, T., FUKUSHIMA, C. & HUNT, J. 2002 The turbulent/non-turbulent interface at the outer boundary of a self-similar turbulent jet. *Exp. Fluids* **33** (6), 873–878.

WESTERWEEL, J. & SCARANO, F. 2005 Universal outlier detection for PIV data. *Exp Fluids* **39** (6), 1096–1100.

WESTFALL, P. H. 2014 Kurtosis as Peakedness, 1905 – 2014. R.I.P. *The Am. Stat.* **68** (3), 191.

WESTPHAL, R. V., JOHNSTON, J. P. & EATON, J. K. 1984 Experimental study of flow reattachment in a single-sided sudden expansion. Technical Report CR-3765. NASA, Washington, DC.

WILTSE, J. M. & GLEZER, A 1993 Manipulation of free shear flows using piezoelectric actuators. *J. Fluid Mech.* **249**, 261–285.

WYNGAARD, J. C. 1968 Measurement of small-scale turbulence structure with hot wires. *J. Phys. E: Sci. Instrum.* **1** (11), 1105.

ZHOU, Y. & VASSILICOS, J. C. 2017 Related self-similar statistics of the turbulent/non-turbulent interface and the turbulence dissipation. *J. Fluid Mech.* **821**, 440–457.

Francesco STELLA

Caractérisation d'un décollement turbulent sur une rampe : entraînement et lois d'échelle

Résumé :
Les décollements turbulents massifs sont des phénomènes communs qui peuvent causer des pertes et de nuisances aérodynamiques importantes dans les écoulements industriels, par exemple à l'arrière d'une aile d'avion. Ce travail contribue à leur compréhension par l'analyse phénoménologique d'un décollement turbulent, représentatif d'un grand nombre d'écoulements réels. Le premier objectif est d'identifier les lois d'échelle des décollements turbulents, notamment en rapport avec les caractéristiques de l'écoulement à l'amont de la rampe. Un deuxième objectif est l'analyse, à grande et à petite échelle, des mécanismes de transport de fluide qui pilotent le fonctionnement des décollements. A cet effet, une approche originale est proposée, basée sur une description expérimentale et analytique de la couche cisaillée décollée et des interfaces turbulentes qui la délimitent. Nos résultats suggèrent que les lois d'échelle du décollement varient de façon complexe selon l'interaction de la couche limite à l'amont, de la couche cisaillée et de l'écoulement potentiel extérieur. La taille du décollement est liée à l'intensité de l'entraînement turbulent de masse dans la couche cisaillée, qui à son tour dépend de la turbulence dans la couche limite, bien à l'amont du point de décollement. Cette dépendance pourrait s'appliquer à toute la gamme d'échelles turbulentes responsables du transport de masse. Ces observations montrent clairement le rôle de la couche cisaillée dans le fonctionnement des décollements massifs et suggèrent la faisabilité de stratégies de contrôle nouvelles, de type *retro-action* ou *prédictif*, basée sur l'entrainement turbulent.

Mots clés : décollement turbulent, couche cisaillée décollée, entraînement, lois d'échelle

Characterisation of a turbulent separation over a ramp: entrainment and scaling laws

Abstract :
Massive turbulent separations are common phenomena that can cause sizeable aerodynamical losses and detrimental effects in industrial flows, for example on airplane wings. This work contributes to their understanding with a phenomenological analysis of a canonical turbulent separation, representative of a large number of real flows. The first objective is to identify the scaling laws of turbulent separations, in particular with respect to their dependencies on the characteristics of the flow upstream of the ramp. A second objective is the analysis, both at large and small scale, of the transfert mechanisms that drive the functioning of separated flows. To this end, a new approach is proposed, centered on the experimental and analytical description of the separated shear layer and of the turbulent interfaces that bound it. Our results suggest that the scaling laws of the separated flow vary in a complex way, in function of the interaction of the incoming boundary layer, the separated shear layer and the free-stream. The size of the separation is related to the intensity of turbulent mass entrainment within the shear layer, which in turn depends on the turbulence in the incoming boundary layer, well upstream of the separation point. This dependency might apply over the entire range of turbulent length scales that are responsible for mass transfer. These observations clearly show the role of the shear layer in the functioning of massive separation. They also suggest the feasibility of new control strategies, both of *feedback* and *feed-forward* type, based on turbulent entrainment.

Keywords : turbulent separation, separated shear layer, entrainment, scaling laws

PRISME
Laboratoire Pluridisciplinaire de Recherche Ingénierie des Systèmes, Mécanique, Énergétique

Laboratoire PRISME
8 rue Léonard de Vinci
45072 Orléans Cedex 2

Labex CAPRYSSES
Cinétique chimique et Aérothermodynamique pour Propulsions et Systèmes Énergétiques PROPRES et SÛRS